Controlling Photon and Ion Fluxes in Low Pressure Low Temperature Plasmas

by

Peng Tian

A dissertation submitted in partial fulfillment
of the requirements for the degree of
Doctor of Philosophy
(Electrical Engineering)
in the University of Michigan
2018

Doctoral Committee:

Professor Mark J. Kushner, Chair
Professor John E. Foster
Professor Brian E. Gilchrist
Professor Yogesh B. Gianchandani
Associate Professor Eric Johnsen
Associate Research Scientist Brendan Kochunas

ORCiD: 0000-0001-5042-6219

tianpeng@umich.edu

ACKNOWLEDGEMENTS

The road to a Ph.D. is a long journey. Standing unprepared at the beginning of it, I was burdened with past failures, and my heart was filled with a mixed feeling of self-denial and hope. Marching through the bumpy years, I have learned and changed more than I could have ever imagined, and finally got to the end of it. I could never have done this alone.

The first person to thank is my great advisor, Professor Mark J. Kushner. Having been through all the ups and downs together, he guided me through this journey with his patience, wisdom, knowledge and attitude of life. I will always miss those close talks over the years, and I am truly honored and grateful to be an apprentice of his both in work and in life.

I would like to give my special thanks to the members of my committee- Prof. Brian E. Gilchrist, Prof. John E. Foster, Prof. Yogesh B. Gianchandani, Prof. Eric Johnsen and Dr. Brendan Kochunas for their thoughtful comments and suggestions. I have been well benefitted from their insight of this work along the way.

I am also grateful to all the members I have crossed path with in our lab. Thank you for everything you all have taught me over the years, and for all the fun we had in the office (bar). Fighting an uphill battle on this battle ground is so much easier with you guys around. I also need to thank our legendary secretary Dr. Julia Falkovitch-Khain for taking care of all the travel and paper works, and for the best seminar caterings in town. I want to thank all my collaborators over the years as well, for putting up with my working style and for the new world I was shown from your intriguing studies.

I have been gifted with some wonderful friends in this small town – I was fed after struggling for two days over a deadline, when no restaurant was open; I was housed in the middle of a -20^{o}C winter night, when the heater in my apartment decided to take a break; I was accompanied by them after a heart-broken break up, when I tried to bury myself with work; I was saved on a star-shining highway, when my car finally reached the end of its life; I was needed and granted trust for help, when I stored so much gratitude waiting for them to finally come to me. I would not have survived without them over the years, not to mention the fun we had together that warmed my heart in this lovely but freezing little town.

I would also want to show a special gratitude to our team of Chinese Culture Salon, and to everyone that supported, enjoyed and loved this community of our own. The world as it is has been a much bigger place to me ever since, and I started to truly feel like a part of it. It has been my honor to have served and taken over this organization from the hand of my predecessor: Shuai Niu, Zhichen Zhao and Jingchen Wu. I am glad that I did not abandon our traditions, and I believe the spirit of it will continue to stay alive in this country. Interesting minds will always find a way to meet one another.

Family would always be the last part of an acknowledgement. I have a big family, and we love each other. I have received invaluable supports from all my brothers, sisters, aunts and uncles. They are my forever treasures.

I have a grandma, and she is amazing. She guided me through the darkest time. She raised me up as a child, and she raised me up again and again. She is my angel.

Finally, to my parents. I love you.

TABLE OF CONTENTS

LIST OF FIGURES

LIST OF APPENDICES

LIST OF ACRONYMS

CCP	Capacitively Coupled Plasma
ICP	Inductively Coupled Plasma
VUV	Vacuum Ultra Violet
TE	Thermodynamic Equilibrium
LTE	Local Thermodynamic Equilibrium
non-TE	Non-Thermodynamic Equilibrium
LTP	Low Temperature Plasma
RF	Radio Frequency
CW	Continuous Wave
DC	Direct Current/Duty Cycle
RIE	Reactive Ion Etching
IED	Ion Energy Distribution
IAD	Ion Angular Distribution
IEAD	Ion Energy and Angular Distribution
EED	Electron Energy Distribution
LF	Low Frequency
HF	High Frequency
DF-CCP	Dual Frequency Capacitively Coupled Plasma
TF-CCP	Tri-Frequency Capacitively Coupled Plasma
EAE	Electrical Asymmetric Effect
HPEM	Hybrid Plasma Equipment Model
EMM	Electromagnetic Module
EETM	Electron Energy Transport Module
FKPM	Fluid Kinetics-Poisson Module
RTMCM	Radiation Transport Monte-Carlo Module
PCMCM	Plasma Chemistry Monte-Carlo Module
FDTD	Finite Difference Time Domain
eMCS	electron Monte-Carlo Simulation
S-G	Scharfetter-Gummel
FWHM	Full-width Half-maximum
MPD	Microplasma Devices

ABSTRACT

Low temperature plasmas are widely used in both industry and everyday life, from fluorescent lighting, water purification to important processes in semiconductor industry fabricating electronic devices. In most of these applications, the flux of various energetic species generated by low temperature plasmas are the main promoter of necessary reactions facilitating the applications, by efficiently delivering energy for chemical reactions at molecular level. For example, in the process of plasma etching for semiconductor material processing, fluxes of radicals and ions can selectively react with material on the surface of the wafer, creating surface structures on the order of 10s of nm over the surface area of 10^3 cm^{-2}. In the work of this thesis, the possibility of gaining a better understanding at controlling those fluxes is explored numerically using a two-dimensional plasma equipment model.

In the semiconductor industry, control of ion fluxes and ion energy distributions is critical to optimizing fabrication process and pushing the limit of Moore's law. In this thesis, an unconventional tri-frequency capacitively coupled plasma (CCP) is investigated for scaling of ion fluxes and energy over power of individual frequencies. Compared with the conventional single-frequency and state-of-the-art dual-frequency CCP, we discovered that additional control of ion energy distributions can be achieved by the power of two lower frequencies. Ion fluxes scale positively with increasing power at all frequencies, and are more sensitive to low frequency power.

Vacuum-Ultra-Violet (VUV) photon fluxes are also discovered to have important effects during plasma etching, such that controlling of VUV photon fluxes could potentially benefit to process optimization. This work studied dynamics of a low pressure inductively coupled plasma (ICP), trying to develop approaches of separately controlling VUV and ion fluxes. It was discovered that the ratio of VUV and ion flux, β, can be controlled by pressure, gas mixture and even surface conditions of the reactor wall. β can also be a function of duty cycle in pulsed inductively coupled plasmas (ICPs), caused by the customized electron energy distribution facilitated by the pulse power.

Pulsed ICP has been widely studied for its unique tunability of electron energy distributions. Normally operating with radio frequency sources, power delivery to the ICP can be sensitive to the matching circuit of the system. In this thesis, the dynamics of a pulsed ICP was investigated as a function of the matching network characteristics. Instead of considering power mismatch as a limiting factor, a deliberately tuned off-match condition was used to control the plasma density of a pulsed ICP. Both experimental and computational results show that the time at which the power matches to the ICP determines the plasma properties. Pulsed ICP that matches at a later time exhibits delayed density rise time with a larger final density.

Low temperature plasma sources were also investigated as a device for chemical analysis. A microwave excited microplasma, operated at several watts, was generated in dielectric cavities of hundreds of microns as ionization sources for a novel concept of mass spectroscopy. VUV photon fluxes produced from such microplasma source are then used to ionize samples for spectrometry. Result shows that the power efficiency of VUV emission is less than 1% and saturates as power increases. The VUV spectra can be individually tuned by using Penning gas mixtures.

CHAPTER 1 INTRODUCTION

1.1 What is plasma (Fourth state of matter-plasma)

From the classical view of physics, states of matter are macroscopic reflections of microscopic forces between atoms and molecules of the matter. While all intra-molecular forces share an electromagnetic nature, their range and strength vary significantly depending on the enthalpy, or specifically, average energy of the molecules in the system. Consequently, molecules can show drastically different behaviors which determine the state of the system.

This classical categorization includes solid, liquid, gas, and the forth state of matter, plasma. A solid system has a relative low enthalpy in which low-energy molecules are tightly bonded by intermolecular forces. Atoms and molecules vibrate near a fixed location, maintaining the macroscopic shape of the solid. When enthalpy is increased in a solid system, the energy of individual molecules rises, eventually breaking the strong intermolecular bonds of the solid. Molecules can thus move freely within the boundary of material which loses the ability to maintain its shape, transforming from solid into liquid. Further increases in enthalpy provide molecules with higher energy, enabling them to overcome the intermolecular forces in liquid and move freely in space. Gas is thus formed from liquid. Intermolecular forces in gas are significantly smaller than those in liquid, such that gas can be easily compressed or diffused to fill space. When energy is further delivered into the gas state of the matter, bonds start to break within molecules. This bond-breaking process not only produces dissociated radicals from molecules, it also removes electrons from molecules and atoms, creating electron-ion pairs in space. These free charged particles in plasma, both ions and electrons, preserve a neutral charge for the overall system. At this point, the majority of the intermolecular (or rather inter-particle) forces become electrostatic forces between the charged particles. The behavior of the resulting ionized gas is significantly different from the cooler gas. This new state of matter is called plasma.

During the late 1870s in Sir William Crookes' lab, a partial vacuum glass tube started to glow under high voltage [1]. This was the first observation of plasma in a controlled environment, which was then described as "radiant matter". Several decades later, in 1920s, the term 'plasma' was coined by Irving Langmuir, since the transport of electrons reminded him of "the way blood plasma carries red and white corpuscles and germs" [2,3]. Plasma has since been widely studied. The term plasma is now normally defined as a quasi-neutral gas of charged and neutral particles that exhibits collective behavior [4-6]. It is now believed plasma may be the most abundant form of ordinary matter in the universe, existing in drastically different forms. In an operating inertial confined fusion reactor, plasma can reach an electron density n_e up to 10^{24} cm^{-3} and electron thermal temperature T_e up to 10^3 eV (1 eV ≈ 11,605 K), orders of magnitude higher than the atmosphere of the sun; a much lower electron density is sustained in plasma in a fluorescent light at 10^{10} cm^{-3} and temperature of less than 10s of eV. Interstellar space, commonly believed to hold 99 percent of plasmas in the universe, is filled with ultra-low density plasma of n_e less than 10^2 cm^{-3} and T_e ranging from 10^{-2} – 10^{-1} eV. In Fig. 1.1, plasmas are characterized by n_e and T_e.

With a large range of parameter space of n_e and T_e, plasma is normally classified into three categories based on the kinetic energies (temperatures) of different species, including electrons, ions and neutral particles:

- Thermodynamic Equilibrium (TE) Plasma: temperatures of all species reach equilibrium in the whole system. This equilibrium requires particle velocities of all species obey a Maxwell-Boltzmann distribution [7,8] at a corresponding temperature. Ionization state densities follow Saha-Langmuir ionization equation [9,10] and radiation is described by black body Planck function for a common temperature. TE plasma is a highly idealized plasma that needs to be maintained by extremely high energy and high collision rates between particles, thus TE plasma is rarely seen in its natural form other than in deep layers of stars' atmospheres.
- Local Thermodynamic Equilibrium (LTE) Plasma: a less idealized plasma, in which disturbance of process balancing by radiation is considered. All temperatures are still equal in the system, while radiation deviates from Planck's Law. An example of LTE plasma is a high-intensity electric arc at atmospheric pressure, in which electrons and heavy particles (ions and neutrals) reach an equilibrium temperature up to several eV with a high collision rate.
- Non-Thermodynamic Equilibrium (non-TE) Plasma: temperatures of particles are not necessarily equal. Normally, due to the lower mass of electrons, electron temperature (T_e = 1 – 10s eV) is not in equilibrium with ion temperature (T_i = 0.1-1 eV), both of which are much larger than neutral particles near room temperature (T_n = 298 K = 0.0235 eV). Non-TE plasma is thus normally called low temperature plasma.

Being highly diverse in temperatures of different species, non-TE plasma is a much more complicated system compared with TE and LTE plasmas. The dynamics of non-TE plasma has been a popular research topic for decades and is still under extensive study [11]. The major topic of this thesis focuses on scientific problems of application of such non-TE plasmas, particularly on controlling fluxes of species from such plasmas that are important in plasma-surface interactions. To accommodate conventional notation in the field, non-TE plasma will be referred to as low temperature plasma (LTP) throughout this thesis.

1.2 Low temperature plasma (LTP) sources

Rarely seen in natural conditions, LTPs are normally generated in controlled environments by pumping energy into pure gas or gas mixtures. One widely used source of energy is an electric field. Residual electrons in ambient gas first gain kinetic energy from acceleration, then distribute the energy to gas molecules through collisions. Energy transferred in the electron-molecule collision process is largely stored in electronic states of gas molecules due to the less efficient kinetic energy transfer caused by great mass difference between the two. When energy transfer in a collision exceeds the ionization threshold energy of gas molecules (normally above 10 eV), gas molecules can be ionized, creating additional electrons which will gain energy from the electric field and repeat the process. An avalanche of these ionization processes eventually creates enough charged particles to form a LTP. Such energy transfer in LTP efficiently delivers energy at the molecular level for chemical reactions, while resulting in much less gas heating to the system. This unique feature of LTP has been widely used in various fields of modern society such as material surface processing, fluorescent lighting, satellite propulsion systems, water sterilization, etc. LTP can have drastically different dynamics depending on applications.

1.2.1 Capacitively Coupled Plasma for semiconductor processing

In the semiconductor material processing industry, one widely used plasma source is capacitively coupled plasma (CCP). The term CCP comes from the resemblance of the configuration to capacitors. As shown in Fig. 1.2, in CCP, an electromagnetic field is coupled through two parallel metal plates inside a plasma reactor, on which RF voltage is applied with frequencies ranging from 0.1 – 100 MHz. Plasma discharge is generated in the space between the two plates. This configuration benefits from its optimal uniformity control over the large area of parallel plate electrodes, brought by the uniform distribution of electric field on the electrodes. The applied voltages also accelerate positive ion fluxes from the plasma to the powered electrodes, enabling efficient surface chemical/physical reactions enhanced by ion energies. The bombardment of ion fluxes creates secondary electron emission from surfaces, which is a major contribution to the ionization process in CCP.

1.2.2 Inductively Coupled Plasma for semiconductor processing

Inductively coupled plasma (ICP) sources are motivated by the increasing demand for high density plasma sources in the semiconductor industry. As shown in Fig. 1.3, ICP sources deliver power through a planer (Fig. 1.3a) or cylindrical (Fig. 1.3b) coil antenna [12,13]. RF current applied to the antenna creates time-varying electromagnetic fields in the reactor. Plasma discharge is sustained by the electrons accelerated in the inductive fields. Compared with CCP, electron loss along the path of acceleration is significantly reduced, since electrons trajectories are mostly on revolving paths in the ICP reactor parallel to the reactor wall. In addition, power delivered to plasma in ICP is not partitioned into ion acceleration as it is in CCP. These features enable ICP to produce high density plasmas more efficiently than CCP. More energetic species required for certain applications can thus be generated. In other applications where ion energies are crucial to the process, additional RF/DC bias voltages are applied to substrates, providing independent control of ion fluxes and energies [14].

1.2.3 Microplasma for mass spectrometer ionization source

In chemical analysis applications, miniature plasma sources have been widely studied to develop miniaturized tools for ‘lab-on-chip’ applications [15-20]. Normally called microplasmas, the miniature plasma sources have the size of < 1 mm and operate at relative high pressures (10 Torr – 760 Torr) to leverage Paschen’s scaling law of discharge breakdown. These miniature devices have the benefit of smaller size and lower power consumption, providing unique potential for the development of smaller devices and mass production. In the past decade, progress has been reported in various microplasma types, including miniature ICPs, miniature CCPs, dielectric barrier discharges, microhollow cathode discharges and microwave-induced microplasmas. This thesis examines a microwave-induced microplasma as a vacuum ultraviolet (VUV) photon source. Such microwave-induced microplasmas sustain a discharge in a cavity having typical dimensions of a few hundred microns by accelerating electrons in the fast resonating electric field, which also limits the loss of electrons and ions by drift in the electric field.

1.3 Plasma-surface interaction in LTP

LTPs can generate an extensive variety of species through electron collision processes. For example, in a LTP sustained in an argon and oxygen gas mixture, the following species will be produced: electron e; positive ions: Ar^+, O_2^+, O^+; negative ions: O^-, O_2^-; electronic excited states: Ar^*, O^*, O_2^*; vibrational excited states: $O_2(v)$; rotational excited states: $O_2(r)$; dissociation products (radicals): O. These species are not simply confined in the bulk plasma body, they also generate constant fluxes exiting plasmas, bombarding the surrounding surface. The electronic/kinetic energy of these species is efficiently delivered through bombardment and alter the properties of the surfaces or other targets. These interactions of fluxes of species with surfaces/targets are critically important in most low temperature plasma applications. For example, in water sterilization, discharges created in air produce high fluxes of oxygen radicals O and O_3. Surface interaction of radical fluxes with water is at the core of water purification process [21-24]; in semiconductor processing, etching is enabled/enhanced by ion fluxes from plasma sources delivering energy to the surface of the wafer [25-30]; high energy VUV photon fluxes are generated in LTP in fluorescent lamps. When interacting with phosphor at the inner surface of the light tube, VUV photons excite photons at visible frequencies and provide illumination. Controlling fluxes in LTP applications is important in performance optimization.

1.3.1 Ion fluxes and energy control in CCPs.

Capacitively coupled plasma sources are widely used for plasma etching processes in the semiconductor industry. In the Reactive Ion Etching (RIE) process, energetic ion fluxes from plasma sources bombard the surface of a wafer, selectively removing material on the surface through chemical reactions [25-28]. Selectivity and reaction rates of an RIE process are normally a function of both the magnitude of ion fluxes and the kinetic energy those fluxes carry at the time of bombardment [29,30]. The scaling of selectivity and reaction rate requires control of both ion fluxes and ion energy through the dynamics of the CCP source. In CCP, ion fluxes are strongly determined by the ion density of the plasma, which is normally proportional to the fraction of total applied power that coupled into plasma heating. Meanwhile, the rest of the applied power translates into kinetic energy of these ion fluxes through the voltage drop in the sheath region. The sheath is a transition region between the bulk plasma and contacting surface where charge neutrality starts to break down. In the sheath region of LTP, the higher kinetic energy and smaller mass of electrons produce a larger thermal flux of electrons compared to positive ions, therefore creating greater loss of electrons to the surfaces. Current balance of the fluxes is achieved by a self-generated negatively charged surface, creating a potential drop between the bulk plasma and the surface. This electric field in the sheath repels electron fluxes and accelerates ion fluxes, thus provides large kinetic energy (10s – 100s eV) to the ion fluxes bombarding the surface.

The ion bombardment energy is also crucial to controlling the feature profile of etching. Being accelerated by the sheath voltage, ions gain a large velocity perpendicular to the etching surface. The resulting highly vertical incident angle enables removal of material only from the bottom of the narrow trench, while leaving the material on the side wall unaffected as shown in Fig. 1.4. This anisotropic etching feature of RIE is essential to achieve high resolution pattern transfer in semiconductor processing [31]. In this regard, the ion incident angle is also an important factor. Since the ion energy and incident angle normally distribute over a range of values as opposed to a single value, the two features will be referred to as ion energy distribution (IED), ion angular distribution (IAD), and in its combined form, ion energy and angular distribution (IEAD).

Research on IEDs in a CCP RF sheath was first conducted by Metze et al. [32]. The IED in CCPs is closely related to the sheath dynamics near wafer surface. In a typical CCP in semiconductor etching, the sheath thickness is similar to the Debye length of the plasma, which is normally on the order of hundreds of microns to millimeters. When ions enter the sheath region and are accelerated to the surface, the ion traveling time t_{ion} is determined by both RF voltage and ion inertial mass. Meanwhile, potential drop in the sheath is a function of time following instantaneous RF voltage of period t_{rf} on the electrode. The ratio of t_{ion} and RF voltage period t_{rf} is widely believed to be the critical parameter determining IEDs, which divides the ion fluxes dynamics into multiple regimes in the studies of IEDs [33]. When $t_{ion}/t_{rf} << 1$, the ion travels sufficiently fast that it responds to instantaneous sheath potential as a DC sheath. The energy of ion fluxes is determined by the time at which they enter the sheath. This low frequency (LF) regime produces a bimodal IED averaged over RF cycles of a sinusoidal power supply, exhibiting a low energy peak and a high energy peak as shown in Fig. 1.5. Observation of such behavior is made both experimentally and in simulation by Liu *et al*. [34] and numerically in simulations performed by Tsui, Barnes and Kushner [33,35,36]. In the high frequency (HF) regime in which $t_{ion}/t_{rf} >> 1$, it takes ion fluxes multiple cycles of RF voltage before they cross the sheath. The ions experience an averaged sheath potential regardless of their entry time, exhibiting a single-peaked IED. As frequency moves from LF to HF, an increasing t_{ion}/t_{rf} shrinks the energy gap between the dual peaks in the bimodal profile, eventually merging them to a single peak. Similarly, with a fixed RF excitation, ions with different masses exhibit IEDs deviant from each other due to discrepancies on t_{ion}/t_{rf}. The dependence of IEDs with ion mass is shown in Fig. 1.5 from experiment results of Coburn [37]. In the intermediate frequency (IF) regime ($t_{ion} \approx t_{rf}$), excitation frequency is faster than LF but slow enough for ion inertia to respond to the time-varying electric field in the sheath.

The basic CCP plasma reactor is powered by a single-frequency RF source. RF power is applied to the electrode on which the wafer resides. A DC-blocking capacitor connects the power supply and the electrode, enabling sheath bias voltage generation caused by current self-balancing. The resulting overall sheath potential is the addition of RF excitation voltage and dc bias voltage on the blocking capacitor. However, there are strong limitations on the single-frequency configuration of CCP. The two critical features, ion fluxes and ion energy, are closely coupled to the single power source. Therefore it is difficult to execute independent control of the two features. This issue was first addressed by Goto et al. in the early 1990s by introducing a second frequency to CCPs [38]. The idea of dual frequency CCP (DF-CCP) is to utilize the frequency scaling law in CCP dynamics, which states that the plasma ohmic heating scales positively with the frequency of power sources. In a simplified form, ohmic heating of plasma is $S_{heating}=\omega^2 T_e^{1/2} V_{rf}$, in which ω is RF angular frequency, T_e is electron temperature, and V_{rf} is RF voltage [39]. Goto et al. designed a CCP with a high frequency (HF) source on the top electrode and a low frequency source at the bottom electrode. The HF power in the setup is used to efficiently produce bulk plasma density which controls the ion fluxes, while the LF power at the bottom electrode is intended to control IEAD. A separate control of ion fluxes and IEAD can be partly achieved when using a wide separation of the two frequencies, providing flexibility in etching process [34,40]. However, as noted in multiple studies of frequency coupling, complete separation in control may not be easy to achieve in dual frequency configurations. For example, Booth et al. observed an increase of electron density when increasing the LF power in a 2/27 MHz Ar/O_2 DF-CCP. They found that the 2 MHz power contributed to plasma heating through ion-flux-induced secondary electron emission. They also observed that when increasing the HF power at 27 MHz, voltage of LF decreased even at fixed LF power, which affected the IED to the substrate. The coupling was induced by increasing the ion current to the power supply [41]. Gans et al. also observed coupling of two disparate frequencies in a DF-CCP affecting dynamics of electron density profile, indicating challenges in controlling IEAD and fluxes in DF-CCP configuration of this type [42].

In the early 2000s, Czarnetzki et al. proposed a novel dual frequency CCP [43], in which both frequencies are applied on the same electrode at the wafer. This configuration exploits the coupling between two frequencies, one of which is an even harmonic of the other. Instead of frequencies or magnitude of RF voltage, dynamics of the sheath is controlled through the phase difference of the harmonic frequencies. The superimposed RF wave form varies with the phase difference which induces electrical asymmetry of current balances on the surfaces. As a result, the self-generated DC bias scales with different degrees of asymmetry of current balance on the blocking capacitor to produce different shapes of IED as a function of phase difference (Figure1.6). The ion fluxes in this configuration stay relatively constant over the range of phase variation. This is known as the electrical asymmetric effect (EAE). For example, Schulze et al. first measured the DC bias and IED of a DF-CCP in argon at 13.56/27.12 MHz. They observed tunability of DC bias voltage with phase difference by more than half of the applied RF voltages in the experiment. The resulting mean ion energy at 90-degree phase difference was 80 percent larger than that at 0-degree. Ion fluxes in this experiment remains constant to a close approximation [44]. EAE effect indicates a promising path in separate control of ion fluxes and IEAD and has been widely studied in recent years [45-47].

1.3.2 Photon fluxes / photon ion fluxes ratio in LTPs.

Photons are the product of relaxation of high energy excited states in molecules and atoms. Photon fluxes are ubiquitous in LTPs since they are continuously emitted from the electronic excited molecules and atoms, and the plasma is only visible to the naked eye through photon emission in the band of visible light. Photon dynamics are drastically different from other species. As the quantum representation of electromagnetic waves, photon transport occurs at the speed of light. The ‘collisional’ interactions of photons with molecules and ions are also strictly of a quantum nature; that is, the ‘collision’ of a photon with molecules and ions can only happen when photon’s energy is fully transferred to the colliding partner, at which time the photon vanishes from the system. As shown in Fig. 1.7, resonant photons in plasmas may undergo many absorptions and reemissions between the site of initially being emitted and leaving the plasma.

This process of absorption and reemission is known as radiation trapping and has the overall effect of lengthening the effective lifetime of the excited state as observed from outside the plasma [48]. This extended lifetime is expressed as a radiation trapping factor – the ratio of the effective lifetime including reabsorption to the natural lifetime of the excited state. At high pressures, the trapping factor can be 10^4 or larger, resulting in the resonant radiative excited state being effectively metastable. Photons that do escape the plasma tend to be at frequencies in the wings of the optical line shape function where the likelihood for absorption (and emission) is small compared to line center. The flux of photons that do escape the plasma are a small fraction of total photon flux in the middle of the plasma due to absorption and reemission. For radiation transport that is heavily trapped, the vast majority of photons are emitted, absorbed and remitted many thousands of times before escaping the plasma.

Photon fluxes can carry energy ranging from 0.1 – 10s eV, which could be efficiently delivered to surfaces for chemical reactions. Particularly, the importance of high energy photons in the UV/VUV range increases in the semiconductor processing industry as the feature size of semiconductor devices keeps scaling down. In certain cases, VUV fluxes during processing can induce damage to microelectronics materials. For example, ultra-low dielectric constant films, such as porous SiOCH, are used as the interlayer dielectric in interconnect wiring in microelectronics devices, and can be damaged by VUV photons during plasma etching [49,50]. Bond breaking by VUV photons and subsequent water uptake into the films increases the dielectric constant of the film. Other effects are synergistic that result from simultaneous fluxes of VUV photons and ion bombardment. For example, the roughening of photo-resist has different characteristics as a function of temperature depending on whether the films receive only ion fluxes or fluxes of both ions and VUV photons [51,52]. The third includes photon stimulated processes. Recent measurements have shown that VUV photon fluxes from ICPs onto halogen passivated silicon can enable etching even when the energies of the ion fluxes are below the accepted thresholds for ion produced etching [53].

These observations have motivated studies of VUV fluxes in plasma processing. Woodworth et al. [54] measured absolute intensities of VUV emission from ICPs in the context of plasma etching of metals. They found that the total VUV intensity (95 nm – 250 nm) from a 10 mTorr Cl_2/BCl_3 plasma powered at 1100 W exceeded 0.5 mW/cm^2, or a flux of 5×10^{14} $cm^{-2}s^{-1}$. This emission was dominated by the resonance lines of neutral Cl at 137-138 nm. Woodworth et al. [55] made similar measurements of VUV fluxes sustained in fluorocarbon and argon/fluorocarbon gas mixtures at pressures of tens of mTorr and powers of hundreds of watts. In pure fluorocarbon gases (C_2F_6, CHF_3, C_4F_8), VUV fluxes in the range of 70-140 nm were 1.0×10^{14} $cm^{-2}s^{-1}$ principally from the resonance lines of neutral C and F. When diluting the fluorocarbon gases with argon (e.g., Ar/C_2F_6 = 50/50), the total VUV flux increased by an order of magnitude, 1.1×10^{14} $cm^{-2}s^{-1}$ to 1.15×10^{15} $cm^{-2}s^{-1}$, due to the additional radiation resulting from the resonance lines of Ar at 104.8 nm and 106.7 nm.

1.4 Modeling of LTP

Modeling of LTP has become increasingly important in both scientific and industrial applications over the years. As a scientific tool, modeling platforms can provide more detailed information and unparalleled controllability of LTP problems that are difficult to obtain in experiment. These advantages assist researchers to gain more insight and improved understanding of the underlying scaling and physics of the problem.[11,56] Additionally, computational platforms are also used as a critical instrument of designing plasma equipment in modern industry. The increasingly sophisticated design of such equipment, especially in semiconductor industry, can benefit from appropriate simulations on both time and cost.

Simulation of LTP is a multi-physics-chemistry problem that addresses kinetics of species, electromagnetic fields, radiation transport and large number of plasma gas reactions and surface interactions. LTP models normally share similar technique updating electromagnetic fields by solving Maxwell/Poisson’s equations, and can be categorized based on how species are treated: fluid, kinetics (particle) and hybrid modeling. In fluid models, plasma species are numerically addressed as fluid. Density, transport and temperature of such species are calculated by solving continuity, momentum and energy equation individually in the model.[57,58] Compared with kinetic and hybrid methods, fluid modeling is computationally effective and can be advantageous in problems that are time sensitive or with complicated plasma chemistries. Meanwhile, kinetic simulations are more time-consuming, since a large number of pseudoparticles (up to 10^6-10^7) is normally used to represent plasma species.[59-61] Kinetic equations are solved for each pseudoparticle that together describe the collective bulk plasma behavior. This provides better kinetic fidelity of plasma properties at the cost of computational power. With understanding of both fluid and kinetic approaches, hybrid models attempt to balance the computational speed and accuracy in plasma simulation. Kinetic approaches are used for species that requires accurate energy distribution calculation, e.g. electrons, while other plasma species are treated as fluid.[62]

Over the past decades, different platforms developed in those categories have aided LTP community for improving understanding of plasma processes and performance of plasma equipment.[57-62] The outcome of those simulation investigations is sensitive to the accuracy of the fundamental parameters used in the model, including physical parameters, material properties, reaction rate and collision cross sections. Most of fundamental physical parameters and material properties, e.g. permittivity, conductivity, mass of species, are well characterized with accurate values. The reaction rate and collision cross sections of chemical reactions, however, is not as well measured and archived. For example, in a typical Ar/C_4F_8/O_2 plasma for SiO_2 etching, electron impact processes of C_4F_8 will produce up to 20 dissociation species of C_xF_y. These dissociation products all have corresponding positive or negative ions. Considering multiple excited states of Ar and oxygen dissociation products, the overall heavy species (species other than electron) can be more than 60, from which the gas phase plasma chemistry mechanism needs to be assembled. The electron impact reaction cross sections of those species are the foremost data to be acquired, since those reactions determine power delivery from energetic electrons to the bulk plasma. However, for transient or uncommonly used species, e.g. $C_2F_{6,}$ reliable experiment data are not readily available. Collisions between heavy species are another class of reactions, in which reaction rates have not been characterized by previous work. This considerable gap between experimental data and simulation input can partly be filled with theoretical calculations.[63] In other cases, estimates need to be made in analogy with similar species.[64,65]. One of the most complete C_4F_8 mechanism in the literature developed by Vasenkov *et.al.* still has more than 10% reactions requires those techniques to find the reaction rate.[66] A sensitivity study on reaction mechanism indicates that this shortage of experimental reaction data could have considerable impact on the outcome of the LTP simulation.[67] Consequently, comparison between LTP experiment and simulation results is not as ideal as modeling results in other field like optics or computational fluid dynamics, in which most of the input of the model stands on solid experimental results. The outcome of LTP modeling is often considered sound within the order of magnitude of matching with experiment measurement, and is most often used as a tool to investigate fundamental mechanisms of physics or scaling trends of certain control parameters.

1.5 Summary

Under the pressure of Moore’s Law, the semiconductor industry is pushing the limit of critical dimensions to below 10 nm. As a crucial and irreplaceable technology, LTP processing is facing increasing demands to understand the dynamics and control fluxes in those applications. Meanwhile, the rapid development of reliable and novel miniature chemical/medical diagnostic devices also requires better understanding of LTP processes in microscale reactors. This thesis addresses topics in these areas through computational methods. Specifically, the thesis presents results on the study of controlling the dynamics and ion and photon fluxes in the following LTPs: inductively coupled plasma, capacitively coupled plasma and microwave-induced microplasma. A 2-D modular hydrodynamic plasma model, the Hybrid Plasma Equipment Model (HPEM), was used for simulating plasma properties and surface fluxes in plasma reactors. The structure of this thesis is as follows:

In Chapter 2, the numerical tool HPEM will be discussed in detail with modifications incorporated in the modules. The structure of the code will be introduced with dominating equations that describe different physical/chemical processes addressed in a modular manner.

Chapter 3 discusses studies of the dynamics of a pulsed ICP. Instead of a fully matched circuit, a mismatch caused by change of plasma properties is introduced for ICP simulation. Instantaneous impedance of the plasma and coil parasitic are solved by a distributed circuit model coupled with a circuit match box. Power reflection at the input of match box is then calculated to adjust the power delivery in the bulk of the plasma. With a small pulse frequency of several kHz, impedance of the plasma is constantly changing at the beginning of the pulse. It is discovered by both experiments and simulation that by varying the match box parameter which is fixed over the pulsing of ICP, power reflection during the pulse can be continuously tuned, which translates to control of the dynamics of a pulsed ICP as a function of pressure and matching time in the pulse period.

Results from a computational investigation of VUV fluxes produced in low-pressure (tens of mTorr) continuous wave (CW) and pulsed ICPs sustained in Ar, Ar/Xe and He/Ar gas mixtures will be reviewed in Chapter 4. VUV fluxes are characterized in the results. The chapter will also propose methods to control the absolute value of VUV fluxes, their spectra and the ratio of VUV fluxes to ion fluxes. It is found that in rare gas ICPs, flux of VUV photons can be controlled via power form and plasma pressure. Coarse tuning of the VUV emission spectrum is also possible through the mole fractions of the rare gas mixture components.

Chapter 5 further investigates control of VUV photon fluxes and VUV/ion fluxes ratio in the context of actual etching gas mixture used in industry plasma etching reactors, motivated by the VUV photon assisted etching for ions below etching threshold in halogen-containing plasmas [53]. This section reports observations of controlling VUV photon fluxes, and VUV/ion fluxes ratio in a Ar/Cl_2, partially ion-ion inductively coupled plasma. A key finding emerging from this study is that the ratio of total VUV photon flux to ion fluxes can be controlled by pressure, pulse power and gas mixtures in ICPs sustained in Ar/Cl_2 mixtures. A pulsed power can tune the plasma more favorable to producing radiative states of VUV photons, leaving the peak and cycle-averaged photon/ion fluxes ratio a function of the pulse power. The work also discovered that VUV emission from Cl atoms is strongly influenced by surface conditions of plasma reactor, through Cl related surface reactions.

In Chapter 6, control of ion fluxes and ion energy distribution is studied in a tri-frequency capacitively coupled plasma (TF-CCP). Motivated by separately controlling ion fluxes and energy by different frequencies, and EAE effects, three harmonic frequencies of 5/10/40 MHz were applied to the same electrode. Plasma dynamics, ion fluxes and ion energy distribution are carefully discussed as a function of various individual power of each frequency. It is observed that with the same fixed power input, the sheath dynamics is largely affected by the low frequency due to its higher voltage. As a result, IEDs in TF-CCP is most sensitive to the power of low frequency. Ion fluxes and plasma density however, are not individually tunable by high frequency power. Coupling of the low and high frequencies is stronger at TF-CCP since the ion fluxes influence power delivery of both lower frequencies..

A microwave-excited microplasma is investigated in Chapter 7 as a VUV photon source for a novelty design of a mass spectrometer. Plasma properties, VUV emission and experimental measurements are discussed in a HPEM model. The microplasma device is discovered to have a VUV emission power efficiency of a few percent with low power deposition (several W). Saturation of VUV emission with increasing power is also observed.

In Chapter 8, content of the thesis will be summarized with future work proposed.

1.6 Figures

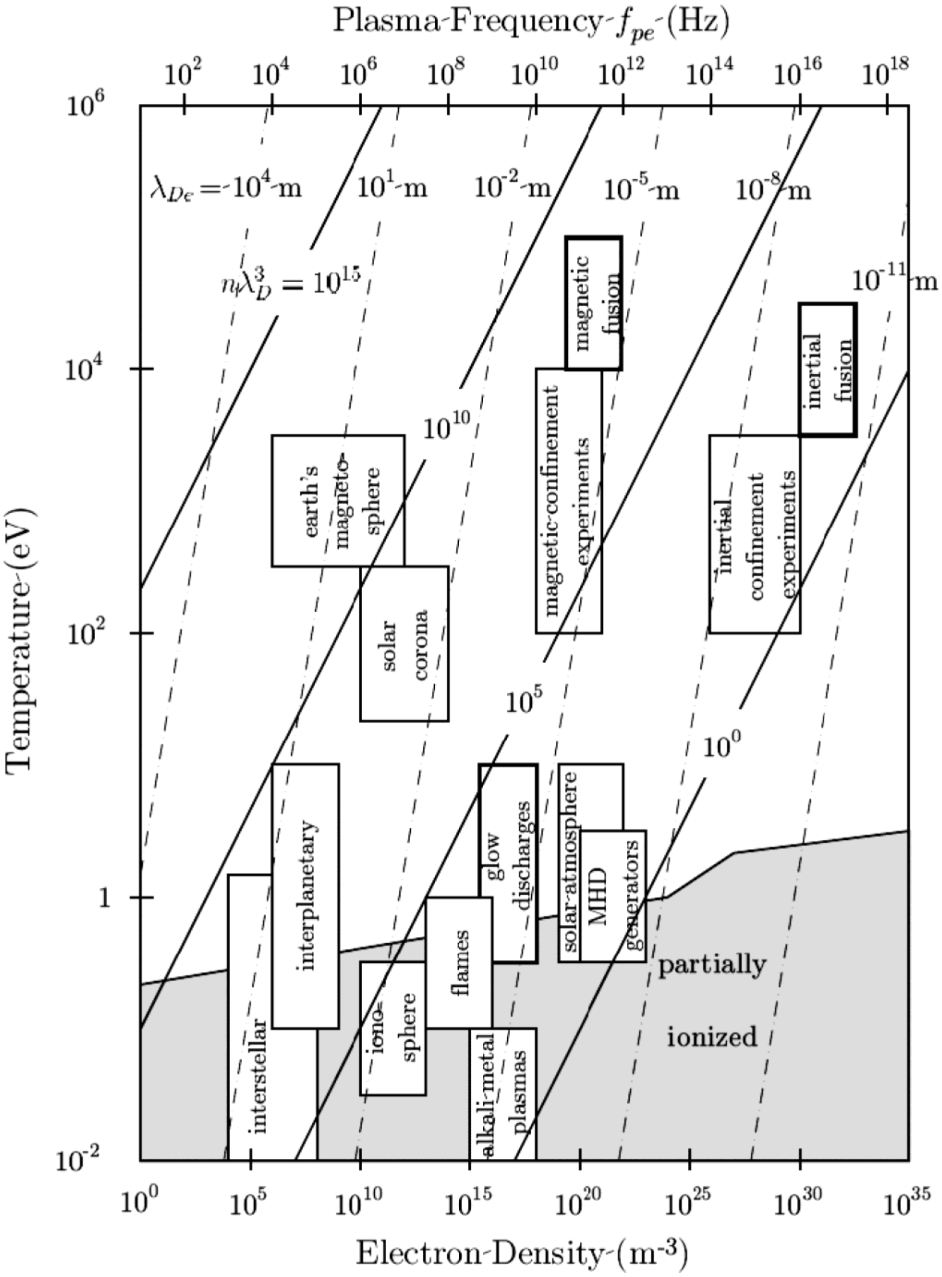

Fig. 1.1 Plasma characterized by electron density and temperature [4].

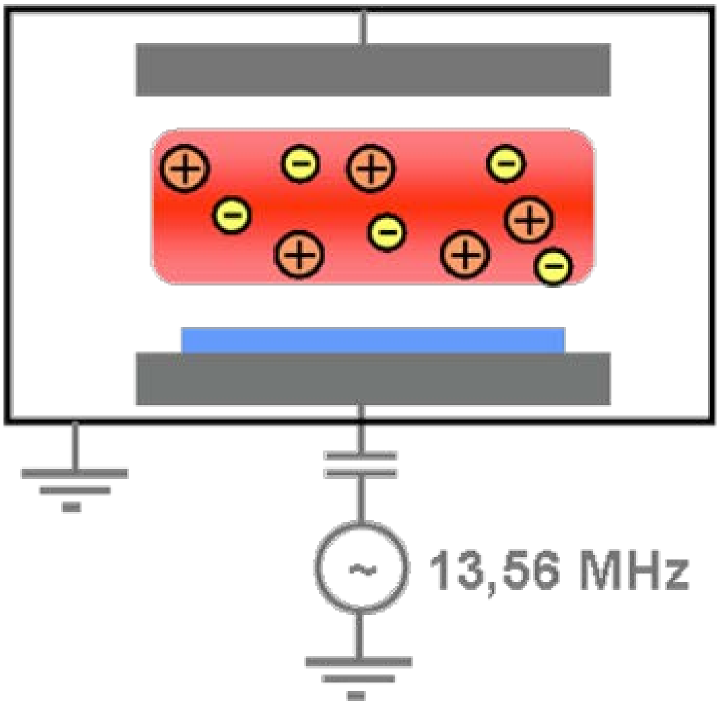

Fig. 1.2 Geometry of a single-frequency capacitively coupled plasma

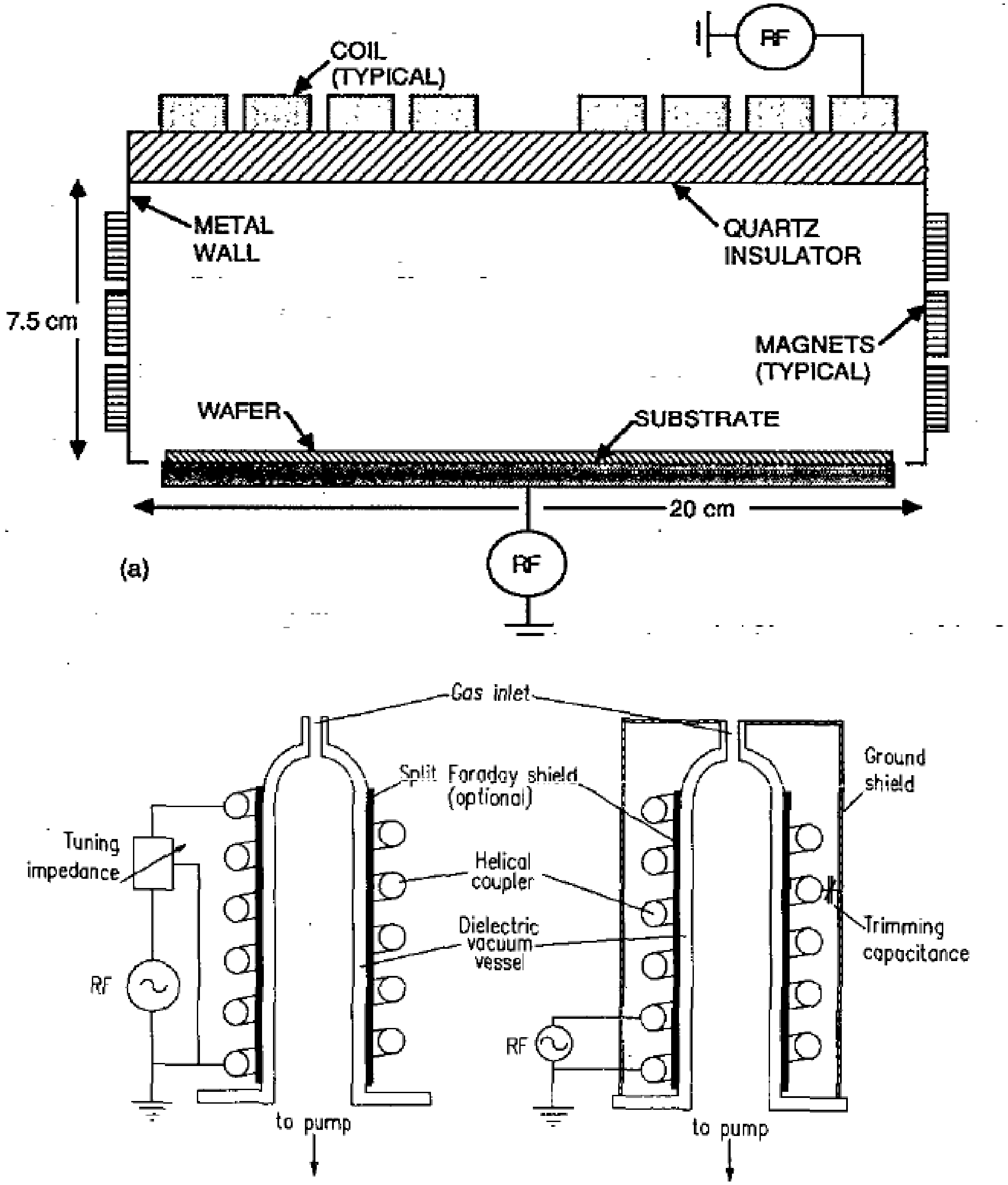

Fig. 1.3 Examples of ICP reactors: a) planar coil antenna [12] and b) cylindrical coil antenna [13].

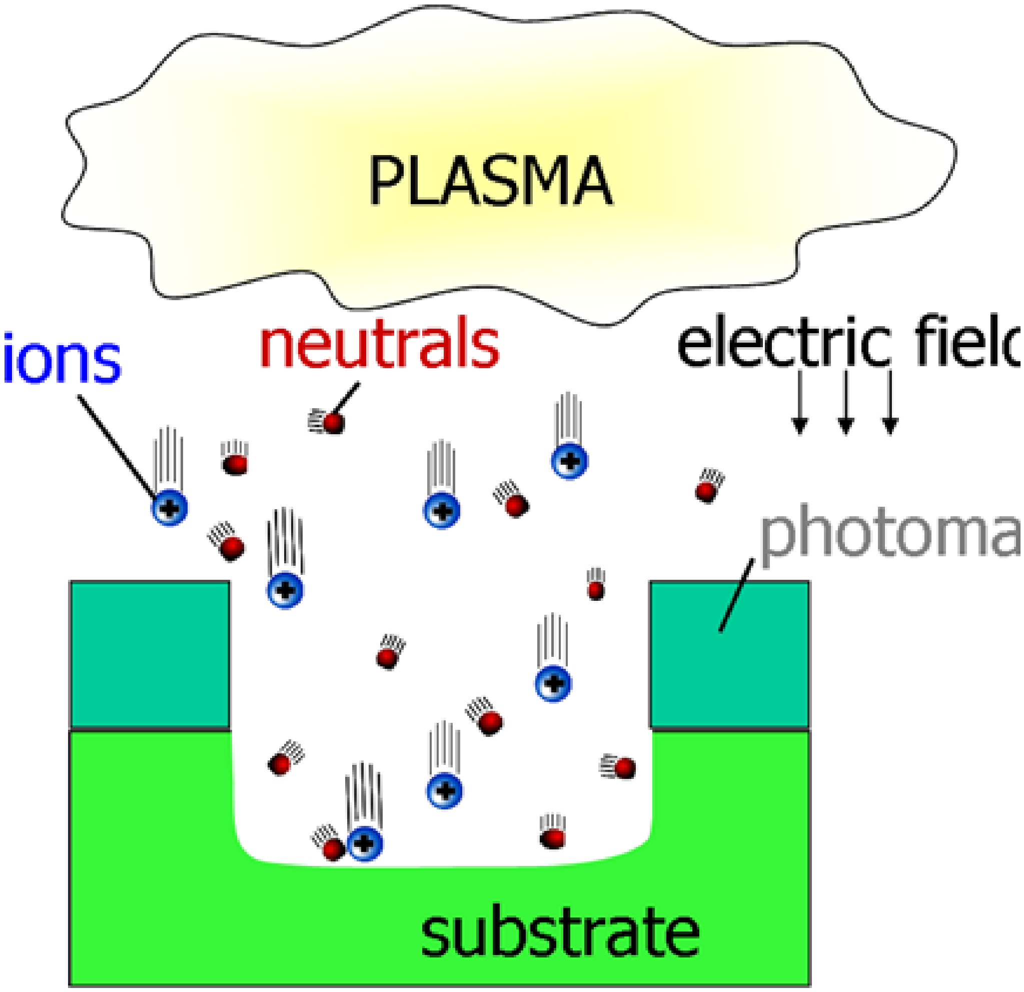

Fig. 1.4 Anisotropic etching by low temperature plasma

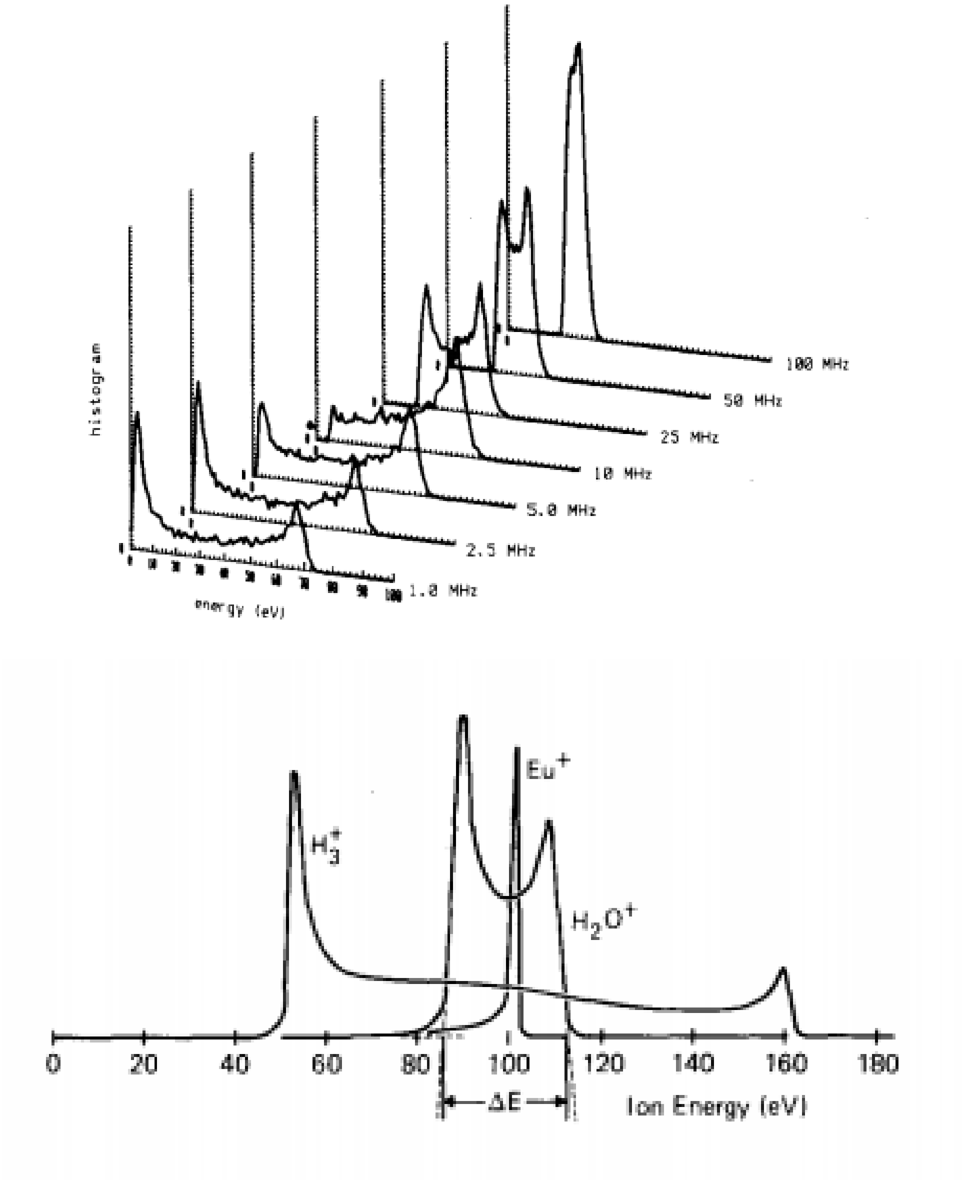

Fig. 1.5 a) ion energy distribution in CCP as a function of frequency [33], b) dependence of ion energy distribution in CCP with ion mass [37].

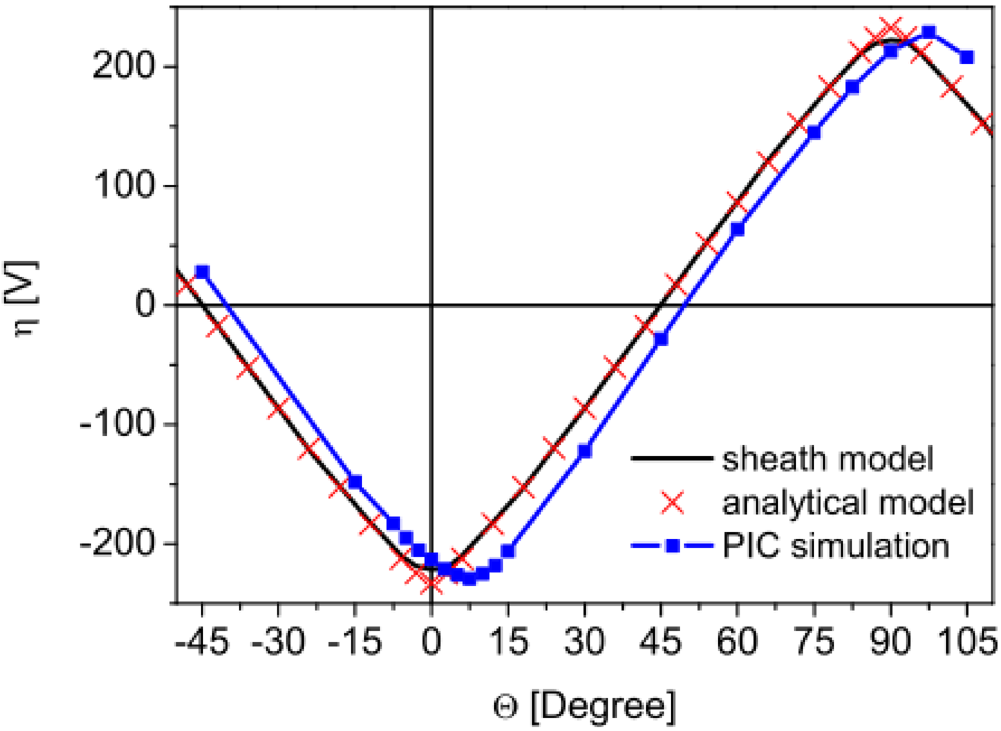

Fig. 1.6 Change of relative DC self-bias in a dual-frequency CCP as function of phase difference of the two harmonic frequencies [42].

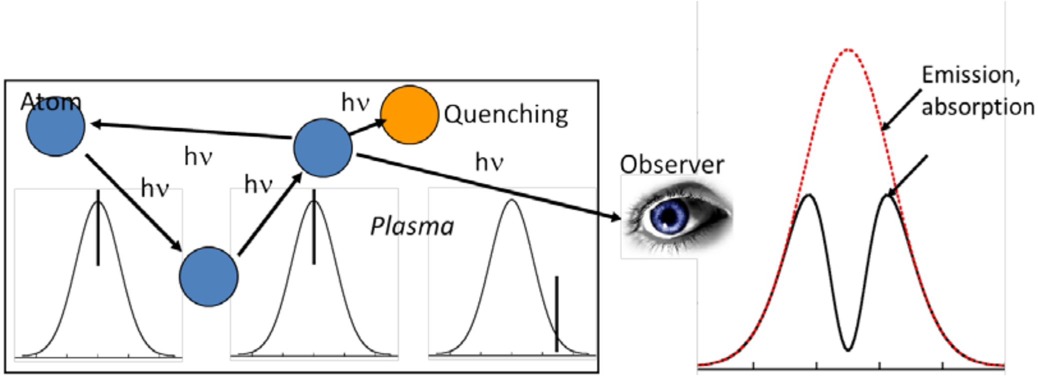

Fig. 1.7 Radiation trapping process in low temperature plasmas and the observed line shape function of photons from outside.

1.7 References

[1] Lecture by William Crookes at British Association for the Advancement of Science, Sheffield, Aug. 1879

[2] I. Langmuir, Proc. Nat. Acad. Sci. U.S., **14**, 628 (1928)

[3] L. Tonks and I. Langmuir, Phys. Rev. **33,** 195 (1929)

[4] F. F. Chen, Introduction to Plasma Physics and Controlled Fusion. Vol. I: Plasma Physics, Springer, 2006.

[5] James D. Callen, Fundamentals of Plasma Physics, University of Wisconsin, Madison, 2006.

[6] Y. P. Raizer, Gas Discharge Physics, Springer, 1991.

[7] J. C. Maxwell, the London, Edinburgh, and Dublin Philosophical Magazine and Journal of Science, 4th series, **vol.19**, 19 (1860)

[8] J. C. Maxwell, the London, Edinburgh, and Dublin Philosophical Magazine and Journal of Science, 4th series, **vol.20**, 21 (1860)

[9] M. N. Saha, Philosophical magazine. Series 6, **40(238)**, 472 (1920)

[10] K. Kingdon, I. Langmuir, Physical Review, **22(2),** 148 (1923)

[11] S. Samukawa, M. Hori, S. Raulf, K. Tachibana, P. Bruggeman, G. Kroesen, J. Ch. Whitehead, A. B. Murphy, A. F. Gutsol, S. Starikovskaia, U. Kortshagen, J.-P. Boeuf, T. J. Sommerer, M. J. Kushner, U. Czarnetzki and N. Mason, J. Phys. D: Appl. Phys. **45** 253001 (2012)

[12] P. L. G. Ventzek, T. J. Sommerer, R. J. Hoekstra and M. J. Kushner, Appl. Phys. Lett. **63,** 605 (1993)

[13] J. Hopwood, Plasma Sources Sci. Technol. **1**, 109 (1992)

[14] M. Schaepkens, T.E. F. M. Standaert, N. R. Rueger, P. G. M. Sebel, G. S. Oehrlein and J. M. Cook, J. Vac. Sci. Technol. A **17(1)**, 26 (1999)

[15] D. Luo, Y. Duan, Trends in Analytical Chemistry, **Vol 39**, 254 (2012)

[16] A. Bass, C. Chevalier and M. W. Blades, J. Anal. At. Spectrom., **16**, 919 (2001)

[17] V. Karanassios, K. Johnson and A. T. Smith., Anal Bioanal Chem., **388**, 1595 (2007)

[18] S. Weagant, V. Karanassios, Anal Bioanal Chem., **395**, 577 (2009)

[19] S. Weagant, V. Chen, V. Karanassios, Anal Bioanal Chem., **401**, 2865 (2011)

[20] V. Karanassios, Spectrochimica Acta Part B, **59**, 909 (2004)

[21] B. Eliasson and U. Kogelschatz, IEEE Trans. on Plasma Sci, **vol 19**, 1063 (1991)

[22] M. Kogoma and S. Okazaki, J. Phys. D: Appl. Phys. **27**, 1985 (1994)

[23] B. Eliasson, M. Hirth and U. Kogelschatz, J. Phys. D: Appl. Phys., **20**, 1421 (1987)

[24] M. A. Malik, A. Ghaffar and S. A. Malik, Plasma Sources Sci. Technol. **10**, 82 (2001)

[25] J. Hayes and T. Padhumsoporn, Solid State Technol. **11**, 71 (1980)

[26] B. Chapman, Glow Dicharge Processes: Sputtering and Plasma Etching (Wiley, New York, 1980)

[27] M. Armacost *et al.*, IBM J. Res. Dev. **43**, 103 (1999)

[28] Sergey K. Tolpygo and Denis Amparo, J. Phys.: Conf. Ser. **97** 012227, (2008)

[29] D. Zhang and M. J. Kushner, J. Vac. Sci. Technol. A **19(2)**, 524 (2001)

[30] G. S. Oehrlein, P. J. Matsuo, M. F. Doemling, N. K. Rueger, B. E. E. Kastenmeier, M. Schaepkens, T. Standaert, and J. J. Beulens, Plasma Sources Sci. Technol. **5**, 1193 (1996)

[31] V. Donnelly and A. Kornblit, J. Vac. Sci. Technol.A **10**, 3048 (1992)

[32] A. Metze, D. W. Ernie and H. J. Oskam, J. Appl. Phys. **65**, 993 (1989)

[33] M. S. Barnes, J. C. Forster, and J. H. Keller, IEEE Trans. On Plasma Sci. **19**, 2241 (1988)

[34] J. Liu, Q-Z. Zhang, Y-X. Liu, F. Gao and Y-N. Wang, J. Phys. D: Appl. Phys. **46**, 235202 (2013)

[35] R. T. C. Tsui, Phys. Rev. **168**, 107 (1968)

[36] M. J. Kushner, J. Appl. Phys. **58**, 4024 (1985)

[37] J. W. Coburn and E. Kay, J. Appl. Phys. **43** 4965 (1972)

[38] H. H. Goto, H. D. Lowe and T. Ohmi, J. Vac. Sci. Technol.A **10**, 3048 (1992)

[39] M. A. Lieberman and A. J. Lichtenberg, Principles of Plasma Discharges and Materials Processing, Wiley-Interscience, New Jersey, 2005

[40] J. Liu, Y-X. Liu, Z-H. Bi, F. Gao and Y-N Wang, J. Appl. Phys. **115**, 013301 (2014)

[41] J. P. Booth, G. Curley, D. Marić and P. Chabert, Plasma Source Sci. Technol., **19**, 015005 (2010).

[42] T. Gans, J. Schulze, D. O’Connell, U. Czarnetzki, R. Faulkner, A. R. Ellingboe and M. M. Turner, Appl. Phys. Lett. **89**, 261502 (2006)

[43] U. Czarnetzki, B. G. Heil, J. Schulze, Z. Donkó, T. Mussenbrock and R. P. Brinkmann, 2nd Int. Workshop on Non-equilibrium Processes in Plasmas and Environmental Science, (2009)

[44] J. Schulze, E. Schungel and U. Czarnetzki, J. Phys. D: Appl. Phys. **42**, 092005 (2009)

[45] J. Schulze, A. Derzsi and Z. Donkó, Plasma Sources Sci. Technol. **20** 045008 (2011)

[46] T. Lafleur and J. P. Booth, Appl. Phys. Lett. **102**, 154104 (2013)

[47] D. Hrunski, A. Janssen, T. Fritz, T. Hegemann, C. Clark, U. Schreiber, G. Grabosch, Thin Solid Films **532**, 56 (2013)

[48] M. T. Herd, J. E. Lawler, and K. L. Menningen, J. Phys. D: Appl. Phys. **38**, 3304 (2005).

[49] J. Lee and D. B. Graves, J. Phys. D **43,** 425201 (2010).

[50] S. Uchida, S. Takashima, M. Hori, M. Fukasawa, K. Ohshima, K. Nagahata, and T. Tatsumi, J. Appl. Phys. **103,** 073303 (2008).

[51] D. Nest, D. B. Graves, S. Engelmann, R. L. Bruce, F. Weilnboeck, G. S. Oehrlein, C. Andes and E. A. Hudson, Appl. Phys. Lett. **92**, 153113 (2008).

[52] M. J. Titus, D. B. Graves, Y. Yamaguchi, and E. A. Hudson, J. Phys. D: Appl. Phys. **44**, 085204 (2011).

[53] H. Shin, W. Zhu, V. M. Donnelly, and D. J. Economou, J. Vac. Sci. Technol. A **30**, 021306 (2012).

[54] J. R. Woodworth, M.G. Blain, R. L. Jarecki, T. W. Hamilton, and B. P. Aragon, J. Vac. Sci. Technol. A **17**, 3209 (1999).

[55] J. R. Woodworth, M. E. Riley, V. A. Amatucci, T. W. Hamilton, and B. P. Aragon, J. Vac. Sci. Technol. A **19**, 45 (2011).

[56] H. C. Kim, F. Iza, S. S. Yang, M. Radmilovic-Radjenovic and J. K. Lee, J. Phys. D: APpl. Phys. **38**, R283 (2005)

[57] A. Stewart, P. Vitello, and D. B. Graves, J. Vac. Sci. Technol. B. **12**, 478 (1994)

[58] A. Stewart, P. Vitello, D. AB. Graves, E. F. Jaeger, and L. A. Berry, Plasma Sources Sci. Technol. **4**, 36 (1995)

[59] C. K. Birdsall, IEEE Trans. Plasma Sci. **19**, 65 (1991)

[60] V. Vahedi, M. Surendra, Computer Physics Communication. **87**, 179 (1995)

[61] G. Wakayama and K. Nanbu, IEEE Trans. Plasma Sci. **31**, 638 (2003)

[62] M. J. Kushner, J. Phys. D. **43**, 185206 (2010)

[63] H. Kazumi, R. Hamasaki and K. Tago, Plasma Sources Sci. Technol. **5**, 200 (1996)

[64] S. Rauf and P. L. G. Ventzek, J. Vac. Sci. Technol. A **20(1)**, 14 (2002)

[65] G. I. Font, W. L. Morgan and G. Mennenga, J. Appl. Phys. **91**, 3530 (2002)

[66] A. V. Vasenkov, X. Li, G. S. Oehrlein and M. J. Kushner, J. Vac. Sci. Technol. A **22(3)**, 511 (2004)

[67] D. Edelson and D. L. Flamm, J. Appl. Phys **56**, 1522 (1984)

CHAPTER 2   DESCRIPTION OF THE MODEL

The Hybrid Plasma Equipment Model (HPEM) was utilized to perform plasma dynamic simulations at reactor scale for this thesis. HPEM is a two-dimensional hybrid plasma model which combines both fluid and kinetics approaches. Different physical processes of plasma dynamics are addressed by separate modules in the hierarchical structure in HPEM [1-5]. Developed for low pressure (< 10 Torr) and low temperature plasma (LTP) simulation, HPEM is capable of modeling a broad range of plasma processing reactors. For simulations of a specific reactor type, computational load is minimized by calling modules that are specifically optimized for the application, which the modular design of HPEM enables. Physical processes of the same nature can be addressed by separate modules depending on the plasma operation scheme. For example, interaction of an electromagnetic power source with plasma for different reactor designs is addressed by three different modules in HPEM: the electromagnetic module (EMM), the microwave excitation module, and the finite difference time domain electromagnetics module. These correspond to inductively coupled plasma, electron cyclotron resonance plasma and high frequency capacitively coupled plasma with wave effect, respectively. In EMM, the electromagnetic field of an inductive coil is calculated by solving Maxwell's equation in frequency domain. For ECR plasma simulation, the incoming microwave is solved using a finite difference time domain (FDTD) approach with the input boundary condition set as the aperture of the source antenna. The Maxwell wave module also solves Maxwell's equation using a FDTD algorithm to address a RF field source from co-axial cable of a CCP reactor. The resulting electron energy distribution, f_e, can also be obtained by either solving an electron energy equation or using a Monte-Carlo technique. The application-based module selection greatly increases the computation efficiency of the model. In the following sections, modules that are used in the scope of this thesis will be described in detail, including the EMM, the Electron Energy Transport Module (EETM), the Fluid Kinetics-Poisson Module (FKPM), the Radiation Transport Monte-Carlo Module (RTMCM) and the Plasma Chemistry Monte-Carlo Module (PCMCM).

In HPEM, time evolution of plasma dynamics is achieved through sequential calling of modules in an iterative manner. Physical processes are addressed in serial by different modules, while updates of physical properties are exchanged between modules within one global time step. Fig. 2.1 depicts HPEM's information exchange. Using ICP as an example, one global iteration in the HPEM starts with an estimation of species' densities provided as input parameters. The calculated plasma conductivity is then pipelined into EMM to solve for inductively coupled electromagnetic fields $\vec{E}$ and $\vec{B}$ from frequency domain Maxwell equations which provide a frequency domain wave equation. $\vec{E}$ and $\vec{B}$ are then combined with a static electric field for the total electromagnetic field $\vec{E}$ and $\vec{B}$. EETM calculates electron kinetics properties from $\vec{E}$, $\vec{B}$ and species' densities, using either the electron energy equation, or a Monte-Carlo technique. It produces electron energy distribution f_e, electron temperature T_e and electron impact source functions S_e that are transported into FKPM. In FKPM, electrostatic field $\vec{E}_s$, densities N, fluxes $\vec{\phi}$ and temperatures T of all species are updated by solving a transport and continuity equation and the Poisson equation. The electron temperature can be updated in real time, or the electron temperature can be periodically updated within FKPM by calling EETM with the evolution of electric field and species' densities and temperatures. The updated species' densities and temperatures are then transferred into RTMCM, in which fluxes of photons species and change of species' densities are calculated by addressing radiation transport and photon-induced reactions. The resulting values of those variables from all the above modules are then exported into PCMCM. Pseudo-particles representing species are launched from mesh points based on a density profile, and their trajectories are integrated by interpolating electric fields recorded as a function of phase and space from FKPM. Collisions are accounted for using null-reaction technique [6] along the trajectories until the pseudo-particles strike the surface. Their energy and angular distributions are then recorded and integrated over time for statistics. The end of PCMCM constitutes a full iteration in HPEM in which time evolves one global time step. Normally, tens to hundreds of such iterations are required to achieve convergence of a simulation, at which point a steady state is achieved. In HPEM, the time step varies in individual modules depending on the requirement of addressed physical processes. Consequently, with a global time step normally on the order of micro-seconds, the individual time step in Monte-Carlo modules and FKPM can be as small as one tenth of a nanosecond. The information exchange between modules is carefully performed through a time-slicing technique [1].

2.1 The Electromagnetics Module (EMM)

The EMM module solves the inductive electromagnetic field in ICP plasma simulations based on the azimuthal current component in antenna coils. First, the electric field is calculated by solving the following wave equation in frequency domain:

$$-\nabla\left(\frac{1}{\mu}\nabla\cdot\vec{E}\right)+\nabla\cdot\left(\frac{1}{\mu}\nabla\vec{E}\right)=\omega^{2}\varepsilon^{2}\vec{E}+i\omega\left(\vec{J}_{coil}+\overline{\overline{\sigma}}\cdot\vec{E}\right) \tag{2.1}$$

where μ is permeability, ω is angular electromagnetic frequency, ε is permittivity, $\vec{J}$ is current density. Two distinct current sources contribute to the electric field: the external antenna current $\vec{J}_{atenna}$, and the conduction current density $\vec{J}_{plasma} = \overline{\overline{\sigma}} \cdot \vec{E}$ generated by electron transport in the plasma with σ representing conductivity of the plasma. Ion current density is ignored in the wave equation due to the large inertia of ions compared with electromagnetic frequency (normally 1 – 10s of MHz) and size of the reactor (10 – 100s of cm). In the absence of a static magnetic field, conductivity of plasma is a scalar indicating isotropic behavior:

$$\sigma_0 = \frac{q_e^2 n_e}{m_e} \frac{1}{\nu_m + i\omega} \tag{2.2}$$

where q_e is unit charge of electron, n_e is the electron density, m_e is mass of electron, ν_m is the electron momentum collision frequency which is calculated from EETM in the previous iteration or estimated in the case of the beginning of simulation. Only an isotropic electric field will be produced in this situation. In the presence of a static magnetic field, magnetized electrons will exhibit anisotropy of mobility in bulk plasma, represented by tensor conductivity in equation (3) in the following form (cylindrical symmetric coordinate system):

$$\overline{\overline{\sigma}} = \frac{\sigma_0}{(\alpha^2 + |B|^2)} \times \begin{pmatrix} \alpha^2 B_r^2 & \alpha B_z + B_r B_\theta & -\alpha B_\theta + B_r B_z \\ -\alpha B_z + B_r B_\theta & \alpha^2 + B_\theta^2 & \alpha B_r + B_\theta B_z \\ \alpha B_\theta + B_r B_z & -\alpha B_r + B_\theta B_z & \alpha^2 + B_z^2 \end{pmatrix} \tag{2.3}$$

where

$$\sigma_0 = \frac{q_e^2 n_e}{m_e} \frac{1}{\nu_m + i\omega} \tag{2.4}$$

$\vec{B}$ represent the magnetic field magnitude components. The wave equation is then solved in its tensor form with the electric field in the other two directions.

The magnetic field is also solved in EMM, both in its electromagnetic and static forms. The time-varying magnetic field generated by the antenna coil is directly calculated from electric field:

$$\vec{B} = (i/\omega)\nabla \times \vec{E} \tag{2.5}$$

With an all-metal boundary condition required by HPEM. The static magnetic field, $\vec{B}$, is either implemented as a user-specified field source as an input, or calculated from the pre-defined magnetic dipole material in the mesh. Magnetic dipoles in the mesh are treated as consecutive current loops with current density from the input file $\vec{j}_c$. The static magnetic field is then obtained from the current source and vector potential $\vec{A}$:

$$\frac{1}{\mu}\nabla \times \vec{B} = \vec{j}_c,\ \vec{B} = \nabla \times \vec{A} \tag{2.6}$$

Both the electric field and magnetic field are solved using a succession-over-relaxation (SOR) method to convergence.

The input power of the inductive current source is calculated in EMM as well, assuming a full ohmic heating of the inductive power:

$$P_a = \mathrm{J} \cdot \vec{\mathrm{E}} \tag{2.7}$$

When eMCS is used in EETM module, the total power is addressed as the power absorbed by electrons and is computed by integrating the trajectories of the electron pseudo-particles in the electromagnetic field:

$$P_a = \frac{1}{\tau}\int_0^{\tau} \sum_i q w_i \left(\vec{v}_i \cdot \vec{E}\right) dt \tag{2.8}$$

The integral is calculated over the RF period τ, summation is over pseudo-particles representing w_i electrons per particle having velocity v_i. P_a is then used to normalize the antenna currents, and the magnitudes of the electromagnetic fields are calculated in the EMM to deliver the desired power. In prior studies, we found this technique provided essentially the same plasma properties as computing plasma currents in the eMCS and using those currents in solution of Maxwell's equations [7].

2.2 The Electron Energy Transport Module (EETM)

With total electric and magnetic fields $\vec{E}$ and $\vec{B}$ as input, EETM calculates electron energy distribution f_e which is a function of both fields and species' densities. Electron temperature T_e, electron impact source k_e and electron transport properties are also calculated based on f_e. In the scope of this thesis, the electron properties are calculated by two different approaches: solving a time-dependent electron energy equation or utilizing an electron Monte-Carlo simulation (eMCS). Both approaches are described below.

2.2.1 Electron Energy Equation

In the electron energy equation method, electron energy distribution is calculated by solving a two-term Boltzmann equation with collisional term over a range of values of electric field/total gas density (E/N).

$$\frac{\partial f_e}{\partial t} = -\vec{v}\nabla_r f_e - \frac{e\left(\vec{E} + \vec{v} \times \vec{B}\right)}{m_e} \cdot \nabla_v f_e + \left(\frac{\partial f_e}{\partial t}\right)_{collisions} \tag{2.9}$$

where f_e is the electron energy distribution, which is initially assumed in the form of a Maxwellian distribution and then solved by integrating the partial differential equation over time to convergence. ∇_r is spatial gradient, ∇_v is velocity gradient, m_e is electron mass, and $\left(\frac{\partial f_e}{\partial t}\right)_{collisions}$ represents all the collision terms. Averaged electron temperature T_e and source function of electron collisional reaction rates k_j are derived based on f_e.

$$k_j(\vec{r})\left[cm^3s^{-1}\right]=\sum_{i=1} f_{bi}(\vec{r})\sigma_j(\varepsilon_i)\left(\frac{2\varepsilon_i}{m_e}\right)^{1/2}\nabla\varepsilon_i \tag{2.10}$$

f_e, T_e and k_j are calculated and tabulated for each individual value of E/N by repeating the process. Time-dependent electron temperature T_e in plasma is then calculated by solving the electron energy equation:

$$\frac{\partial\left(\frac{3}{2}n_e k_B T_e\right)}{\partial t}=\nabla k\nabla T_e+\nabla\cdot\left(\vec{\phi}_e T_e\right)=P \tag{2.11}$$

where k is the thermal conductivity of electrons, $\vec{\phi}_e$ is electron fluxes, and P_e is the electron power deposition:

$$P_e = j\cdot\vec{E}=q_e\left(-D\nabla n_e-\mu_e n_e\vec{E}\right)\cdot\vec{E} \tag{2.12}$$

The electron fluxes are updated in FKPM by drift-diffusion method or a Scharfetter-Gummel (S-G) expression [8], which will be described in the next section. The electron transport properties and source function of electron collisional reactions k_j are then extracted from the tabulated data. While time-dependent electron temperature and electron impact collision rate are updated multiple times in FKPM, tabulated data is updated once every global iteration.

2.2.2 Electron Monte-Carlo Simulation (eMCS)

Alternatively, electron properties can be extracted using a Monte-Carlo method in EETM by eMCS, a fully kinetic treatment resolving electron transport in electromagnetic fields using a semi-implicit technique. Though HPEM is a 2-D hydrodynamic model, the electron transport in eMCS is tracked in an overlaid 3-D Cartesian sub-mesh to resolve magnetized behavior of charged particles by integrating the Lorentz equation in an implicit form:

$$\frac{d\vec{v}}{dt} = \frac{q_e}{m_e}\left(\vec{E} + \vec{v}_e \times \vec{B}\right) \tag{2.13}$$

The electric and magnetic fields, $\vec{E}$ and $\vec{B}$, are also time-dependent values produced by FKPM and EMM. In FKPM, Poisson's equation is solved for static electric field in a phase-resolved manner over one RF cycle, with a time resolution less than one percent of the period of the highest applied RF frequency. The electrostatic field is then recorded over one period and combined with electromagnetic field from EMM, then transferred to eMCS. In eMCS, the cylindrically symmetric values of $\vec{E}$ and $\vec{B}$ are first mapped to the 3-D Cartesian sub-mesh. The fields are then used to integrate trajectories of electron pseudo-particles of three types: electrons in the bulk, secondary electron beams, and field-enhanced thermionic emitted electrons from surfaces.

The bulk electron simulation in eMCS calculates electron energy distribution. Electron pseudo-particles are first initialized in the reactor with a spatial distribution following the electron density profile calculated in the fluid part of HPEM. Energy of the pseudo-particles is randomly picked assuming a Maxwellian-Boltzmann distribution. After the first iteration, electron pseudo-particles are launched from their coordinates at the end of last call of eMCS, based on historical distribution. Trajectories of the pseudo-particles are then integrated using a second order Euler method in the 3-D Cartesian sub-mesh. In eMCS, the time step Δt of advancing particle trajectories is individually chosen that satisfies five different constraints: Δt has to be within a specified fraction of the RF cycle; the particle cannot travel further than half of the computation mesh in any of the three directions; Δt has to be smaller than the time interval between two collisions; the particle cannot be decelerated to a speed of zero; and the overall traveling time adding current Δt cannot exceed the time when statistics are collected, T_f, which is the same for all pseudo-particles. T_f is also the termination time for each particle in eMCS.

Collisions are then addressed through a Monte-Carlo type null-collision technique along the trajectory of particles. This is accomplished by adding an additional fictitious process referred to as a null collision such that all electrons within a given energy range appear to have the same collision frequency v_{mj}, which is the maximum collision frequency in an energy range j based on both electron energy and density of collision partners. Null-collision frequency is then calculated as $v_{nj} = v_{mj} - v_j$ [6]. Where v_j is total collision frequency in energy range j calculated on an energy grid of electrons which divides specific energy ranges into multiple energy bins. For this thesis, 500 energy bins were used to resolve five energy ranges of 0 – 5, 5 – 12, 12 – 50, 50 – 300, and 300 – 1000 eV (100 bins/range). The high-energy ranges were mainly used to capture the sheath accelerated secondary electrons which could have large kinetic energy accelerated by sheath potential. For each energy bin j, v_j is calculated by summing all possible electron impact collisions:

$$v_i = \left(\frac{2\varepsilon_i}{m_e} \right)^{1/2} \sum_{j,k} \sigma_{ijk} N_j \tag{2.14}$$

where ε_i is the center energy of bin i, m_e is electron mass, σ_{ijk} is electron impact cross-section of reaction k with heavy species j, and N_j is the density of heavy species j. Collisions are then checked every time step which is randomly chosen based on maximum collision frequency, $\Delta t = -\ln(r_1)/v_{mj}$, where r_1 is a random number uniformly distributed in (0,1). The type of collision is determined by another random number r_2, independently generated from the same distribution. If $r_2 > (1 - v_{nij}/v_{mj})$, then the collision is taken as a 'null collision' and the electron trajectory continues unhindered. Otherwise, a real collision occurs. Electron energy is then modified based on the nature of the collision, and the direction of the electron pseudo-particle's velocities is re-calculated by applying a scattering matrix:

$$\begin{aligned} v_x &= v\cdot\left(\cos\beta\cdot\cos\alpha\cdot\sin\theta\cdot\cos\phi+\cos\beta\cdot\sin\alpha\cdot\cos\theta-\sin\beta\cdot\sin\theta\cdot\sin\phi\right)\\ v_y &= v\cdot\left(\cos\beta\cdot\cos\alpha\cdot\sin\theta\cdot\cos\phi+\sin\beta\cdot\sin\alpha\cdot\cos\theta+\cos\beta\cdot\sin\theta\cdot\sin\phi\right)\\ v_z &= v\cdot\left(-\sin\alpha\cdot\sin\theta\cdot\cos\phi+\cos\alpha\cdot\cos\theta\right) \end{aligned} \tag{2.15}$$

Here, β and α are the polar and azimuthal Eulerian angles, respectively, of the electron velocity prior to the collision; θ and ϕ are the polar and azimuthal scattering angles, respectively, and v is the post-collision electron speed.

Electron-electron collisions can also be addressed in eMCS using a particle mesh technique. An energy-resolved background electron fluid is assumed to be the source of the collision partner of the Monte-Carlo electron pseudo-particles. The electron collision partner's energy is randomly chosen from the distribution function f_e from previous run of eMCS, while the partner electron's velocity direction is randomly determined assuming an isotropic angular distribution.

Statistics for electron energy distribution f_e are collected on each time step, using the same energy grid as in the null collision method:

$$F_{il} = \sum_j w_j \delta\left[\left(\varepsilon_i \pm \frac{1}{2}\Delta\varepsilon_i\right) - \varepsilon_i\right]\delta\left[\vec{r}_l \pm \Delta\vec{r} - \vec{r}_j\right] \tag{2.16}$$

where w_j is the weighting of particle j, which is proportional to the product of the number of electrons each pseudo-particle represents and the time spent in advancing the particle trajectory. A finite particle size technique is used to distribute the particle weighting to its own cell and neighboring cells. At the end of an eMCS call, at which time all pseudo-particles reach T_f, electron energy distributions, f_e, at each location is calculated from the normalized statistics:

$$\sum_i F_{ij}\Delta\varepsilon_i = \sum_i f_e(\varepsilon,\vec{r})\varepsilon_i^{1/2}\Delta\varepsilon_i = 1 \tag{2.17}$$

The electron impact source and transport rate coefficients can then be solved similarly to the electron energy equation option.

Secondary electrons in eMCS are likewise addressed as bulk Monte-Carlo electrons. Pseudo-particles of secondary electrons are perpendicularly launched from the surfaces with energy of 4 eV. Since the statistical weighting of the particles w_j (number of electrons/s), can be addressed in two approaches, two launching schemes of secondary electron particles are implemented in HPEM.

The first scheme is equal-weighted pseudo-particle. The release rate R_{Sk} (1/s) is then calculated as a function of secondary electron stimulating fluxes $\vec{\phi}_j$ from FKPM and area of the electron emitting surface A_k at cell k:

$$R_S = \sum_k R_{Sk}\, , \quad R_{Sk} = \sum_k \gamma_j \vec{\phi}_j(\vec{r}_k)A_k \tag{2.18}$$

Statistics of electrons from a highly emitting surface with a large area benefit from the large amount of particles proportion to it. For lower emitting surfaces, a statistically unfavorable situation might occur due to significantly less pseudo-particles released. This could be problematic for cases with large dynamic range secondary emissions. The issue is addressed by evenly distributing pseudo-particles over all emitting mesh cells, while weighting of the particles is a function of the emitting current at each cell location.

Trajectories of secondary emitted pseudo-particles are integrated over much longer time spans compared with bulk electrons – until the particles disappear by striking a surface and are recorded as surface charges or eliminated when they fall below the lowest electronic excitation threshold ε_t and are recorded as current to the bulk plasma electrons.

2.3 Fluid Kinetics-Poisson Module (FKPM)

In FKPM, dynamics of all species in the plasma are addressed including electrons, ions and neutrals. Electromagnetic fields, electron energy distribution, and electron impact reaction rates are transferred from EMM and EETM into FKPM, producing updates of species' fluxes, density profiles and temperatures by solving continuity equation, momentum equation and energy equation for all species. The integration over time is resolved by a self-sustained time step, which is limited by a specific fraction of RF period (normally less than one percent) and the dielectric relaxation time, which is the ratio of permittivity of free space to the plasma conductivity. Multiple iterations are performed in solving the transport/energy equations before reaching the time step of a global iteration.

2.3.1 Continuity, momentum and energy equations for ions and neutrals

For the heavy particles (ions and neutrals), equations are solved assuming a non-equilibrium temperature scheme:

$$\frac{\partial N_i}{\partial t} = -\nabla \cdot \vec{\phi}_i + S_i - \left[\sum_j \gamma_{ij} \left(\nabla \cdot \vec{\phi}_j \right) \right]_S \tag{2.19}$$

$$\frac{\partial \vec{\phi}_i}{\partial t} = \frac{\partial \left(N_i \vec{v}_i \right)}{\partial t} = -\frac{1}{m_i} \nabla \left(k N_i T_i \right) - \nabla \cdot \left(N_i \vec{v}_i \vec{v}_i \right) + \frac{q_i N_i}{m_i} \times \left(\vec{E}_S + \vec{v}_i \times \vec{B} \right) - \nabla \cdot \overline{\overline{\tau}}_i - \sum_j \frac{m_j}{m_i + m_j} N_i N_j k_{ij} \left(\vec{v}_i - \vec{v}_j \right) + S_{mi}$$

$$\frac{\partial \left(N_i c_i T_i \right)}{\partial t} = \nabla \cdot \kappa_i \nabla T_i - P_i \nabla \cdot \vec{v}_i - \nabla \cdot \left(N_i \vec{v}_i \varepsilon_i \right)$$

$$+ \frac{N_i q_i^2}{m_i \nu_i} E_S^2 + \frac{N_i q_i^2 \nu_i}{m_i \left(\nu_i^2 + \omega^2 \right)} E_\Theta^2$$

$$+ \sum_j 3 \frac{m_{ij}}{m_i + m_j} N_i N_{ji} k_{ij} k_B \left(T_j - T_i \right) \pm \sum_j 3 N_i N_j R_{ij} k_B T_j$$

where $\vec{\phi}_i$, N_i, $\vec{v}_i$, m_i, T_i, $\overline{\overline{\tau}}_i$, P_i and ε_i represent the flux, density, velocity, mass, temperature, viscosity, pressure and total energy of species i. Viscosity terms are only included for neutrals. In the scope of this thesis, this term is negligible due to the much lower density of ion fluids. The transport properties are either taken from literature or calculated from Lenard-Jones parameters. For the momentum equation, a slip boundary condition is employed as described by Thompson [9]. For the third equation, energy contributions are addressed from heat transfer (thermal conductivity, compressive heating and advective transport), electromagnetic field, and collisional terms (elastic collision and charge exchange collisions).

2.3.2 Electron continuity and energy equations

Instead of solving a momentum equation, electron transport in FKPM is addressed by solving a continuity equation with assumptions of either a drift-diffusion approximation or a Scharfetter-Gummel flux. In the absence of a static magnetic field, the conventional drift-diffusion approximation is described as:

$$\vec{\phi}_e = n_e \overline{\overline{\mu_e}} \cdot \vec{E} - \overline{\overline{D_e}} \cdot \nabla n_e \tag{2.20}$$

n_e, $\vec{\phi}$, μ_e, $\vec{E}$, D_e are electron density, electron flux, electron mobility, electric field and electron diffusion coefficient, respectively. The electric field is the combination of the electrostatic field calculated in the Poisson solver (described later in the FKPM section) and the electromagnetic field from the EMM module. A static magnetic field would produce a tensor form of the mobility and diffusivity $\overline{\overline{A}}$ derived from their isotropic values A_0.

$$\overline{\overline{A}} = \frac{A_0}{(\alpha^2 + |B|^2)} \times \begin{pmatrix} \alpha^2 B_r^2 & \alpha B_z + B_r B_\theta & -\alpha B_\theta + B_r B_z \\ -\alpha B_z + B_r B_\theta & \alpha^2 + B_\theta^2 & \alpha B_r + B_\theta B_z \\ \alpha B_\theta + B_r B_z & -\alpha B_r + B_\theta B_z & \alpha^2 + B_z^2 \end{pmatrix} \tag{2.21}$$

where

$$\alpha = m_e(\nu_m + i\omega)/q \tag{2.22}$$

A more commonly used scheme is the Scharfetter-Gummel flux discretization which combines upwind and downwind techniques [8]. The flux between a mesh point (i, i+1) is given by:

$$\vec{\phi}_{i+\frac{1}{2}} = \frac{\delta \overline{D}\left(n_{i+1} - n_i \exp(\delta \Delta x)\right)}{\left(1 - \exp(\delta \Delta x)\right)} \tag{2.23}$$

where δ is given by

$$\delta = \frac{\left(\frac{q}{|q|}\right)\overline{\mu}\left(\frac{\Phi_{i+1} - \Phi_i}{\Delta x}\right)}{\overline{D}} \tag{2.24}$$

Δx is the grid size between mesh points, $\vec{\phi}_{i+\frac{1}{2}}$ is the half-mesh electron flux, $\overline{D}$ and $\overline{\mu}$ are the averaged diffusion coefficient and mobility in the interval.

2.3.3 Poisson’s equation

As discussed in the introduction, the electrostatic force between internal charged particles is the most distinguished feature of plasma. The electrostatic field is normally calculated by numerically solving Poisson’s equation. However, the explicit method has the fundamental limit of dielectric relaxation time which can be as small as pico-seconds in applications. This would cause great computational burden on the simulation. In HPEM, a semi-implicit technique is used to relieve the constraint of dielectric relaxation time [10]. The semi-implicit form of Poisson's equation is described as:

$$\nabla \cdot \left(\varepsilon \nabla \Phi\left(t + \Delta t\right)\right) = -\rho(t + \Delta t) = -\rho(t) - \Delta t \left.\frac{\partial \rho}{\partial t}\right|^{t+\Delta t} \tag{2.25}$$

and

$$\rho(t) = \rho_m(t) + \sum_i q_i N_i(t) \tag{2.26}$$

$$\begin{aligned} \left.\frac{\partial \rho}{\partial t}\right|^{t+\Delta t} &= \frac{\partial \rho_m(t')}{\partial t} - q_e \nabla \cdot \left(\vec{\phi}_e(t) + \frac{\partial \vec{\phi}_e}{\partial \Phi}\left[\Phi_S\left(t + \Delta t\right) - \Phi_S(t)\right]\right) \ldots, \\ &- \sum_j q_j \nabla \cdot \left(\vec{\phi}_j(t) + \frac{\Delta t}{2} \frac{\partial \vec{\phi}_j(t)}{\partial t} \right) \end{aligned} \tag{2.27}$$

where ρ_m is the charge density on surfaces and in materials, ε is the local permittivity either in the plasma, non-plasma gases or materials, $\vec{\phi}$ are the fluxes of electrons and ions. Implicitness is provided by evaluating potentials at $t + \Delta t$, while ρ_m and N_i are evaluated at t. The Jacobian elements are the first-order partial derivatives of electron fluxes with respect to Φ, which are numerically evaluated manually by computing change in $\vec{\phi}_e$ while perturbing Φ by a small fraction value. The discretized equations are then solved using either an SOR method [11] or by direct sparse matrix solvers, which in HPEM are dslucs and dslugm obtained from SLAP library [12]. The Jacobian elements are calculated in the case of direct sparse matrix method by:

$$\frac{\partial \vec{\phi}_{i,j}}{\partial \Phi_{i+1,j}} = \frac{\vec{\phi}_{i,j}\left(\Phi_{i+1,j} + \Delta \Phi_{i+1,j}\right) - \vec{\phi}_{i,j}\left(\Phi_{i+1,j}\right)}{\Delta \Phi_{i+1,j}} \tag{2.28}$$

where $\Delta\Phi$ is predefined perturbation typically set as five percent of the current value.

Boundary conditions when solving Poisson’s equation are forced to be metal at the edge of the computational region. When power is applied to metals, the instantaneous applied electric potential is also included as a boundary condition in the calculation. In the case of a CCP plasma reactor, a DC bias is also accounted for in the Poisson solver as part of the boundary condition. The DC bias is sustained on the blocking capacitor connected between the powered electrode and power supply as discussed in the previous section. In the case of RF power, displacement current is also addressed when calculating current balance on the surfaces.

Acceleration techniques are used to speed up the convergence rate in FKPM. At the end of specified averaging periods within FKPM, densities of all species are extrapolated based on the recorded rate of variation following a linear equation:

$$N_i(t+\Delta t) = N_i(t)(1+\delta),\ \delta = \xi \frac{N_i(t) - N_i(t+\Delta t)}{N_i(t)} \tag{2.29}$$

where N_i is density of different species, delta is the fractional change, and ξ represents a manually tunable acceleration factor, typically set as a large value for low density plasma and a small value for high density plasma. Due to the different rates of change between different species, acceleration could potentially break the net charge density conservation and cause unphysical transience in the simulation. To prevent such a problem, net charge density after acceleration is restored to the value before acceleration by adjusting the electron density accordingly.

2.4 Radiation Transport Monte-Carlo Module (RTMCM)

Radiation transport in the RTMCM is addressed using a Monte Carlo technique [13-15]. Photon pseudo-particles are isotropically launched from locations in the plasma weighted by the density of the radiating states, for example, Ar($1s_4$) and Ar($1s_2$) in the case of argon plasmas. The photon pseudo-particles are advanced in line-of-site trajectories until the pseudo-particles hit a surface, are resonantly absorbed by ground state Ar or are non-resonantly absorbed through, for example, photoionization of excited states. The absorbed quanta of energy represented by the pseudo-particles are then either reradiated assuming partial frequency redistribution [16,17] or are quenched. By quenching, we mean that the quanta of energy resident in the excited state undergoes a collision (e.g., electron impact ionization or super-elastic relaxation, Penning ionization) prior to that quanta of energy being reradiated as a photon. The line shape function of the emitted photons is a Voigt profile using the local gas temperature and collision frequency to determine broadening. Photon pseudo-particles' fluxes are recorded as a function of position in the gas phase and on surfaces. The fluxes in the gas phase are used to produce photoionization sources used in the FKPM, while the fluxes striking surfaces are used for sources of secondary electrons by photoelectron emission and also represent the optical output of the plasma. The details of the RTMCM follow.

The RTMCM tracks quanta of photons that are initially emitted in proportion to excited state densities. For any given run of the RTMCM, a probability array is constructed which provides the mean free path for absorption of a photon emitted from transition i as a function of position and frequency.

$$\lambda_i(\vec{r},\nu)=\left[\sum_j N_j(\vec{r})\sigma_{0j}g_j(\vec{r},\nu)+\sum_k N_k(\vec{r})\sigma_{ik}\right]^{-1} \tag{2.30}$$

In Equation 2.30, the first sum accounts for resonant absorption by species j having density $N_j(\vec{r})$, line center absorption cross section σ_{0j} and Voigt line shape function $g_j(\vec{r},\nu)$. The spatial dependence of the line shape function comes through the possible spatial dependence of gas temperature and collision frequency. The sum over species for resonant absorption accounts for closely spaced transitions as might occur for hyperfine splitting and isotopes. The second sum accounts for non-resonant absorption of photon i by species k having density $N_k(\vec{r})$ with cross section σ_{ik} as might occur in photoionization. The minimum mean free path in the plasma is then determined by $\lambda_{im}(\nu) = \min\left\lceil \lambda_i(\vec{r},\nu) \right\rceil$.

Another array is constructed for the frequency of quenching collisions of the excited state that produces a photon from transition i,

$$f_{Qi}(\vec{r},\nu) = \sum_m N_m(\vec{r}) k_{Qmi}(\vec{r}) \tag{2.31}$$

where the sum is over collisions with species m having density N_m that quenches the excited state producing photon i with rate coefficient k_{Qmi}. A third array, f_{Ni}, is constructed which is analogous to f_{Qi} but which accounts for non-quenching but broadening or velocity changing collisions having rate coefficient $k_{Nmi}(\vec{r})$.

The optical frequency of the initially emitted pseudo-particle for the photon from transition i emitted at $\vec{r}$ is randomly chosen from $g_i(\vec{r},\nu)$ using the following procedure. The Voigt profile can be reduced to a function that depends on the ratio of the homogeneous line width, $\Delta\nu_H$ and the inhomogeneous line width, which in this case is the Doppler line width, $\Delta\nu_D$,

$$g_i(\vec{r},\nu') = \frac{\gamma_i(\vec{r})}{\pi^{3/2}} \int_{-\infty}^{\infty} \frac{e^{-y^2}}{\gamma(\vec{r})^2 + (\nu_i'(\vec{r}) - y)^2} dy, \quad \gamma_i(\vec{r}) = \frac{\Delta\nu_{iH}(\vec{r})}{2\Delta\nu_{iD}(\vec{r})}, \; \nu_i'(\vec{r}) = \frac{\nu - \nu_{i0}}{\Delta\nu_{iD}(\vec{r})}, \tag{2.32}$$

where ν_{i0} is the absolute line center for transition i. $\Delta\nu_{iH}$ is the sum of the natural decay rate for photon i given by the Einstein A_i coefficient and the sum of the rate of broadening collisions with species m,

$$\Delta\nu_{iH}(\vec{r}) = \frac{1}{2\pi}\left(A_i + A_l + 2 f_{Qi}(\vec{r},\nu)\right). \tag{2.33}$$

A_l is the natural decay rate of the lower level of the transition which for resonant radiation is zero. The Doppler line width is

$$\Delta \nu_{iD}(\vec{r}) = \left(\frac{8 k_B T_i(\vec{r}) \ln 2}{M_i c^2} \right)^{1/2} \nu_{i0} \tag{2.34}$$

where $T_i(\vec{r})$ is the temperature of the atom emitting photon i having mass M_i. (k_B is Boltzmann's constant and c is the speed of light.) Since the calculation of $g_i(\vec{r},\nu')$ is computationally expensive and its value is required frequently, $g_i(\vec{r},\nu')$ is pre-computed and recorded in an array spanning a specified number of Doppler widths, typically 8-10. The initial emission frequency of a photon ν_k is that value of the frequency that satisfies

$$\frac{1}{G} \sum_{m=1}^{k-1} g_i(\vec{r},\nu_m) \Delta \nu_m < \rho < \frac{1}{G} \sum_{m=1}^{k} g_i(\vec{r},\nu_m) \Delta \nu_m, \quad G = \sum_m g_i(\vec{r},\nu_m) \Delta \nu_m \tag{2.35}$$

where ρ is a random number distributed on (0,1), the sums are over frequency bins in the $g_i(\vec{r},\nu)$ array, G is the sum over all bins in the array and $\Delta \nu_m$ is the frequency width of the mth bin. Note that for every process requiring a random number ρ, a separate independent random number generator sequence is used. The direction of the photon is randomly selected from 4π steradians. A mean free path for absorption of the photon, $\lambda' = -\lambda_{im}(\nu) \ln(\rho)$, is randomly selected from $\lambda_{im}(\nu)$. The pseudo-particle is given a weighting $w_i(\vec{r})$ which represents the number of photons per second emitted in the optical transition i from $\vec{r}$. This weighting is

$$w_i(\vec{r}) = \frac{N_i(\vec{r}) A_i \Delta V(\vec{r})}{n_i(\vec{r})} \tag{2.36}$$

where $\Delta V(\vec{r})$ is the volume of the numerical cell from which the photon is emitted, and $n_i(\vec{r})$ is the number of pseudo-particles emitted from that location, described below. The photon's initial position in the numerical mesh representing the reactor geometry is randomly distributed in three dimensions. The emission is assumed to have occurred after a randomly selected lifetime of the excited state, $\tau_i = -A_i^{-1}\ln(\rho)$. A tally of the cumulative lifetime the quanta of energy carried by the photon is initialized with $\tau_{Ci} = \tau_i$.

The trajectory of the pseudo-particle is then integrated for a distance λ’, while accounting for blockage or absorption by physical obscurations. If the pseudo-particle leaves the plasma, its weighting and equivalent flux are binned as a function of frequency and location. These quantities summed over all pseudo-particles emitted by a particular transition will provide the spectrum and photon flux leaving the plasma. If the photon remains in the plasma after traversing a distance λ’ to location $\vec{r}\,'$ an absorption may have occurred depending on the mean free path at $\vec{r}\,'$ compared to the randomly selected λ’ based on the minimum mean free path $\lambda_{im}(\nu)$. A random number ρ is selected. If $\rho \le \lambda_{im}(\nu)/\lambda_i(\vec{r}\,',\nu)$, then an actual absorption occurred. If the inequality does not hold, then the absorption was null. In that case, another randomly selected mean free path is chosen, and the photon’s trajectory continues to be integrated in the same direction. As the pseudo-particle moves through the mesh, its trajectory and weighting are recorded and summed to provide a photon flux for transition i as a function of position, $\phi_i(\vec{r})$.

If an actual absorption occurs, then the particular absorption process that occurred, j, is determined from the process that satisfies

$$\lambda_i(\vec{r},\nu)\sum_{k=1}^{j-1} N_k(\vec{r})\sigma_k(\vec{r},\nu) < \rho < \lambda_i(\vec{r},\nu)\sum_{k=1}^{j} N_k(\vec{r})\sigma_k(\vec{r},\nu) \qquad (2.37)$$

where both resonant and non-resonant absorption processes are included in the sums. If the absorption is non-resonant, then the pseudo-particle is removed from the simulation since that quantum of energy will not be directly re-emitted by the same transition. If the absorption is resonant, then another randomly chosen lifetime is computed, $\tau_i = -A_i^{-1}\ln(\rho)$, as the duration of time that this quantum of energy resides in the excited state. If $\tau_i > -\ln(\rho) f_{Qi}^{-1}$, then a quenching collision occurs before the absorbed quantum of energy could be re-emitted as a photon, and that quantum of energy is removed from the RTMCM. If the inequality does not hold, then the quantum of energy is re-emitted as a photon. At that point, we increment the running tally of the cumulative lifetime of the quanta of energy, $\tau_{Ci} = \tau_{Ci} + \tau_i + L/c$, where L is the length of the path from its previous emission to the absorption site. (In practice L/c is much smaller than τ_i.) The frequency of the re-emitted photon is selected in the following manner consisted with partial frequency redistribution.

If $\tau_i < -\ln(\rho) f_{Ni}^{-1}$, then the quantum of energy is emitted prior to a non-quenching, broadening or velocity changing collision occurring. In this case, energy conservation requires that the photon be re-emitted within the natural uncertainty of the frequency of the absorbed photon. The frequency of emission is randomly selected from a Lorentzian broadened line shape function, $g_H(\nu)$ centered on the frequency of absorption having full-width, half-maximum (FWHM) $\Delta\nu'_{iH} = \frac{1}{2\pi}(A_i + A_l)$.

If $\tau_i \geq -\ln(\rho) f_{Ni}^{-1}$ then a non-quenching collision occurred prior to emission. If that collision is a velocity changing collision, then the photon is emitted with a frequency randomly chosen from the Voigt profile $g_i(\vec{r},\nu)$ to reflect the new Doppler shifted frequency of emission. If the collision is a phase changing collision, then the emission frequency is again chosen from a Lorentzian line shape where the FWHM is $\Delta\nu_{iH}(\vec{r})$. Another randomly selected mean free path

λ' is chosen based on the minimum mean free path of the new frequency $\lambda_{im}(\nu)$ and the photon is emitted in a random direction. The photon's trajectory is then integrated as described above. The process is continued until the pseudo-particle leaves the system by striking a surface or is absorbed by a gas phase species. The model does not now allow reflection of photons from surfaces. However, this feature could be implemented by specifying a reflection probability and the nature of the reflection (specular or diffuse) and reinitializing the trajectory of the photon pseudo-particle back into the plasma upon striking a reflective surface.

This process has an intrinsic weakness in that very few particles are emitted in the wings of the line shape function. These are precisely the photons that have a sufficiently long mean free path to escape the plasma, so the resulting photon fluxes leaving the plasma have poor statistics. An alternate method of initializing the photon pseudo-particles is to randomly but uniformly distribute the initial frequency of emission across the Voigt profile. In this case, the initial weighting of the pseudo-particle is given by $w_i(\vec{r}) = \dfrac{N_i(\vec{r})A_i\Delta V(\vec{r})}{n_i(\vec{r})} g_i(\vec{r},\nu')$. The formerly described method is cleaner in that the weighting of the pseudo-particles is more uniform. However, it has the disadvantage of having to use a large number of particles to populate the wings of the line shape function. The latter technique requires fewer pseudo-particles to properly represent the full line shape function but results in the weightings of the particles having a large dynamic range.

The number of pseudo-particles emitted from each numerical mesh cell, $n_i(\vec{r})$, for each transition varies between the user specified limits n_{min} and n_{max} depending on the relative density of the excited state at that location,

$$n_i(\vec{r}) = n_{\min} + (n_{\max} - n_{\min}) \frac{\log(N_i(\vec{r})) - \log(N_{i\min})}{\log(N_{i\max}) - \log(N_{i\min})} \tag{2.38}$$

where $N_{i\min}$ and $N_{i\max}$ are the minimum and maximum values of N_i in the numerical mesh. The RTMCM is executed during every iteration through the HPEM, which can number into the hundreds, so a tradeoff is required between computational expediency and fully resolving the spectral features. Having made this tradeoff, typical values are $n_{\min}$ =100 and $n_{\max}$ =1000, which for numerical meshes on the order of 80 × 80 (in the plasma zone), results in about 3×10^6 pseudo-particles per transition every time the RTMCM is called. Given trapping factors of many hundreds, the number of absorptions and remissions per call to the RTMCM is on the order of 10^9.

After the trajectories of all the pseudo-particles from a given transition are completed, the average lifetime of the photon pseudo-particles in the plasma is calculated from the weighted sums of τ_{Ci}. This weighted sum, normalized by the total weighting of the escaping photons yields the effective radiative lifetime, τ_{ei}, of the resonant excited state producing photon i as observed from outside the plasma. The radiative trapping factor for the transition i is then T_i = $\tau_{ei} A_i$.

Photon pseudo-particles are emitted from all locations in the plasma having an excited state population. A spatially average radiation trapping factor, T_i, is computed by

$$T_i = A_i \frac{\sum_k w_k \tau_{Ck}}{\sum_k w_k} \tag{2.39}$$

where the sum is over all the photon pseudo-particles emitted for the particular transition. The radiative lifetime of the excited state in the FKM in the next iteration of the HPEM is then extended by the radiation trapping factor T_i. This is done on a plasma-wide basis which involves another tradeoff involving computational expediency. Since T_i is dominated by the density and temperature of the absorbing state and collision partners, which do not significantly vary for these conditions where the density of radiating states is large, this spatially averaged trapping factor is acceptably accurate.

2.5 Plasma Chemistry Monte Carlo Module (PCMCM)

Similar to eMCS, PCMCM is a 3-D simulation overlaid on 2-D mesh of HPEM to calculate heavy particle (ions and neutrals) trajectories in electric fields. The energy and angular distribution of these species are collected on specific surfaces. Time-resolved electric and magnetic fields, temperature of different species, cycle averaged species' densities and source functions are collected from EMM, EETM and FKPM for PCMCM calculation.

Pseudo-particles representing ions or neutral species are launched from meshes at times randomly chosen in the RF period. The number of pseudo-particles is proportional to the source function for specific species at each location. Initial velocities are randomly chosen from a temperature-specified Maxwell-Boltzmann distribution with isotropic angular distribution. The trajectories of the pseudo-particles are then advanced in the same manner as in eMCS using the interpolated electric and magnetic fields. A second-order predictor-corrector method is used in the integration of particle trajectories. Collisions and energy are also addressed using a null-collision technique as in eMCS on a separately defined energy grid. A set of collision probability arrays for heavy particle reactions are computed in advance to account for all possible collisions and provide actual collision frequency for the null-collision technique. The time step is dynamically chosen such that it is not longer than a specific fraction of RF period or the time to traverse a specific fraction of a computational mesh cell. In bulk plasma, this value is usually 0.2

– 0.5. When a pseudo-particle approaches a surface entering the sheath region, the fraction is reduced such that a higher resolution can be achieved for collected ion energy on the surface. Energy bins of the pseudo-particle reaching a specific surface are recorded and averaged over the total surface area, until the end of PCMCM call when all pseudo-particles launched have terminated on a surface.

2.6 Figures

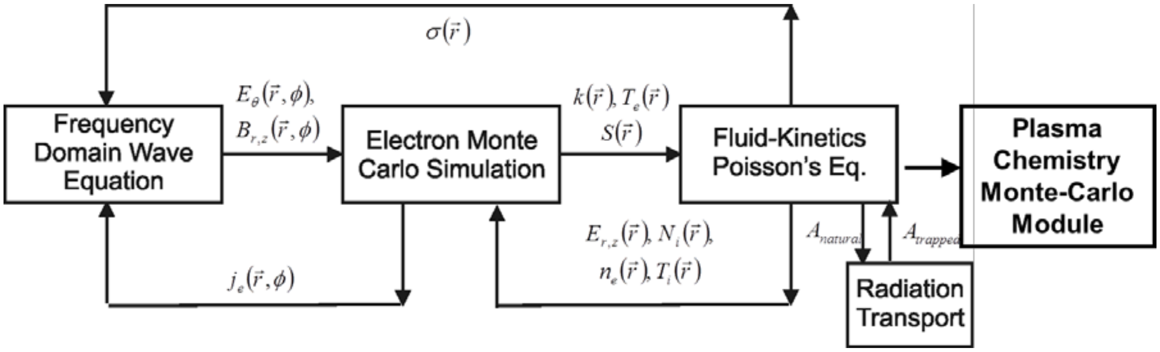

Fig. 2.1 Information exchange between modules of HPEM

2.7 References

[1] M. J. Kushner, J. Phys. D: Appl. Phys. **42**, 194013 (2009)

[2] M. J. Grapperhaus and M. J. Kushner, J. Appl. Phys. **81**, 569 (1997)

[3] A. Sankaran and M. J. Kushner, J. APpl. Phys. **92**, 736 (2002)

[4] Y. Yang and M. J. Kushner, J. Vac. Sci. Technol. A **25**, 1420 (2007)

[5] A. Agarwal and M. J. Kushner, J. Vac. Sci. Technol. A **27**, 37 (2009)

[6] S. L. Lin and J. N. Bardsley, J. Chem. Phys. **66**, 435 (1977)

[7] S. Rauf, and M. J. Kushner, J. Appl. Phys. **81**, 5966 (1997)

[8] D. L. Scharfetter, and H. K. Gummel, IEEE Trans. Electron Devices **ED-16**, 64 (1969)

[9] P. A. Thompson, Compressible Fluid Dynamics, McGraw-Hill, New York, 1994, Chapter 2.

[10] P. L. G. Ventzek, T. J. Sommerer, R. J. Hoekstra and M. J. Kushner, Appl. Phys. Lett. **63**, 605 (1993)

[11] W. H. Press, B. P. Flanney, S. A. Teukolsky and W. T. Vetterling, Numerical Recipes: The Art of Scientific Computing, Cambridge University Press, 1987

[12] SLAP Sparse Matrix Library, online at www.netlib.org

[13] M. T. Herd, J. E. Lawler, and K. L. Menningen, J. Phys. D: Appl. Phys. **38**, 3304 (2005)

[14] K. L. Menningen, and J. E. Lawler, J. App. Phys. **88**, 3190 (2000)

[15] J. E. Lawler, and M. G. Raizen, J. Phys. D: Appl. Phys. **46**, 415204 (2013)

[16] G. J. Parker, W. N. G. Hitchon, and J. E. Lawler, J. Phys. B: At. Mol. Opt. Phys. **26**, 4643 (1993)

[17] J. E. Lawler, J. J. Curry, and G. G. Lister, J. Phys. D: Appl. Phys. **33**, 252 (2000)

[18] D. Zhang and M. J. Kushner, J. Vac. Sci. Technol. A. **19**, 524 (2001)

CHAPTER 3 THE EFFECT OF MATCHING CIRCUIT IN PULSED LOW PRESSURE INDUCTIVELY COUPLED PLASMA

3.1 Introduction

In the semiconductor industry, low pressure inductively coupled plasma (ICP) reactors are extensively used for plasma material processing such as etching and deposition [1-4]. Such ICPs are normally operated with a continuous wave (CW) power source at radio-frequency (RF) to sustain the plasma. Pulsed power has gained increasing attention in ICP applications as it provides an additional degree of freedom to broaden the parameter space to customize the electron energy distribution, which in turn affects the performance of plasma processes [5-7]. In pulsed ICPs, RF power is applied over a fraction of a repetitively pulsed cycle. The interchanged sources (during pulse-on) and losses (during pulse-off) of electron and ions result in unique dynamics on radical formations [8-10].

For ICPs powered at RF frequency, power delivery is affected by impedance matching between the power source and the plasma load [11-13]. This is commonly observed in the well-known E-H transition of an ICP plasma [12,13]. Normally, a circuit match box is connected between the RF source and plasma reactor, such that power delivery efficiency can be controlled and optimized. However, in the aforementioned pulsed ICP, time-varying properties of the plasma constantly change the impedance of the load, causing circuit mismatch and power reflection over the pulse period. In this chapter, results from a simple ICP reactor will be reported both experimentally and numerically to study this phenomenon. The ICP is operated by pulsed power through a circuit matching box at low pressure and low power in pure argon. The effect of impedance matching during the pulse period is investigated as a function of matching box parameters. We discovered that dynamics of a pulsed ICP can be controlled by adjusting only the matching box setup for the RF power. Though not directly used to control fluxes in LTPs, the modeling platform was also validated through this investigation, demonstrating that the sophisticated pulsed ICP process can be well-simulated in HPEM. The discussion of electron density and temperature dynamics in a pulsed ICP is also helpful in understanding fluxes control using pulsed power discussed in Chapters 4 and 5.

3.2 Description of the Experiment and the Computational Model

This work was done in collaboration with the experimental group of Professor Steven Shannon at North Carolina State University. Fig. 3.1 provides a schematic of the experimental setup. In the experiment, pulsed power is generated by modulating a 13.56 MHz RF power source by a pulse waveform generator. The pulsed RF power is delivered through a tunable matching network to the plasma through a helical antenna. The feed-forward power and reflected power are separately coupled using a directional coupler into an oscilloscope in order to monitor the power matching in real-time. Instantaneous plasma properties are measured by a hairpin resonant probe at the center of the reactor. Design of the hairpin probe is similar to that in Ref. [14] and is shown in Fig. 3.2. The hairpin resonance probe operates on a similar principle to the cavity perturbation technique, which relies on the resonance frequency shift induced by the plasma’s lossy dielectric properties to infer electron density. The equation used for electron density measurement in this work is:

$$n_e = \frac{m_e \varepsilon_0 (\omega_r^2 - \omega_0^2)}{e^2 \left(1 - \frac{\omega_0^2 \left(\ln \frac{w-a}{w-b} + \ln \frac{b}{a}\right)}{\omega_r^2 \ln \frac{w-a}{a}}\right)}$$

where

$$\varepsilon_p = f\binom{p}{lasma} + f(sheath), \qquad \omega_r \approx \frac{\pi c}{(2l + w)\sqrt{\varepsilon_p}}$$

a is the wire radius and b is the sheath thickness. The match box in the system is a customized circuit with a 700 nH inductor and two tunable capacitors configured as shown by the schematic in Fig. 3.3. Z_{load} is the total impedance of the ICP. For each run of the pulsed ICP, values of the two capacitors remain fixed throughout the pulse period, while instantaneous electron density and forward/reflected power are recorded as a function of time.

The computational investigation of pulsed ICP is performed by HPEM. As described in detail in Chapter 2, HPEM is a 2-D modular simulator which combines both fluid and kinetic approaches. Modules addressing different physical processes are executed sequentially on time scales short enough to resolve pulsed periods, while exchanging information in a hierarchical manner. The modules used in this chapter are briefly described in their executing order. First, the electromagnetics module (EMM) is used to compute the electromagnetic field coupled by the coil antenna into the plasma region by solving Maxwell's equation in the frequency domain. The initial delivered power P_i is then calculated by integrating the product of squares of the inductive electric field and plasma conductivity over the computation region. While matching is not addressed in HPEM, this delivered power is then used to scale the magnitude of the electric field compared with the specified input power P_0. To address the power mismatch and the resulting dynamics of plasma for the work of this chapter, an enhanced circuit model was developed in this thesis to calculate matching of the forward power. To calculate impedance of the reactor, a distributed circuit model was implemented which treats plasma as a secondary coil of the RF antenna. The overall impedance is calculated combining both the antenna inductance and plasma impedance as Z_{load}. The reflection coefficient Γ at the source side of the circuit is computed based on the matching box configuration, while mismatched power delivered into the plasma, P_m, is extracted based on the resulting reflection coefficient, $P_m = P_0 \times \Gamma$. Scaling of the electric field is then performed following the ratio of P_i and P_m. The entire circuit model is incorporated into EMM in each iteration and does not influence the normal flow of the code.

The scaled electromagnetic field is transferred to fluid-kinetic Poisson module (FKPM), where density, temperature and fluxes of ions and neutrals are updated by solving continuity, momentum and energy equations. Poisson's equation is also solved in a semi-implicit manner for the electrostatic field in FKPM. Next, the electron temperature and transport coefficients are updated in the electron energy transport module (EETM) using information of species density and electric/magnetic field from EMM and FKPM. The modules are iteratively executed until the result reaches a global convergence.

3.3 Dynamics of pulsed ICP with power mismatch

In the experiment, the plasma pulsing is performed with a fixed configuration of matching network. The pulse repetition frequency and duty cycle are 1 kHz and 50%, respectively. By adjusting the tunable capacitors C_1 and C_2, the circuit can be tuned to 'match' at different times in the beginning of the pulse, at which time power reflection is a minimum. A typical experimental result of an Ar ICP at 5 mTorr with flow rate of 13 sccm is shown in Figs. 3.4 and 3.5. With different matching network configurations, the power match points are tuned at 5 us, 25 us, and 100 μs indicated by the light blue reflecting power. The yellow signal is the overall forwarded power including both power delivered into plasma and power reflected from the circuit. The resulting electron density dynamics at the beginning of the pulse are shown in

Fig. 3.5. Delay of electron density rise at the beginning of the pulse corresponds to the later match points, while the final electron density is larger as the match points move further into the pulse.

To replicate and investigate this phenomenon, simulations were performed in an ICP reactor mesh resembling the experiment. As shown in Fig. 3.6, the cylindrically symmetric structured mesh is used to resolve the reactor geometry, which is a helical type reactor with four turns of ICP coils around the side of the chamber. Inductive power is coupled through the dielectric side walls to the bulk plasma. Gas is injected into the reactor from the top and pumped at the bottom. A pressure sensor is embedded in the simulation mesh to keep the chamber pressure constant. The base case for simulation is at same condition in 5 mTorr Ar with a flow rate of 13 sccm. Forward power from the power supply is 17 W at 13.56 MHz. Pulsing in the simulation is implemented by modulating the RF power with a pulsed envelope, which has a ramp-up time of 6 us at the beginning of the pulse. Repetition frequency of the experiment pulse is 1 kHz, which translates to a pulse period of 1 ms. Computationally, running such long pulses while resolving the transients of the pulse is very expensive. Considering that the power mismatch occurs only at the beginning of the pulse, an alternate ‘pulsing’ scheme is implemented as shown in Fig 3.7a. At the beginning of the simulation, plasma is populated by a continuous wave (CW) power at 17 W until the density reaches steady state. Power is then turned off for 50 μs allowing relaxation of the plasma, mimicking the afterglow in an actual pulsing scheme. Then, pulse power is applied to the plasma for a 50 μs pulse-on period. It is understood that electron densities and position of the match point may not be the same value as in the experiment considering the scale-down of the pulse time. However, dynamics of ICP should qualitatively have similar scaling when tuning the matching network. A typical case of this simulation runs over 1000 iterations with a time step of 0.1 μs, which normally takes two to three days of computation time.

Matching networks in the simulation also requires special handling since it is not practical to manually vary the capacitor values until a match point is found. To address this, a calibration case is first run with the circuit model implementing a fully matched circuit over the whole simulation time as demonstrated in Fig. 3.7a. This is achieved by developing a RF circuit solver that instantaneously calculates a matching network configuration such that a full match is maintained at each time step. Such configurations (value sets of C_1 and C_2) are then recorded from the beginning of the pulse as a function of time. An example of evolution of C_1 and C_2 values over pulsing time is shown in Fig. 3.7b. Individual pairs of C_1 and C_2 can then be hardwired for fixed matching network configurations. These individual configurations of matching networks are used to re-run pulsed ICPs, with circuit model and power mismatch turned on. An example result with a match point at 9 μs into the pulse is shown in Fig. 3.8. At the ramp-up phase of the pulse power, most power is reflected due to the highly mismatched condition. When plasma impedance evolves to the time at which matching network configuration provides a perfect match, power reflection decreases to minimum value at 9 μs. Further evolution of ICP impedance drive the circuit out from the matching point, and power reflection starts to increase, eventually reaching a steady state where the actual delivered power balances the power loss of ICP. This is a qualitatively good match with observations in the experiment.

Simulation is then performed for more capacitor pairs. The calculated power reflection/ delivery is plotted in Fig. 3.9. With different matching network configuration for values of C_1 and C_2, the pulsed ICP can be operated with a series of delayed match points extending from the beginning further into the pulse. As the matching point moves from earlier to later in the pulse, reflected power at steady state decreases from 80 percent to 20 percent of forward power, corresponding to Γ from 0.8 to 0.2. This is due to a stronger mismatch for the matching network set at the earlier matching point. The resulting reactor averaged electron density rise is also delayed with a later match point (Fig. 3.10a) but reaches a larger steady state value due to the better power matching when matching network is set towards the steady state of the pulse. Near the location of each matching point, electron temperature overshoots due to a rapid rising of delivered power (Fig. 3.10b). The overshooting electron temperature $T_{e\text{-}peak}$, however, is not monotonically increasing with the higher power delivery at the later match point. As matching extends into the pulse, $T_{e\text{-}peak}$ increases at the beginning to a peak value of 14 eV for matching point of 7 μs, then decreases with matching point delays. This is a result of power delivery balancing and electron density evolution. At the beginning of the pulse, the electron density is small, and the better power matching dominates for $T_{e\text{-}peak}$ increases. As the plasma develops later into the pulse, the increase in electron density produces a smaller inductive impedance of the plasma, thereby lowering the overshoot in electron temperature. The scaling of the dynamics of reflecting power and electron density in the simulation results matches the trend observed in the experiment.

3.4 Concluding Remarks

In this Chapter, a pulsed low pressure inductively coupled plasma was investigated for Ar at 5 mTorr, 13 sccm, both numerically and experimentally. The plasma dynamics at the beginning of the pulse are strongly affected by the matching network in the circuit. By carefully choosing the configuration of the matching network, a perfect match point can be produced at various times in the pulse when power reflection is minimized or even becomes zero. The resulting plasma properties can thus be controlled by adjusting the location of such match points.

When plasma is matched early within the pulse, plasma density rises faster but settles at a lower value at steady state, resulting from the larger mismatch as impedance of the plasma deviates further into the pulse. When the matching network is fixed such that power reflection minimized at a later time, the steady state power delivery can be significantly larger while producing a higher density plasma during the pulse-on period.

3.5 Figures

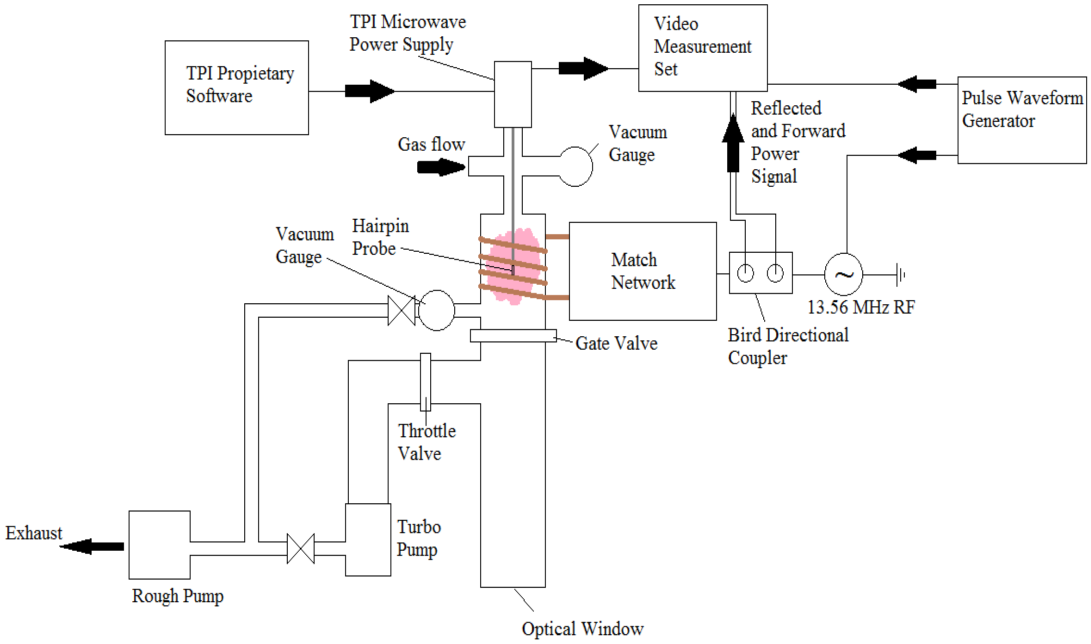

Fig. 3.1 Experiment Setup of the pulsed ICP reactor with matching network from NCSU

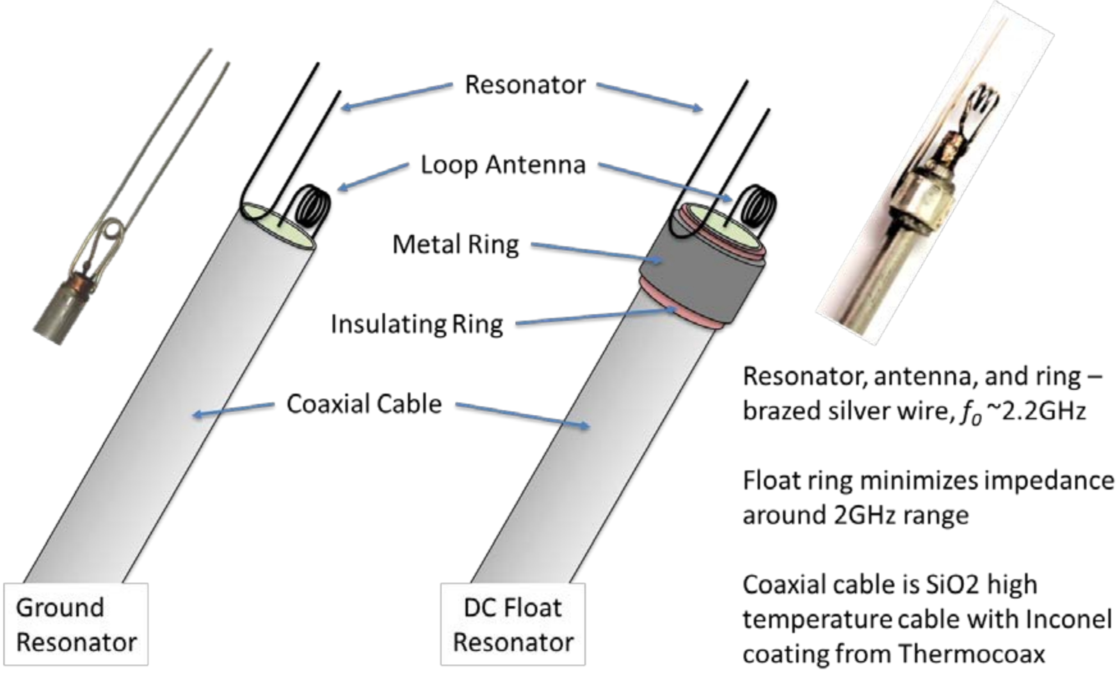

Resonator, antenna, and ring – brazed silver wire, f_0 ~2.2GHz

Float ring minimizes impedance around 2GHz range

Coaxial cable is SiO2 high temperature cable with Inconel coating from Thermocoax

Fig. 3.2 Hairpin Probe used in the experiment.

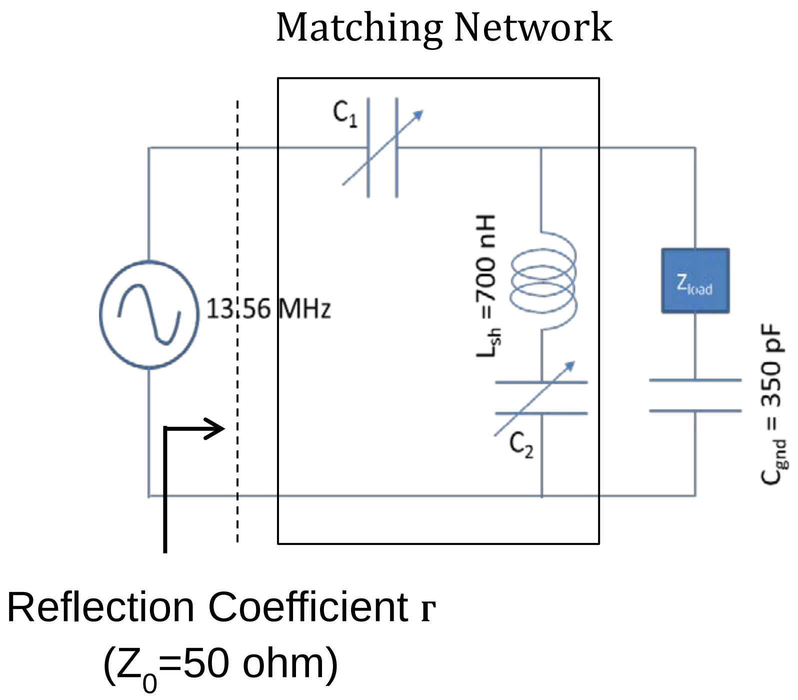

Fig. 3.3 Configuration of matching circuit for ICP power coupling

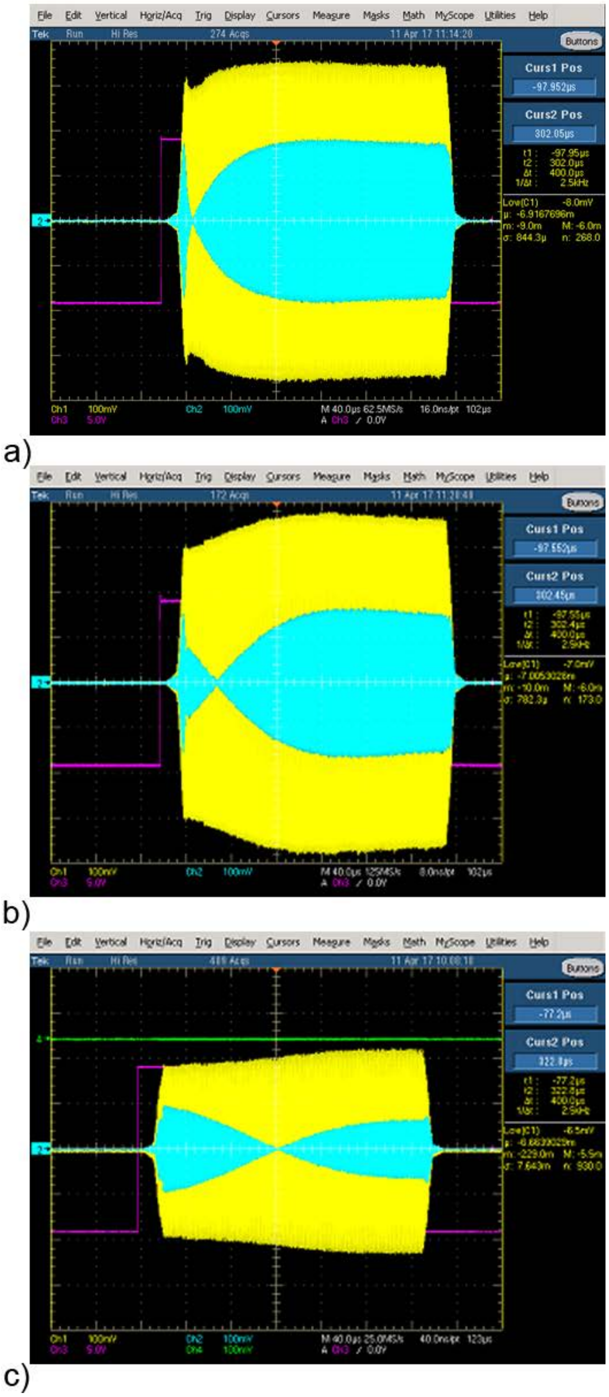

Fig. 3.4 Experimental results: forward power (yellow), reflected power (blue) and pulse envelope (pink) at different matching point in pulsed ICP: a) 5 µs, b) 25 µs, c) 100 µs

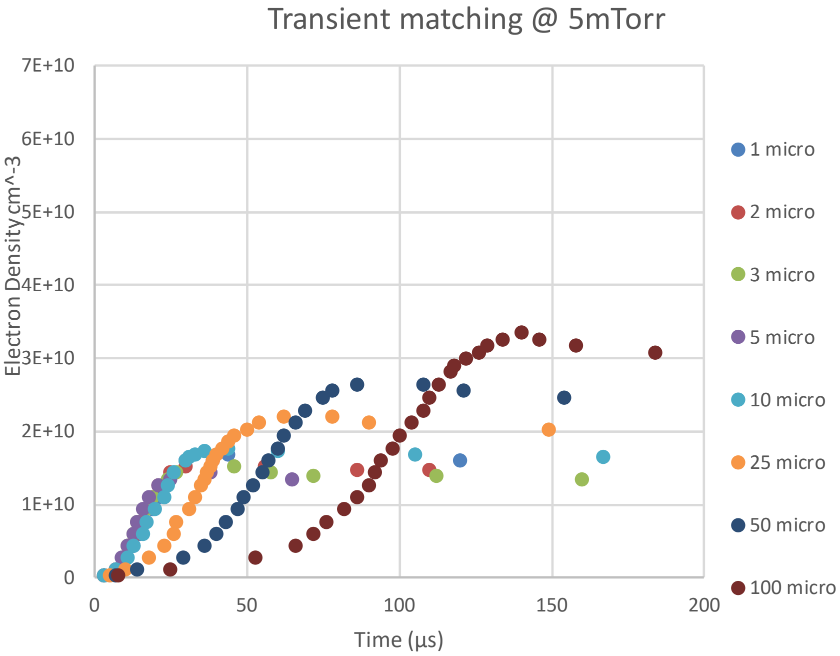

Fig. 3.5 Experiment results: electron density measured by hairpin probe at the beginning of the pulse for different match points in pulsed ICP.

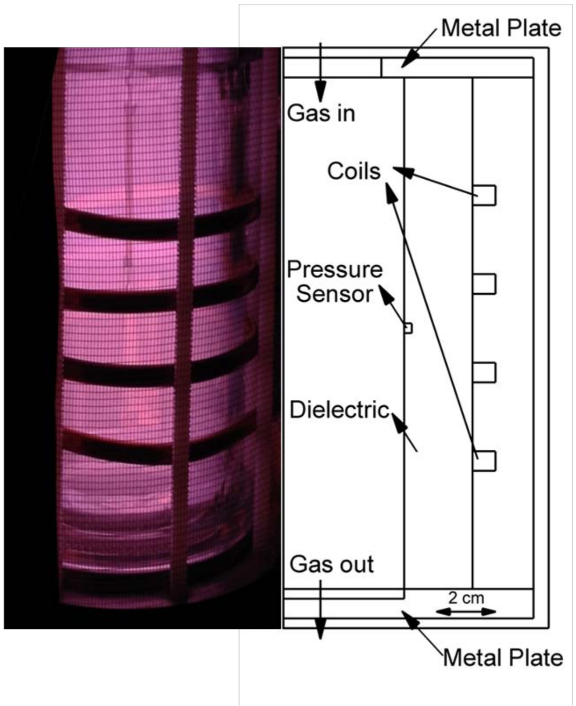

Fig. 3.6 ICP reactor geometry. Left: picture of operating reactor in experiment; Right: simulation geometry of a cylindrically symmetric mesh.

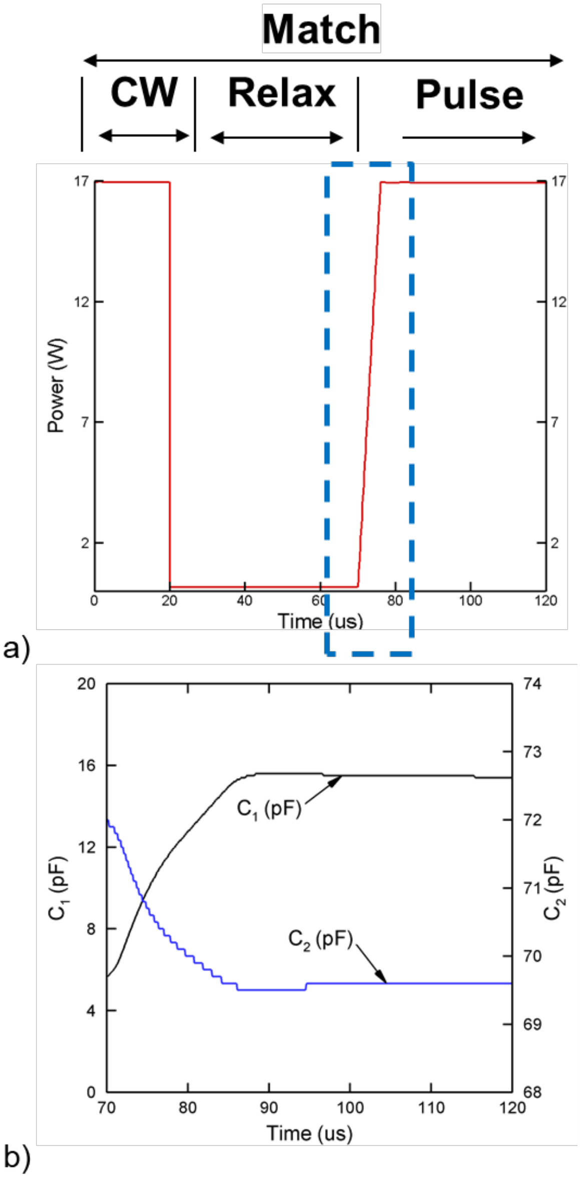

Fig. 3.7 Simulation results: power deposition and capacitor values over simulating time. a) Forward power profile; b) evolution of C_1 and C_2

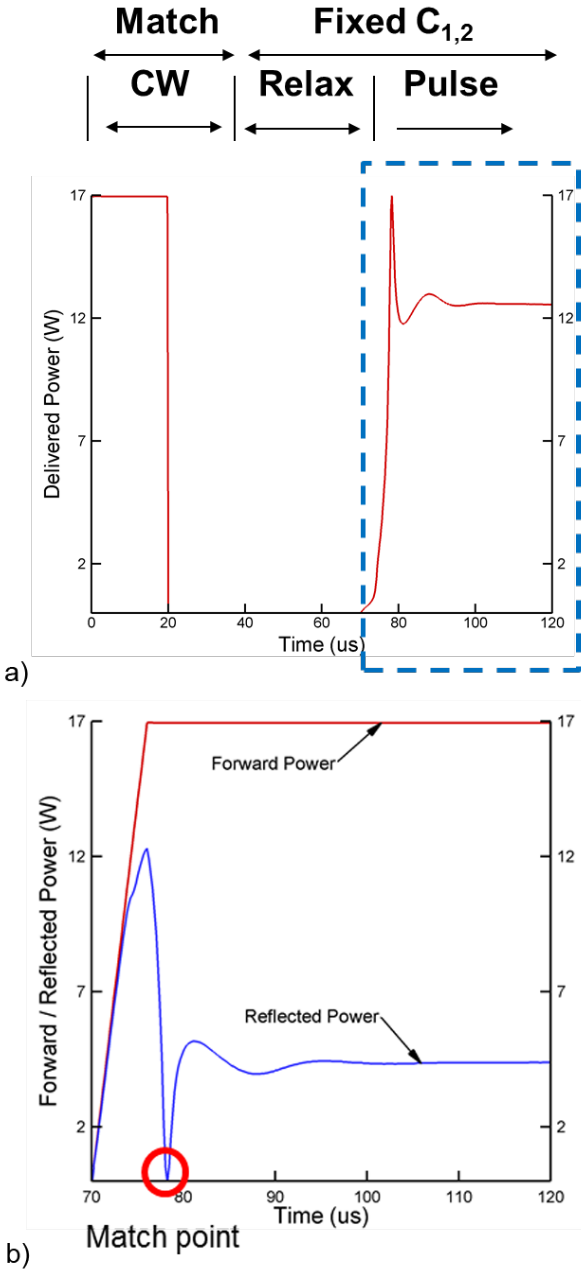

Fig. 3.8 Simulation results: a) Delivered power over the span of simulation and b) reflected power from the beginning of the pulse with match point

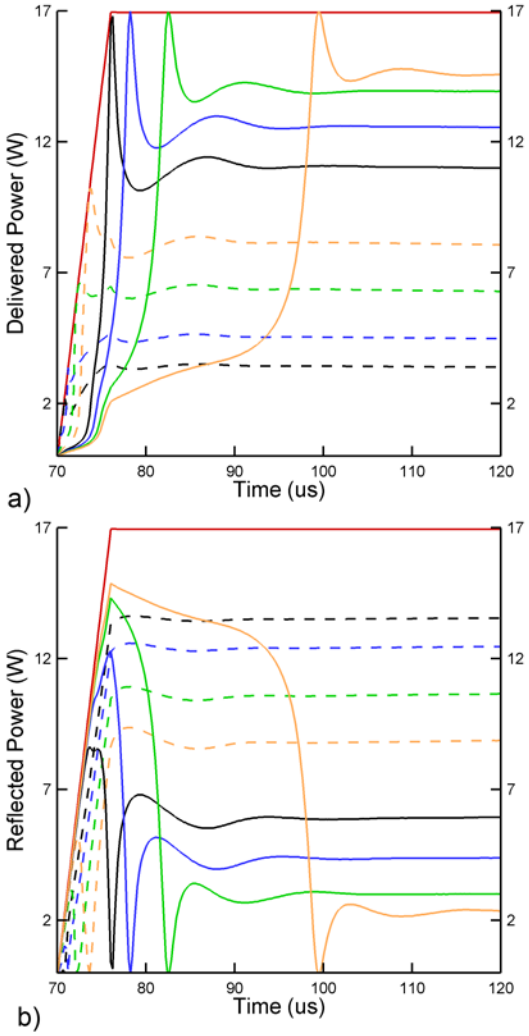

Fig. 3.9 Simulation results: delivered and reflected power at the beginning of pulse power for match points at different time during the pulse.

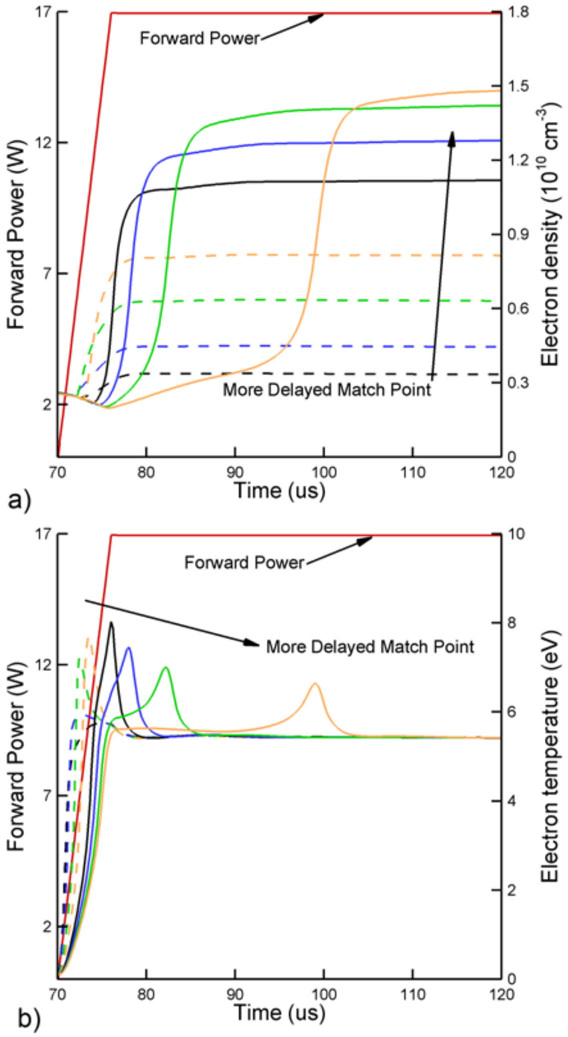

Fig. 3.10 Simulation results: reactor averaged a) electron density and b) electron temperature at the beginning of pulse power, for match points at different time during the pulse.

3.6 References

[1] F. A. Khan, and I. Adesida, Appl. Phys. Lett. **75**, 2268 (1999)

[2] R. J. Shul, G. B. McClellan, S. A. Casalnuovo, and D. J. Rieger, APpl. Phys. Lett. **69**, 1119 (1996)

[3] J. Hopwood, Plasma Sources Sci. Technol. **1**, 109 (1992)

[4] T. Ichiki, T. Momose, and T. Yoshida, J. Appl. Phys. **75**, 1330 (1994)

[5] S. Banna, A. Agarwal, G. Cunge, M. Darnon, E. Pargon, and O. Joubert, J. Vac. Sci. Technol. A **30**, 040801 (2012)

[6] C. Cardinaud, M.-C. Peignon, and P.-Y. Tessier, Appl. Surf. Sci. **164**, 72 (2000)

[7] K. Takahashi, M. Hori, and T. Goto, Jpn. J. Appl. Phys. Part 1 **32**, 1088 (1993)

[8] M. Bauer, T. Schwarz-Selinger, H. Kang, and A. von Keudell, Plasma Sources Sci. Technol. **14**, 543 (2005)

[9] P. Bodart, M. Brihoum, G. Cunge, O. Joubert, and N. Sadeghi, J. Appl. Phys. **110**, 113302 (2011)

[10] G. Cunge, P. Bodart, M. Brihoum, F. Boulard, T. Chevolleau, and N. Sadeghi, Plasma Sources Sci. Technol. **21**, 024006 (2012)

[11] B. Kim, J. Vac. Sci. Technol. A **18**(1), 58 (2000)

[12] G. Cunge, B. Crowley, D. Vender and M. M. Turner, Plasma Sources Sci. Technol. **8**, 576 (1999)

[13] Z. F. Ding, G. Y. Yuan, W. Gao, and J. C. Sun, Physics of Plasma **15**, 063506 (2008)

[14] Sands *et al.*, Plasma Sources Sci. Technol. **16**, 716 (2007)

CHAPTER 4 CONTROLLING VUV PHOTON FLUXES IN LOW PRESSURE INDUCTIVELY COUPLED PLASMAS I-RARE GAS MIXTURE

4.1 Introduction

As discussed in Chapter 1, low pressure, non-equilibrium inductively coupled plasmas (ICPs) are widely used for materials processing in microelectronics fabrication.[1-10] In these materials processing applications, there has been considerable attention paid to controlling the fluxes of radicals and ions, and the distribution of ion energies to the substrate, in order to optimize the process. Gas mixtures, power format [continuous wave (CW) or pulsed] and coil design have been investigated with the goal of having uniform fluxes of reactants of the user's choosing onto the substrate. This control is particularly important in applications where damage to the substrate may occur, for example, as a result of differential charging of microelectronics features.[11-13] Less attention has been paid to the fluxes of vacuum-ultraviolet (VUV) photon fluxes produced by these low pressure plasmas and the consequences of those fluxes on materials properties.

In Chapter 1, work of Woodworth *et al.* on VUV photon measurement in LTPs was discussed. In pure argon for similar conditions, the VUV fluxes increased to 3.5×10^{16} $cm^{-2}s^{-1}$ compared to fluorocarbon plasmas. The plasma density was a few 10^{11} cm^{-3}, producing ion fluxes to the substrate of 3×10^{16} $cm^{-2}s^{-1}$. So VUV fluxes were comparable to the ion fluxes. Similar intensities of VUV fluxes, 10^{15}-10^{16} $cm^{-2}s^{-1}$, were measured by Jinnai et al using an on-wafer VUV sensor in ICP plasmas sustained in Ar, CF_3I and C_4F_8.[14] Titus et al. [15] measured absolute fluxes of resonance radiation from Ar (104.8, 106.7 nm) and ion fluxes from ICPs in pure Ar at pressures of 1 – 50 mTorr and powers of 25 – 400 W. They found that at all pressures, the VUV flux increased linearly with power with a maximum value of 1.5×10^{16} $cm^{-2}s^{-1}$ at 1 mTorr and 400 W. In general, the VUV flux was approximately half of the ion flux.

These observations motivate the development of methods to independently control VUV photon fluxes or to control the ratio of VUV fluxes to ion fluxes in ICPs used for materials processing. Radiation trapping process of VUV photons, as discussed in Chapter 1, is important in addressing the dynamics of VUV fluxes emission in such ICPs.

In this chapter, we discuss results from a computational investigation of VUV fluxes produced in low-pressure (tens of mTorr) cw and pulsed ICPs sustained in Ar, Ar/Xe and He/Ar gas mixtures. The goal of this investigation is to characterize the VUV fluxes and propose methods to control the absolute value of VUV fluxes, their spectra and the ratio of VUV fluxes to ion fluxes. We found that in cw ICPs sustained in Ar at constant power, VUV fluxes to the bottom substrate are a function of gas pressure, with an asymptotic constant maximum VUV fluxes being produced at high pressure. This result, though, is a function of geometry and aspect ratio of the plasma chamber. Ion fluxes to the bottom substrate, on the other hand, monotonically decreased with increasing pressure. In pulsed Ar ICPs, the cycle averaged VUV fluxes increase as duty cycle increases, while ion fluxes are less sensitive to changes of duty cycle. This scaling then provides a means to control the ratio of photon to ion fluxes by duty cycle. When rare-gas mixtures are used, some coarse tuning of the VUV emission spectrum is possible through the mole fractions of the rare gases. However, the proportion of VUV flux from each component is highly non-linear. For example, in Ar/Xe mixtures, the VUV fluxes from Xe exceed those from

Ar when the mole fraction of Xe exceeds 20%. In He/Ar mixtures, the VUV flux from Ar dominates until the He mole fraction exceeds 99%.

The model used in this investigation is described in Section II, followed by a short discussion of the plasma dynamics of ICPs in Section III, including validation of the model. The scaling of VUV fluxes are discussed in Sections IV and V followed by our concluding remarks in Section VI.

4.2 Description of the Model

The model used in this investigation is the Hybrid Plasma Equipment Model (HPEM), which is described in detail in Chapter 2. Briefly, the HPEM is a modular simulator in which different physical processes are addressed in an iterative manner. In this investigation, the major modules used in the HPEM are the Electromagnetics Module (EMM), the electron Monte Carlo Simulation (eMCS) within the Electron Energy Transport Module (EETM), the Fluid Kinetics Poisson Module (FKPM) and the Radiation Transport Monte-Caro Module (RTMCM). The densities of all charged and neutral species, and the electric potential, are obtained from the FKM. Separate continuity, momentum and energy equations are integrated in time for all heavy particles. The electron density is obtained from integrating a continuity equation with fluxes provided by the Sharffeter-Gummel formulation which analytically provides upwind or downwind fluxes. The electric potential is obtained by a semi-implicit solution of Poisson's equation. Charge densities are computed on surfaces as being due to the fluxes of electrons and ions from the bulk plasma, secondary electrons leaving the surface and secondary electrons from other locations collected by those surfaces. Inductively coupled electromagnetic fields are produced by the EMM using a frequency domain solution of Maxwell's equations which provides a stationary wave equation. Given the symmetry of the reactor (here, cylindrical), the inductively coupled electric fields are in the azimuthal direction and the magnetic fields are in the (r,z) plane. The calculation provides the amplitudes and phase angles of each field. The plasma conditions we investigated are at low enough pressures that the electromagnetic skin depth may be anomalous.[16-18] To better represent the power deposition under these conditions, power of ICP is calculated using eMCS model as discussed in Chapter 2.

In this paper, we discuss results for ICPs sustained in Ar, He/Ar and Ar/Xe gas mixtures. The atomic model for Ar consists of 8 levels, Ar, Ar($1s_5$), Ar($1s_4$), Ar($1s_3$), Ar($1s_2$), Ar(4p), Ar(4d) and Ar^+. Ar(4p) is a lumped excited state that includes Ar(4p, 3d, 5s, 5p). Ar(4d) is a lumped excited state that includes Ar(4d, 6s, Rydberg states). The molecular states $Ar_2^*$and Ar_2^+ were also included, however their densities are 100-1000 times lower than their atomic counterparts. The reaction mechanism for Ar is in Appendix A. The two resonance transitions Ar($1s_4$) $\rightarrow$ Ar (104.8 nm), Ar($1s_2$) $\rightarrow$ Ar (106.7 nm), and excimer emission from Ar_2^* at 121 nm are tracked in the RTM. The secondary emission coefficient for electrons on the substrate by ions is 0.15 and is 0.05 on other surfaces. For excited states, the secondary emission probability was 0.03 on the substrate and 0.01 on other surfaces. For VUV photons, the secondary emission probability was 0.01 on all surfaces.

To investigate tuning of the VUV spectra emitted by low pressure ICPs, two additional gas mixtures were considered – Ar/Xe mixtures that will produce VUV from Xe with longer wavelengths than from Ar, and Ar/He mixtures that will produce VUV from He with shorter wavelengths than from Ar. The reaction mechanism for Ar/Xe mixtures has the following additional species: Xe, Xe($1s_5$), Xe($1s_4$), Xe($1s_3$), Xe($1s_2$), Xe(6p), Xe(5d), Xe(7s), Xe(7p), Xe^+, $Xe_2^*$and Xe_2^+. The Xe(7p) state is an effective lumped state comprising Xe(7p, 6d, 8s, 7d, 9s, 9d, 10s, 10d, higher Rydberg states). The two resonance transitions Xe($1s_4$) $\rightarrow$ Xe (129.76 nm) and

$Xe(1s_2) \rightarrow Xe$ (147.1 nm), and excimer emission from Xe_2* at 174 nm are tracked in the RTM. The additional reactions for Ar/Xe mixtures are listed in Appendix B. The reaction mechanism for Ar/He mixtures has the following additional species: He, $He(2^3S)$, $He(2^1S)$, $He(2^3P)$, $He(2^1P)$, He(3s), He(3p) and He^+. He(3p) is a lumped state of all higher states. Emission from $He(2^1P) \rightarrow He$ (59.1 nm) is considered in RTM. The additional reactions for Ar/He mixtures are listed in Appendix C.

4.3 Plasma Dynamics in ICP

A schematic of the reactor used in this investigation is shown in Fig. 4.1. The simulation is cylindrically symmetric and 2-dimensional. The intent of this study was not to model a specific configuration but rather to discuss more general properties of VUV emission from ICPs, and so we have chosen a simple geometry. The reactor has a diameter of 22.5 cm and substrate to window height of 12 cm. Gas is fed into the reactor through an annular nozzle at the top and exhausted by an annular pump-port at the bottom. VUV and ion fluxes will be discussed averaged over the substrate. The plasma is sustained by inductively coupled electromagnetic fields produced by a three-turn coil powered at 10 MHz. We will first discuss VUV emission from the base case plasma sustained in Ar at 20 mTorr and a cw power of 150 W.

The electron density, n_e, and temperature, T_e, and densities of the metastable $Ar(1s_5)$ and radiative $Ar(1s_4)$ states are shown in Fig. 4.2. The VUV within the plasma for the 106.7 and 104.8 nm transitions are also shown. In the steady state, the diffusive plasma has a peak electron density of 2.8×10^{11} cm^{-3}. The metastable $Ar(1s_5)$ and radiative $Ar(1s_4)$ states have peak densities of 3.2×10^{11} cm^{-3} and 9.8×10^{10} cm^{-3} respectively. T_e peaks beneath the coils at up to 3.5 eV. The excited state densities are skewed towards the location of maximum power deposition under the coils. The lifetimes, either radiative or by electron collision quenching, of the excited states are shorter than the lifetime of ions due to loss by diffusion. The distribution of excited states therefore more closely reflect their sources by electron impact, which are maximum under the coils, compared to the spatial distribution of ions. The density of Ar under the inlet is 5.2×10^{14} cm^{-3}, whereas near the axis of the reactor beneath the coil the Ar density is 3.4×10^{14} cm^{-3}. (The gas near the axis of the reactor beneath the coil is additionally rarefied by gas heating producing a temperature of 571 K).

The VUV fluxes have maximum values of 10^{17} cm^{-2} s^{-1} for the 104.8 nm transition and 10^{18} cm^{-2} s^{-1} for the 106.7 nm transition. The larger VUV fluxes for the transition originating from the lower $Ar(1s_4)$ resonant state is in large part a consequence of the collisional coupling of the heavily populated $Ar(1s_5)$ which refreshes the density of the $Ar(1s_4)$, and maintains its density about an order magnitude higher than the $Ar(1s_2)$. The VUV fluxes internal to the plasma are more than 100 times the magnitude of VUV fluxes escaping from the plasma and striking surfaces (see discussion below). The vast majority of the VUV flux internal to the plasma results from the emission, absorption and re-emission of photons near the center of the lineshape where the optical depth is greatest. The majority of photons escaping the plasma are from the less populated wings of the lineshape. This recirculation of the VUV photons internal to the plasma increases the average VUV flux relative to that observed from the outside.

The electron energy distributions, $f(\varepsilon)$, as a function of height at the half-radius are shown in Fig. 4.3a. The $f(\varepsilon)$ are 2-temperature with the transition occurring approximately at the inelastic threshold for the $Ar(1s_n)$ manifold. The low-energy temperature, 4.0 eV, is essentially uniform as a function of height due to the high plasma density enabling electron-electron collisions to efficiently conduct power throughout the chamber. The high energy temperature decreases from 2.0 eV at a height of 11 cm to 1.2 eV at 2.4 cm, a consequence of inelastic collisions as the electron transport from the region of maximum power deposition under the coils to lower in the reactor.

Fluxes of ions and photons are collected on the substrate surface at the bottom of the reactor. The ambipolar-driven ion fluxes Ar^+ and Ar_2^+ are calculated and recorded from the FKM. Photon fluxes of the two resonant transitions [Ar($1s_4$) $\rightarrow$ Ar (104.8 nm), Ar($1s_2$) $\rightarrow$ Ar (106.7 nm)] and excimer emission (Ar_2^* at 121 nm) are from the RTM. When averaged across the substrate, the ion flux in the base case is 8.1×10^{15} $cm^{-2}s^{-1}$ and VUV photon flux is 1.1×10^{16} $cm^{-2}s^{-1}$ with 80% of the VUV flux coming from the Ar($1s_4$) $\rightarrow$ Ar (106.7 nm) transition. This corresponds to 20.5 mW-cm^{-2} in the VUV or a power efficiency of about 15%-20% at producing VUV radiation that escapes the plasma. The fluxes of Ar_2^+ (2.8×10^{14} $cm^{-2}s^{-1}$) and of excimer emission are small in comparison due to the lack of 3-body collisions at low pressure. The volume averaged radiation trapping factors are 226 for the Ar($1s_4$) $\rightarrow$ Ar (104.8 nm) transition and 586 for the Ar($1s_2$) $\rightarrow$ Ar (106.7 nm) transition. For these conditions, the flux of VUV photons to the substrate exceeds that of the ions. The magnitude of the VUV fluxes are commensurate to those experimentally measured for similar conditions.[14,15].

All excited states of Ar can be photo-ionized by the VUV fluxes. The random VUV fluxes in the middle of the reactor are 2.2×10^{18} $cm^{-2}s^{-1}$, which are comparable to or can exceed the random thermal electron fluxes. However, the cross sections for photoionization of Ar excited states are small, 10^{-19} cm^2. The end result is that rate of photoionization is small, having a maximum value of 2.4×10^{11} $cm^{-3}s^{-1}$, compared to ionization by bulk electrons having a maximum value of 8.7×10^{15} $cm^{-3}s^{-1}$.

4.4 Controlling photon fluxes in Ar ICP

4.4.1 Photon and ion fluxes vs. pressure

To investigate methods to control the relative magnitudes of the ion and photon fluxes, we varied the pressure from 5 to 50 mTorr while keeping other conditions the same as the base case. The photon and ion fluxes to the bottom substrate as a function of pressure are shown in Fig. 4.4. Representative lineshape functions and radiation trapping factors are in Fig. 4.5. For these conditions, total VUV fluxes monotonically increase while asymptotically approaching a maximum at higher pressures of 1.5×10^{16} $cm^{-2}s^{-1}$ (or 28 mW cm^{-2}). Ion fluxes to the substrate are maximum at low pressure and decrease monotonically with increasing pressure. These trends in both ion and photon fluxes are a bit artificial since fluxes are recorded on the lower substrate where, for example, a wafer may be located. With increasing pressure, the source function for ionization becomes progressively more confined to the skin depth of the electromagnetic field below the insulator, and so move closer to the top surface. The loss of ions is therefore preferentially to the top surface at higher pressures. At low pressures, the skin depth is anomalous, resulting in high energy electrons and the ionization sources being more uniformly distributed in the reactor. This results in the ion flux to the substrate decreasing on a relative basis compared to other surfaces when the pressure increases.

The monotonic, but saturating, increase in the VUV flux to the substrate for constant power deposition with increasing pressure results from competing effects. In argon ICPs, the electron density and excited densities increase with increasing pressure over this range of pressures.[19-21] However, the shortening of the mean free paths and increase in plasma density which shortens the electromagnetic skin depth localizes the production of VUV photons closer to the top of the reactor near the coils. This localization of the production of VUV photons, more remote from the substrate, might otherwise decrease the VUV flux to the substrate. At the same time, the higher pressure produces a larger radiation trapping factor that lengthens the lifetime of the radiating states that makes those states more susceptible to being quenched by both electron and heavy particle collisions. For our geometry and operating conditions, the incremental increase in the source of excited states dominates over quenching at lower pressures and nearly balances the sources at higher pressures. Meanwhile, a constant power ultimately limits the VUV flux that can be generated in the absence of an increase in efficiency of excited state production

With an increase in photon fluxes and decrease in ion fluxes to the substrate as a function of pressure, the ratio of the VUV to ion flux incident onto the substrate, β, increases as the pressure increases as shown in Fig. 4.4c. At 5 mTorr, ion fluxes are larger than VUV fluxes and $\beta = 0.3$. As the pressure increases above 10 mTorr, VUV fluxes become larger than ion fluxes to the substrate, with $\beta = 3.0$ at 50 mTorr.

The lineshape functions for the 106.7 nm transition, shown in Fig. 4.5a, display the transition from moderate trapping at 5 mTorr (trapping factor 115) to severe trapping at 25 mTorr (trapping factor 630). These lineshape functions are for the VUV flux that escapes from the plasma overaged over all surfaces, and so would be the spectrum observed looking into the plasma from the outside. The severity of trapping is indicated by the self-absorption at line center. Photons emitted near line center are reabsorbed with a mean free path of <100 μm and are isotropically reemitted. These photons generally recirculate within the plasma through hundreds of emissions and reabsorptions until that quantum of energy is either quenched or the photon is statistically emitted in the wings of the lineshape function. Photons emitted in the wings have proportionately longer mean-free-paths which enable the photons to escape from the plasma. The width of the self-absorbed core of the lineshape function is determined in large part by the Doppler width at low pressure, which for these conditions is 9-10 GHz.

The general trends discussed there for magnitudes of VUV fluxes and ratios of VUV to ion fluxes generally agree with prior experimental measurements.[14] Woodworth et al. [14] measured VUV fluxes from ICPs sustained in pure Ar at 20 mTorr and 200 W rf power. Their values for VUV fluxes, 3.5×10^{16} $cm^{-2}s^{-1}$ or 52 mW/cm^2, at 200 W compares favorably to the results of the simulation, 1.1×10^{16} $cm^{-2}s^{-1}$ or 20.5 mW/cm^2 at 150 W. Jinnai et al. also measured VUV fluxes in ICPs sustained in pure Ar at 5 mTorr on the order of 10^{15}-$10^{16}cm^{-2}s^{-1}$.[13] The VUV fluxes from our simulation at 5 mTorr (5.4×10^{15} $cm^{-2}s^{-1}$) are in the same range.

A more quantitative comparison to experiment can be made for VUV emission from ICPs sustained in Ar reported by Boffard et al.[19] In this work, ICPs were sustained in Ar at pressures of 1 mTorr to 25 mTorr for a power of 600 W. The total flux of VUV emissions (dominated by the transitions at 104.8 nm and 106.7 nm) were measured on the bottom substrate of their reactor using a calibrated VUV photodiode. The geometry and operating conditions of Boffard et al. were implemented in our model. A comparison to the experimental results is shown in Fig. 4.6. In the simulation, photon fluxes were averaged over the substrate, and random thermal ion fluxes are measured in the center of the reactor. The trends of computed results match the experiment. The experimental results show a broad maximum in the VUV flux at 10-12 mTorr whereas the simulation shows the maximum at 15 mTorr. The absolute magnitude of the VUV fluxes agree to within a factor of 2. Note that the random thermal ion fluxes measured in the center of the reactor increase with increasing pressure whereas the ion fluxes incident onto the substrate decrease with pressure.

This comparison to the results of Boffard et al. emphasizes the importance of geometry in assessing the VUV and ion fluxes to the substrate. The differences in the pressure dependence of the VUV fluxes shown in Fig. 4.5b and in Fig. 4.6a are dominantly a result of geometry since the reaction mechanisms are identical. For example, the VUV photons in these two cases originate in different locations in the reactor with respect to the substrate and so the substrate subtends a different solid angle.

4.4.2 Pulsing: photon and ion fluxes vs. duty cycle (DC)

With cw excitation, there is limited ability to control the ratio of VUV to ion flux. For a given pressure and power deposition there is a single reactor averaged T_e that produces the steady state plasma. As a result, the balance between populating the resonant states and ionization is fairly constrained. Pulsed excitation provides additionally flexibility since T_e can considerably vary during the pulsed cycle and so the ratio of excitation of resonant states and ionization is not constrained to a single reactor averaged value.[6,22,23]

With the goal of controlling the average fluxes of VUV photons and ions to the substrate, we investigated pulsed plasma excitation of the ICP. The pulsed power waveform is characterized by the pulse repetition frequency, PRF, the number of power pulses per second; the duty cycle, DC, the fraction of the pulsed period the ICP power is applied; and the cycle average power deposition, CAP. The base case for pulsing is Ar at 20 mTorr, with a PRF of 50 KHz (20 μs period), 15% duty cycle and CAP of 150 W.

The electron temperature T_e, ion density and the density of Ar(1s$_4$) state density during the pulse cycle are shown in Fig. 4.7-9. During the pulse-on period, T_e spikes to 4.8 eV compared with the cw value of 3.5 eV. This is the over-shoot effect [6,22,23] where upon applying power to the lower electron density at the end of the preceding afterglow, T_e increases above the cw value in order to avalanche the electron density. Electrons are heated in the skin depth between the coils – and convect to the lower part of the reactor. At the trailing edge of the power pulse, T_e decreases to 2.3 eV in the afterglow, nearly uniformly distributed in the reactor. T_e is maintained during the afterglow by super-elastic relaxation of the metastable states of Ar, while thermal conduction provides the uniform distribution.

Electron energy distributions at different times during the pulsed cycle are shown in Fig. 4.3b at radius of 5.6 cm and height of 11.1 cm at the edge of the skin depth. The time during the pulse period for each plot is shown in the diagram at the bottom of the figure. At the beginning of the pulse, the larger electric field required to avalanche the plasma to higher densities produces an extended high energy tail, which begins to relax during the pulse-on period producing a 2-temperature distribution. At the end of the power-on pulsed, the temperature of the bulk and tail are 5.2 eV and 3.3 eV, respectively. The tail of $f(\varepsilon)$ rapidly decays at the end of the power pulse while the low energy portion of the distribution is sustained by super-elastic electron heating of the long lived metastable states.

The modulation in T_e also produces a modulation in the electron and Ar^+ densities The maximum ion density occurs at the end of the power-on pulse, 3.4×10^{11} cm^{-3}. For this PRF, the inter-pulse period is not long enough to produce significant loss by diffusion during the afterglow, and so the intra-pulse modulation in the ion density is small, about 15%. The resonant $Ar(1s_4)$ state has an intra-pulse modulation of about 50%. The relatively long persistence of the resonant state results, in part, from its radiation trapped lifetime of about 5 μs, and due to mixing with the metastable state $Ar(1s_5)$ whose density decays slowly due to electron collision quenching and diffusion.

The differences in the decay rates of Ar^+ and $Ar(1s_4)$ during the pulse period, imply that the ratio of the VUV to ion fluxes incident onto the substrate will vary during the pulse period. For example, the VUV fluxes to the substrate as a function of time for different duty cycles are shown in Fig. 4.10. The corresponding ion fluxes, ratio of VUV-to-ion flux, β, and electron temperatures are shown in Fig. 4.11. The ICP was sustained in Ar at 20 mTorr with a CAP of 150 W for DCs from 10% to 50% and PRF of 50 KHz. The quasi-dc value of T_e is 3.3 eV, a value that is reached after about 3-4 μs for the 50% DC. With shorter duty cycle, T_e peaks to a higher value upon application of power, 4.2 eV for 10% DC. This is, in part, a consequence of the higher peak power applied during the shorter cycle to produce the same cycle averaged power deposition. With the exception of the shortest duty cycle, the T_e at the end of the afterglow period is about 2 eV, largely sustained by super-elastic relaxation. The modulation in the ion flux to the substrate during the pulsed cycle is about 15%-20%.

The modulation in the flux to the substrate of the 104.8 nm line originating with $Ar(1s_4)$ is a factor of 15-16 whereas the modulation in the 106.7 nm line originating with the $Ar(1s_2)$ is a factor of 3-4. The cascade downward of excited states during the afterglow terminates with the $Ar(1s_5)$ metastable state that is collisionally coupled to the $Ar(1s_4)$, which has density of 8-10 $\times 10^{10}$ cm^{-3} during the afterglow. This collisional coupling replenishes the $Ar(1s_4)$ to maintain a density of 1.2-1.5 $\times$ 10^{10} cm^{-3} while the trapped optical lifetime is 5 μs. The end result is that there is significant VUV emission at 106.7 nm after the power is terminated and T_e decreases. The $Ar(1s_2)$ is efficiently collisionally coupled to $Ar(1s_3)$ have a density of 8-10 $\times 10^9$ cm^{-3}, but less efficiently collisionally coupled to the $Ar(1s_5)$. The $Ar(1s_2)$ is therefore less likely to be replenished during afterglow by the reservoir of $Ar(1s_5)$. The VUV emission at 104.8 nm therefore more closely follows the electron temperature and its trapped lifetime of 0.4 μs. The ratio of VUV-to-ion flux, β, during the pulse period is highly modulated. The maximum value of β at the end of the power-pulse is 2.4 for 10% DC to 2.0 at 50% DC. β decreases to 0.6-0.9 at the end of the afterglow, compared to a cw value of $\beta = 1.7$. During most of the pulse period, the VUV flux exceeds the ion flux. However, at the end of the afterglow, ion flux could be larger due to the longer life time of ions.

The peak (maximum during the pulse) and cycle averaged VUV and ion fluxes, and ratio of VUV-to-ion flux, β, are shown in Fig. 4.12 as a function of DC. The VUV fluxes are the sum of the fluxes for the 104.8 and 106.7 nm lines. The peak VUV fluxes increase with decreasing duty cycle by about 10% from a DC of 50% to 10%. The peak VUV flux is 2.2×10^{16} $cm^{-2}s^{-1}$ (40.9 mW/cm^2) at a DC of 10% compared to the cw value of 1.1×10^{16} $cm^{-2}s^{-1}$ (20.5 mW/cm^2). This increase reflects the peaking of the electron temperature to higher temperatures with lower DC. The cycle averaged VUV flux increases with DC, indicating that the longer power-on period more efficiently produces VUV flux, though with a lower peak flux. The peak and cycle averaged ion fluxes are essentially constant for different dc, since the average power deposition is also constant. As a result, as DC increases from 10% to 50%, peak ratio of VUV to ion fluxes decreases from 2.3 to 2.0 and the average ratio increases from 1.1 to 1.5.

4.5 Controlling spectra of photon fluxes in Ar/Xe, He/Ar ICPs

Some coarse control over the VUV spectra obtained from low pressure ICPs can be obtained by gas mixture. For example, Ar/Xe gas mixtures will produce additional longer wavelength VUV lines at 147.1 nm [$Xe(1p_4) \rightarrow Xe(5s^25p^6)$] and 129.76 nm [$Xe(1p_2) \rightarrow Xe(5s^25p^6)$]. Ar/He mixtures will produce additional shorter wavelength VUV, dominantly at 59.1 nm [$He(1s2p\ ^3P^0) \rightarrow He(1s^2\ ^1S)$]. We first discuss results for Ar/Xe mixtures, where the base case is Ar/Xe = 75/25 at 20 mTorr with 150 W cw ICP power. Densities of Ar^+ and Xe^+, and the resonant states densities Ar($1s_4$) and Xe($1s_4$) are shown in Fig. 4.13. The maximum Xe^+ density is 6.4×10^{11} cm^{-3} while that of Ar^+ is 4.5×10^{10} cm^{-3}. The higher Xe^+ density results from its lower ionization potential compared to Ar (12.1 eV vs. 16 eV). The metastable and resonant states of Ar do not have sufficient energy to Penning ionize Xe, though the Ar(4p) and Ar(4d) states are capable of Penning reactions. However, due to the low densities of these states, their contribution to the higher Xe^+ density is not large. The maximum Penning ionization rates by Ar(4p) and Ar(4d) are 3.7×10^{12} $cm^{-3}s^{-1}$ and 7.8×10^{11} $cm^{-3}s^{-1}$ respectively, much larger than photoionization, 5×10^{10} $cm^{-3}s^{-1}$. However these values are small compared to bulk ionization by electron impact, 1.0×10^{16} $cm^{-3}s^{-1}$. The densities of the resonant states of Ar and Xe are commensurate. The density of Xe($1s_4$) is 1.6×10^{10} cm^{-3} and that of Ar($1s_4$) is 1.5×10^{10} cm^{-3}. Although the electron impact cross section for excitation of Xe($1s_4$) from ground state has a lower threshold and is 5 times larger than that of Ar($1s_4$), there are few other processes that further discriminate the formation of the two states other than the lower rate of diffusion loses by the heavier Xe atoms.

EEDs at the edge of the electromagnetic skein depth are shown in Fig.14a for different Xe fractions. For a Xe fraction of 1%, $f(\varepsilon)$ is a 2-temperature distribution with the bulk and tail temperatures of 3.0 eV and 2.1 eV. The breakpoint between the temperatures,11 eV, is approximately the inelastic thresholds for the Ar(4s) manifold. As the Xe fraction increases, $f(\varepsilon)$ retains its 2-temperature character with the transition energy between the two temperatures moving close to the Xe threshold at 8-9 eV. The high energy tail at large Xe fraction is depleted by the relative low threshold inelastic collisions of Xe. The bulk and tail values of T_e for a Xe mole fraction of 40% are 2.2 eV and 1.4 eV

The scaling of VUV intensity as a function of Ar/Xe gas mixture demonstrating coarse spectral control is shown in Fig. 4.15a for constant power and pressure. The total VUV emission from Ar and Xe (sum of their respective resonant transitions), the total VUV flux and the ratio of VUV flux from Xe compared to total fluxes are shown for Xe fractions up to 40%. The total VUV flux decreases by about 40% with increasing Xe fraction from 0 to 40%. This decrease is in part due to the larger proportion of power deposition expended in ionization of Xe relative to excitation compared to Ar. For example, at an electron temperature of 4 eV in pure Ar, about 1% of the power dissipated by electron collisions with the ground state produce ionization whereas 53% of the power produces excitation of the Ar(4s) manifold. In pure Xe at 4 eV, 32% of the power produces ionization and 23% produces excitation of the Xe(6s) manifold. The higher plasma density with increasing Xe fraction also produces more electron collision quenching of the resonant states. Electron temperature T_e decreases from 3.1 eV with 1% of Xe to 2.1 eV at 40% of Xe.

The proportion of the VUV flux due to emission from Xe increases somewhat linearly with increasing Xe fraction up to 20% before beginning to saturate. With 20% Xe, the fraction of the VUV flux due to Xe emission is 60%. With 40% Xe, the fraction of VUV flux due to Xe emission is 85%. The absolute VUV flux saturates at a Xe fraction of 30%. At this Xe fraction, the majority of power deposition is expended in Xe.

Spectral lineshapes for Ar (106.7 nm) and Xe (147.1 nm) emission and radiation trapping factors are shown in Fig. 4.16 for at different Xe fractions. The trapping factor for Ar only moderately decreases as the Ar fraction decreases from 99% to 60%. As the Xe fraction increases from 1% to 40%, the trapping factor increases from 58 to 170. The resulting lineshape functions reflect these trends in trapping factor. The lineshape function for Ar 106.7 nm emission is only moderately less self-absorbed as the Ar fraction decreases over this range. The lineshape function for 147.1 nm Xe emission becomes significantly more self-absorbed with increasing Xe fraction.

The control of spectrum in Ar/Xe mixtures was also investigated using pulsed power for a duty cycle of 15% and cycle average power of 150 W. The VUV intensity from Xe and Ar, total VUV intensity and fraction of intensity due to Xe as a function of Xe fraction are shown in Fig. 4.15b for constant CAP and pressure. Qualitatively, the trends are similar to cw excitation – decrease in total VUV flux with increasing Xe fraction and saturation in the VUV flux from Xe at a fraction of about 30%. The difference is that the fraction of the VUV flux due to Ar is larger than with cw excitation. For example, with 20% Xe, the fraction of the VUV flux due to Xe emission is 50%. For a Xe fraction of 40%, the fraction of VUV flux due to Xe emission is 80%. This decrease in the proportion of VUV emission due to Xe and increase in emission due to Ar results from the increase in T_e that occurs by pulsing power. (See, for example, Fig. 4.9 for pure argon.) Higher electron temperatures favor excitation of Ar compared to Xe due to the higher threshold energies for exciting Ar.

Control of the VUV spectrum was also investigated in He/Ar mixtures where VUV emission from He at 59.1 nm adds a shorter wavelength photon. The cw base case is He/Ar = 75/25, 20 mTorr and 150 W. The densities of Ar^+, He^+, $Ar(1s_4)$ and $He(2^1P)$ are shown in Fig. 4.16. The Ar^+ density is 1.9×10^{11} cm^{-3}, 2 orders of magnitude larger than that of He^+, 2.3×10^9 cm^{-3}. The density of the radiating state $Ar(1s_4)$ is 3.4×10^{10} cm^{-3} and $He(2^1P)$ is 4.9×10^7cm^{-3}. These densities have similar disparities as the ion densities, with the He excited state density being 3 orders of magnitude lower than that for Ar.

EEDs for He/Ar mixtures at the edge of skin depth are shown in Fig.14b for different Ar fractions. For small mole fractions of Ar the tail of the $f(\varepsilon)$ extends well above 50 eV, an indication of the low stopping power of pure He plasmas. The cut-off at the ionization potential of He, 24.6 eV, is only minor. As the Ar fraction increases to as little as 10-20%, $f(\varepsilon)$ assumes the 2-temperature distribution associated with pure Ar discharges. T_e in the bulk and tail of $f(\varepsilon)$ are 6.0 and 5.5 eV for 0.5% of Ar. T_e for the bulk and tail of $f(\varepsilon)$ are 3.1 eV and 2.2 eV for 40% Ar.

In He/Ar mixtures, the vast majority of power is dissipated into Ar having the lower threshold energies while all excited states of He are capable of Penning ionizing Ar. For example, based on collisions with the ground state, for an Ar/He=50/50 mixture with an electron temperature of 4 eV, only 3% of the discharge power is dissipated by collisions with He, and the majority of those collisions are elastic. (These values were obtained from stationary solutions of Boltzmann's equation for the electron energy distribution.) The end result is that the vast majority of VUV emission from the plasma originates from Ar until large mole fractions of He. For example, the VUV flux originating from He and Ar, total VUV flux and fraction of VUV flux from He are shown in Fig. 4.18a as a function of He fraction. First, with increasing He fraction, the total VUV flux decreases. This is in large part a consequence of a smaller fraction of power being dissipated in exciting the radiative states with increasing He fraction. With trapping factors of 190-240 for VUV emission at 59.1 nm, the lifetime for He(2^1P) is extended to 0.10-0.13 μs. With the rate coefficient for Penning ionization of 1×10^{-9} cm^{3}s^{-1}, the frequency of Penning ionization of Ar by He excited states is 2×10^5 s^{-1}, or a lifetime of about 5 μs. So resonant states of He are more likely to radiate than to be quenched by Penning collisions. However the lifetime for Penning collisions is much shorter than the rate of collisional mixing or radiative cascade that may populate He(2^1P) form higher levels. So a large fraction of the energy producing excited states of He is consumed by Penning processes before cascading to the He(2^1P). The Ar^+ produced by these processes then does not radiate. So power dissipated into excited states of He does not efficiently produce VUV emission compared to power dissipated into Ar.

The cross section for photoionization Ar ground state at 59.1 nm is 3.5×10^{-17} cm^2 which produces a mean free path for these conditions of 30-100 cm. So there is only a moderate fraction of the 59.1 nm emission that is consumed by photoionization of Ar. The VUV emission from He/Ar mixtures is dominantly from Ar for mole fractions of Ar exceeding 5%. The VUV emission is 99% due to Ar for Ar mole fractions greater than 65%. The VUV emission is 99% due to He for He mole fractions exceeding 99%.

Trapping factors and VUV spectra from Ar at 106.7 nm and from He at 59.1 nm are shown in Fig. 4.19 for Ar mole fractions of 1% to 40%. For both mixtures, the He emission is heavily trapped. The trapping factor for 59.1 nm is 240 for He/Ar=99.5/0.5 and 184 for He/Ar = 60/40. The self-absorption in the lineshape function is 3-4 times broader for He than for Ar due to the higher thermal speed of He. The lineshape function for Ar in the He/Ar=99.5/0.5 mixtures shows little self-absorption and the trapping factor is 2.7. The 106.7 nm transition is essentially optically thin. For the He/Ar=60/40 mixture, the trapping factor is 407 and the 106.7 nm transition is optically thick with self-absorption at line center.

The VUV flux originating from He, Ar, total VUV flux and fraction of VUV flux from He are shown in Fig. 4.18b for pulsed power (duty cycle 15%) as a function of He fraction. The general trends for the pulsed ICP are similar to those for cw results. As was the case with Ar/Xe mixtures, when pulsing the higher T_e favors excitation of the atom with the higher threshold energies. Therefore, pulsing will produce more excited states and more ions in He compared to the same conditions for cw excitation. This produces more relative emission from He but less total emission. Quenching of He excited states channels more power into Ar^+ and less to VUV fluxes. So the total photon fluxes with pulsing are 27% lower than for cw excitation.

4.6 Concluding Remarks

Results from a computational investigation suggest that VUV photon fluxes incident onto substrates in ICP reactors can be controlled to a certain extent. In pure Ar plasmas for constant power, the magnitudes of VUV photon fluxes to the substrate are tunable by changing the gas pressure. However, the details of these trends depend on the details of the operating conditions and geometry of the reactor. In our base case, photon fluxes monotonically increased with pressure, asymptotically reaching a constant value at high pressure. In this process, the increase in plasma density that typically occurs with increasing pressure produced a larger density of resonant states, which dominated over the adverse effects of more quenching and smaller view-angle of the substrate to the source of VUV fluxes. (The reduced view angle resulted from the electron impact source for excited states being more confined to the skin depth.) In contrast in the work of Boffard et. al. [19] as well as in our corresponding simulations, VUV fluxes to the substrate had a maximum at pressures of 10-15 mTorr. For this geometry, the increased quenching and reduced view-angle of the substrate at higher pressures dominated over the increase in radiating state densities.

Pulsing the ICP power allows for additional control over VUV photon fluxes. The rising edge of the power pulse will produce an over shoot of E/N, thus raising the tail of EEDs above that occurring with cw excitation. Due to this over shoot, VUV fluxes to the substrate have a larger peak value at lower duty cycles (larger over shoot of E/N) while the ion fluxes are less sensitive to duty cycle. The instantaneous ratios of VUV to ion fluxes are therefore sensitive functions of duty cycle.

The spectra of VUV photon fluxes can also be discretely tuned by changing the gas mixtures of the plasma. Two rare gas mixtures, Ar/Xe and He/Ar were investigated. The rare gas component with the lower threshold energies for populating the resonant states will dominate the VUV spectra until the higher threshold gas has a large mole fraction. The efficiency of total VUV photon production was higher for large mole fractions of Ar in both mixtures. In Ar/Xe mixtures, a larger proportion of energy is expended in ionizing Xe compared to excitation when the Xe fraction is increased. In He/Ar mixtures, through Penning reactions, electronic excitation of He produces ground state Ar^+ which does not directly radiate. So although one gains the ability to tune the VUV spectra in these mixtures, that advantage is offset by a decrease in efficiency of VUV production.

4.7 Figures

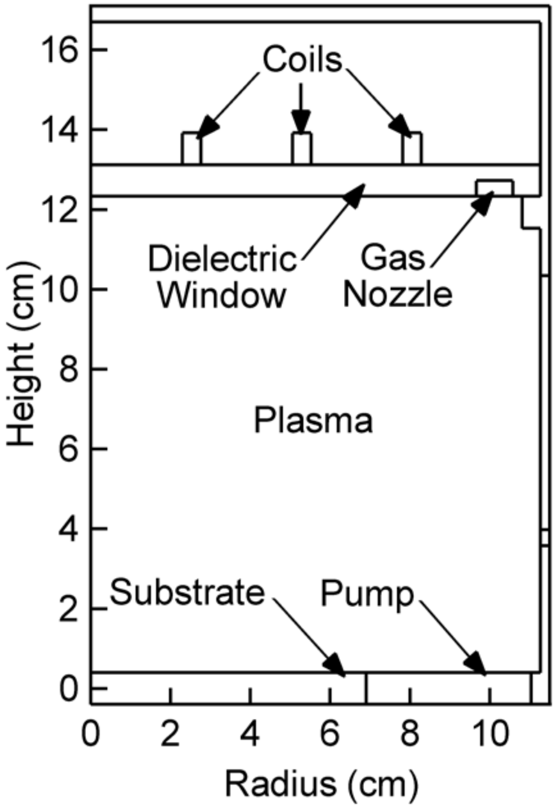

Fig. 4.1 Schematic of the inductively coupled plasma reactor used in the model.

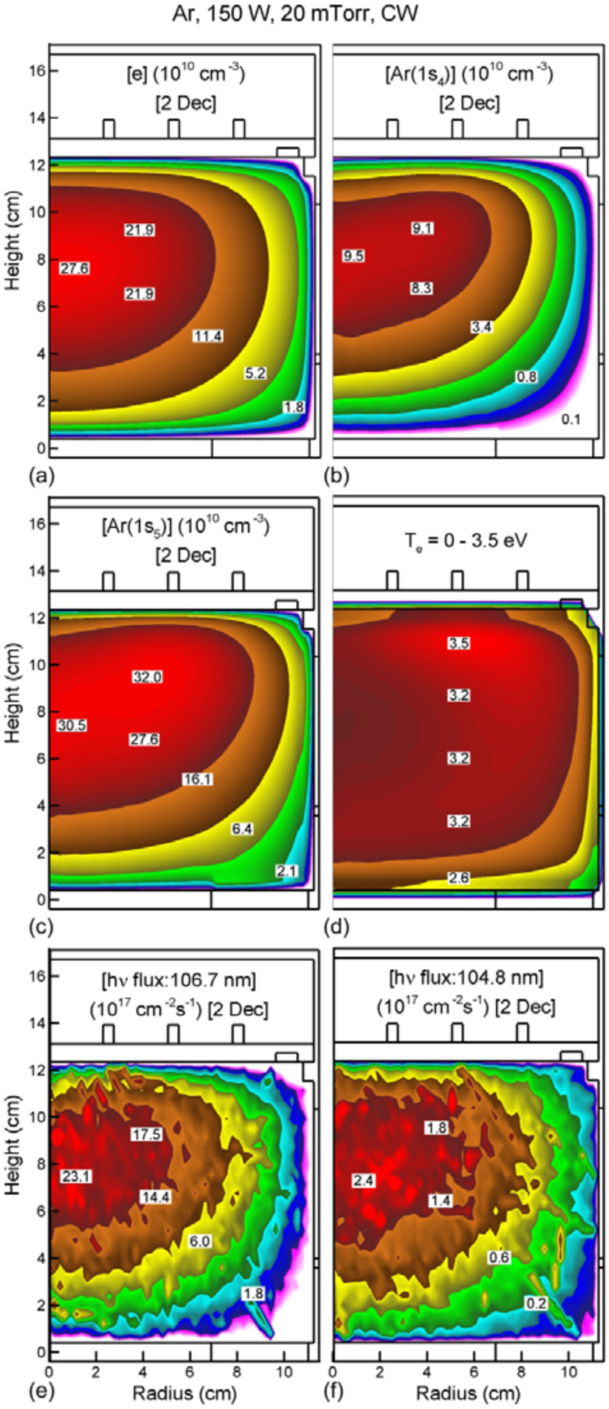

Fig. 4.2 Time averaged plasma properties under base case conditions (Ar, 20 mTorr, 200 sccm, 10 MHz, 150 W cw). (a) Electron density, (b) resonant Ar(1s$_4$) density, (c) metastable Ar(1s$_5$) density, (d) electron temperature, (e) random VUV fluxes for 106.8 nm and for (f) 104.8 nm. The densities are on log-scales of 2 decades.

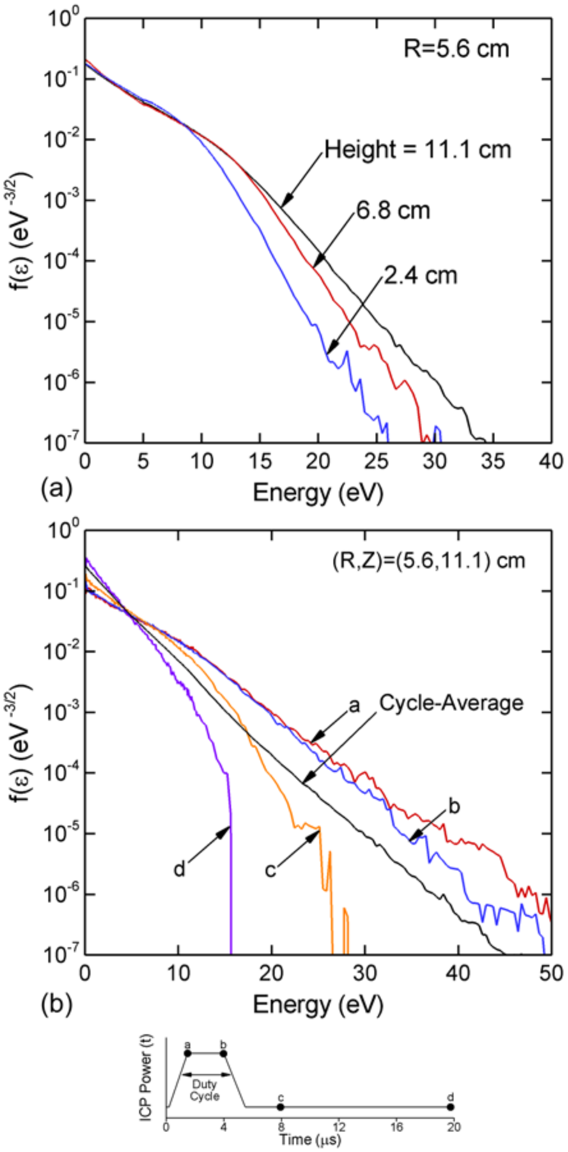

Fig. 4.3 Electron energy distributions at a radius of 5.6 cm and different vertical locations for the base case conditions (Ar, 20 mTorr, 200 sccm, 10 MHz, 150 W cw).

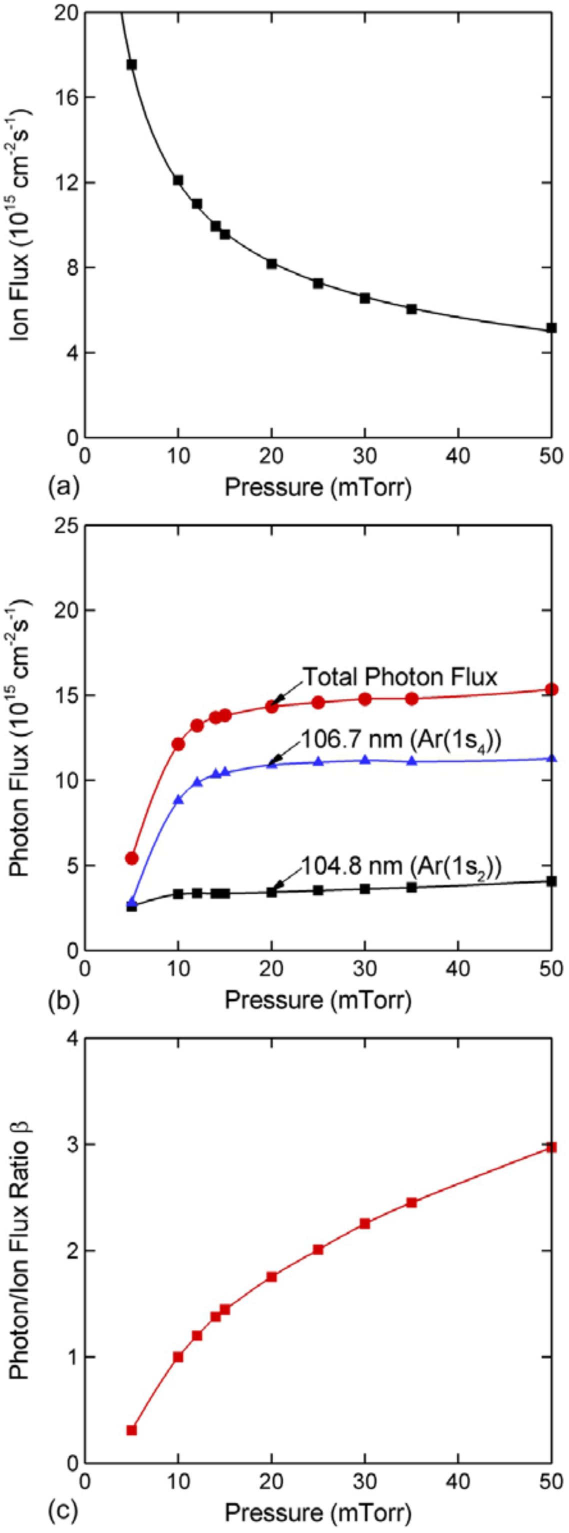

Fig. 4.4 Substrate averaged fluxes for different pressures in Ar (200 sccm, 10 MHz, 150 W cw). (a) Ion fluxes, (b) photon fluxes, (c) total photon/ion flux ratio. Total photon fluxes are the sum of 106.7 nm and 104.8 nm.

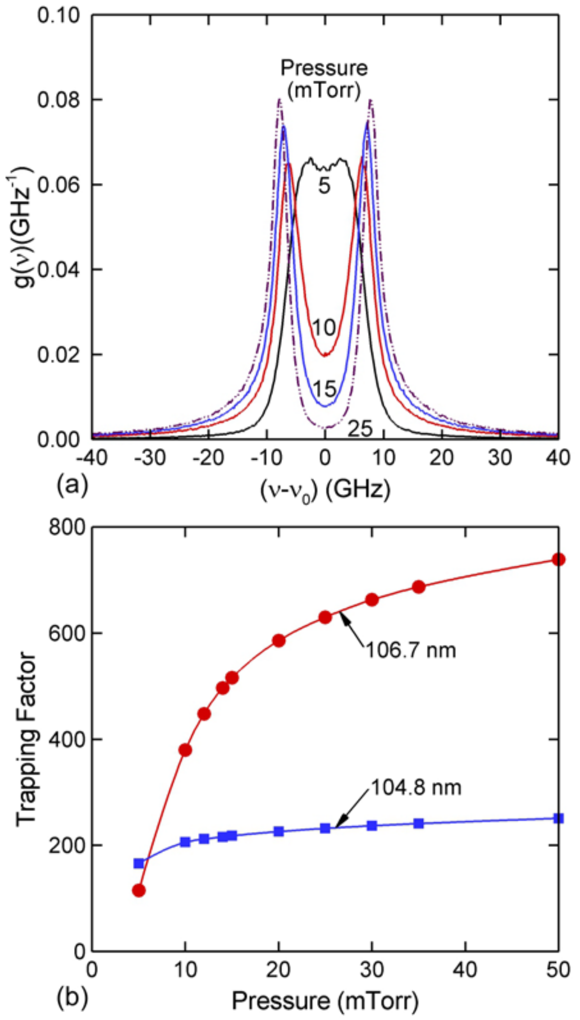

Fig. 4.5 Optical properties for different pressures in Ar (200 sccm, 10 MHz, 150 W cw). (a) Line shape function of 106.7 nm emission. (b) Trapping factor for 106.7 nm and 104.8 nm Ar emission.

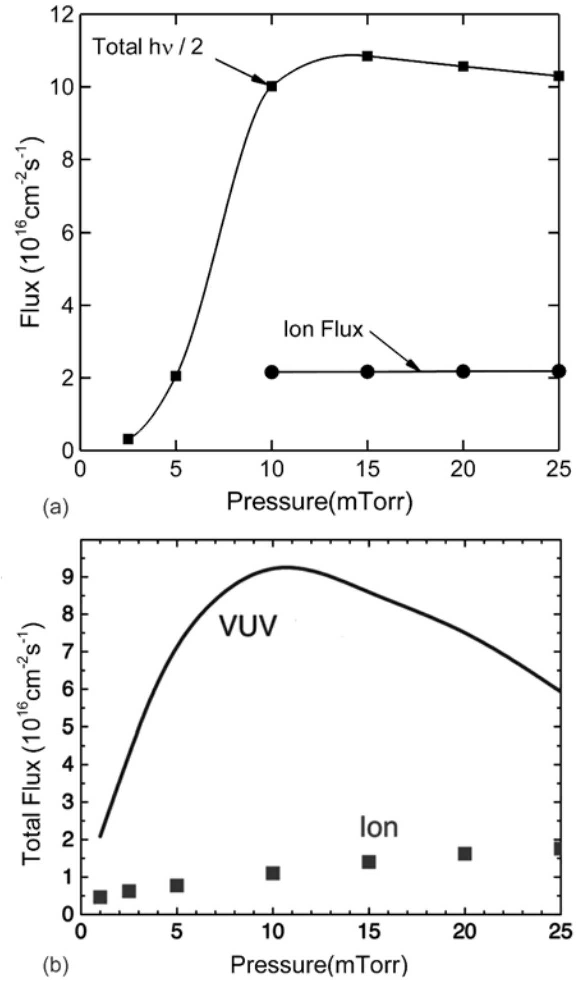

Fig. 4.6 Photon and ion fluxes for the experimental conditions of Boffard *et al.* [19]. (Ar, 6 sccm, 600 W cw). (a) Simulation and (b) experimental results.

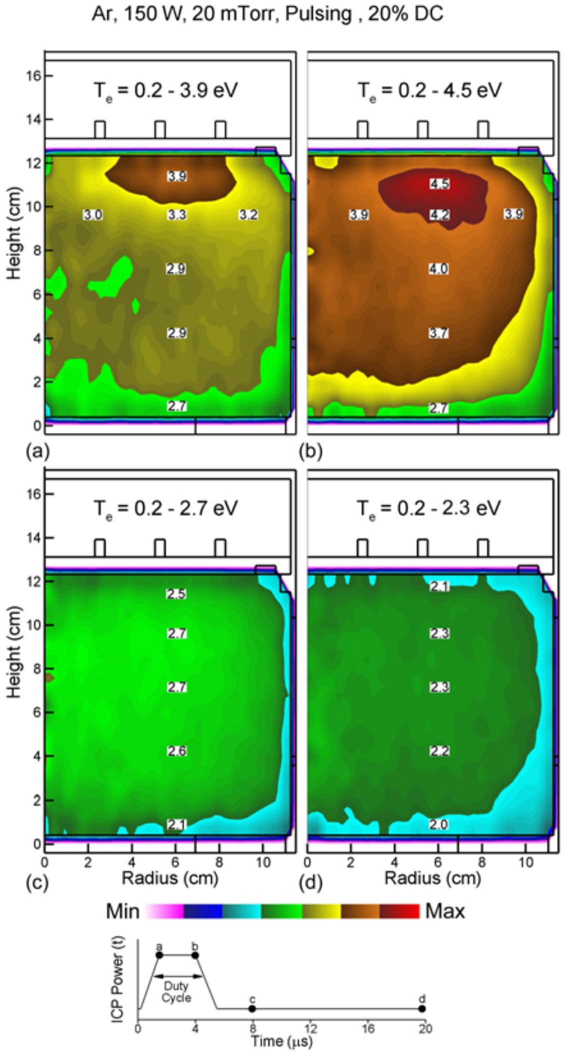

Fig. 4.7 Electron temperature at different times during a pulsed cycle. Plasma conditions are Ar, 20 mTorr, 200 sccm, 10 MHz, 150 W pulsed-period-averaged power, PRF = 50 kHz, duty cycle =20%. (a) At leading edge of the power-on period, (b) at trailing edge of power-on period, (c) 2.5 μs into afterglow period, (d) end of afterglow period. These times are indicated in the schematic at the bottom of the figure.

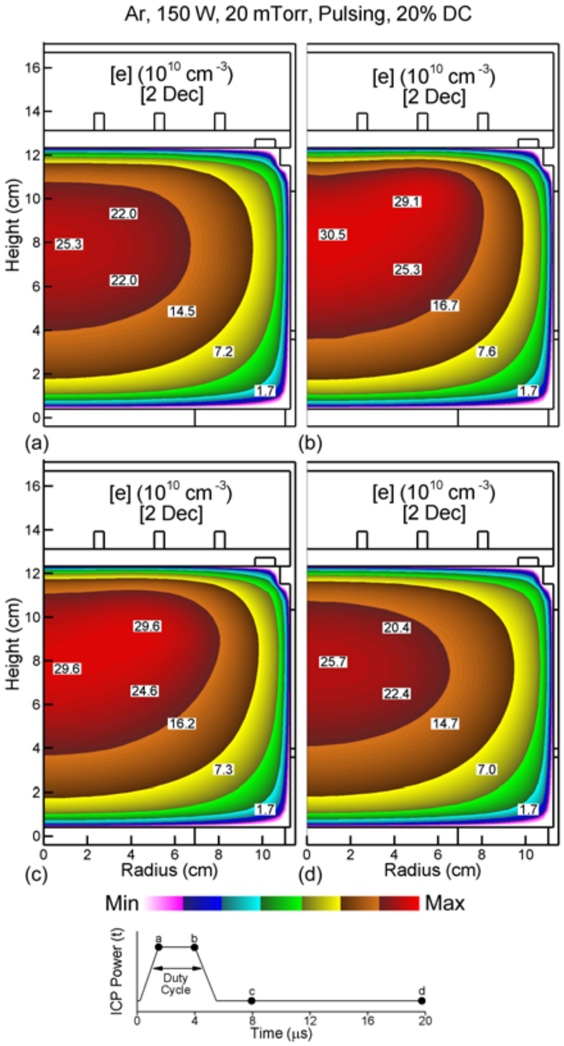

Fig. 4.8 Electron density at different times during a pulsed cycle for the conditions of Fig. 7. (Ar, 20 mTorr, 200 sccm, 10 MHz, 150 W pulsed-period-averaged power, PRF = 50 kHz, duty cycle =20%). %. (a) At leading edge of the power-on period, (b) at trailing edge of power-on period, (c) 2.5 μs into afterglow period, (d) end of afterglow period. These times are indicated in the schematic at the bottom of the figure. Values are plotted on a 2-decade log-scale.

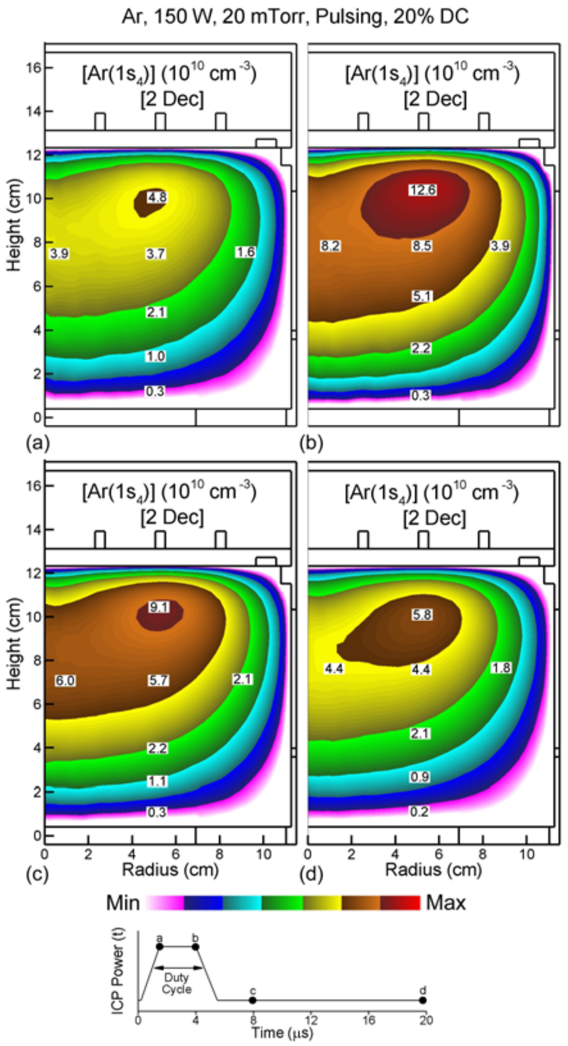

Fig. 4.9 Density of the radiative state Ar(1s$_4$) at different times during a pulsed cycle for the conditions of Fig. 7. (Ar, 20 mTorr, 200 sccm, 10 MHz, 150 W pulsed-period-averaged power, PRF = 50 kHz, duty cycle =20%). %. (a) At leading edge of the power-on period, (b) at trailing edge of power-on period, (c) 2.5 μs into afterglow period, (d) end of afterglow period. These times are indicated in the schematic at the bottom of the figure. Values are plotted on a 2-decade log-scale.

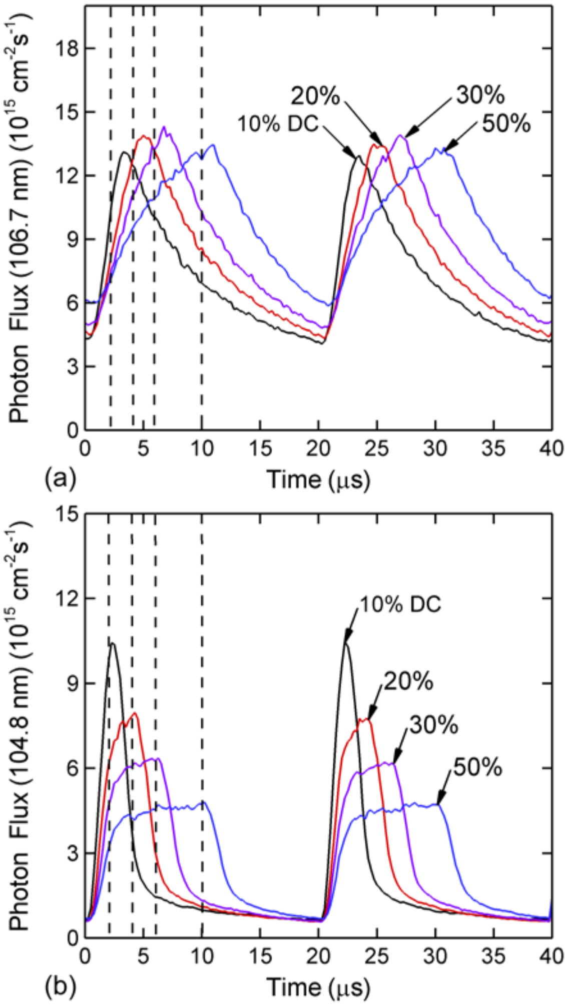

Fig. 4.10 Photon fluxes collected on and averaged over the bottom substrate as a function of time for two discharge pulses for different duty cycles. (a) 106.7 nm [originating from Ar(1s$_4$)] and (b) 104.8 nm [originating from Ar(1s$_2$)]. The dashed lines indicate the end of power-on period. Plasma conditions are Ar, 20 mTorr, 200 sccm, 10 MHz, 150 W CAP, PRF = 50 kHz.

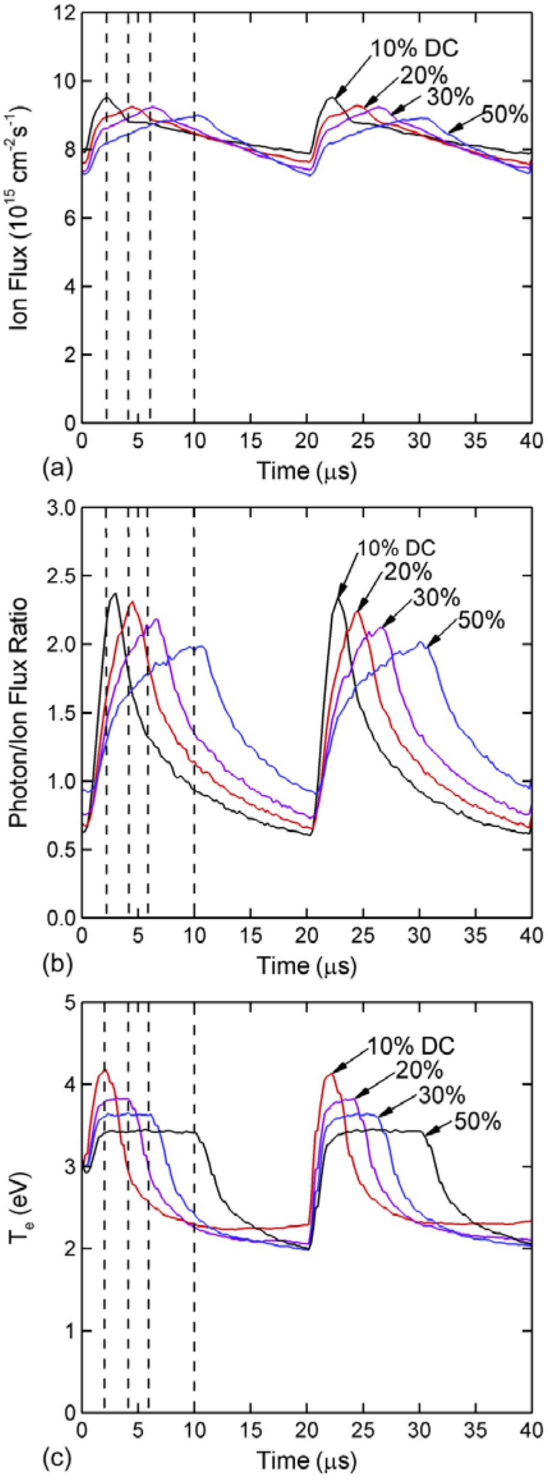

Fig. 4.11 Plasma properties as a function of time for two discharge pulses with different duty cycles. Fluxes are are collected on and averaged over the substrate. (a) Ion flux, (b) Ratio of total VUV flux to ion flux. (c) electron temperature. Dashed lines indicate the end of power-on period. Plasma conditions are Ar, 20 mTorr, 200 sccm, 10 MHz, 150 W CAP, PRF=50 kHz.

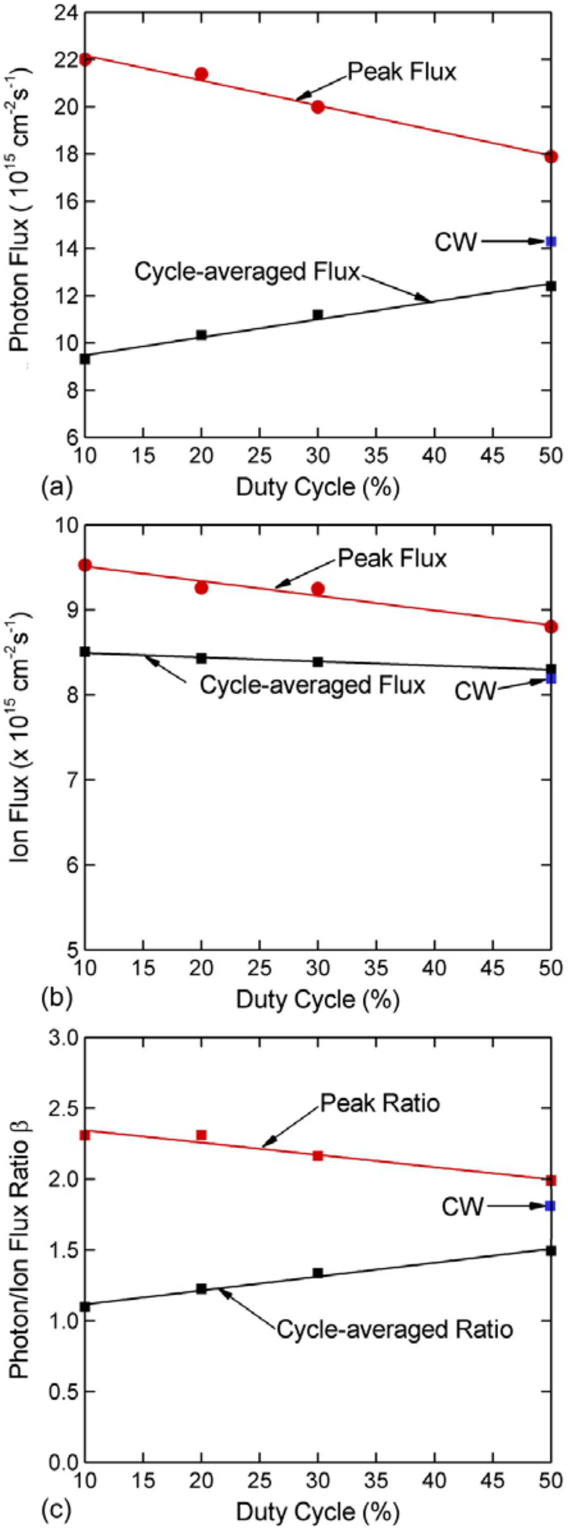

Fig. 4.12 Properties of fluxes striking and averaged over the substrate for pulsed excitation for different duty cycles and for cw excitation. (a) Total VUV photon flux, (b) ion flux, (c) ratio of VUV flux to ion flux. Plasma conditions are Ar, 20 mTorr, 200 sccm, 10 MHz, 150 W CAP, PRF= 50 kHz.

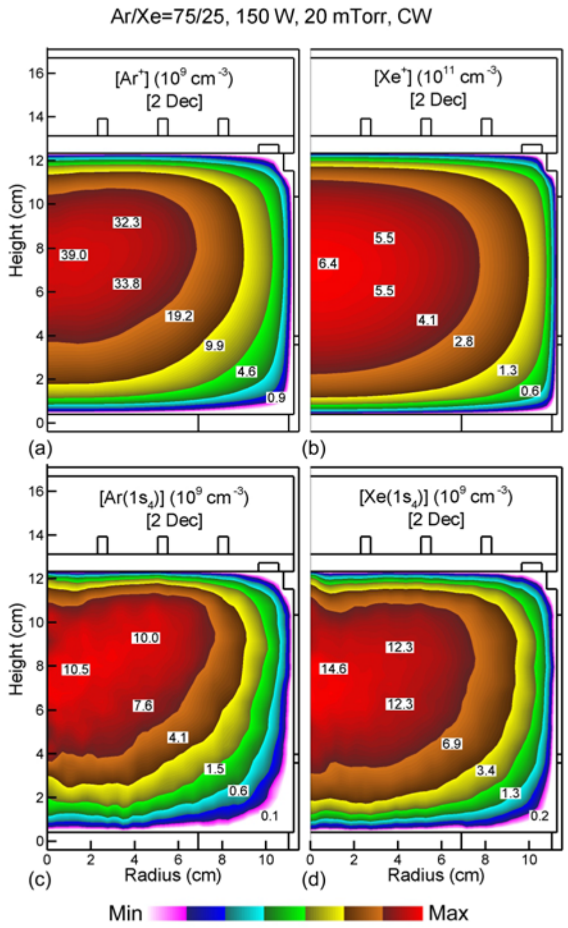

Fig. 4.13 Plasma properties for an Ar/Xe=75/25 mixture with cw excitation. (20 mTorr, 200 sccm, 10 MHz, 150 W). (a) Ar^+ density, (b) Xe^+ density, (c) Ar(1s$_4$) resonant state density and (d) Xe(1s$_4$) resonant state densities. The densities are plotted on log-scales of 2 decade range.

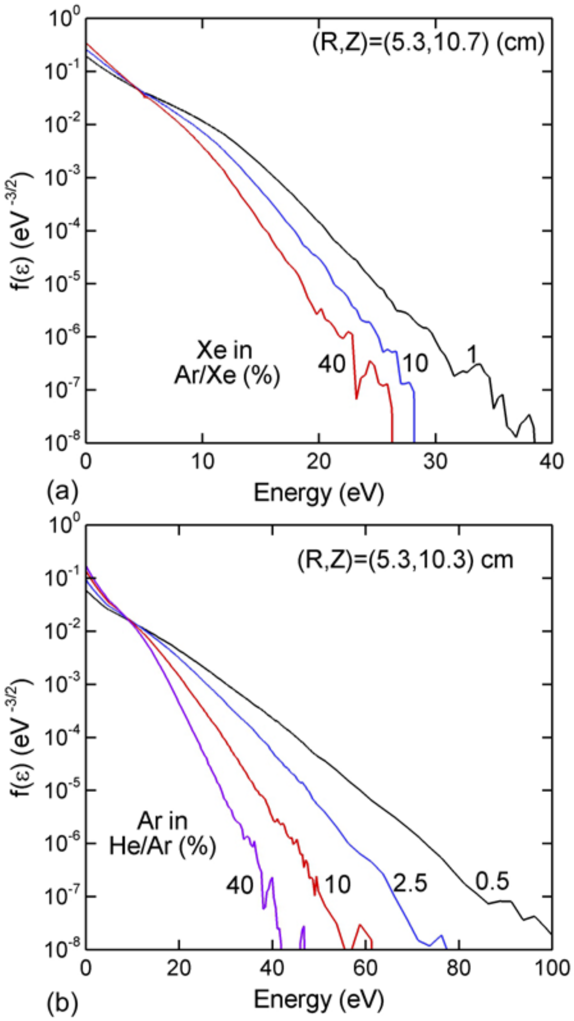

Fig. 4.14 Electron energy distributions in cw ICPs for different gas mixtures. The EEDs are at the edge of skin-depth at a radius of 5.3 cm. (20 mTorr, 200 sccm, 10 MHz, 150 W). (a) Ar/Xe mixtures with Xe fractions of 1-40%. (b) and He/Ar mixtures with Ar fraction of 0.5 to 40%.

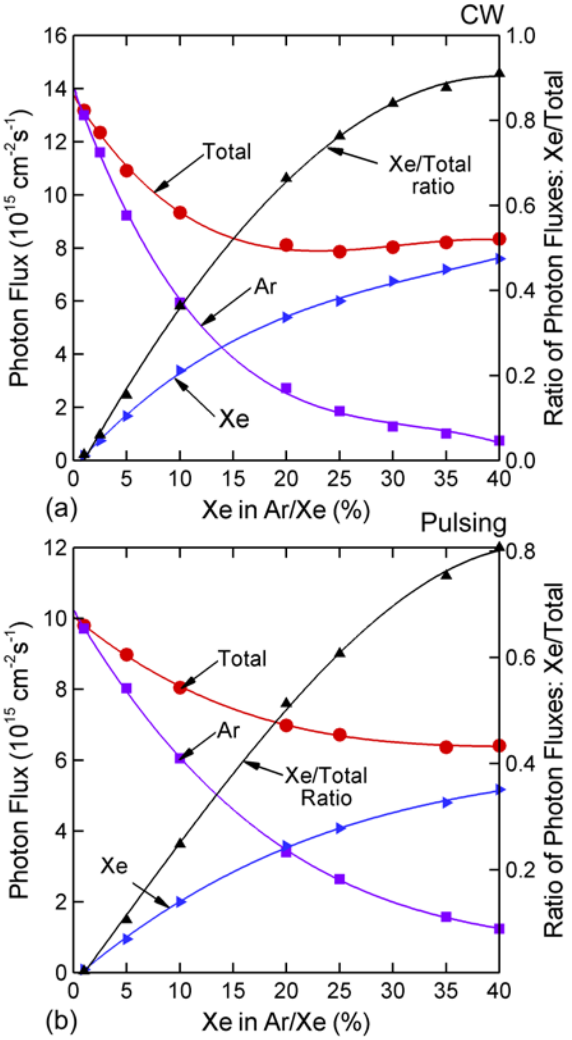

Fig. 4.15 VUV fluxes as a function of Xe fraction in Ar/Xe mixtures for cw ICPs (20 mTorr, 200 sccm, 10 MHz, 150 W cw or CAP)., (a) cw excitation, (b) pulsed excitation. The Ar flux is the sum of the 106.7 nm and 104.8 nm transitions. The Xe flux is the sum of 147 nm and 129.8 nm transitions. The total flux is the sum of VUV fluxes from both Ar and Xe.

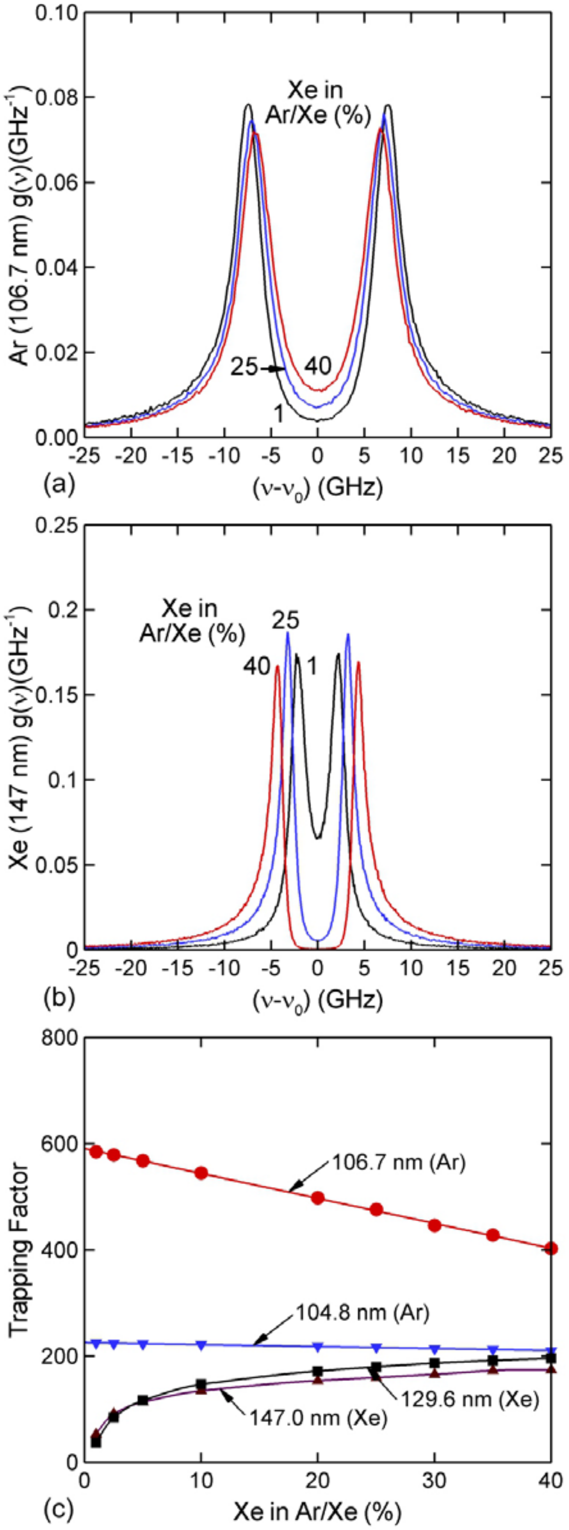

Fig. 4.16 Optical properties for Ar/Xe ICPs for different fractions of Xe. (a) Lineshape function for 106.7 nm Ar emission. (b) Lineshape for 147 nm Xe emission and (c) radiation trapping factors for Ar and Xe emission.

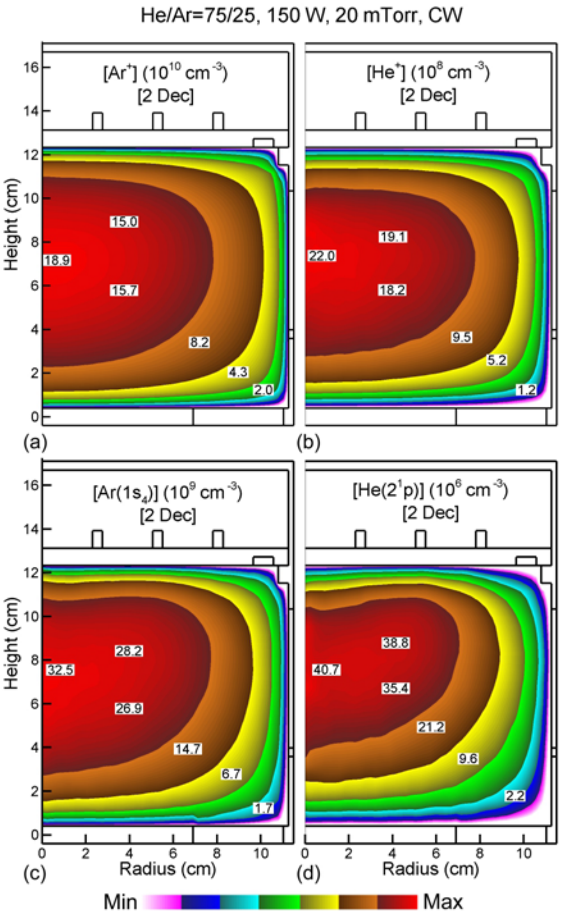

Fig. 4.17 Plasma properties for an He/Ar=75/25 mixture with cw excitation. (20 mTorr, 200 sccm, 10 MHz, 150 W). (a) Ar^+ density, (b) He^+ density, (c) $Ar(1s_4)$ resonant state density and (d) $He(2^1P)$ resonant state densities. The densities are plotted on log-scales of 2 decade range.

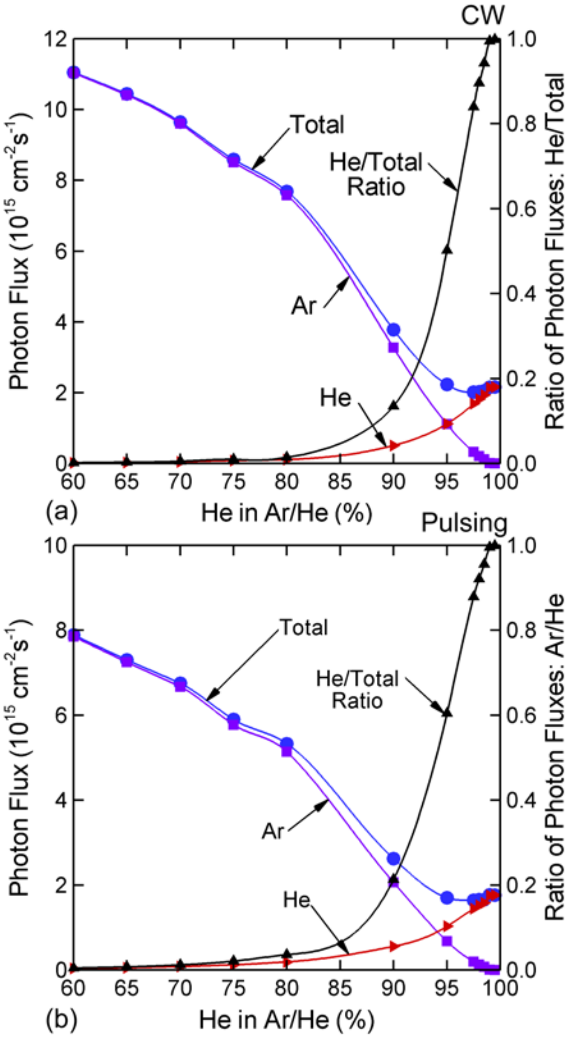

Fig. 4.18 VUV fluxes as a function of He fraction in He/Ar mixtures for cw ICPs (20 mTorr, 200 sccm, 10 MHz, 150 W cw or CAP)., (a) cw excitation, (b) pulsed excitation. The Ar flux is the sum of the 106.7 nm and 104.8 nm transitions. The He flux is the 59.1 nm transition. The total flux is the sum of VUV fluxes from both Ar and He.

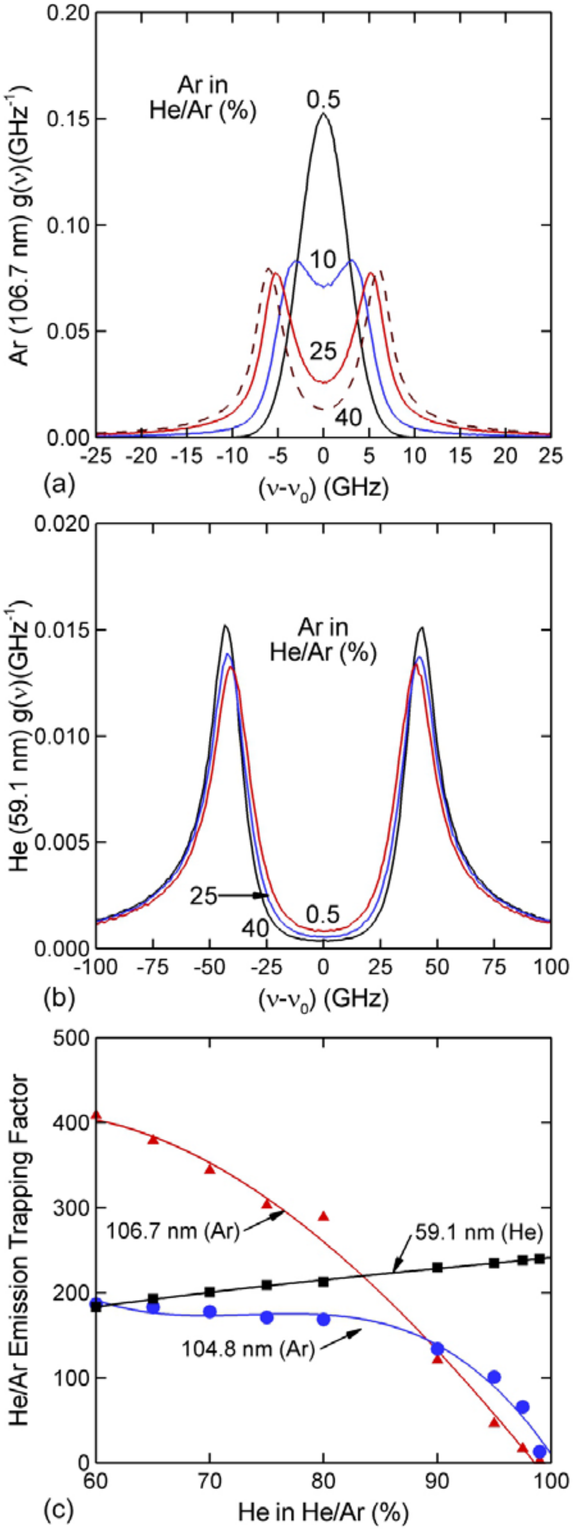

Fig. 4.19 Optical properties for He/Ar ICPs for different fractions of Ar. (a) Lineshape function for 106.7 nm Ar emission. (b) Lineshape for 59.1 nm He emission and (c) radiation trapping factors for Ar and He emission

4.8 References

[1] S.-B. Wang and A. E. Wendt, J. Vac. Sci. Technol. A **19**, 2425 (2001).

[2] S. D. Athavale, and D. J. Economou, J. Vac. Sci. Technol. A **13**, 966 (1995).

[3] M. Schaepkens, G. S. Oehrlein, and J. M. Cook, J. Vac. Sci. Technol. B **18**, 848 (2000).

[4] M. J. Barela, H. M. Anderson, and G. S. Oehrlein, J. Vac. Sci. Technol. A **23**, 408 (2005).

[5] S. Banna, A. Agarwal, K. Tokashiki, H. Cho, S. Rauf, V. Todorow, K. Ramaswamy, K. Collins, P. Stout, J.-Y. Lee, K. Shin, S.-J. Choi, H.-S. Cho, H.-J. Kim, C. Lee, and D. Lymberopoulos, IEEE Trans. Plasma Sci. **37**, 1730 (2009).

[6] Agarwal, P. J. Stout, S. Banna, S. Rauf, and K. J. Collins, J. Vac. Sci. Technol. A **29**, 011017 (2011).

[7] L. Xu, D. J. Economou, V. M. Donnelly, and P. Ruchloeft, Appl. Phys. Lett. **87**, 041502 (2005).

[8] H. S. Lee, P. K. Tiwari, and J. K. Lee, Plasma Source Sci. Technol. **18**, 025024 (2009).

[9] V. X. Qin, Y-H. Ting, and A. E. Wendt, Plasma Sources Sci. Technol. **19**, 065014 (2010).

[10] P. Diomede, D. J. Economou, and V. M. Donnelly, J. Appl. Phys. **109**, 083302 (2011).

[11] G. S. Hwang, and K. P. Giapis, J. Vac. Sci. Technol. B. **15**, 70 (1997).

[12] R. A. Gottscho, C. W. Jurgensen, and D. J. Vitkavage, J. Vac. Sci. Technol. B. **10**, 2133 (1992).

[13] M. Schaepkens and G. S. Oehrlein, Appl. Phys. Lett. **72**, 1293 (1998).

[14] B. Jinnai, S. Fukuda, H. Ohtake, and S. Samukawa, J. Appl. Phys. **107**, 043302 (2010).

[15] M. J. Titus, D. Nest, and D. B. Graves, Appl. Phys. Lett. **94**, 171501 (2009).

[16] E. S. Weibel, Phys. Fluids **10**, 741 (1967).

[17] V. I. Kolobov, and D. J. Economou, Plasma Sources Sci. Technol. **6**, R17 (1997).

[18] Yu. O. Tyshetskiy, A. I. Smolyakov, and V. A. Godyak, Phys. Rev. Lett. **90**, 255002 (2003).

[19] J. B. Boffard, C. C. Lin, C. Culver, S. Wang, A. E. Wendt, S. Radovanov, and H. Persing, J. Vac. Sci. Technol. A **32**, 021304 (2014).

[20] J. Hopwood, C. R. Guarnieri, S. J. Whitehair, and J. J. Cuomo, J. Vac. Sci. Technol. A **11**, 152 (1993).

[21] V. A. Godyak, R. B. Piejak, and B. M. Alexandrovich, Plasma Sources Sci. Technol. **11**, 525 (2002).

[22] S. Ashida, M. R. Shim, and M. A. Lieberman, J. Vac. Sci. Technol. A **14**, 391 (1996).

[23] T. H. Ahn, K. Nakamura, and H. Sugai, Plasma Sources Sci. Technol. **5**, 139 (1996).

CHAPTER 5 CONTROLLING VUV PHOTON FLUXES IN PULSED INDUCTIVELY COUPLED PLASMAS-II AR/CL$_2$ GAS MIXTURE AND POTENTIAL APPLICATIONS IN PLASMA ETCHING

5.1 Introduction

In this chapter, investigation on controlling VUV photon fluxes and VUV/ion relative fluxes in ICP will be continued following similar approaches in Chapter 4, in industry silicon etching gas mixtures Ar/Cl$_2$.

Previous experimental investigations have focused on measuring VUV emission from reactive ICPs sustained in halogen-containing mixtures including Cl$_2$, BCl$_3$, and fluorocarbon gases. Using an on-wafer monitoring technique, Jinnai et al. measured VUV emission (70 – 140 nm) of 1.5×10^{15} cm^{-2}s^{-1} ($\approx$3 mW/cm^2) from an ICP sustained in 5 mTorr of C$_4$F$_8$ at 1000 W.[1] Similar results were obtained by Woodworth et al. For a 10 mTorr ICP at 200 W, they observed VUV emission from C$_4$F$_8$, CHF$_3$, C$_2$F$_6$ plasmas of 8.6×10^{14} cm^{-2}s^{-1}, 1.1×10^{15} cm^{-2}s^{-1} and 3.0×10^{15} cm^{-2}s^{-1} respectively, which was dominated by resonance lines of neutral C and F. With the dilution of Ar, the total VUV flux increased by an order of magnitude, from 1.1×10^{15} cm^{-2}s^{-1} to 1.2×10^{16} cm^{-2}s^{-1}($\approx$20 mW/cm^2). The increase in VUV flux was principally due to the two argon resonance lines at 104.8 and 106.7 nm.[2] Woodworth et al. also measured VUV fluxes in Cl$_2$/BCl$_3$ plasmas for metal etching. In ICPs sustained in 10 mTorr mixtures of Cl$_2$/BCl$_3$ with 1100 W (and 200 W substrate bias), the total VUV intensity from 95 – 250 nm exceeded 5×10^{14}

$cm^{-2}s^{-1}$ (≈0.7 mW/cm^2). at the surface of the substrate. Neutral Cl emission at 138-139 nm was the principal resonance line in the spectrum.[3]

In those halogen-containing mixtures, photon stimulated or assisted plasma etching was recently observed in experiments by Shin et al. who found that VUV photons from Cl and Br containing ICPs can produce etching on silicon surfaces even when the energies of the incident ion fluxes are below the threshold for ion stimulated etching.[4,5] Fukasawa et al. also observed enhanced etch rates of SiN_x:H films with the simultaneous irradiation of VUV photons and radical fluxes in CF_4/O_2 plasma compared to that produced in the absence of the VUV flux.[6]

Motivated by these observations, in the results of last chapter, it is found that for ICPs sustained in rare gas mixtures, the absolute fluxes of VUV photons and relative fluxes of VUV photons to ions can be controlled by combinations of pressure and pulse power formats. The spectra of photon fluxes can also be coarsely tuned by varying the ratio of rare gases in the mixtures. In this work, we report on results from a computational investigation of methods to control VUV photon fluxes and ratios of VUV to ion fluxes from ICPs sustained in Ar/Cl_2 mixtures as a model system representative of conductor plasma etching used in microelectronics fabrication, and how that control can be leveraged to tune etch profiles. ICPs were sustained at low-pressure (tens of mTorr) with both continuous wave (cw) and pulsed excitation. This process is further complicated compared to rare gas mixtures by the reactivity of the Cl_2 chemistry that feeds back to the radiation transport. For example, the VUV fluxes from the resonant transition of Cl can be directly correlated with the reaction probability for Cl recombination on the side walls. The goal of this study is to further our understanding of methods to control VUV fluxes in reactive gases and the effect of such control on silicon etching profiles.

We found that the ratio of total VUV photon flux to ion fluxes, β, can be controlled by pressure, pulse power and gas mixtures in ICPs sustained in Ar/Cl_2 mixtures. For example, β increases with pressure from 0.07 (10 mTorr) to 2.3 (100 mTorr) due to the increased electronegativity of the plasma and more diffusive nature of ion transport at high pressure. With pulsed power, the electron energy distributions (EEDs) can be tuned such that it is more favorable to produce radiative states during the pulse, and so the β is a sensitive function of duty cycle of the pulse. The ratio of VUV to ion fluxes can also be controlled by gas mixtures. By increasing the fraction of Cl_2 in the gas mixture, β decreases from 0.43 (5% Cl_2) to 0.02 (95% Cl_2). The spectrum of the VUV fluxes, for example, emission from Ar emission compared to Cl emission, to first order is controlled by gas mixture but mixture also changes other plasma parameters. The intensity of VUV fluxes from Cl can be almost independently tuned by changing the wall conditions and which affect the surface recombination probability of Cl.

Descriptions of the model and reaction mechanisms used in this investigation are in Section II. The plasma dynamics of Ar/Cl_2 ICPs are discussed in Section III. Characterization and control of VUV fluxes and ion fluxes are discussed in Section IV. The effects of different ratios of VUV to ion fluxes on etch profiles of Si are demonstrated in Section V. Our concluding remarks are in Section VI.

5.2 Description of the Model

In this Chapter, in addition to the model of HPEM are used as in Chapter 4, IEADs of ion fluxes on the substrate are also collected using Plasma Chemistry Monte Carlo Module (PCMCM). When the plasma properties reach a steady or quasi-steady state, ion and trajectories and fluxes from the bulk plasma to surfaces will be computed and recorded in PCMCM. As discussed in Chapter 2, source functions for those species, as well as electric fields are extracted from the results of the FKPM to PCMCM. Pseudoparticles, representing ions, and neutrals are launched at locations weighted by these source functions throughout the plasma volume. The trajectories of the pesudoparticles are then integrated in time using time-electric fields interpolated from the results of FKPM. The magnitude of fluxes, energy and angle distribution of such pseudoparticles striking surfaces are then recorded.

In this chapter, we discuss results for ICPs sustained in Ar/Cl_2 gas mixtures. The atomic model for Ar consists of 8 levels, Ar, Ar($1s_5$), Ar($1s_4$), Ar($1s_3$), Ar($1s_2$), Ar(4p), Ar(4d) and Ar^+. Ar(4p) is a lumped excited state that includes Ar(4p, 3d, 5s, 5p). Ar(4d) is a lumped excited state that includes Ar(4d, 6s, Rydberg states). The molecular states Ar_2*and Ar_2^+ were also included, however their densities are at least 100-1000 times lower than their atomic counterparts. The molecular/atomic model for Cl_2 consists of 9 species, Cl_2, Cl_2(v), Cl($3p^5$), Cl($3p^4$4s), Cl($3p^4$4p), Cl($3p^4$3d), Cl_2^+, Cl^+ and Cl^-. The reaction mechanism for Ar/Cl_2 used in this investigation is listed in Appendix D. The table includes only reactions for the chlorine species and between the chlorine and argon species. The reaction mechanism for argon only is the same as in Chapter 4. The two resonance transitions of Ar, Ar($1s_4$) → Ar (104.8 nm), Ar($1s_2$) → Ar (106.7 nm); the resonance transition of Cl, Cl($3s^4$4s) → Cl($3p^5$) at 139 nm; and excimer emission from Ar_2* at 121 nm are tracked in the RTMCM. The secondary emission coefficient for electrons on the substrate by ions is 0.15 and is 0.05 on other surfaces. For excited states, the secondary emission probability was 0.03 on the substrate and 0.01 on other surfaces. For VUV photons, the secondary emission probability was 0.01 on all surfaces. For Cl surface recombination process, a series of reactions including chlorination, photon and Cl desorption of chlorinated sites are included, with an effective recombination probability near 0.15 on all surfaces.

5.3 Plasma Dynamics in Ar/Cl_2 ICP

The simplified ICP reactor geometry used in this investigation is schematically shown in Fig. 5.1. The reactor is intended to be a generic ICP to focus on the study of ion and VUV fluxes scaling without necessarily addressing the details of a specific industrial tool. The cylindrically symmetric reactor is 22.5 cm in diameter with a plasma region of 12 cm in height. ICP power is coupled into plasma by a 3-turn planar antenna from the top through a dielectric window. We assumed purely inductive coupling without a capacitive component from the coil voltage. Gas is injected from an annular inlet beneath the dielectric window and pumped out through an annular exhaust port at the bottom. A substrate is at the bottom of plasma region, over which ion and VUV fluxes are averaged. The conditions of the base case are Ar/Cl_2 = 80/20 at 20 mTorr with 200 sccm gas flow with the plasma sustained by 150 W ICP power at 10 MHz.

In the steady state for the base case, a diffusive plasma is formed with a peak electron density of 1.4×10^{11} cm^{-3} at the center of reactor, as shown in Figs. 2 and 3. The maximum electron temperature is 2.8 eV beneath the coil and gradually decreases to 1.1 eV near the substrate. The majority of positive ions are Cl_2^+ and Cl^+, with maximum densities of 1.1×10^{11} cm^{-3} and 0.8×10^{11} respectively. The density of Ar^+ is over an order of magnitude lower, due to its higher threshold energy for ionization (16 eV) compared to Cl_2 and Cl (11.5 and 13 eV) and loss through charge exchange processes to Cl_2 and Cl. Due to their lower mobilities, the spatial distributions of the positive ions are skewed towards the electromagnetic skin depth centered beneath the coil where most of the power is deposited. An exception is Cl_2^+, whose spatial distribution is relatively uniform as a function of height at the edge of skin depth. This structure results from Cl_2^+ having the lowest ionization potential among the ions, a condition that makes it the terminal species for charge exchange reactions. Ar^+ and Cl^+ quickly charge exchange to form Cl_2^+, after which Cl_2^+ undergoes dominantly diffusive transport. The density of Cl^-, reaches up to 9×10^{10} cm^{-3}, comparable to the electron density.

The densities of metastable and resonant states of both Ar and Cl follow the same spatial distributions as for the ions. In spite of superelastic collisions and heavy particle quenching reactions, the effective lifetime of the metastable states are still long, resulting in the peak densities of the metastable states being an order of magnitude higher than the corresponding radiative states (which share the same profile). For example, density of the metastable state $Ar(1s_5)$ is 3×10^{10} cm^{-3} while that of the resonant state $Ar(1s_4)$ is 5×10^9 cm^{-3}. The density of the Cl metastable state $Cl(3p^44p)$ and resonant state $Cl(3p^44s)$ have densities of 1.7×10^{11} cm^{-3} and 5.5×10^9 cm^{-3} respectively.

Transport of VUV photons at 104.8 [radiating state $Ar(1s_2)$], 106.7 [$Ar(1s_4)$] and 139 nm [$Cl(3p^44s)$] are addressed in the simulation. As shown in Fig. 5.3, the random flux of 106.7 nm photons has a maximum value of 3×10^{17} $cm^{-2}s^{-1}$ (≈0.6 W/cm^2) which is 5 times and 20 times larger than for 104.8 and 139 nm photons. Those random fluxes inside the plasma are magnified by the re-circulation of photons in the bulk plasmas as a result of radiation trapping and are orders of magnitude higher than the fluxes observed from outside the plasma or reaching the substrate. The collisional coupling between metastable state $Ar(1s_5)$ and radiative state $Ar(1s_4)$ is stronger than that between $Ar(1s_3)$ and $Ar(1s_2)$, a condition that maintain the $Ar(1s_4)$ density an order of magnitude higher than $Ar(1s_2)$. Since both of the resonance lines of Ar are absorbed by the ground state of the feedstock gas Ar that has a high density throughout the reactor, the radiation trapping factors are large, 216 for the 104.8 nm transition, and 368 for the 106.7 nm transition. However, the resonant line of Cl is absorbed by a dissociation product which intrinsically has a lower density and is less uniformly distributed. The radiation trapping factor for 139 nm is smaller, 10, and so its circulating intensity is smaller.

Fluxes of ions and VUV photons were collected and averaged over the substrate. The total ion flux reaching the substrate is 4.5×10^{15} cm^{-2}s^{-1} for the base case. The majority of the ions reaching the substrate are Cl_2^+, ≈77% of the total flux, with Cl^+ constituting 21% and Ar^+ being about 2% of the flux. Charge exchange reactions favor transfer of Cl^+ and Ar^+ to Cl_2^+. Production of the Ar^+ and Cl^+ takes place primarily in the skin depth of the electromagnetic wave from the coil, after which both species charge exchange along the diffusion length from the skin depth to the substrate. On the other hand, the largest portion of the VUV flux onto the substrate results from Ar emission. The total VUV photon flux reaching the substrate is 6.2×10^{14} cm^{-2}s^{-1} (1.14 mW/cm^2) of which 106.7 nm [Ar(1s$_4$)] and 104.8 nm [Ar(1s$_2$)] photons constitute 90% of the spectra, with fluxes of 3.7×10^{14} cm^{-2}s^{-1} and 1.9×10^{14} cm^{-2}s^{-1} respectively.

5.4 Controlling ion and photon fluxes in Ar/Cl_2 ICPs

5.4.1 Photon and ion fluxes vs. pressure

The scaling of ion and VUV fluxes to the substrate was investigated as a function of pressure from 10 to 100 mTorr. To maintain a constant residence time for the injected gases, the flow rate was scaled with pressure. All other conditions are the same as for the base case. Reactor averaged plasma properties as a function of pressure are shown in Fig. 5.4, and VUV photon and ion fluxes to the substrate are shown in Fig. 5.5. Representative lineshape functions and radiation trapping factors as a function of pressure are shown in Fig. 5.6. With a constant power of 150 W, the electron and total positive ion densities monotonically decrease with increasing pressure. The electron temperature T_e decreases with increasing pressure up to 60 mTorr until reaching a near plateau at 2.2 eV, perhaps slightly increasing. The negative ion density monotonically increases with increasing pressure, albeit becoming nearly constant above 60 mTorr. With increasing pressure the rate of loss of charged particles by diffusion decreases, which enables a decrease in T_e to lower the rate of ionization to match losses. This trend continues until the plasma transitions to an ion-ion plasma at about 60 mTorr. At this time, charged particle losses are dominated by ion-ion neutralization. The rate of charged particle loss then remains nearly constant, and so T_e is nearly constant. The plasma potential decreases from 20 V at 10 mTorr to 13.5 V at 100 mTorr. This decrease is monotonic in spite of T_e not continuing to decrease since the electronegativity of the plasma continues to increase.

At 10 mTorr, positive ions dominantly consist of Cl^+ (7.4×10^{10} cm^{-3}), nearly double the density of Cl_2^+ (3.7×10^{10} cm^{-3}). As the pressure increases to 100 mTorr, the density of Cl^+ decreases to 3.9×10^9 cm^{-3} while that of Cl_2^+ increases to 5.7×10^{10} cm^{-3}. The change in the identity of the chlorine ions has several reasons. First, with constant power and increasing pressure, the fraction of Cl_2 dissociation decreases from 51% to 22%. So on a relative basis fewer Cl^+ are produced by electron impact ionization. Second, since Cl^+ has a higher ionization potential compared with Cl_2^+, the lower T_e at higher pressure is more favorable towards ionization impact Cl_2. Finally, a higher ion collision frequency at higher pressure results in more charge transfer reactions, producing the lower energy state Cl_2^+.

The reactor averaged density of radiative states shows two diverging trends. The density of VUV radiating states of Ar decrease with increasing pressure – Ar($1s_4$) decreases from 1×10^9 cm^{-3} to 4.8×10^8 cm^{-3} and Ar($1s_2$) decreases from 2×10^8 cm^{-3} to 7.4×10^7 cm^{-3} from 10 mTorr to 100 mTorr. This decrease is in part due to the decrease in T_e but is also attributable to the increasing rate of quenching of Ar($1s_2$) (from 6.6×10^{12} cm^{-3}s^{-1} at 10 mTorr to 6.5×10^{13} cm^{-3}s^{-1} at 100 mTorr) and Ar($1s_4$) (1.3×10^{12} cm^{-3}s^{-1} to 1.0×10^{13} cm^{-3}s^{-1}) by chlorine species.

Meanwhile, the density of Cl($3p^44s$) increases with pressure: from 1.2×10^9 cm^{-3} at 10 mTorr to 9.2×10^9 cm^{-3} at 100 mTorr. The increase in Cl($3p^44s$) density is in part due to the increase in trapping factor for 139 nm radiation, from 4 at 10 mTorr to 110 at 100 mTorr. This increase in radiation trapping extends the lifetime of Cl($3p^44s$) to 11.6 μs. With increasing pressure and decreasing mean free path (MFP) for electron collisions, the specific power deposition (W/cm^3) beneath the coils increases in a small volume. Although the reactor averaged densities of Ar($1s_2$) and Ar($1s_4$) decrease with increasing pressure, the density of the radiating states increases in this small volumes adjacent to the dielectric under the coils. For example in this small volume, the density of Ar($1s_2$) increases from 4.5×10^8 cm^{-3} at 10 mTorr to 2.5×10^9 cm^{-3} at 100 mTorr; and the density of Ar($1s_4$) increases from 2.1×10^9 cm^{-3} to 1.5×10^{10} cm^{-3}. This disproportionate increase in density of radiating state close to the top surface impacts the trapping factors, discussed below.

For these conditions, both the total VUV flux and total ion flux to the substrate decrease with increasing pressure. The VUV flux decreases by a factor of four, from 9.5×10^{14} cm^{-2}s^{-1} to 2.2×10^{14} cm^{-2}s^{-1}. In contrast, the ion flux to the substrate decreases by a factor of 100, from 1.3×10^{16} cm^{-2}s^{-1} to 0.9×10^{14} cm^{-2}s^{-1}. In addition to the decrease in ion densities with increasing pressure, the dominant loss for ions transitions from diffusion to ion-ion neutralization, which then reduces the ion fluxes leaving the plasma.

The decrease in the ion flux also has a contribution from the spatial distribution of electron impact sources. At low pressure, the MFP for electrons is longer, while the skin depth is anomalous which results in fluxes of high energy electrons emanating out of the skin depth. This results in the electron impact ionization sources being more uniformly distributed throughout the reactor. At high pressure, the shorter MFP of electrons and the thinner skin depth being largely collisional produces a relatively confined plasma beneath the coils, where ions tend to diffuse more towards the top surface of reactor. As a result, the substrate at the bottom of reactor then collects a comparably smaller flux of ions. As the ion flux decreases with pressure the composition also changes. At 10 mTorr, the majority of the ion flux is Cl^+, 8.7×10^{15} $cm^{-2}s^{-1}$ compared with Cl_2^+ at 4.2×10^{15} $cm^{-2}s^{-1}$. At 100 mTorr, the Cl^+ flux drops to 5×10^{10} $cm^{-2}s^{-1}$ while the Cl_2^+ is essentially the entire flux at 8.4×10^{13} $cm^{-2}s^{-1}$. The dominance in the Cl_2^+ flux to the substrate is much larger than its contribution to the total reactor averaged ion density. This dominance in ion flux is due to the charge exchange reactions that occur as the Cl^+ and Ar^+ ions diffuse from the source region to the substrate.

The VUV photon flux that reaches the substrate not only decreases in magnitude but also undergoes a spectral shift. Due to the decrease in the density of argon radiative states and the shift in their maxima towards the top of the reactor, the VUV fluxes to the substrate from Ar (104.8 nm and 106.7 nm) decrease by a factor of 10 while increasing pressure 10 to 100 mTorr. Meanwhile the VUV flux from $Cl(3p^44s)$ (139 nm) increases by a factor of two, and becomes the dominant VUV photon flux. The ratio of total VUV flux versus ion flux, β, then monotonically increases with pressure, from 0.07 at 10 mTorr to 2.33 from at 100 mTorr. Photon fluxes are comparable with ion fluxes at 60 mTorr and exceed ion fluxes by a factor of two at 100 mTorr. The smaller decrease in photon flux compared to ions is in large part due to the VUV flux that does reach the substrate being emitted in the wings of the lineshape function where the MFP is longer than the size of the reactor even at 100 mTorr.

The VUV spectra for 106.7 nm and 139 nm, and trapping factors for all lines as a function of pressure are shown in Fig. 5.6. The lineshape functions are for VUV photons collected and averaged on all the surfaces in contact with the plasma. With a smaller MFP and so a higher probability of reabsorption, photons with frequencies near the center of the lineshape function are trapped longer in the plasma, during which time the quanta energy of those photons are more likely to be quenched by collisional reactions. Photons emitted in the wings of the Voigt profile have a proportionately longer MFP and have a higher probability of escaping from the plasma. An inverted profile at the center of the lineshape function therefore indicates heavily trapped photon emission. The lineshape function for Ar emission at 106.7 nm transitions from being moderately trapped at 10 mTorr (trapping factor 161) to heavily trapped at 100 mTorr (trapping factor 428). Cl emission at 139 nm is not significantly trapped in this pressure range due to the low Cl ground state density. The trapping factor increases from 5 to 110 when increasing pressure from 10 to 100 mTorr.

The trapping factors for Ar emission saturate with pressure, which is at first counter-intuitive as one expects trapping factors to monotonically increase with pressure. This monotonic increase would be the case if the distribution of excited states was uniform throughout the volume of the plasma. The dominant cause for the saturation in trapping factors is the confinement of the region of high power deposition closer to the top dielectric with increasing pressure. This confinement results in a larger fraction of the radiative states being located closer to a surface. From the perspective of radiation transport, having excited states closer to the surface has the same effect on radiation trapping as the plasma being in a chamber of smaller radius or height which produces a lower radiation trapping factor.

5.4.2 Sensitivity of photon and ion fluxes to Cl recombination on surfaces.

In other studies of Cl_2 containing plasmas, investigators have discussed factors affecting the rate of dissociation of Cl_2 producing Cl radicals, the recombination of Cl on surfaces, and their influence on the electronegativity of the plasma (density of Cl^- ions).[7-10] For example, at low pressure, the major source of negative ions is dissociative attachment to Cl_2 as the three-body rates of direct attachment to Cl_2 and Cl are small. The recombination of Cl on surfaces not only replenishes Cl_2 but also provides a means to replenish the source of Cl^-. The recombination of Cl atoms on surfaces is often characterized by surface recombination coefficient γ, which is the probability of a Cl atom abstracting a Cl atom from the chlorinated surface and returning to the plasma as Cl_2. This recombination probability is a function of the material properties, surface temperature and Cl surface coverage. For example, γ can vary from 0.02 to 0.85 for materials ranging from ceramics to stainless steel.[11] In other experiments, Luc *et.al* [12] and Joydeep *et.al* [13] measured γ in real-time in an ICP sustained in Cl_2. They reported values for γ of 0.004 to 0.03 for anodized Al, and 0.01 to 0.1 for stainless steel, lower values believed to be the result of passivation of the surface. Saurabh. *et.al* [14] and Cunge *et.al* [15,16] observed that the Cl atom density as a function of power varies with different wall conditions, indicating the influence surface recombination probabilities for Cl.

During an etching process, it is common for the surface conditions of the walls to change which, in turn, may affect γ.[11,15,16] This change in γ not only affects the balance between Cl and Cl_2 but also potentially changes the spectra of VUV fluxes that reach the substrate. To investigate this possibility, we varied the surface recombination coefficient for Cl, γ, from 0.005 to 0.80. This was implemented as having the fraction γ of the flux of Cl atoms, ϕ, striking the wall be lost from the plasma. The Cl atoms return to the plasma as Cl_2 with a flux at the wall of $(\gamma/2)\phi$. We acknowledge that this is a simplification of the actual surface kinetics that results in Cl recombination that may involve some combination of the Eley-Rideal and Langmuir-Hinshelwood mechanisms, which in turn depend on the surface coverage of adsorbed Cl atom.[17] With the goal of isolating the consequences of only surface recombination, we have chosen to use the simpler approach.

Reactor averaged densities, fractional dissociation of Cl_2 and substrate averaged VUV and ion fluxes as a function of γ are shown in Figs. 7 and 8. The gas mixture is $Ar/Cl_2 = 80/20$ at 20 mTorr and 100 mTorr, with a power deposition of 150 W. The flow rates of 200 sccm for 20 mTorr and 1000 sccm for 100 mTorr were implemented to keep a constant average residence time. At 20 mTorr, as γ increases from 0.005 to 0.80, the density of Cl^+ decreases by 78% from 5.6×10^{10} cm^{-3} to 1.2×10^{10} cm^{-3}, while the density of Cl_2^+ increases from 5.2×10^{10} cm^{-3} to 6.5×10^{10} cm^{-3}. The density of Cl_2^+ exceeds Cl^+ as for $\gamma > 0.01$. Though not shown, the densities of the radiative states of Ar [$Ar(1s_2)$ and $Ar(1s_4)$], stay relative constant over this range of γ, at 1.2×10^9 cm^{-3} and 0.15×10^9 cm^{-3} respectively. In contrast, the density of the resonant state of Cl [$Cl(3p^4 4s)$] significantly decreases, from 5.7×10^9 cm^{-3} at $\gamma = 0.005$ to 0.31×10^9 cm^{-3} at $\gamma = 0.8$. This decrease reflects the decrease in the dissociation fraction of Cl_2 from 0.61 to 0.16. As the pressure increases to 100 mTorr, the densities of both Cl^+ and Cl_2^+ decreases over almost the entire range of γ. The density of $Cl(3p^4 4s)$ however, is larger at 100 mTorr due to the higher overall density of Cl species and a lower T_e, which is more favorable to electron-impact excitation reactions than ionization.

As γ increases from 0.005 to 0.80 at 20 mTorr, the fluxes of Cl^+ and of photons at 139 nm (originating from $Cl(3p^4 4s)$) generally decrease. The increasing loss of Cl due to conversion of Cl_2 at the walls is directly reflected in these fluxes. The total fluxes of both ions and photons decrease until γ increases to 0.3 to 0.4, at which point these fluxes saturate since the fraction of Cl_2 remaining in the reactor is determined by residence time due to gas flow. The end result is that the fraction of the VUV flux at 139 nm significantly decreases as γ increases. For example, with γ = 0.005, the fraction of the VUV flux at 139 nm is 25% while for γ = 0.8, the fraction is 2%. The trends for 100 mTorr are similar though the fraction of VUV flux at 139 nm is generally higher, decreasing from 76% with γ = 0.005 to 28% for with γ = 0.8. With the 139 nm flux being a larger fraction of the total at 100 mTorr, the ratio of photon flux to ion flux, β, is also more sensitive to γ at the higher pressure.

These results suggest that the conditions of the walls, which in turn determine recombination coefficients, have a first order effect on the spectra and magnitude of the VUV flux incident onto surfaces. It is true that these dependencies of VUV fluxes on γ find their origins in the dependence of gas phase species on γ, and it is difficult to separate VUV fluxes and gas phase species. However, it is also true that the consequences of ion or radical fluxes, and VUV fluxes on materials properties can have very different outcomes. For example, the processing depth of neutral and ion fluxes on typical semiconductor materials is at best a few nm, whereas VUV fluxes can penetrate tens to hundreds of nm.

5.4.3 Photon and ion fluxes vs. Cl_2 ratio

Another method to tune the spectra of VUV fluxes incident onto the substrate is gas mixture. In this regard, mixtures of Ar/Cl_2 = 95/5 to 5/95, at 20 mTorr and 150 W were investigated. Reactor averaged plasma properties and species densities, dissociation fraction of Cl_2 and substrate averaged VUV and ion fluxes as a function of Cl_2 fraction are shown in Figs. 9 and 10. Spatial distributions electrons and of the radiating states $Ar(1s_4)$ and $Cl(3p^4 4s)$ are shown in Fig. 5.11. The plasma density (total positive ion density) decreases from 1.4×10^{11} $cm^{-3}s^{-1}$ to 0.72×10^{11} $cm^{-3}s^{-1}$ as the Cl_2 fraction increases from 5% to 95%. This lower plasma density is caused by several reasons. First, the rate of power dissipation by electrons colliding with Cl_2 (having vibrational excitation, dissociation and dissociative attachment processes) is greater than for Ar. A larger Cl_2 fraction for a fixed power deposition would require a lower electron density. A decrease the in the electron energy relaxation length and increase in rates of electron energy dissipation produces a lower electron temperature – T_e decreases from 2.5 eV at 5% Cl_2 to 2.1 eV at 95% Cl_2. The lower T_e then favors reactions with lower energy thresholds, thereby directing power flow away from ionization processes in the bulk plasma. The decrease in T_e and the transition to an ion-ion dominated plasma produce a decrease in the plasma potential.

For our conditions this shift in power dissipation to lower energies with the increase in Cl_2 mole fraction increases the rate of dissociative reactions, thereby increasing the density of Cl density by a factor of 3 (2.9×10^{13} cm^{-3} to 7.7×10^{13} cm^{-3}) and the density of Cl^- density by a factor of 7 (7.8×10^{9} cm^{-3} to 4.9×10^{10} cm^{-3}). The increase in Cl^- produces a more electronegative plasma having a lower electron density and lower electron temperature. Collectively these trends produce a plasma in which diffusion plays a smaller role in ionization balance and where ion-ion recombination is a major ion loss channel. This less diffusive regime is shown in Fig. 5.11. For 5% Cl_2, the diffusive plasma has the peak of electron and $Cl(3p^4 4s)$ densities near the center of reactor, while at 95% Cl_2, the plasma is largely confined near the maximum in power deposition within the skin depth of the electromagnetic field.

By about a mole fraction of 30% Cl_2, the majority of discharge power is dissipated in electron collisions with Cl and Cl_2. As power dissipation shifts from Ar to Cl_2 and with the drop in T_e, the densities of $Ar(1s_4)$ and $Ar(1s_2)$ decrease to below $Cl(3p^4 4s)$ by 20% Cl_2. The density of $Cl(3p^4 4s)$ has a broad maximum between 15% and 20% Cl_2 which is caused by competing mechanisms. At low Cl_2 fractions, the rate of excitation of Cl is limited by the low Cl density, and so the increasing density of Cl produces more $Cl(3p^4 4s)$. Meanwhile, the decrease in T_e with increasing Cl_2 fraction, lowers the rate of excitation of Cl($3p^4 4s$), which accounts for its decrease with increasing Cl_2 fraction.

Photon fluxes and ion fluxes to the substrate are shown in Fig. 5.10 as a function of Cl_2 fraction in the mixture. Adding Cl_2 (5% to 95%) decreases ion fluxes to the substrate by a factor of 10, from 1.2×10^{16} $cm^{-2}s^{-1}$ to 1.3×10^{15} $cm^{-2}s^{-1}$. This trend is attributed to a decrease in plasma density, a less diffusive plasma having weaker ambipolar diffusion, ion losses being dominated by ion-ion neutralization (instead of diffusion) and the peak in the ion density being confined more in the electromagnetic skin depth under the coil. Ar^+ and Cl^+ fluxes, dominant at low Cl_2 fraction, are replaced by Cl_2^+ fluxes by 30% Cl_2. Among the three ions, Cl_2^+ fluxes are relatively stable. The variation of Cl_2^+ fluxes is only a factor of 3 for the range of gas mixtures, compared to 2 or 3 orders of magnitude change in Cl^+ and Ar^+ fluxes.

Total photon fluxes and VUV fluxes from the resonant lines of Ar and Cl are shown in Fig. 5.10 and demonstrate the possibility of coarse spectral control using Cl_2 mole fraction. The total VUV fluxes decrease by a factor of 200 from 5.1×10^{15} $cm^{-2}s^{-1}$ to 2.3×10^{13} $cm^{-2}s^{-1}$ when increasing Cl_2 fraction from 5% to 95%. This decrease is in large part due to the decrease of the density of radiative states in the bulk plasma. While VUV emission from Ar has a monotonic decrease, VUV emission from Cl at 139 nm largely follows the density of Cl($3p^4 4s$) and decreases by half from 5% to 95% Cl_2, with a maximum of 5.4×10^{13} $cm^{-2}s^{-1}$. The proportion of VUV emission from Cl in the total VUV spectra steadily increases due to its comparably smaller variation compared to emission from Ar over the range of Cl_2 fraction. With 80% Cl_2, the VUV emission from Cl($3p^4 4s$) is equal to that from Ar($1s_2$,$1s_4$) while dominating the spectrum at higher Cl_2 mole fraction. The ratio of VUV-to-ion fluxes β decreases from 0.4 to 0.02 with increasing Cl_2 fraction.

Spectral lineshape functions for Ar (106.7 nm) and Cl (139 nm) emission and radiation trapping factors are shown in Fig. 5.12 for different Cl_2 fractions. The trapping factor of Cl (139 nm) emission is small and increases from 4 to 11 as Cl_2 increases from 5% to 95%. This moderate increase in trapping factor reflects the increase in Cl density which increases the ground state absorber density and so trapping factor. It also reflects the contraction of the emitting Cl($3p^4 4s$) density towards the top surface, which decreases the trapping factor. Trapping factors for emission from Ar (106.7 nm) greatly decrease, from 534 to 10, as the Ar fraction decreases from 95% to 5%. The lineshape function of Cl (139 nm) has a non-inverted Voigt profile due to its weak trapping. The Ar (106 nm) lineshape function is significantly self-absorbed at low Cl_2 fraction (high Ar fraction) and transitions to being optically thin with no line reversal at 95% Cl_2 fraction.

5.4.4 Pulsing: photon and ion fluxes vs. duty cycle (DC)

As discussed in our prior investigation of rare gas plasmas, pulsing the ICP plasma provides another mechanism to control the VUV-to-ion flux ratio. With continuous wave (cw) excitation, there is limited ability to control species densities for a given set of conditions (e.g., varying pressure, power, mixture, flow rate). The reactor-averaged T_e is constrained by the need to balance sources of resonant states and ionization, and their losses at all times. With pulsed power, the balance between sources and losses need only be balanced averaged over the pulsed period. This considerably larger range for varying T_e through modulating the electron energy distributions enables us to gain additional control over VUV and ion fluxes.[18,19]

With the goal of controlling the fluxes of VUV photons and ions to the substrate in Ar/Cl_2 mixtures, we investigated pulsed plasma excitation of the ICP. The pulsed power waveform is characterized by the pulse repetition frequency, PRF, the number of power pulses per second; the duty cycle, DC, the fraction of the pulsed period the ICP power is applied; and the cycle average power deposition, CAP. The base case for pulsing is Ar/Cl_2 = 80/20 at 20 mTorr, with a PRF of 50 kHz (20 μs period), and CAP of 150 W. The DC duty cycle will be a control variable.

By varying DC while keeping a constant CAP of 150 W, the power density during the pulse-on period, and particularly during the leading edge, is controlled. Smaller duty cycle requires not only more power during the shorter power-on period but also has a smaller electron density at the end of the longer afterglow – both of which contribute to a spiking of the electron temperature during the leading edge of the power-on pulse.[20] This spiking in T_e, often called an overshoot, then translates to a different distribution of excited states and ionization. VUV fluxes, ion fluxes, the ratio of VUV-to-ion fluxes, β, and T_e are shown as a function of time for duty cycles of 10% to 60% in Figs. 13 and 14. The overshoot of T_e reaches up to 5.4 eV at 10% DC and decreases to 3.5 eV at 60% DC, compared to a cw value of about 2.8 eV. In the afterglow, T_e maintains about 1 eV regardless of DC, largely sustained by super-elastic relaxation of excited states.

The modulation of the 104.8 nm fluxes originating with $Ar(1s_2)$ is up to a factor of 50 at 10% DC, whereas the modulation in the 106.7 nm line originating with the $Ar(1s_4)$ at 10% DC is a factor of 9. This smaller degree of modulation of 106.7 nm indicates a longer life time of $Ar(1s_4)$ compared with $Ar(1s_2)$. Other than the intrinsic longer lifetime of $Ar(1s_4)$ (8.4 ns) compared to $Ar(1s_2)$ (2.0 ns), there are two major factors in this disparity. First, the 106.7 nm line has a radiation trapping factor of 360 compared to the smaller trapping factor of 217 for the 104.8 nm transition. Second, $Ar(1s_4)$ is more closely coupled to the lowest metastable state of $Ar(1s_5)$ which has the largest density during the afterglow among Ar excited states, $1.0 - 1.5 \times$

10^{10} cm^{-3}. Being replenished by collisions with Ar($1s_5$), Ar($1s_4$) maintains a relative large density during the afterglow. The 104.8 nm emission originating with Ar($1s_2$) more closely follows to the time evolution of T_e.

The 139 nm line originating with Cl($3p^4 4s$) has a maximum modulation of a factor of 9 at 10% DC. As a result, the spectra of VUV fluxes is highly modulated by the pulse power. For example, the ratio of Ar to Cl VUV emission is shown in Fig. 5.15 as a function of time for different duty cycles. During a single pulse, Ar emission (sum of 104.8 nm and 106.7 nm) reaches up to 29 times the magnitude of Cl emission (139 nm) with 10% DC. The ratio of Ar/Cl photon fluxes approaches 9 by the end of the afterglow. These trends indicate that the over shoot of T_e at the beginning of the pulse is more favorable to producing Ar emission compared to Cl emission. As the DC increases and the overshoot in T_e decreases, the dominance of VUV emission from Ar decreases.

Cycle averaged and peak fluxes of VUV emission from Ar and Cl are shown in Fig.16 The cycle average ratio of Ar emission is 4-5 times that of Cl, decreasing with increasing duty cycle, but is not tremendously sensitive to duty cycle. The maximum of Ar emission is 35 times that of Cl at 10% duty cycle, decreasing to a factor of 12 at the higher duty cycle. This decrease in ratio is dominantly due to the decrease in the overshoot in T_e.

The modulation in the ion fluxes to the substrate during the pulsed cycle is about 35% to 40% and is not as sensitive to DC as either T_e or photon fluxes. This lack of sensitivity is in large part a result of the diffusion times for ion transport to the substrate being commensurate with the pulsed period. The ion fluxes to the substrate then reflect something of an average over the pulsed period. Since, however, the VUV fluxes are modulated during the pulse period, the ratio of overall VUV-to-ion fluxes, β, is also highly modulated over a pulse period, as shown in

Fig. 5.14. The maximum value of β is 0.8 for 10% DC at the beginning of the power pulse, and 0.2 for 60% DC during most of the pulse-on time. β decreases to 0.08 at the end of the afterglow. During the entire pulse, ion fluxes exceed photon fluxes. The peak (maximum during one pulse) and cycle averaged VUV and ion fluxes, and ratio of VUV-to-ion flux, β, are shown in Fig. 5.16. VUV flux is the sum of the fluxes of the 104.8, 106.7 and 139.0 nm lines, whereas ion flux is the sum of the fluxes of Ar^+, Cl^+ and Cl_2^+. The VUV fluxes increase with decreasing DC, whereas ion fluxes decrease at lower DC. The ratio of VUV-to-ion fluxes, β, increases with decreasing DC. This indicates the overshoot in T_e is more favorable to populating excited states of Ar and Cl than for producing more ions for these conditions.

5.5 Optimizing feature profiles during plasma etching

As discussed in the introduction, VUV photon fluxes are now recognized as being important in plasma material processing. The consequences of VUV photons on materials processing is highly dependent on the system. However we anticipate that the impact of VUV stimulated processes is perhaps greatest in semiconductor processing where the need for critical dimension control now approaches a monolayer. To achieve this critical dimension, control of activating fluxes onto wafers should extend beyond ion fluxes to include VUV fluxes. For example, the recent discovery of photon assisted etching of Si in halogen containing plasmas [4,5] emphasizes the need to separately control VUV fluxes, or at least control the ratio of VUV to ion fluxes.

To demonstrate the possible impact of VUV stimulated processes, profile evolution during etching of Si by ICPs sustained in Ar/Cl_2 mixtures was simulated using the MCFPM. As mentioned in Sect. II, VUV photon fluxes are included in the MCFPM in the same manner as ion and neutral fluxes. Since the energy of each photon is fixed, the distribution of individual photon fluxes produced by the HPEM consists of only angular distributions. Otherwise, the algorithms for selecting photon-pseudoparticles and reactions stimulated by the photons on the surface are identical to those for ions.

The reaction mechanism used for Ar/Cl_2 plasma etching of Si is listed in Appendix E. The mechanism consists first of successive passivation of Si sites by Cl atoms

$$SiCl_n(s) + Cl(g) \rightarrow SiCl_{n+1}(s), \quad n=0,1,2 \qquad (1)$$

where (s) and (g) refer to solid and gas phase species. A low rate of spontaneous etching also occurs,

$$SiCl_3(s) + Cl(g) \rightarrow SiCl_4(g) \qquad (2)$$

The vast majority of etch processes proceeds by chemically enhanced ion sputtering and to a lesser degree by direct ion sputtering,

$$SiCl_n(s) + M^+(g) \rightarrow SiCl_n(g) + M(g), \quad n=1,2,3, \ M= Ar, Cl, Cl_2. \qquad (3)$$

$$Si(s) + M^+(g) \rightarrow Si(g) + M(g), \quad M= Ar, Cl, Cl_2. \qquad (4)$$

Hot atoms (usually produced by gazing ions neutralizing on side walls) produce analogous reactions as for ion stimulated processes. When including VUV photon fluxes, we also included the phenomenological reactions

$$SiCl_n(s) + h\nu \rightarrow SiCl_n(g), \quad n=1,2,3 \qquad (5)$$

The probability of reaction for photon stimulated etching, p_n, for $SiCl_n$ was calibrated based on the experimental results of Shin et al. [5] who equated the VUV stimulated etch rate to be equivalent to that of 40 eV ions. With that observation and allowing for higher probabilities for higher states of passivation, the probabilities for photon stimulated etching we used in the model are p_n = 0.15, 0.30 and 0.50 for n = 1, 2 and 3. The same probability was used for all VUV wavelengths (104.8 nm, 106.7 nm, 139 nm).

A second approximation made in this study was that VUV photons can be treated using ray-optics, and for this reason we simulated etching of only fins and not trenches, and reasonably large features. We acknowledge that for the small dimensions of trenches in modern microprocessors and for the wavelengths of interests, diffractive effects are likely important and that ray tracing is at best an approximation.

The conditions for this part of the investigation are an Ar/Cl_2 = 80/20 mixture, 150 W ICP power with a 200 V bias at 10 MHz applied to the substrate for pressures from 10 to 100 mTorr. The photon-to-ion flux ratio, photon and ion angular distributions collected on and averaged over the substrate are shown in Fig. 5.17. Compared to ICPs with unbiased substrates, the total ion fluxes increase with the bias, producing a smaller β between 0.1 to 0.3 (compared with a max β of 2.3 in unbiased condition), with a peak value near 60 mTorr. Angular distributions of VUV fluxes in the bulk plasma are essentially isotropic, and so the angular distribution of photons incident onto the surface resembles a Lambertian distribution, peaked at near normal incidence and falling towards grazing incidence as $\cos(\theta)$. Note that as the pressure increases, there is a small angular asymmetry in the photon fluxes. This asymmetry results from the contraction of the power deposition and maxima in excited states to a small volume in the electromagnetic skin depth of the coil. This contraction is analogous to that shown in Fig. 5.11 for large fractions of Cl_2. As a result, the photon sources begin to look like an off-axis point source that produces a photon flux having an angular slant. In comparison to the photon fluxes, the ion fluxes are essentially anisotropic with angular distributions contained well within 10 degrees of the vertical. These differences in angular distributions (photons being isotropic and ions being anisotropic) in large part explain the results of our simulations.

The geometry used for profile simulation is shown in Fig. 5.19. The photoresist has a width of 120 nm and height of 180 nm over Si. A non-eroding hard-mask is used to isolate the effects of photon-stimulated etching on the profile. The Si has a height of 390 nm over SiO_2. Etching (and over-etching) continued until the feature was cleared. Etch profiles of the Si fin are shown in Fig. 5.19b for pressures of 10, 60 and 100 mTorr. Undercutting of the mask can be observed in these profiles, particularly at higher pressures. The undercutting results from the nearly isotropic VUV fluxes that strike the sidewalls of the feature and stimulate the etch. Since the Cl passivation of the sidewalls is nearly independent of location, the rate of photon stimulated etching is largely determined by the convolution of the view-angle of the surface site to the plasma and the angular distribution of the VUV fluxes.

The photon-stimulated undercutting can be quantified by integrating all volume etched beneath the mask, and plotted against pressure in Fig. 5.19. Undercutting increases with pressure from 10 mTorr, reaching a peak at 60 mTorr and slightly decreasing thereafter. This behavior coincides well with the dependence of β on pressure, which also peaks near 60 mTorr. Since the energies of the incident ions are well above the threshold for Si etching, clearing of the feature is mainly determined by the fluence of ions, and so the total fluence ions is approximately the same at different pressures at the time of clearing the feature. The relative amount of isotropic VUV fluxes which strike the side wall is therefore directly proportional to β, which then determines the amount of undercut.

For $\beta \leq 0.3$, the undercut produced by the isotropic VUV fluxes is noticeable, but may not be that different from what may occur by grazing ions or an unusually broad ion angular distribution. However, as shown above, depending on process conditions β may be as large as 2-4. To demonstrate the potential impact of large VUV fluxes on feature evolution, the magnitudes of photon fluxes were artificially adjusted to produce $\beta = 0$ to 4 while maintaining all other conditions the same for the 20 mTorr case. The resulting profiles are shown in Fig. 5.18c and the amount of undercut is shown in Fig. 5.19. As β increases, the profiles are significantly undercut beneath the mask by the isotropic VUV fluxes. The undercut increases nearly linearly with β. These results indicate that the photon-assisted etching process, which facilitates the undercut, is limited by the fluence of photon fluxes for conditions where the Si remains highly chlorinated.

5.6 Concluding Remarks

In this work, we have discussed results from a numerical investigation of radiation transport in ICPs sustained in Ar/Cl_2 mixtures with the goal of controlling the magnitude of VUV photon fluxes incident onto a substrate, and assessing possible repercussions on etching of Si features. VUV emission originating from Ar($1s_4$) (106.7 nm), Ar($1s_2$) (104.8 nm) and Cl($3p^4 4s$) (139 nm) were compared to ion fluxes to the substrate. Potential control of VUV-to-ion fluxes ratio was demonstrated by changing pressure, Cl_2 fraction in the mixture, and reactor wall conditions (through surface recombination reaction of Cl) with continuous wave power. Coarse spectra control of the spectrum of VUV fluxes can also be achieved through Cl_2 fraction and reactor wall conditions. Pulsed power also provides a means to spectrally control the VUV fluxes due to the overshoot in T_e that is a function of duty cycle.

The potential impact of controlling VUV fluxes, and their ratio to ion fluxes, on semiconductor processing was demonstrated by model predictions of etching Si fins. VUV fluxes from ICPs sustained in Ar/Cl_2 are angularly more isotopic than ion fluxes. VUV stimulated etching processes are, on a relative basis, therefore more important on side walls compared to ion fluxes, and so account for undercutting of the mask in fin-like structures. VUV stimulated processes during semiconductor processing now occur to some degree, in all low plasma systems since all low pressure plasmas produce VUV fluxes to surfaces. Controlling the VUV fluxes provides the opportunity to refine these processes.

5.7 Figures

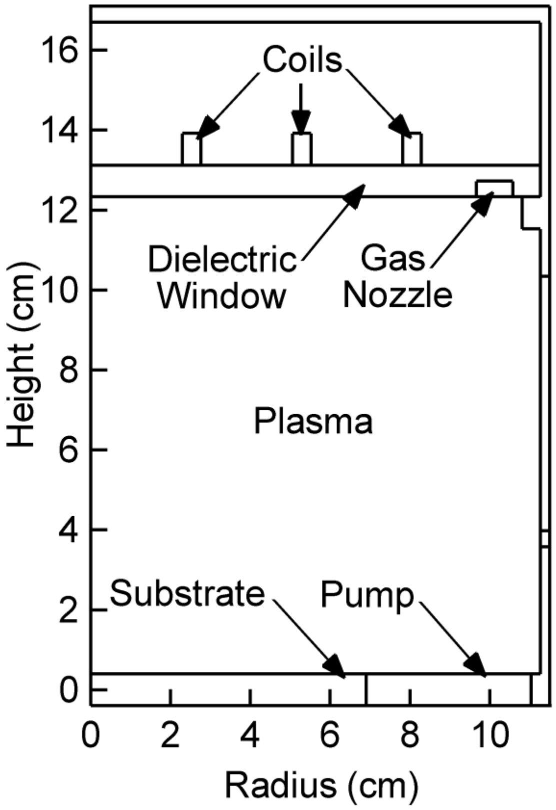

Fig. 5.1 Schematic of the inductively coupled plasma reactor used in the model.

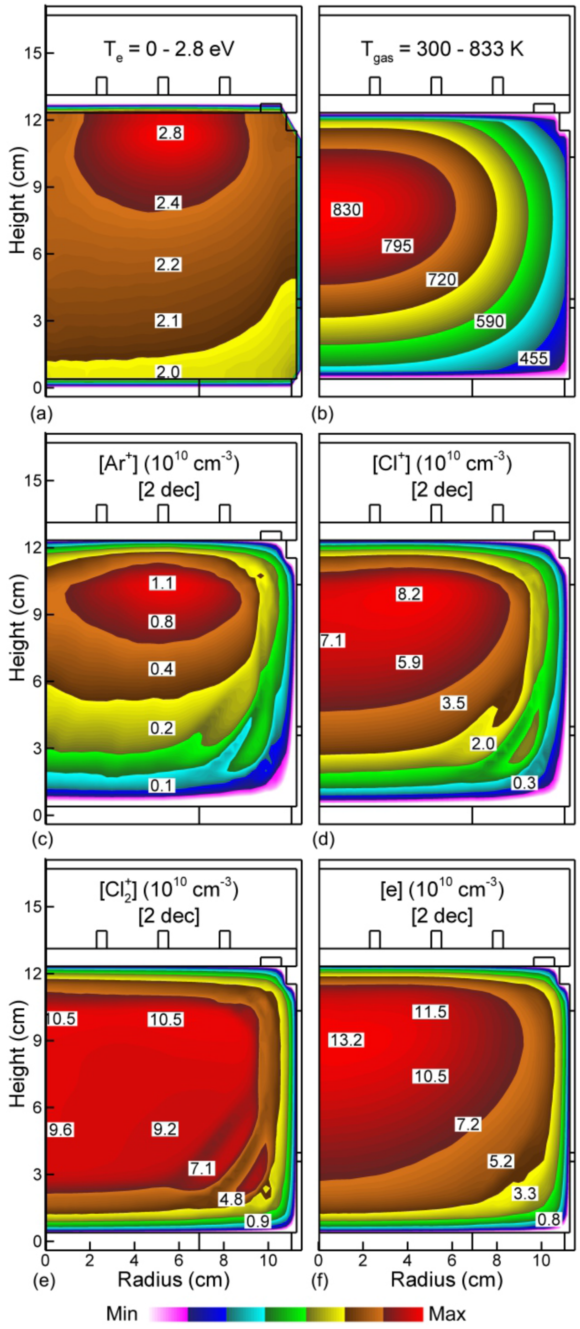

Fig. 5.2 Time averaged plasma properties for base case conditions (Ar/Cl_2=80/20, 20 mTorr, 200 sccm, 10 MHz, 150 W cw). (a) Electron temperature, (b) gas temperature, (c) Ar^+ density, (d) Cl^+ density, (e) Cl_2^+ density, and (f) electron density, The densities are on log-scales of 2 decades.

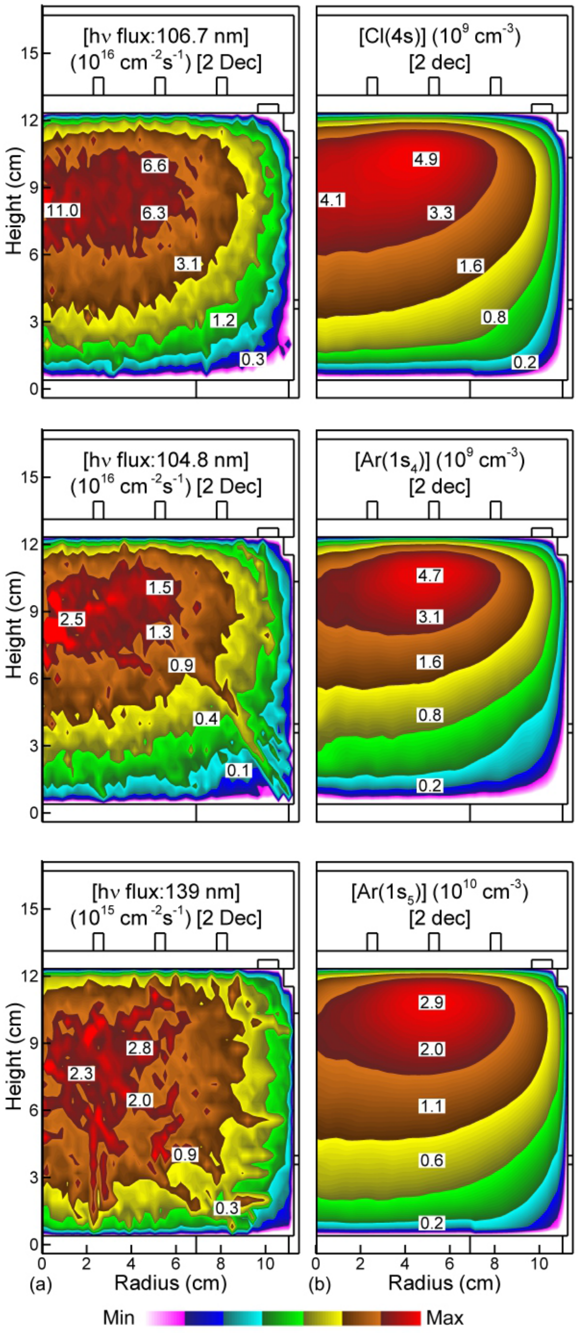

Fig. 5.3 Time averaged plasma properties for base case conditions (Ar/Cl$_2$=80/20, 20 mTorr, 200 sccm, 10 MHz, 150 W cw). (a) Random VUV fluxes for 106.7 nm, 104.8 nm and 139 nm. (b) Densities of Cl(4s), resonant Ar(1s$_4$) and metastable Ar(1s$_5$). The densities and fluxes are on log-scales of 2 decades.

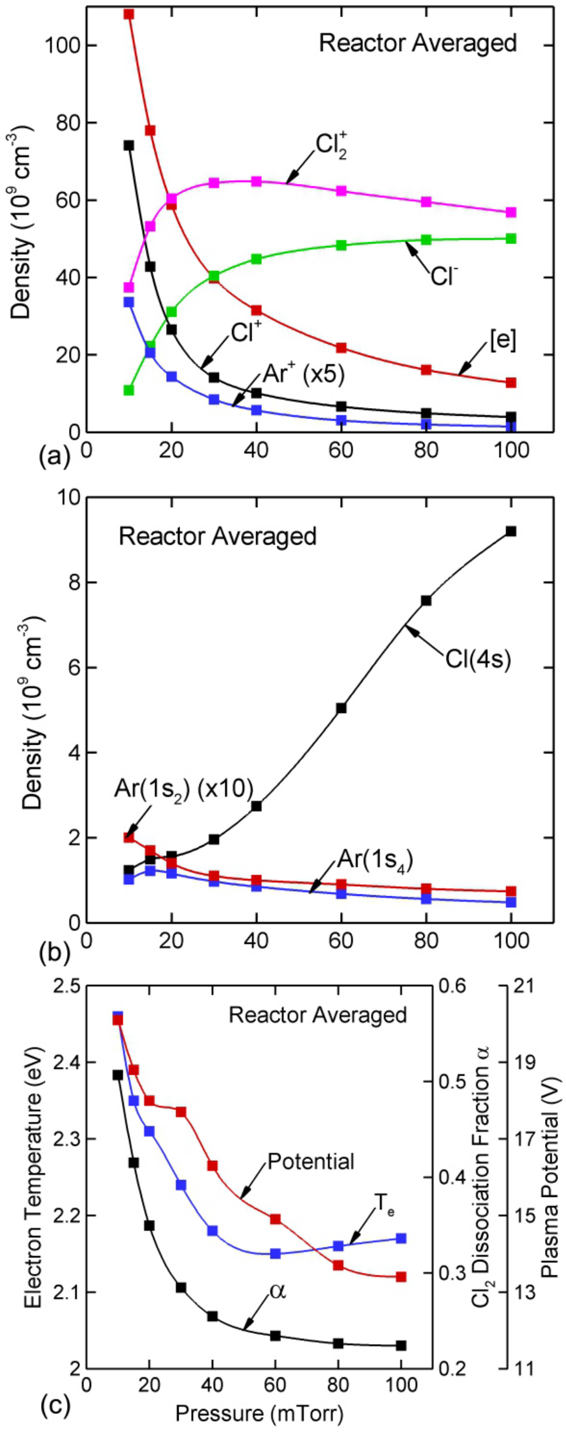

Fig. 5.4 Reactor averaged properties for ICPs sustained in different pressures of Ar/Cl_2=80/20 (10 MHz, 150 W cw). (a) Electron and ion densities, (b) resonant state densities, and (c) plasma potential, electron temperature and Cl_2 dissociation fraction.

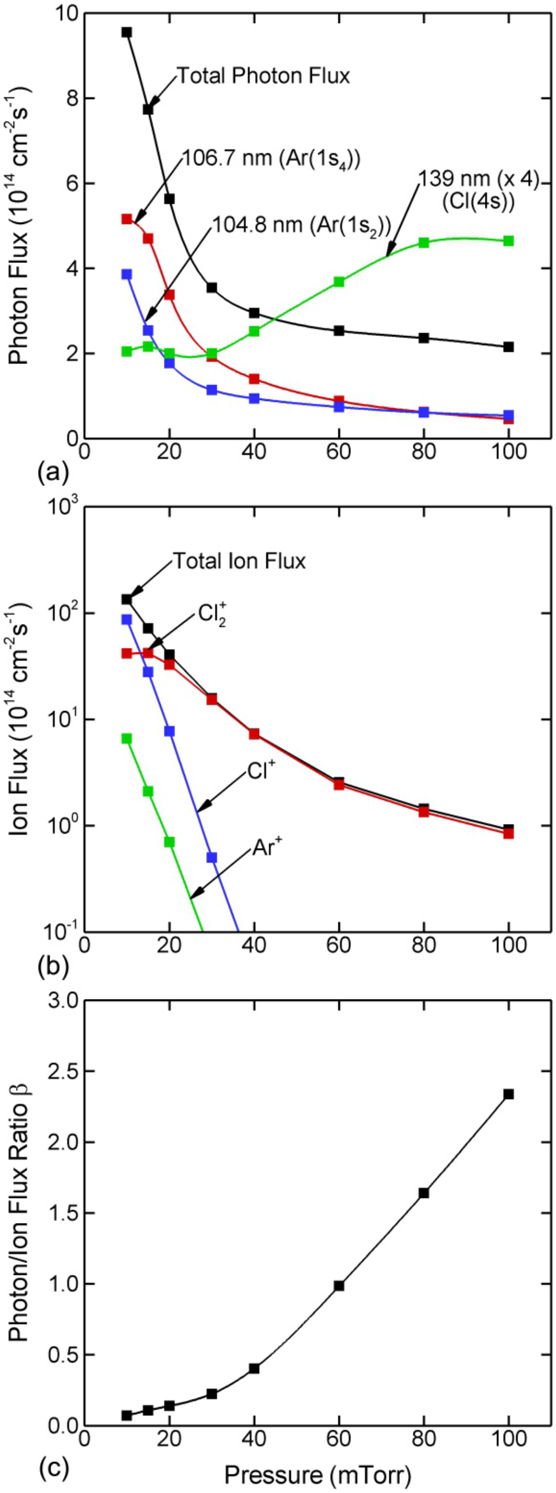

Fig. 5.5 Substrate averaged fluxes for ICPs sustained in different pressures of Ar/Cl$_2$=80/20 (10 MHz, 150 W cw). (a) Photon fluxes, (b) ion fluxes, and (c) total photon/ion flux ratio. Total photon fluxes are the sum of fluxes for 106.7 nm, 104.8 nm and 139 nm.

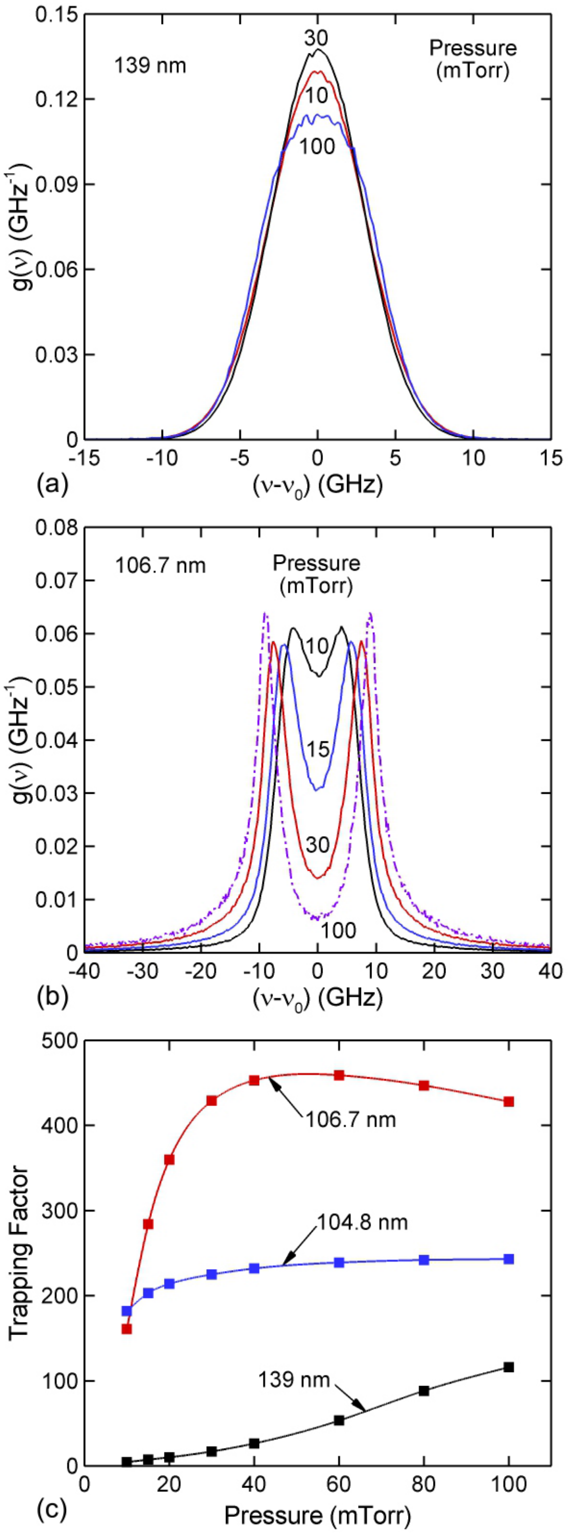

Fig. 5.6 Optical properties for ICPs sustained in different pressures of Ar/Cl_2=80/20 (10 MHz, 150 W cw). (a) Line shape function of 139 nm emission. (b) Line shape function of 106.7 nm emission. (c) Trapping factors for 106.7 nm, 104.8 nm Ar emission and 139 nm Cl emission.

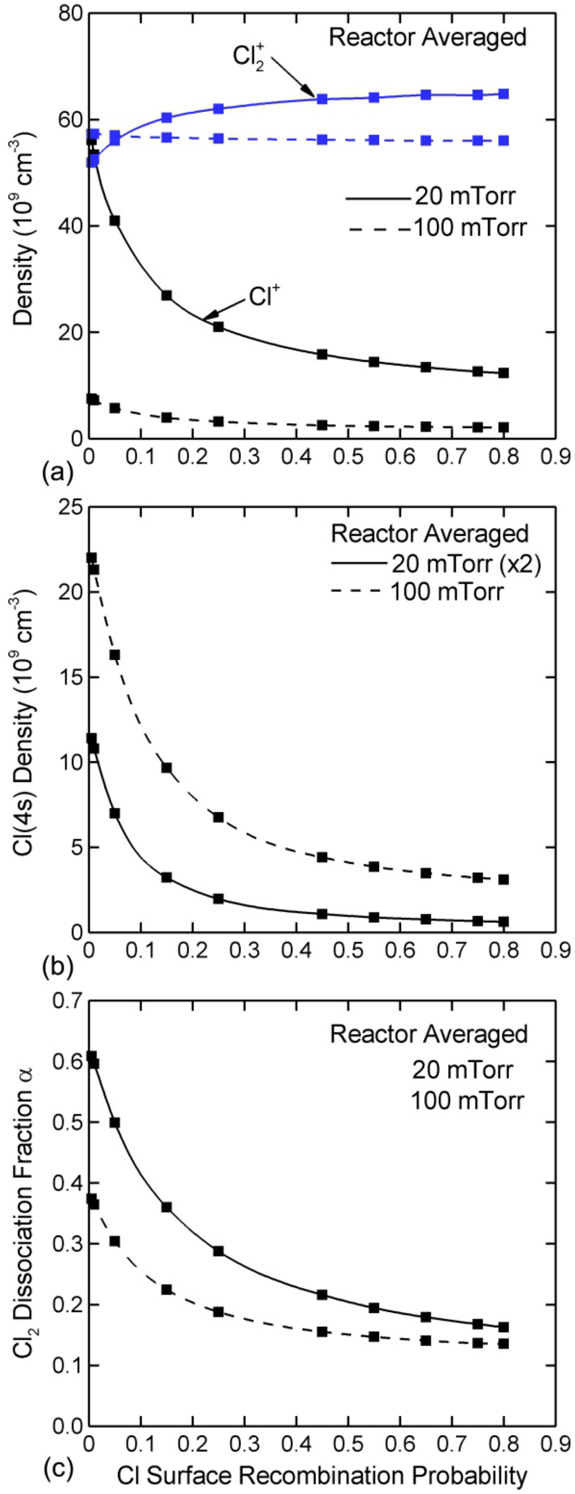

Fig. 5.7 Reactor averaged properties for ICPs having different Cl recombination probabilities in Ar/Cl_2=80/20 (20 mTorr, 200 sccm, 10 MHz, 150 W cw). (a) Cl^+ and Cl_2^+ densities, (b) Cl($3p^4 4s$) densities, and (c) Cl_2 dissociation fraction.

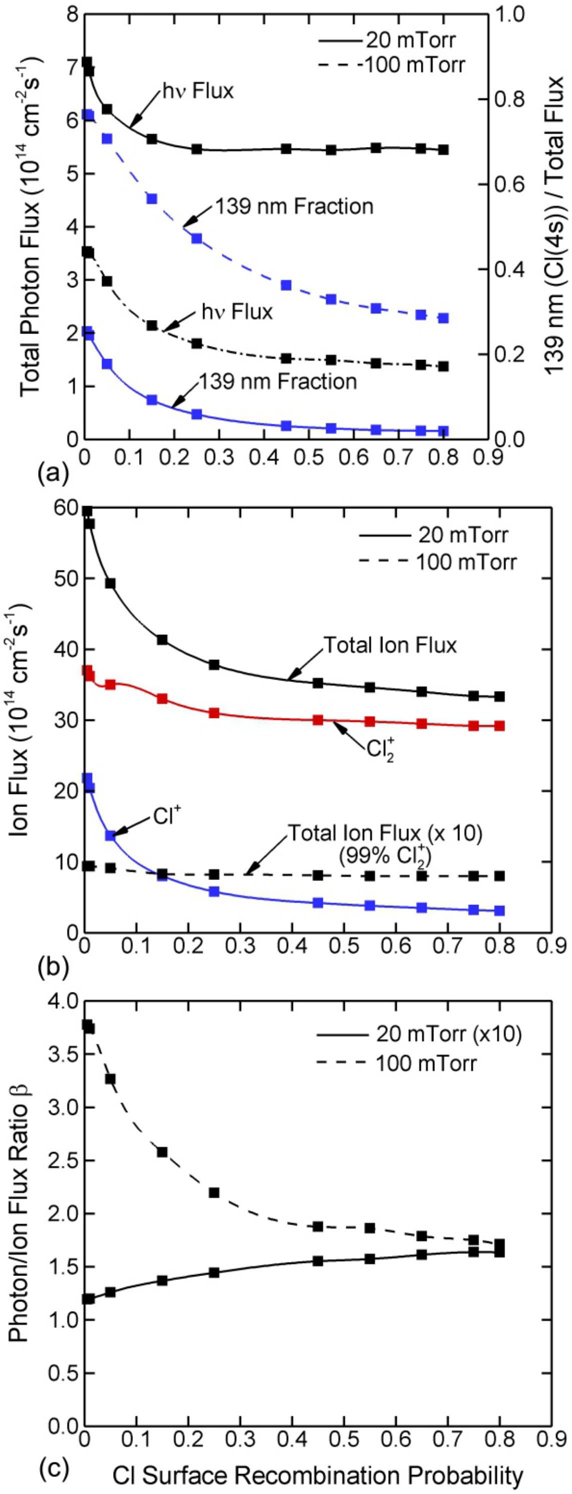

Fig. 5.8 Substrate averaged fluxes for ICPs having different recombination probabilities in Ar/Cl_2=80/20 at 20 and 100 mTorr. (a) Total photon flux and fraction of Cl($3p^4 4s$) emission (139 nm), (b) Cl^+, Cl_2^+ and total ion fluxes, (c) total photon/ion flux ratio. Total photon fluxes are the sum of the fluxes for 106.7 nm, 104.8 nm and 139 nm.

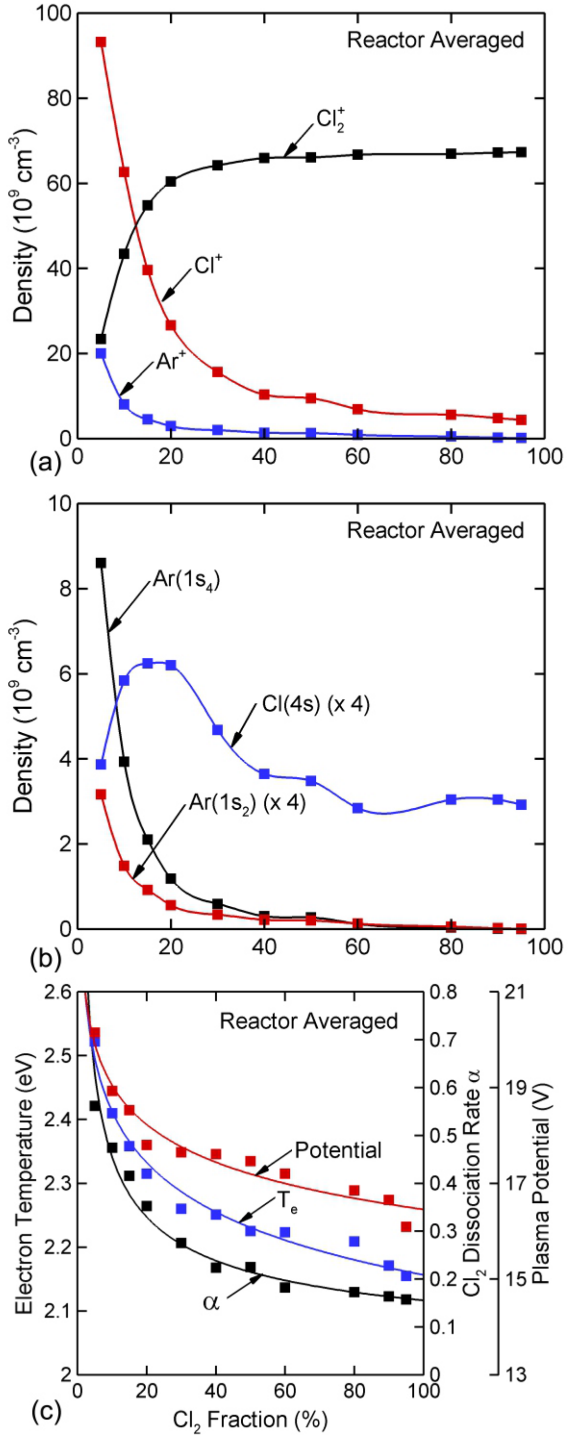

Fig. 5.9 Reactor averaged properties for ICPs having different Cl_2 fractions in Ar/Cl_2 (20 mTorr, 200 sccm, 10 MHz, 150 W cw). (a) Ion densities, (b) resonant state densities and (c) plasma potential, electron temperature and Cl_2 dissociation fraction.

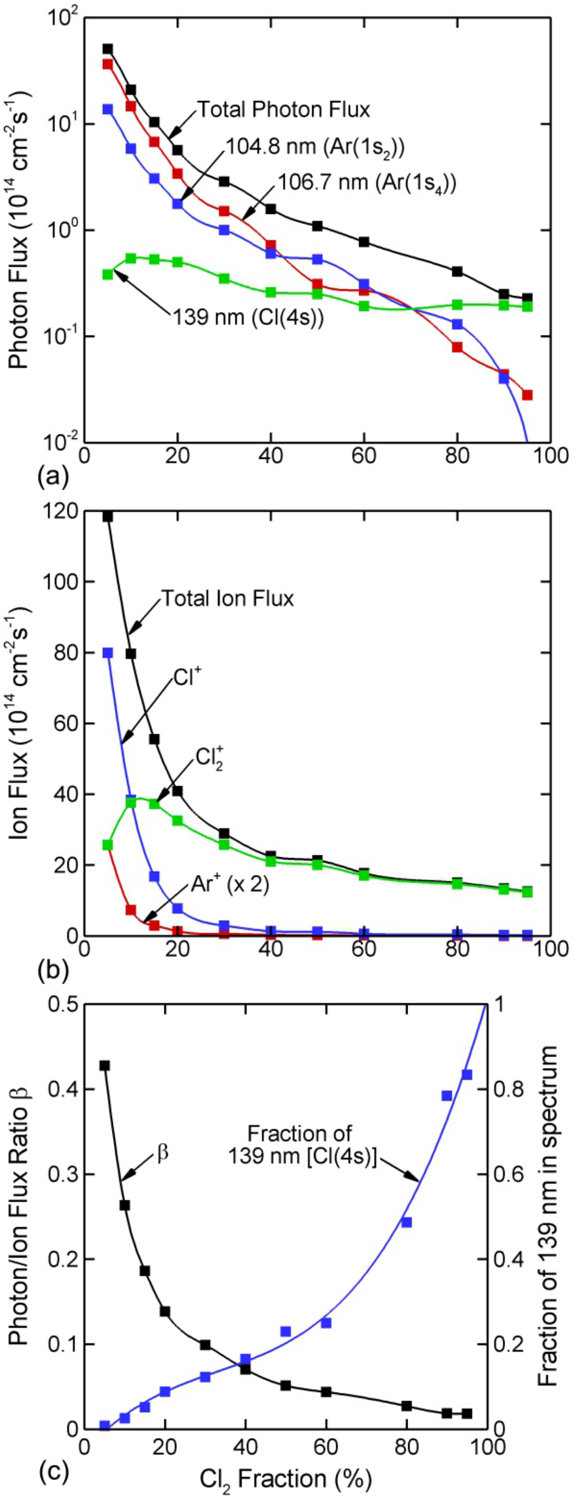

Fig. 5.10 Substrate averaged fluxes for ICPs having different Cl_2 fractions in Ar/Cl_2 (20 mTorr, 200 sccm, 10 MHz, 150 W cw). (a) Photon fluxes, (b) ion fluxes and (c) total photon/ion flux ratio and fraction of 139 nm in the spectra. Total photon fluxes are the sum of fluxes for 106.7 nm, 104.8 nm and 139 nm.

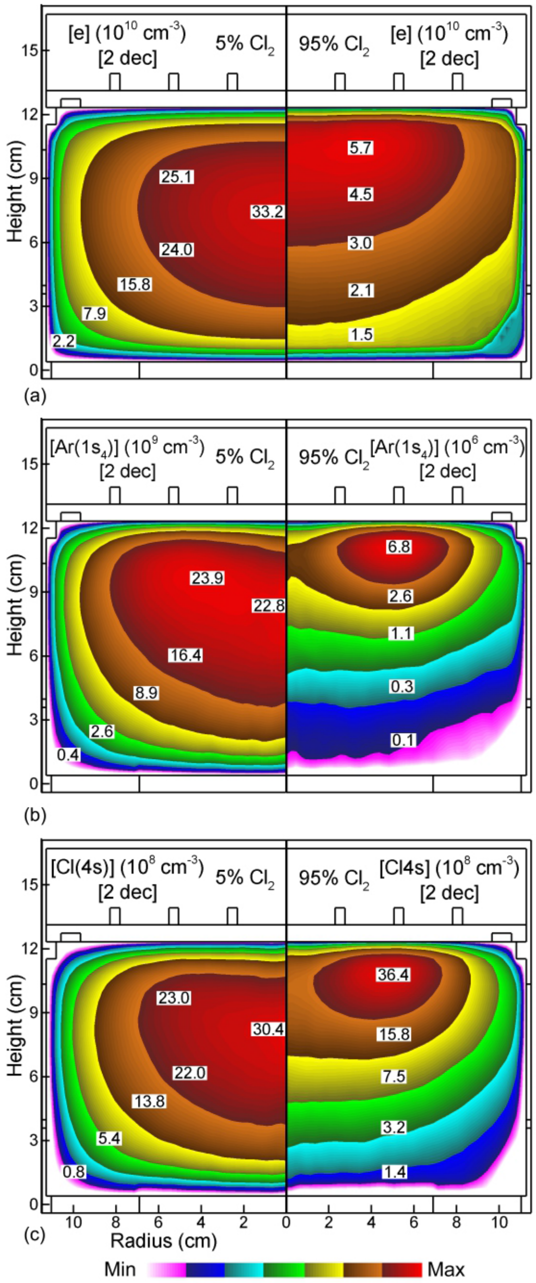

Fig. 5.11 Time averaged plasma properties for ICPs having different Cl_2 fractions in Ar/Cl_2 (Ar/Cl_2=95/5 and 5/95, 20 mTorr, 200 sccm, 10 MHz, 150 W cw). (a) Electron density, (b) resonant Ar($1s_4$) density and (c) Cl($3p^4 4s$) density The densities and fluxes are on log-scales of 2 decades.

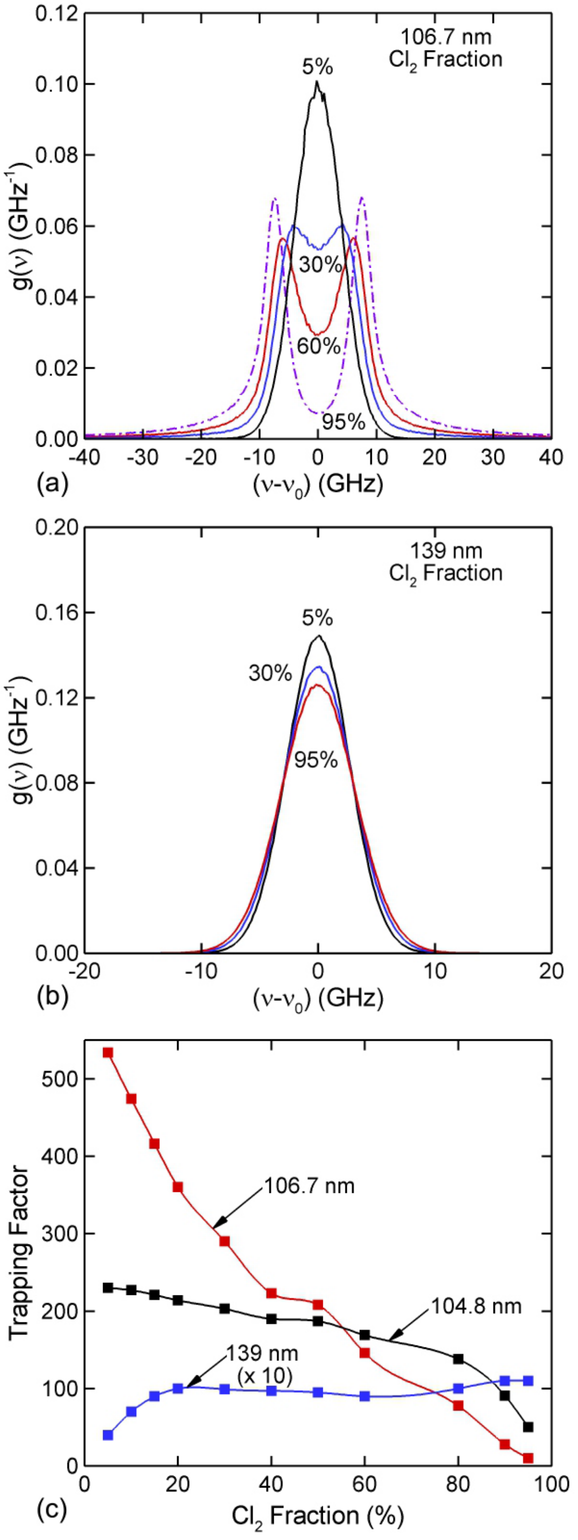

Fig. 5.12 Optical properties for ICPs having different Cl_2 fractions in Ar/Cl_2 (Ar/Cl_2=95/5 to 5/95, 20 mTorr, 200 sccm, 10 MHz, 150 W cw). Lineshape function for (a) 106.7 nm emission and (b) 139 nm emission. (c) Trapping factors for 106.7 nm, 104.8 nm Ar emission, and 139 nm Cl emission.

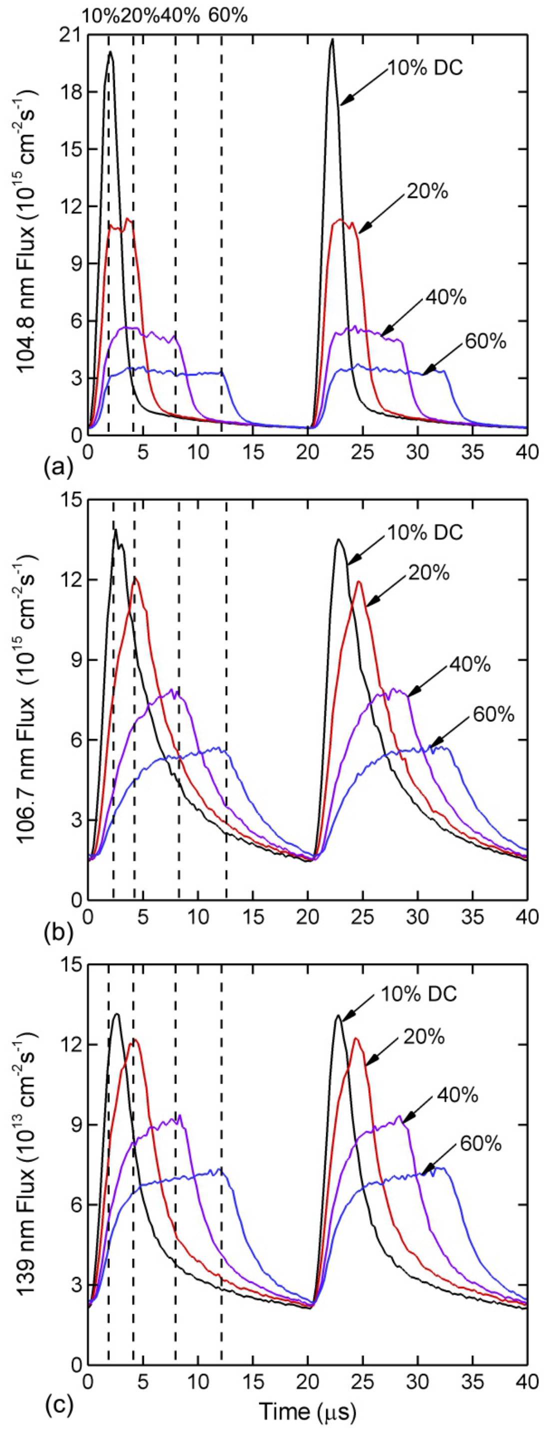

Fig. 5.13 Photon fluxes collected on and averaged over the bottom substrate as a function of time for two ICP pulses for different duty cycles. The dashed lines indicate the end of the power-on period. (a) 106.7 nm [originating from Ar(1s$_4$)], (b) 104.8 nm [originating from Ar(1s$_2$)] and (c) 139 nm [originating from Cl(3p^{4}4s)]. Plasma conditions are Ar/Cl$_2$=80/20, 20 mTorr, 200 sccm, 10 MHz, 150 W CAP, PRF = 50 kHz.

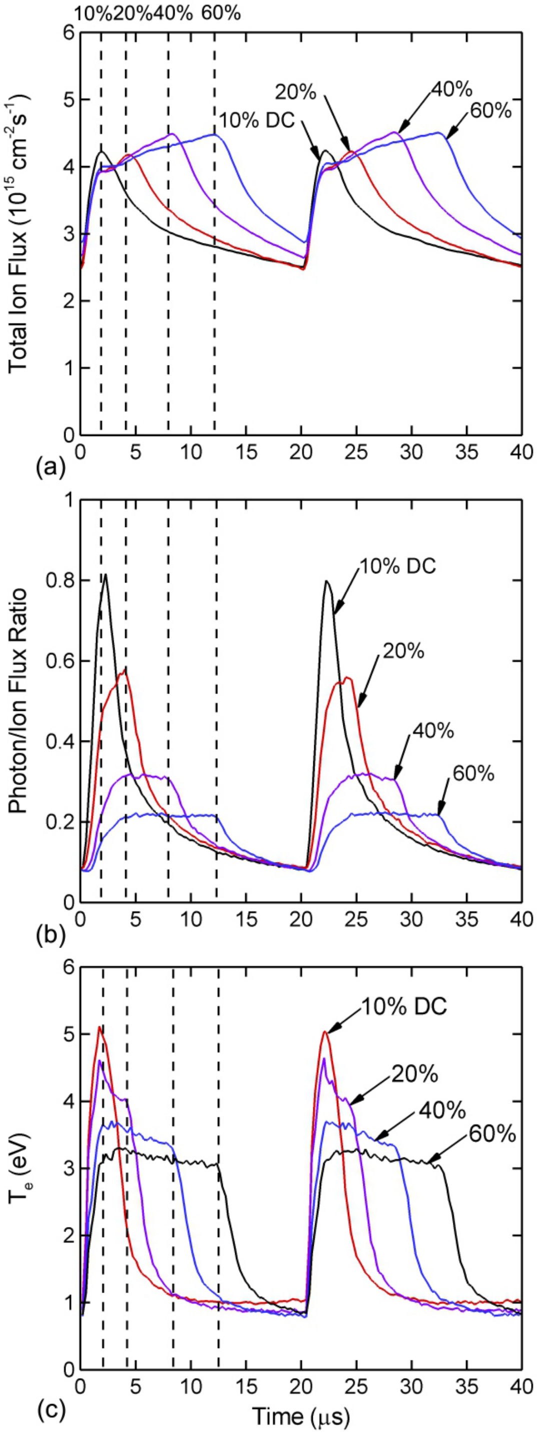

Fig. 5.14 Plasma properties as a function of time for two ICP pulses with different duty cycles. Fluxes are collected on and averaged over the substrate. Dashed lines indicate the end of the power-on period. (a) Ion flux, (b) Ratio of total VUV flux to ion flux, and (c) electron temperature. Plasma conditions are Ar/Cl_2=80/20 , 20 mTorr, 200 sccm, 10 MHz, 150 W CAP, PRF = 50 kHz.

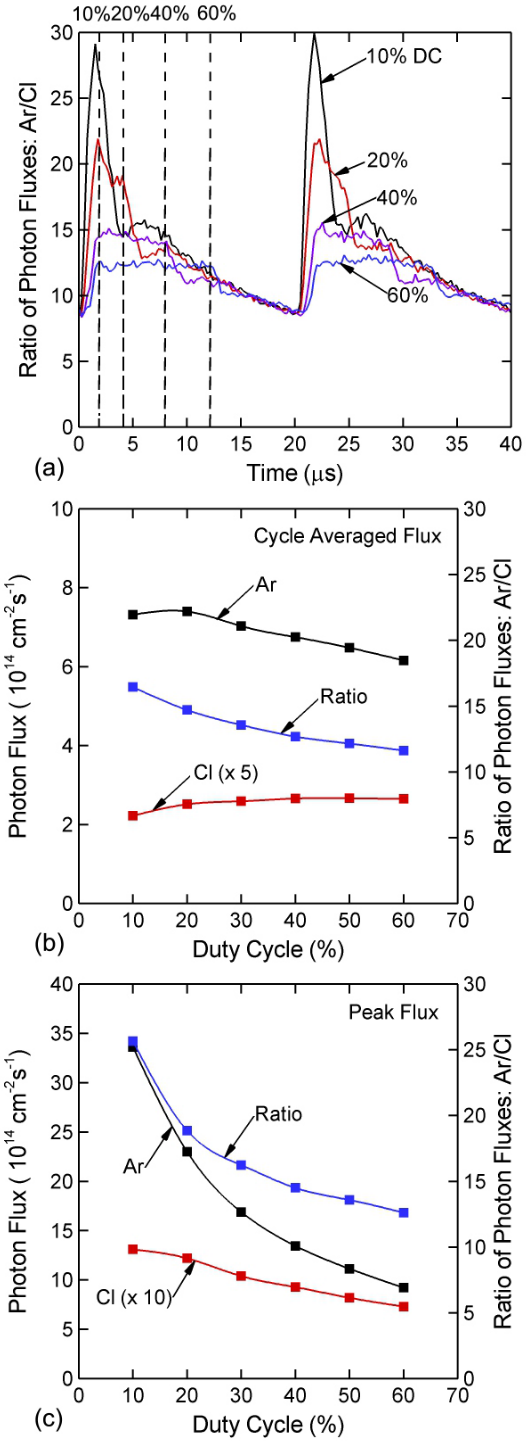

Fig. 5.15 Spectra of VUV fluxes for pulsed ICPs. (a) Ratio of Ar/Cl VUV fluxes over two pulse periods. (b) cycle averaged Ar/Cl photon fluxes ratio as a function of duty cycle, and (c) Peak Ar/Cl photon fluxes ratio as a function of duty cycle. The Ar emission is the sum of fluxes at 106.7 and 104.8 nm.

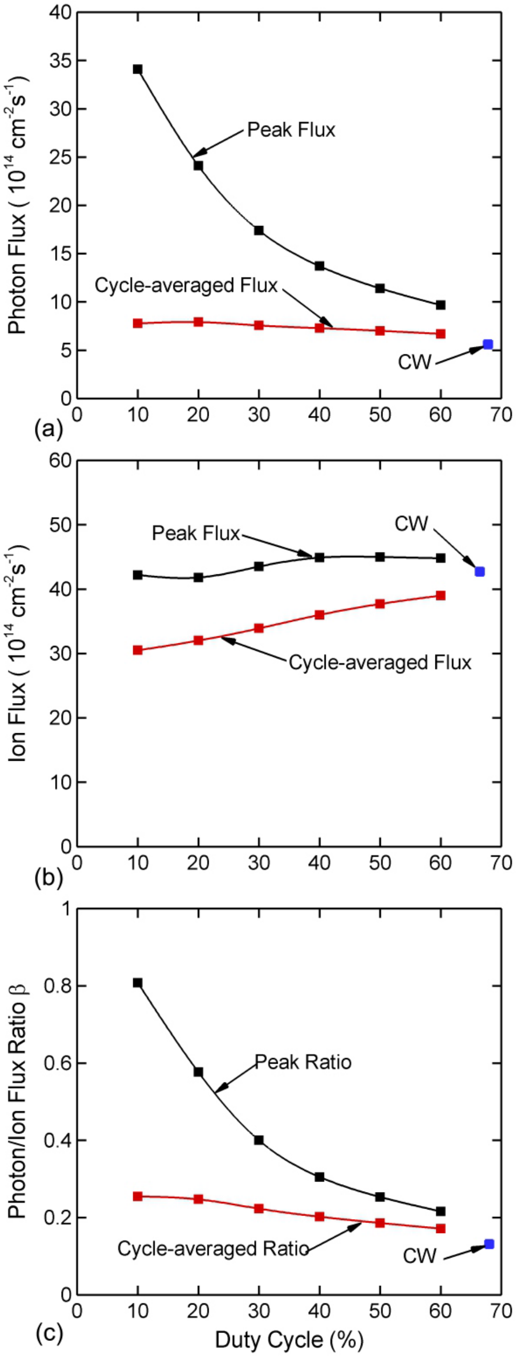

Fig. 5.16 Properties of fluxes striking and averaged over the substrate for pulsed excitation for different duty cycles and for cw excitation. (a) Total VUV photon flux, (b) ion flux and (c) ratio of VUV flux to ion flux. Plasma conditions are Ar/Cl_2=80/20 , 20 mTorr, 200 sccm, 10 MHz, 150 W CAP, PRF = 50 kHz.

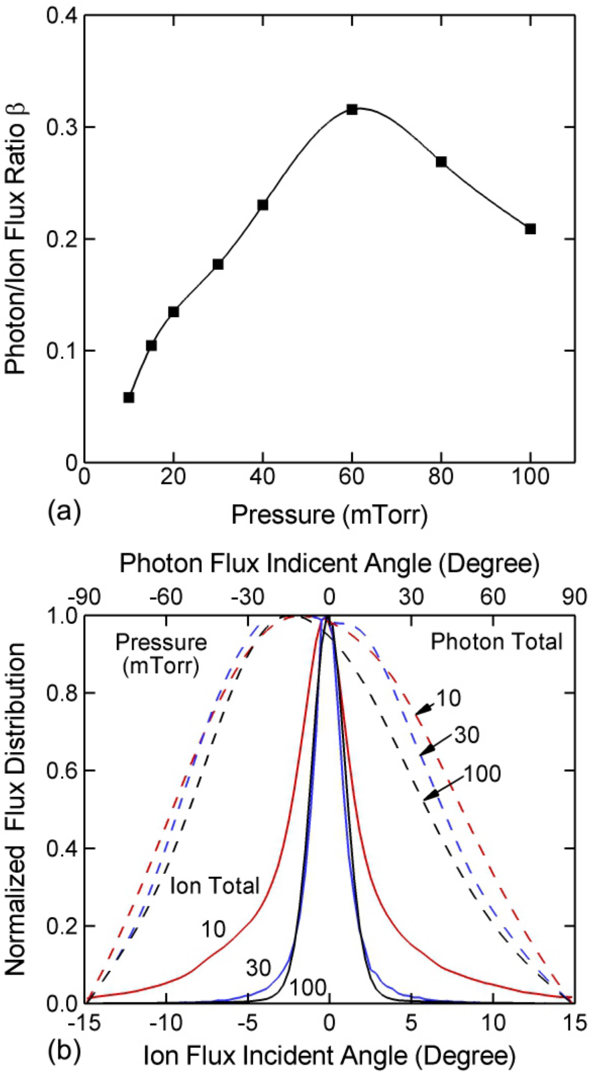

Fig. 5.17 Properties of ion and VUV fluxes in biased ICPs at pressure range 10 - 100 mTorr. (a) ratio of VUV/ion fluxes and (b) angular distribution of total VUV and ion fluxes Plasma conditions are Ar/Cl_2=80/20 , 10-100 mTorr, 10 MHz, 150 W CAP, PRF = 50 kHz, RF bias 10 MHz.

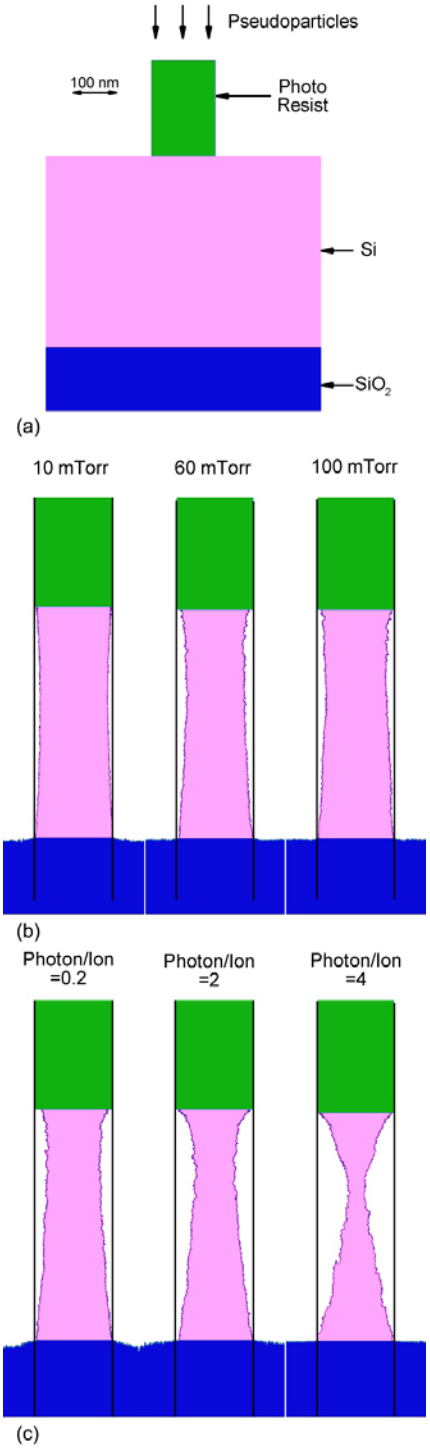

Fig. 5.18 Preditions for feature profiles for Si etching. (a) mask and feature before etching (b) profiles for different pressures (c) profiles resulting from specifying magntidues of VUV fluxes using angular distributions at 20 mTorr.

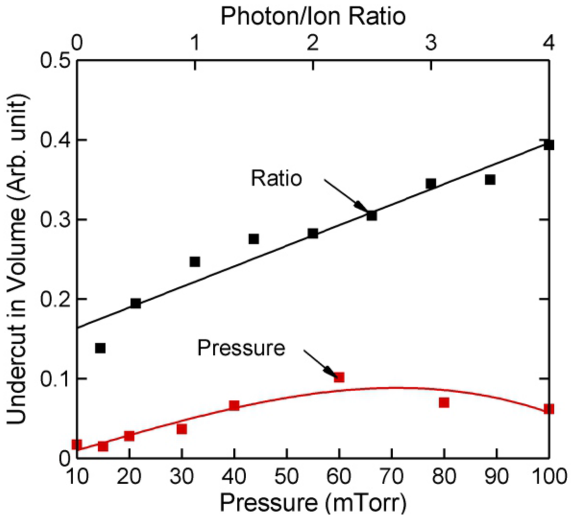

Fig. 5.19 Undercut versus: pressure 10 - 60 mTorr and VUV/ion fluxes ratio from 0.2 to 4

5.8 References

[1] B. Jinnai, S. Fukuda, H. Ohtake, and S. Samukawa, J. Appl. Phys. **107**, 043302 (2010).

[2] J. R. Woodworth, M. E. Riley, V. A. Amatucci, T. W. Hamilton, and B. P. Aragon, J. Vac. Sci. Technol. A **19**, 45 (2011).

[3] J. R. Woodworth, M.G. Blain, R. L. Jarecki, T. W. Hamilton, and B. P. Aragon, J. Vac. Sci. Technol. A **17**, 3209 (1999).

[4] H. Shin, W. Zhu, V. M. Donnelly, and D. J. Economou, J. Vac. Sci. Technol. A **30**, 021306 (2012).

[5] W. Zhu, S. Sridhar, L. Liu, E. Hernandez, V. M. Donnelly, and D. J. Economou, J. Appl. Phys. **115**, 203303 (2014).

[6] M. Fukasawa, Y. Miyawaki, Y. Kondo, K. Takeda, H. Kondo, K. Ishikawa, M. Sekine, H. Matsugai, T. Honda, M. Minami, F. Uesawa, M. Hori, and T. Tatsumi, Jap. J. Appl. Phys. **51**, 026201 (2012).

[7] E. Kemaneci, E. Carbone, J-P Booth, W. Graef, J. V. Dijk, and G. Kroesen, Plasma Sources Sci. Technol. 23 045002 (2014).

[8] T. W. Kin, and E. S. Aydil, Journal. Electrochem. Soc., **150**, G418 (2003).

[9] M. V. Malyshev, V. M. Donnelly, A. Kornblit, and N. A. Ciampa, J. Appl. Phys. **84**, 137 (1998).

[10] V. M. Donnelly, D. L. Flamm, and R. H. Bruce, J. Appl. Phys. **58**, 2135 (1985).

[11] G. P. Kota, J. W. Coburn, and D. B. Graves, J. Vac. Sci. Technol. A **16**, 270 (1998).

[12] L. Stafford, R. Khare, J. Guha, V. M. Donnelly, J.-S. Poirier, and J. Margot, J. Phys. D: Appl. Phys. **42**, 055206 (2009).

[13] J. Guha, V. M. Donnelly, and Y.-K. Pu, J. Appl. Phys. **103**, 013306 (2008).

[14] S. J. Ullal, A. R. Godfrey, E. Edelberg, L. Braly, V. Vahedi, and E. S. Aydil, J. Vac. Sci. Technol. A **20**, 43 (2002).

[15] G. Cunge, N. Sadeghi, and R. Ramos, J. Appl. Phys. **102**, 093304 (2007)

[16] G. Cunge, N. Sadeghi, and R. Ramos, J. Appl. Phys. **102**, 093305 (2007)

[17] E. Meeks and J. Shon, IEEE Trans. Plasma Sci. **23**, 539 (1995).

[18] T. H. Ahn, K. Nakamura, and H. Sugai, Plasma Sources Sci. Technol. **5**, 139 (1996).

[19] A. Agarwal, P. J. Stout, S. Banna, S. Rauf, and K. J. Collins, J. Vac. Sci. Technol. A **29**, 011017 (2011).

[20] K.J. McCann, and M.R. Flannery, Appl. Phys. Lett. **31**, 599 (1977).

CHAPTER 6 CONTROLLING ION FLUXES AND ENERGY DISTRIBUTION IN LOW PRESSURE TRI-FREQUENCY CAPACITIVELY COUPLED PLASMA

6.1 Introduction

Over the past several decades, the developing semiconductor industry has been very successful in fulfilling Moore’s Law of continuing shrinking critical dimensions. While evolving fabrication techniques are pushing the limit of feature size towards tens of or even several nanometers, a higher level of controllability and optimization of all the current processes is critical in this collective effort of technology evolution. As an irreplaceable process in semiconductor fabrication, plasma etching also faces challenges in controlling ion fluxes and ion energy and angular distribution (IEAD). Capacitively coupled plasma (CCP) is widely used in the semiconductor etching processes to generate ion fluxes with optimized ion energy distribution.

Various methods for controlling ion fluxes and IEADs in CCP have been studied over the past few decades. In a single-frequency CCP, ion fluxes and IEADs can be managed using the power and frequency of radio frequency (RF) sources [1,2]. Additional controls were also investigated by applying DC voltage to the plasma. Discovering the limits of coupling of ion fluxes and IEADs in single frequency plasmas motivated the application of dual-frequency CCP (DF-CCP) to separately control the ion fluxes and IEADs. By using high frequency (HF) and low frequency (LF) RF sources with a large frequency separation, it is possible to separately control ion fluxes (primarily controlled by HF power) and IEADs (mostly controlled by LF power) by individually tuning HF and LF power source [3-10]. It has also been determined that when applying harmonic frequencies in geometrically symmetric DF-CCPs, IEADs can be individually controlled by the phase difference between the two frequencies, while ion fluxes stay unhindered [11-20]. CCPs excited with customized waveform have also been studied, demonstrating unique controllability of IEADs caused by unconventional sheath dynamics [21-22]. Meanwhile, as the semiconductor industry moves from DF-CCP towards more frequencies, there are fewer studies in the multi-frequency CCP regime [23]. This chapter discusses the dynamics of a tri-frequency CCP (TF-CCP) and the scaling and controllability of IEDs as a function of power of individual frequencies.

6.2 Description of the model

The computational platform for reactor scale simulation of the TF-CCP is the Hybrid Plasma Equipment Model (HPEM), which Chapter 2 describes in detail. A brief overview of HPEM and power control of TF-CCP in HPEM will be introduced in this section.

HPEM is a 2-D hydrodynamics plasma model addressing multiple physical process which combines both kinetics and fluid approaches. The modular structure of HPEM utilizes individual modules to address separate physical processes, which provides efficiency and flexibility in computational tasks. The modules used in this work in HPEM include the fluid-kinetic Poisson module (FKPM), the electron energy transport module (EETM), and the plasma chemistry Monte-Carlo module (PCMCM). These modules run in series during one iteration of HPEM. First, the transport coefficient and electron energy distribution are calculated by solving a two-term Boltzmann equation with collisional terms in EETM, in which electron temperature, collision frequency and electron impact reaction rate are calculated and tabulated for different ranges of E/N values. Transport and temperature of heavy particles including neutral and ion species are then addressed in FKPM by solving a continuity equation, momentum equation and energy equation using a time-slicing technique, during which electron temperature is constantly updated by solving the electron energy equation. Based on the new electron temperature, the electron transport coefficient and electron impact reaction rate are updated from the tabulated value. The electron flux is then calculated using a Scharfetter-Gummel numerical regime. Finally, the electrostatic field is calculated by solving Poisson's equation in a semi-implicit manner. The resulting species density and temperature distribution, reaction rate distribution and electrostatic field is then fed into PCMCM which implements a kinetic approach to gather statistical information of IEAD on specific surfaces. In PCMCM, trajectories of pseudo-particles of ions are tracked in controlled time steps while collisions are addressed using the null-collision technique.

In HPEM, the RF power applied on the electrode is implemented as a time-resolved boundary condition in the process of solving Poisson's equation in FKPM. For any form of voltage applied to the electrode, the time-averaged power on the electrode can be calculated as:

$$\bar{P}_{rf} = \frac{1}{\tau}\iint V(t)\left[j\left(\vec{r},t\right) + \frac{d\left(\varepsilon\vec{E}\left(\vec{r},t\right)\right)}{dt} \right] dtdA \qquad (1)$$

where A is the electrode surface area, $V(t)$ is the time-dependent voltage on the electrode, $j(\vec{r},t)$ is the conduction current density to the electrode, ε is the permittivity, and $\vec{E}(\vec{r},t)$ is the electric field over the electrode. In multi-frequency CCPs, RF excitation is normally applied in a power-controlled scheme, in which powers associated with different frequencies are kept constant individually over time. In HPEM, power control of individual frequencies is resolved in frequency domain. Within an RF period of the applied frequencies, current is recorded in HPEM as time series with a resolution from 10^3 to 10^4 points per period. These current time series are then used to calculate the discrete Fourier components of incident current at each frequency on the electrode. Up to six harmonics of current at each frequency are resolved. Integration is then performed for current-voltage pairs to calculate power deposition $\overline{P}_{rfi}$ at each applied frequency w_i. At each iteration of HPEM, $\overline{P}_{rfi}$ is compared with the desired power deposition for the corresponding frequencies (an input parameter for HPEM). Voltage of each frequency is then adjusted by a small fraction in the next iteration until the specified power is asymptotically reached for all frequencies. In HPEM, by connecting a blocking capacitor between the power supply and electrode, a DC self-bias is naturally generated on the capacitor which contributes to the instantaneous voltage on the electrode. As discussed in Chapter 1, this DC self-bias is generated through auto-balancing of current on all contacting surfaces and is calculated in FKPM:

$$V_{dc} = \frac{1}{C}\int \sum_i m_i \left(\sum_j \overline{\phi}_j \left(q_j + q\gamma_{ij}\right) \cdot \hat{n}_i + \frac{\partial\left(\varepsilon \vec{E} \cdot \hat{n}_i\right)}{\partial t} \right) dt \qquad (2)$$

where C is the blocking capacitor, $\vec{\phi}_j$ is the flux of charged particle j having net charge q_j incident onto surface i with a local normal direction $\hat{n}_i$ γ_{ij} is the secondary electron emission coefficient for species i on surface material j, and m_i is an indication of the direction of the current in the circuit, depending on whether the surface is on the powered or grounded side of the power supply.

Geometry of the TF-CCP reactor used in this investigation is shown in Fig. 6.1. Design of the reactor resembles CCP reactors in real industry use, in which a 300 mm wafer is placed on top of the bottom electrode confined by a focus ring. The bottom electrode is powered by three distinctive frequencies at 5/10/40 MHz which are individually controlled whose power is controlled to achieve a steady state of the TF-CCP. A blocking capacitor is connected between the bottom electrode and power supply for DC self-biasing. The top electrode is 3 cm above the surface of the wafer and is grounded together with the metal side wall of the reactor. Gas is injected from the shower-head gas inlet which is assigned to the same material as top electrode and exits the chamber from an annular pump at the bottom of the reactor. The secondary electron emission coefficient for ions is 0.15 on all surfaces.

Throughout the investigation detailed in this Chapter, an $Ar/CF_4/O_2$ plasma is sustained in the 3 cm gap between the electrodes with gas volume ratio at 0.75/0.15/0.1. Plasma operates at 25 mTorr with a flow rate of 250 sccm, and the power of the three frequencies is simultaneously applied to the bottom electrode. During the code execution, voltages of the three frequencies are dynamically adjusted to keep a constant power deposition as discussed above. Fluxes and IEADs of ions are collected at and averaged over the wafer surface. A detailed reaction model of $Ar/CF_4/O_2$ is implemented as a simplified version of the $Ar/C_4F_8/O_2$ mechanism used in Ref. [24]. In addition to the Ar species which is the same as in Chapter 4, multiple radicals, ions and excited states are addressed: CF_4, C_2F_6, C_2F_4, CF_3, CF_2, CF, C, F, F_2, CF_3^+, CF_2^+, CF^+, C^+, F_2^+, F^+, CF_3^-, F^-, O_2, $O_2(^1\Delta)$, O_2^+, O, $O(^1D)$, O^+, O^-, COF, COF_2, CO_2, FO, SiF_4, SiF_3 and SiF_2.

6.3 Plasma dynamics of TF-CCP

First, a base case for TF-CCP is established with the power of the three frequencies at 5/10/40 MHz fixed at 300/300/600 W, respectively. Results of a steady state 2-D profile of the base case are shown in Fig. 6.2. Density profiles of electrons, positive ions and negative ions are shown using a log scale over two orders of magnitude. In the base case, an edge-high plasma is produced in the reactor, the result of electric field enhancement at the location where edge of the wafer contacts the focus ring. Peak electron density in this TF-CCP reaches up to 2.4×10^{10} cm^{-3}, while the peak negative ion density is more than double at 5.7×10^{10} cm^{-3}, indicating a highly electronegative plasma. The positive ion density peaks at 8.1×10^{10} cm^{-3}. Compared with ions, the 2-D profile of electrons is more uniform due to the higher electron thermal conductivity for both bulk electrons and beam electrons emitted from secondary electron emission. The profile of positive ions is more graded due to its lower mobility and the highly electronegative nature of the $Ar/CF_4/O_2$ plasma. Negative ions in the plasma show a much more localized profile near the center plane of the reactor due to the confinement of electrostatic force from a slightly positive plasma bulk.

In Fig. 6.2d, the highest electron temperature T_e is produced at the edge of powered sheath surface, reaching up to 7.2 eV. This results from stochastic heating caused by the rapid expansion of the sheath boundary. T_e in the bulk plasma is significantly lowered to 2 eV by electron impact collisions. The low bulk electron temperature is also partly caused by the high electronegativity of the plasma, in which ion loss rate to the surface is considerably decreased by the ion-ion recombination in the bulk plasma with negative ions.

The resulting ionization source by bulk electrons is shown in Fig. 6.2.e. Affected by both electron density profile and electron temperature T_e, bulk ionization peaks at 4.5×10^{15} $cm^{-3}s^{-1}$ at an off-center location in the reactor close to the edge of the stochastic heated electrons. Bulk ionization in the sheath region near the powered electrode is ten percent of peak value, a result of an ion-matrix sheath with significantly lower electron density. At the triple point of the wafer edge, focus ring and plasma, the electric field enhancement creates a locally high ionization region in which bulk ionization source reaches 1×10^{15} $cm^{-3}s^{-1}$. As a comparison, ionization caused by secondary emitted beam electrons is shown in Fig. 6.2f. The electron beam ionization source is an order of magnitude lower than that of bulk ionization, which is partly due to the much longer energy relaxation length of the high energy beam electrons accelerated by the sheath potential, normally over 100 eV. The beam ionization source, however, is more uniform compared with the bulk profile. A radial ionization path of secondary electrons is observed from the triple point to the extended top electrode edge, the outcome of a slanted sheath formed at the edge of the bottom electrode.

A critical factor affecting IEADs, the sheath dynamics at the base of the powered electrode near the wafer surface is shown in Fig. 6.3. The 2-D profile evolution of electron density over a 5 MHz period is presented in Fig. 6.3a and clearly shows that the sheath expands and collapses with higher frequency fluctuations through the cycle. During the sheath movement over the period, electron density in the bulk plasma at steady state varies by less than one percent. This provides us a reasonable criterion for defining the edge of the sheath for the purpose of calculating the dynamics of sheath expansion and collapse. The sheath edge is thus defined as the axial location at which electron density decreases below two orders of magnitude of the peak electron density at the same radial location. For example, if the dynamics of sheath thickness is sampled at radial location of 2 cm off-center, of all electron density values at R = 2 cm at various Z locations, the highest electron density reaches 1.8×10^{10} cm^{-3}. Then, the threshold electron density distinguishing bulk plasma and the sheath region is determined as 1.8×10^{8} cm^{-3}. The edge of the sheath region is defined as the location at which the electron density falls below this threshold value, and the thickness of the sheath is sampled as the distance between the above location and the surface of the wafer at R = 2 cm.

Dynamics of sheath thickness extracted at a radial location at 2 cm as a function of phase in a 5 MHz period are shown in Fig. 6.3b. The corresponding applied voltages on the electrode are shown in Fig. 6.3c. With fixed power at 300/300/600 W for 5/10/40 MHz, the peak voltages significantly vary for different frequencies with values of 570/380/260 V, respectively. The larger voltage of low frequency power, as introduced in Chapter 1, is determined by the frequency scaling law in CCP dynamics: ohmic heating of CCPs is proportional to the square of applied frequency, $S_{heating}=\omega^2 T_e^{1/2} V_{rf}$, in which ω is RF angular frequency, T_e is electron temperature, and V_{rf} is RF voltage [39]. The 40 MHz power in TF-CCP can thus more efficiently deliver energy to the bulk plasma at a lower voltage for twice the power at 5 MHz and 10 MHz. Meanwhile, the frequency scaling law requires voltage to increase by a factor of 32 for 5 MHz, and a factor of 8 for 10 MHz, which is disproportionally larger than the voltages recorded in the base case. This indicates that a considerable fraction of power at 5 MHz and 10 MHz is partitioned into ion acceleration through sheath dynamics.

The overall waveform at the power electrode is primarily modulated by the 5 MHz power, with 10 MHz and 40 MHz modulation added to the waveform. As shown in Fig. 6.3b, sheath dynamics are strongly coupled with the applied voltage. When the applied voltage reaches its positive peak value, the sheath collapses rapidly from 5 mm to almost disappearing. When the applied voltage dips to the negative peak near the end of the cycle, the sheath expands to a maximum thickness of 9 mm. For the majority of the rest of the cycle, the sheath thickness fluctuates near an average value of 7 mm, a result of DC self-bias voltage of -600 V caused by the geometric asymmetry of surface current density over reactor surfaces. The change of sheath thickness at expansion is significantly smaller, limited by the inertia of high density bulk plasma.

The cycle-averaged IEDs and IEADs of three different ion fluxes, F^+, Ar^+, CF_3^+ are shown in Fig. 6.4. A commonly seen dual-peak distribution is observed for all three major ion fluxes in Fig. 6.4a. With increasing mass from F^+ to CF_3^+, the energy difference between the two peaks decreases from 400 eV to 200 eV. The resulting IEADs of the three ions have the same dual peak profile in an energy-angle space in Fig. 6.4b. The incident angles of ions are all within ten degrees from the vertical incident angle, while the lower mass F^+ shows a wider angular distribution at the low energy peak due to its lower vertical velocity (lower low-energy peak).

Since energy of the ion fluxes is primarily gained from sheath potential, the detailed analysis of the effect of sheath dynamics and IEDs, shown in Fig. 6.3b and Fig. 6.4a, respectively, is necessary and beneficial for the following discussion of this work. As noted in Chapter 1, the ratio of ion traverse time through the sheath t_{ion}, and the period of applied RF power, t_{rf}, is a critical factor determining IEDs in RF powered CCPs. In the base condition, the average ion travel time t_{ion} ranges between 0.1 – 0.5 μs, which is comparable to the fundamental period of a voltage cycle at 0.2 μs for 5 MHz power. In this regime, regardless of difficulties in the analytical solution of IEDs, sheath dynamics analysis can be used to explain and predict the IEDs. In the dual-peak distribution of IEDs in Fig. 6.3b, the low energy peak corresponds to ion fluxes that mainly gain energy from the positive peak phase of the applied voltage when sheath potential drop is the lowest. The high energy peak is formed by ions that enter the sheath at the lowest peak of the applied voltage, at which time potential drop in the sheath reaches maximum value. It would seem that with the same ion density, the higher energy ions would contribute larger fluxes due to its higher velocity. The observed IEDs, however, have a significantly larger low-energy peak for all three ions. This counter-intuitive result is caused by the constant change of sheath thickness. As low energy ions enter the sheath region, the collapsing sheath produces a much smaller sheath thickness compared to the sheath expansion phase. Consequently, ions that enter at low-sheath potential phase will take much less time to reach the surface, gaining kinetic energy from the sheath and creating a larger low-energy peak in IEDs.

Fluxes of various species as a function of wafer radial location are shown in Fig. 6.5. As the product of dissociation reactions, radical F has the highest fluxes of 2×10^{17} $cm^{-2}s^{-1}$ to the wafer surface. Other radical fluxes, O and CF_2, are an order of magnitude lower. The largest ion fluxes, Ar^+, is over two orders of magnitude lower than that of radical F and slightly over 10^{15} $cm^{-2}s^{-1}$. These large fluxes of radicals are produced by the electron impact dissociation process which has a lower threshold energy compared with ionization reactions. Fluxes of CF_3^+ and CF are comparable to Ar^+ fluxes, while O^+ and F^+ are much lower with values of 2×10^{13} $cm^{-2}s^{-1}$ and $8 \times 10^{12} cm^{-2}s^{-1}$, respectively.

6.4 Controlling ion fluxes and IEAD by power

This section discusses scaling of ion fluxes and IEDs over power for the three frequencies to gain a better understanding of fluxes and IED control in TF-CCP. For each simulation, the power of one frequency was changed while the powers of the other frequencies remain the same as the base case. Other conditions remain the same. The resulting parameter space is composed of the following data points:

40 MHz:	600 W, 900 W, 1.2 kW, 1.5 kW.
10 MHz:	300 W, 600 W, 900 W, 1.2 kW.
5 MHz:	300 W, 600 W, 900 W, 1.2 kW.

Data points within the same column have the same overall input power combining all three frequencies.

As shown in Fig. 6.6, average densities of Ar^+, F^- and electron are scaled with increasing power of individual frequencies. For the same total input power, scaling of densities of the species is close regardless of the frequency of the increased power. This indicates that power increases at different frequencies can be closely coupled through the non-linear impedance of the sheath. The similar increase of plasma density can be partially explained by the different heating mechanism scales with different frequencies. As the 40 MHz power increase heats the plasma through ohmic heating, power at lower frequency contributes to plasma heating through significantly enhanced secondary electron beam heating. When power increases from 300 W to 1.2 kW for 5 MHz frequency, the secondary electron ionization rate at the center of bulk plasma doubled from 1.6×10^{14} $cm^{-3}s^{-1}$ to 3.4×10^{14} $cm^{-3}s^{-1}$. The resulting increases in plasma density, though they scale similarly with power, can be the representation of two different heating mechanisms.

The scaling of the ion fluxes and DC self-bias voltage is shown in Fig 6.7. Time-averaged ion fluxes are collected at the surface of the wafer, at the same location as the sheath dynamics shown in Fig. 6.3b. When power increases for individual frequencies, flux of Ar^+ also increases. This increase of Ar^+ flux is more sensitive to power at lower frequencies. A power increase at 40 MHz raises Ar^+ fluxes by a factor of 1.2, compared to the two-fold rise when increasing 5 MHz power. A similar trend is also observed for CF_3^+ fluxes to the wafer. This confirms that a large fraction of power at lower frequencies is coupled into ion acceleration.

The higher ion fluxes at larger, low frequency power create a new current balance over the reactor surface. The resulting bias voltage changes as a function of individual frequency power, are shown in Fig. 6.7c. Due to the significant power coupling to ion current, power at both low frequencies strongly affect the bias voltage, decreasing from -600 V to -1 kV as power of either low frequency increases from 300 W to 1.2 kW. However, the DC self-bias voltage is hardly affected by power change at 40 MHz.

In the HPEM, voltage is dynamically adjusted to match the specific power delivery for each individual frequency. As power of 40 MHz increases from 600 W to 1.5 kW, the peak voltage at 40 MHz increases from 215 V to 333 V. Voltages of the other two frequencies decrease with increasing 40 MHz power. This is a consequence of the increased ion current caused by high frequency 40 MHz power. Note that the power of lower frequencies is calculated by integration of voltage and Fourier component of current averaged over time. Voltage of 10 MHz decreases from 394 V to 351 V, while 5 MHz decreases from 629 V to 494 V. These peak voltage changes significantly affect the sheath dynamics through which IEADs tunability is achieved. As shown in Fig. 6.8a, the resulting overall voltage on the powered electrode shows increasing fluctuation on top of the modulated waveform as power of 40 MHz increases. Here an additional data point of 300 W power at 40 MHz is added to better demonstrate the scaling. Positive and negative peaks of the voltage remain unchanged over the 40 MHz power range. In Fig. 6.8b, sheath dynamics associated with changing 40 MHz power are shown in the form of variation of sheath thickness as a function of phase in one period of 5 MHz signal. With sheath collapse unchanged over the power range, average sheath thickness decreases with increasing 40 MHz power for both the sheath fluctuation and sheath expansion phases. This sheath thickness variation is related less to the voltage waveform on the electrode and more to the dynamics of the bulk plasma, where the increase of plasma density shrinks the width of the average sheath region. The resulting IEDs and IEADs of Ar^+ are shown in Fig. 6.9. At the low power of 300 W, the dual peak profile degenerates to a single peak at low energy, which is caused by the large expanding sheath at the lowest peak of applied voltage. Ion transit time through the thick sheath over 11 mm is long enough to average out the higher peak in IED. This high energy peak reemerges as soon as power increases to 600 W. Starting at 900 W, the high plasma density in the bulk again limits the expansion of sheath thickness at lower peak voltage, creating a more observed high energy peak in the dual-peak IED.

Similarly, power at 10 MHz is varied from 300 W to 1.2 kW with voltage increased from 394 V to 1014 V. The voltage of 5 MHz power decreases from 629 V to 448 V. 40 MHz voltage increases from 210 V to 270 V. A combined waveform for powers of 10 MHz is plotted in Fig. 6.10a. Sheath dynamics for corresponding cases are shown in Fig. 6.10b. The increasing 10 MHz voltage dominates the modulation of the applied waveform, producing two additional low/high voltage peaks between the original dual voltage peak at the beginning and end of the 5 MHz period. These two smaller peaks induce a lower degree of sheath expansion and collapse near 35% and 65% of the voltage period, respectively. Sheath expansion at 35% of the time period is limited by saturation of sheath thickness, while the expansion is stronger proportional to the increasing 10 MHz power. The IEDs and IEADs as a function of 10 MHz power show significantly different variations compared with 40 MHz cases. As shown in Fig. 6.11a, the overall energy distribution moves to higher energy ranges. This is the result of decreasing DC self-bias voltage from -600 V to -1000 V as discussed above. The shape of IEDs also evolves as the sheath dynamics changes with power. When power increases to 900 W, the second collapse of the sheath at 65% of the time period reduces the thickness of sheath down to 67% of its value compared with base case. This collapse also has a broader time span compared to the full collapse at the beginning of the cycle. Ion fluxes that enter sheath during this second collapse time have comparably shorter transverse time, thus creating a third energy peak between the original dual peaks. This peak further separates from the low energy peak as power of 10 MHz increases to 1.2 kW, since bias voltage decreases from -850 V to -1000 V. In IEADs shown in Fig. 6.11b, the multi-peak profile is clearly seen in the energy – angle space. Ion angular distribution is limited within five degrees of perpendicular direction due to the high ion kinetic energy at 1.2 kW of 10 MHz.

Changing of 5 MHz power could potentially create the strongest effect on IEDs and IEADs. When increasing 5 MHz power from 300 W to 1.2 kW, voltage of 5 MHz increases from

629 V to 1381 V, voltage of 10 MHz decreases from 394 V to 283 V, while voltage of 40 MHz increases from 210 V to 270 V. Fig 6.12a and 6.12b demonstrate the resulting voltage and sheath thickness dynamics respectively. With increasing 5 MHz power, overall waveform on the electrode is dominantly modulated by the 5 MHz voltage. Increasing the peak voltage at 5 MHz produces a second comparable peak next to the first peak at both positive/negative peak locations. Consequently, shortly after the first sheath collapse, the sheath collapses a second time at higher 5 MHz power, expectedly creating a second low-energy peak at the IED. Such predictive analysis is confirmed as shown in the IEDs of Ar^+ flux in Fig. 6.13a with varying 5 MHz power. In addition to the translation of all IEDs towards higher energy due to the decreasing DC self-bias, an additional low energy peak emerges at 900 W. This corresponds to the fully collapsed sheath caused by the second voltage peak. This peak is at a lower energy than the original low-energy peak caused by the lower potential drop at second sheath collapse. As power at 5 MHz further increases to 1.2 kW, this three-peak structure maintains at a higher overall energy level. Fig 6.13b demonstrates that as ion energy increases with higher 5 MHz power, the ion fluxes develop a narrower angular distribution which is favorable to plasma etching applications.

6.5 Concluding Remarks

In this Chapter, HPEM is used for a numerical investigation of a low pressure tri-frequency capacitively coupled plasma operating in $Ar/CF_4/O_2$ gas mixtures at frequencies of 5/10/40 MHz applied to the same electrode. Unlike dual frequency capacitively coupled plasma with separate powered electrodes, the tri-frequency CCP shows a stronger power coupling between frequencies through the non-linear sheath interaction. Though ohmic heating scales with ω^2 of applied frequency, plasma density is still a strong function of lower frequency power caused by secondary electron ionization sources from the powered electrode. This result matches observation in DF-CCPs from literature regarding similar electro-negative plasmas [10]. The ion fluxes scales more sensitively with lower frequency power, a result of higher voltage and a larger fraction of power delivered into ion acceleration at these low frequencies.

In the configuration of this TF-CCP, ion transit time through the sheath is comparable to the fundamental frequency period, a scenario for which an analytical solution of IED is difficult to achieve. In this work, sheath thickness dynamics is used to explain and predict IEDs of the TF-CCP. With detailed analysis of change of sheath thickness over fundamental RF period at 5 MHz, and the combined waveform of the tri-frequency voltage, evolution of IEDs as a function of power deposition is well explained. Unconventional multi-peak IEDs are also successfully explained and predicted from this sheath analysis technique. This direct analysis of sheath thickness dynamics does not depend on the number or frequency of the applied power voltages, and thus can be used in more general scenarios with the information of applied voltage waveform and change of sheath thickness over time, to qualitatively predict the IEDs of a low pressure plasma source.

6.6 Figures

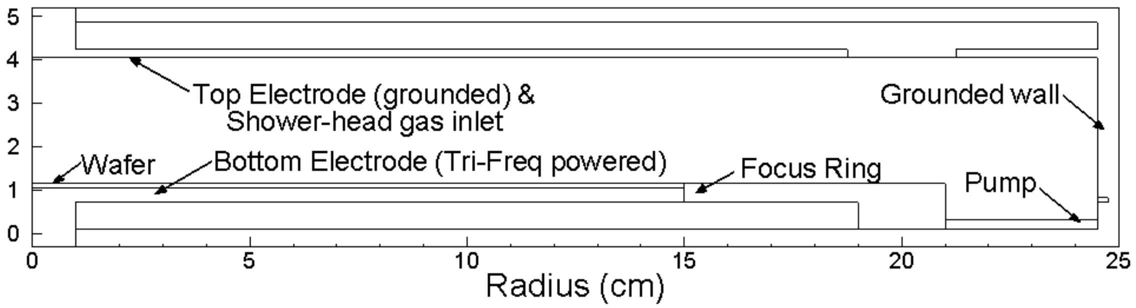
Top Electrode (grounded) &
Shower-head gas inlet
Grounded wall
Wafer
Bottom Electrode (Tri-Freq powered)
Focus Ring
Pump
0
1
2
3
4
5
0
5
10
15
20
25
Radius (cm)

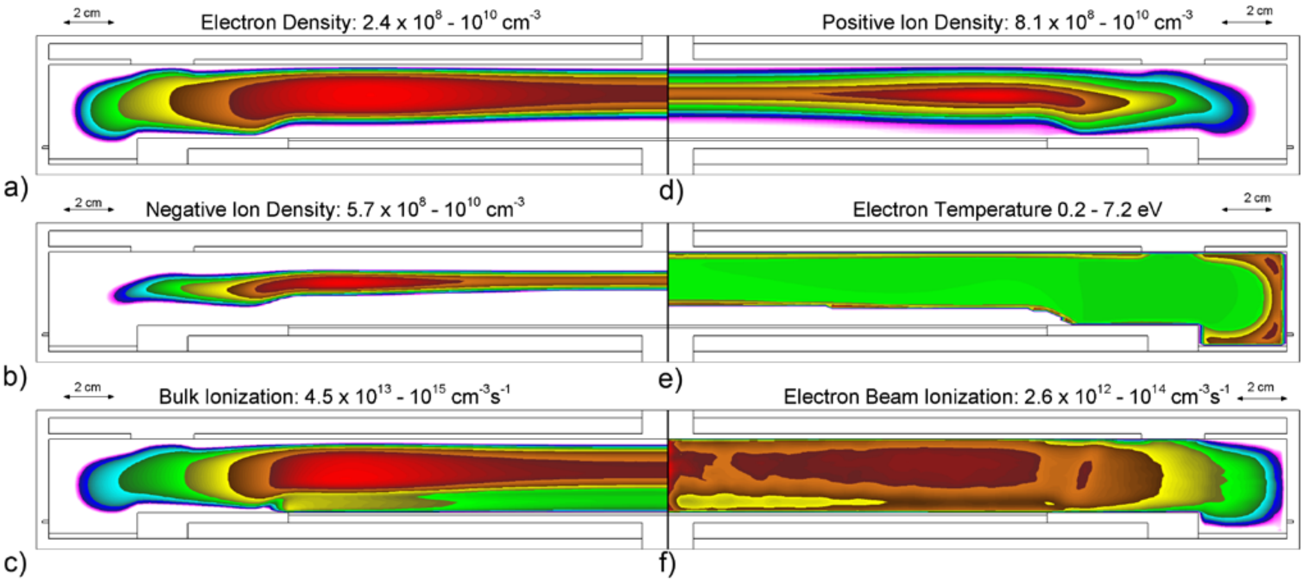

Fig. 6.2 Plasma properties of base case TF-CCP. Plasma sustained in Ar/CF$_4$/O$_2$ = 75/15/10, 25 mTorr, 250 sccm. Power of the three frequencies 5/10/40 MHz is 300/300/600 W respectively. a) Electron density; b) positive ion density; c) negative ion density; d) electron temperature; e) ionization sources by bulk electrons; f) ionization sources by beam electrons.

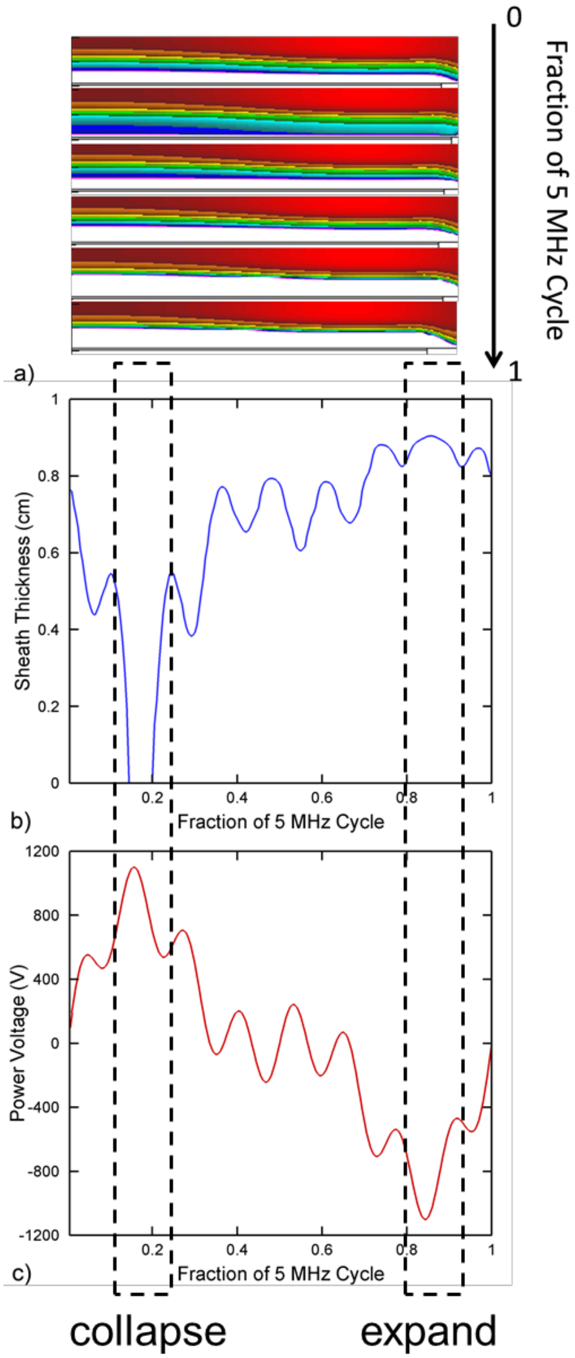

Fig. 6.3 Sheath dynamics and applied voltages for the base case over one cycle of 5 MHz power. a) 2-D profile of change of electron density; b) sheath thickness dynamics and c) combined voltage on the powered electrode.

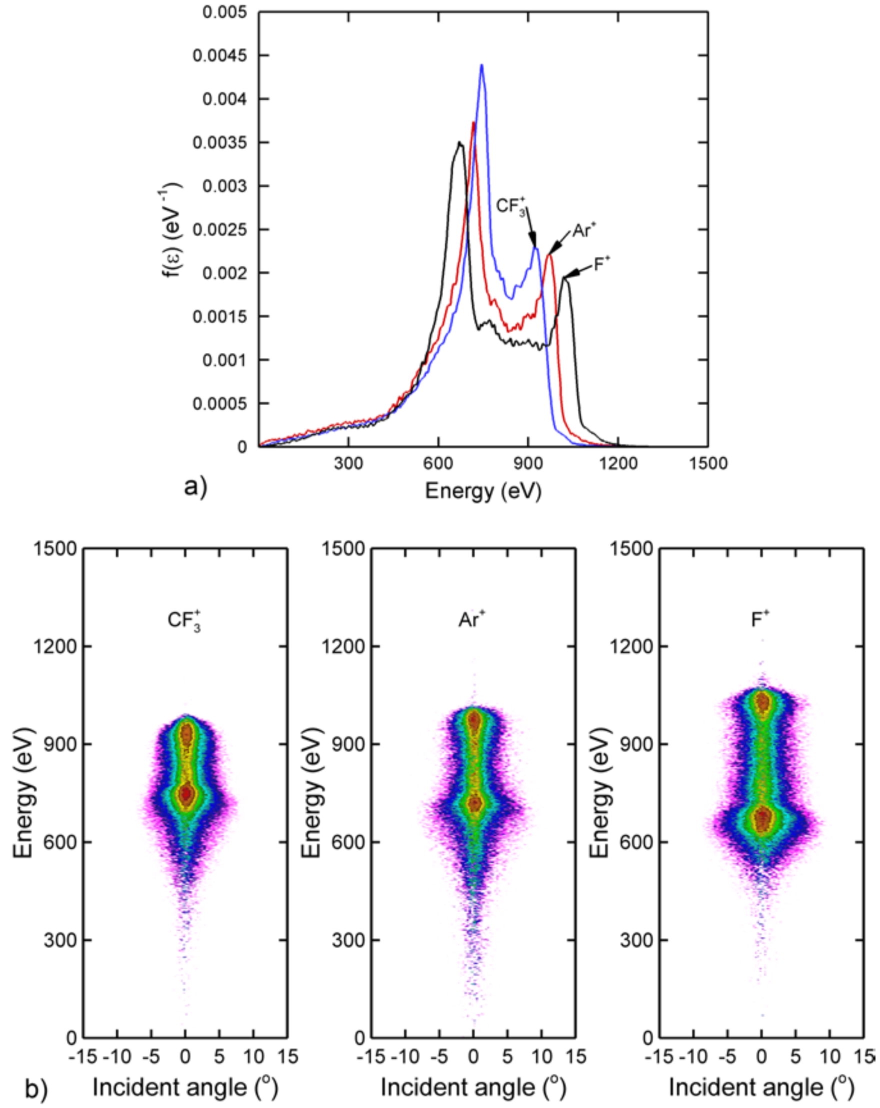

Fig. 6.4 Cycle averaged a) IED and b) IEAD for F$^+$, Ar$^+$ and CF$_3^+$ at base case TF-CCP.

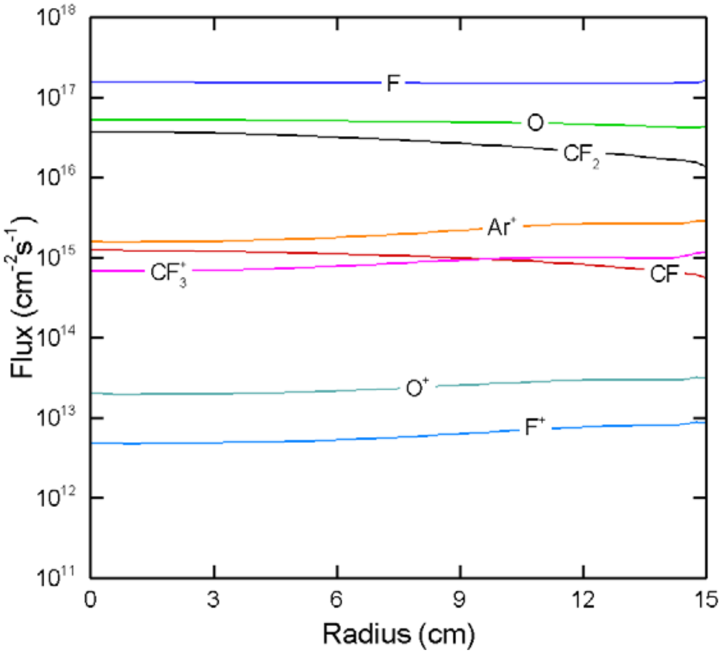

Fig. 6.5 Time-averaged fluxes of major ions and radicals collected on the surface of the wafer for base case TF-CCP.

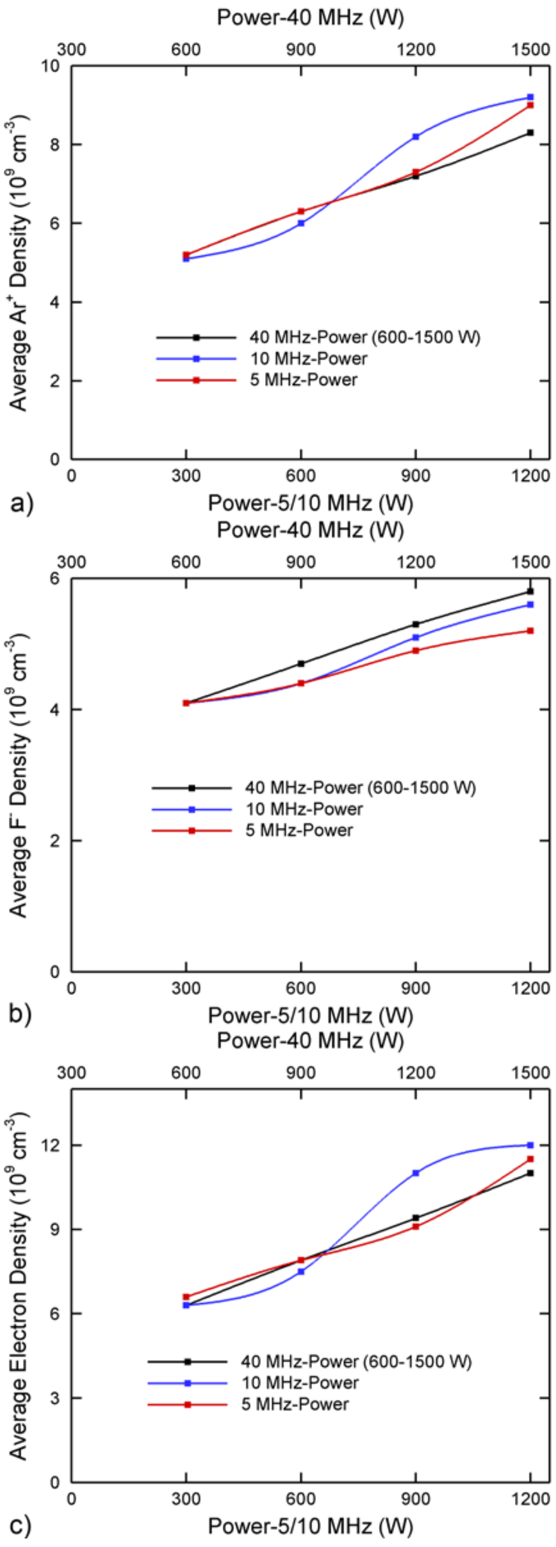

Fig. 6.6 Reactor averaged Ar$^+$, F$^-$ and electron density as a function of power variation at individual frequency.

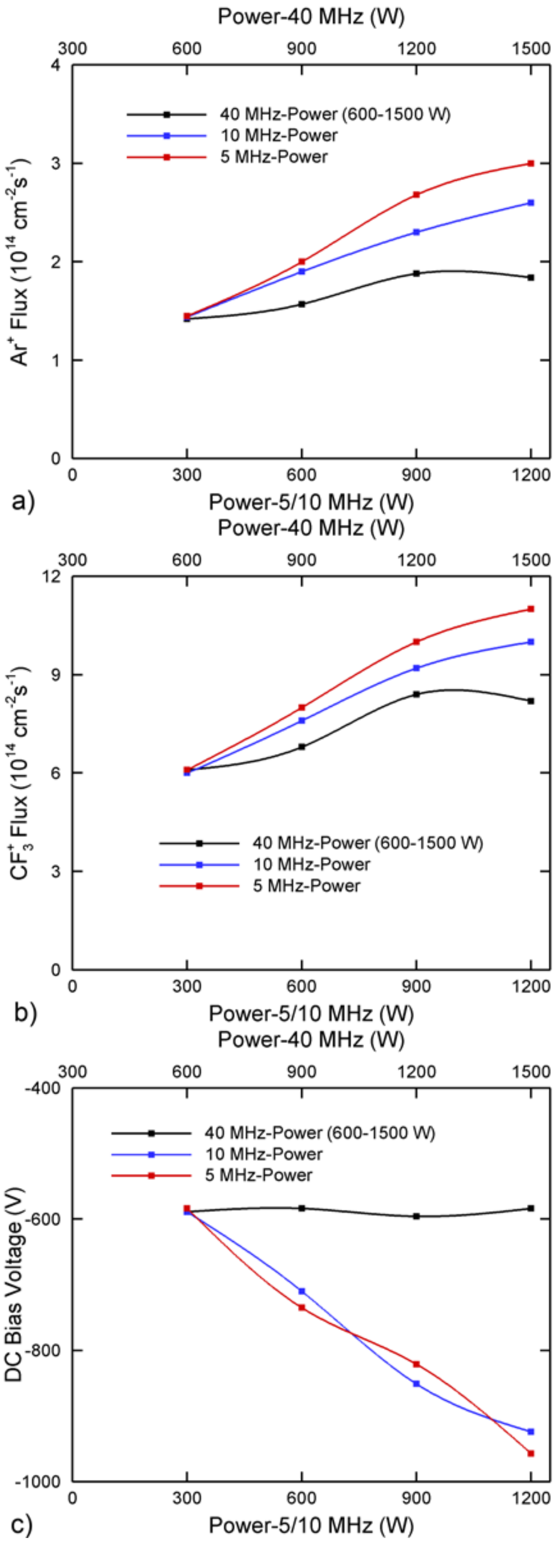

Fig. 6.7 Scaling of Ar^+, CF_3^+ fluxes and dc self-bias voltage as a function of power at individual frequency

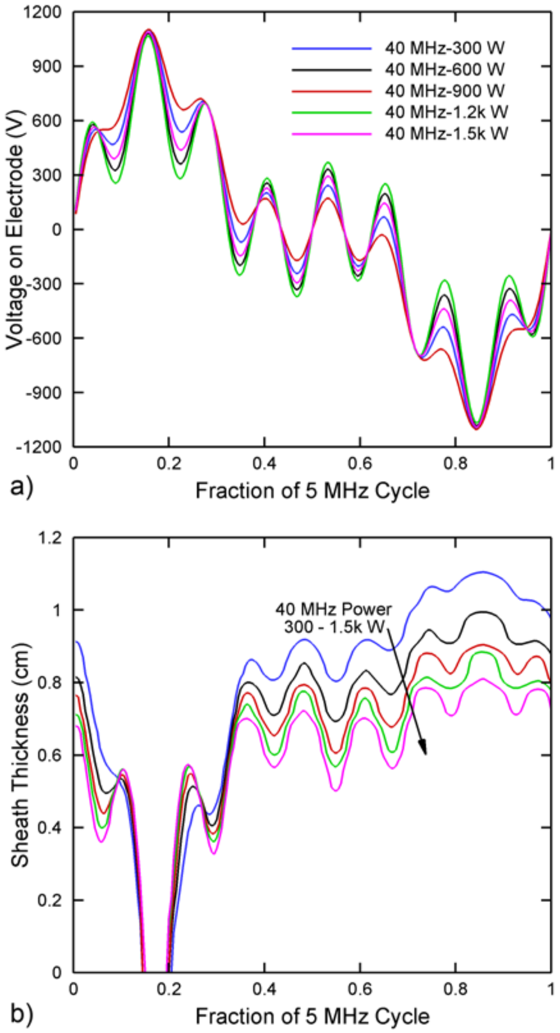

Fig. 6.8 a) Overall applied voltage and b) sheath thickness dynamics of TF-CCP within period of 5 MHz power, as a function of 40 MHz power.

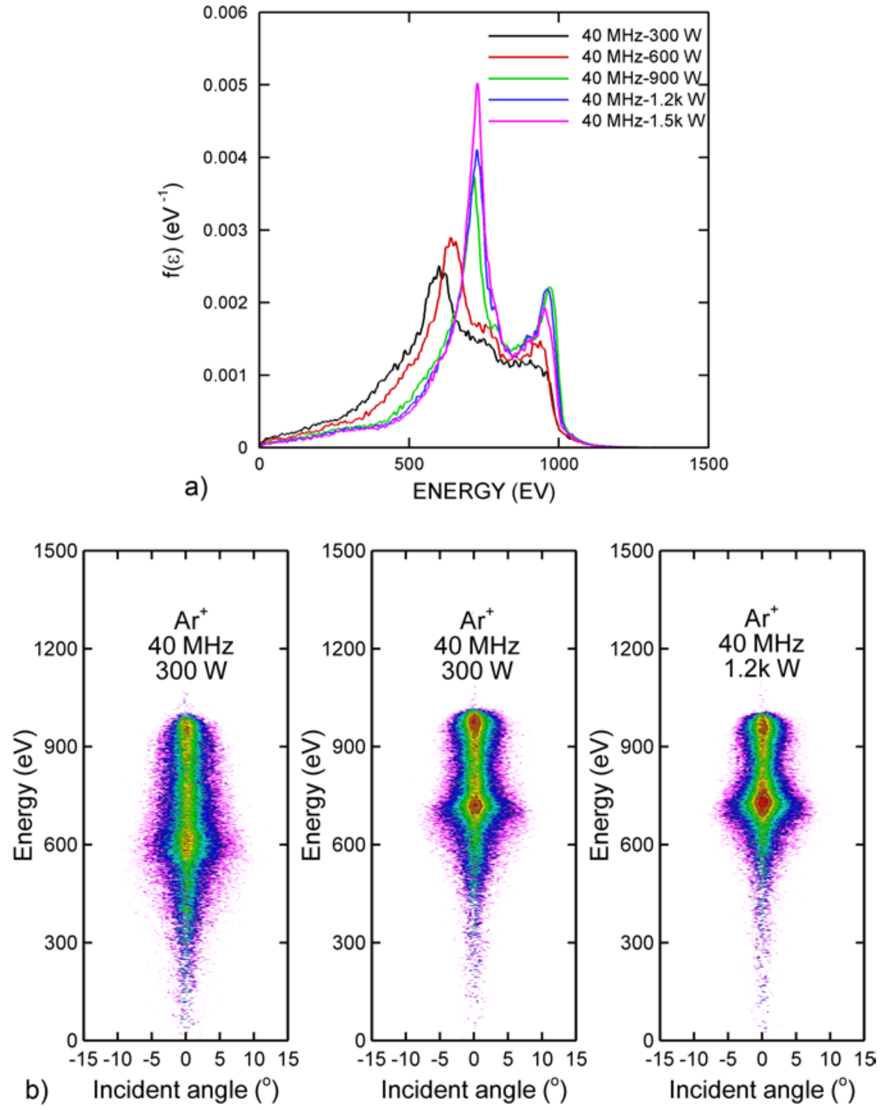

Fig. 6.9 Wafer averaged a) IED and b) IEADs for Ar^+ fluxes as a function of 40 MHz power variation.

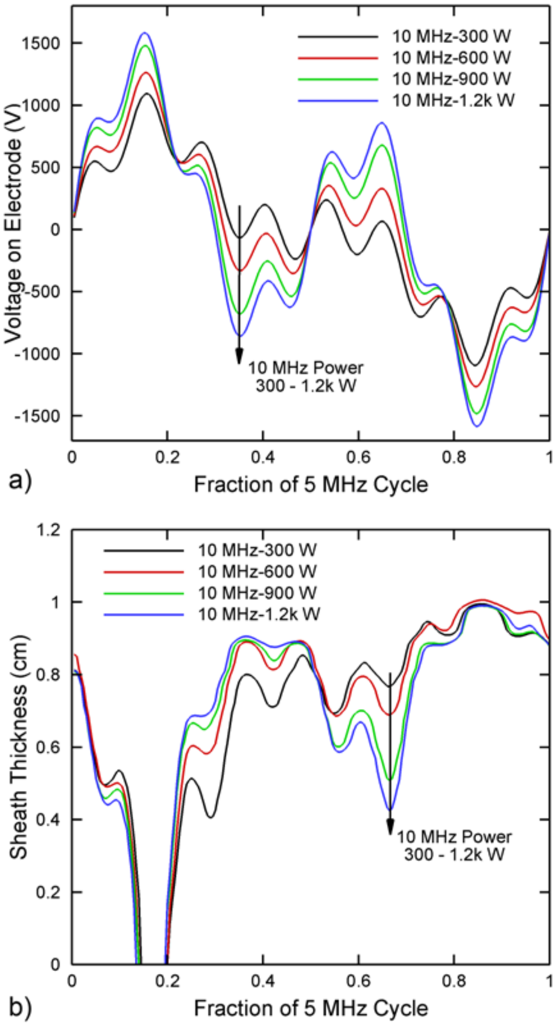

Fig. 6.10 a) Overall applied voltage and b) sheath thickness dynamics of TF-CCP within period of 5 MHz power, as a function of 10 MHz power.

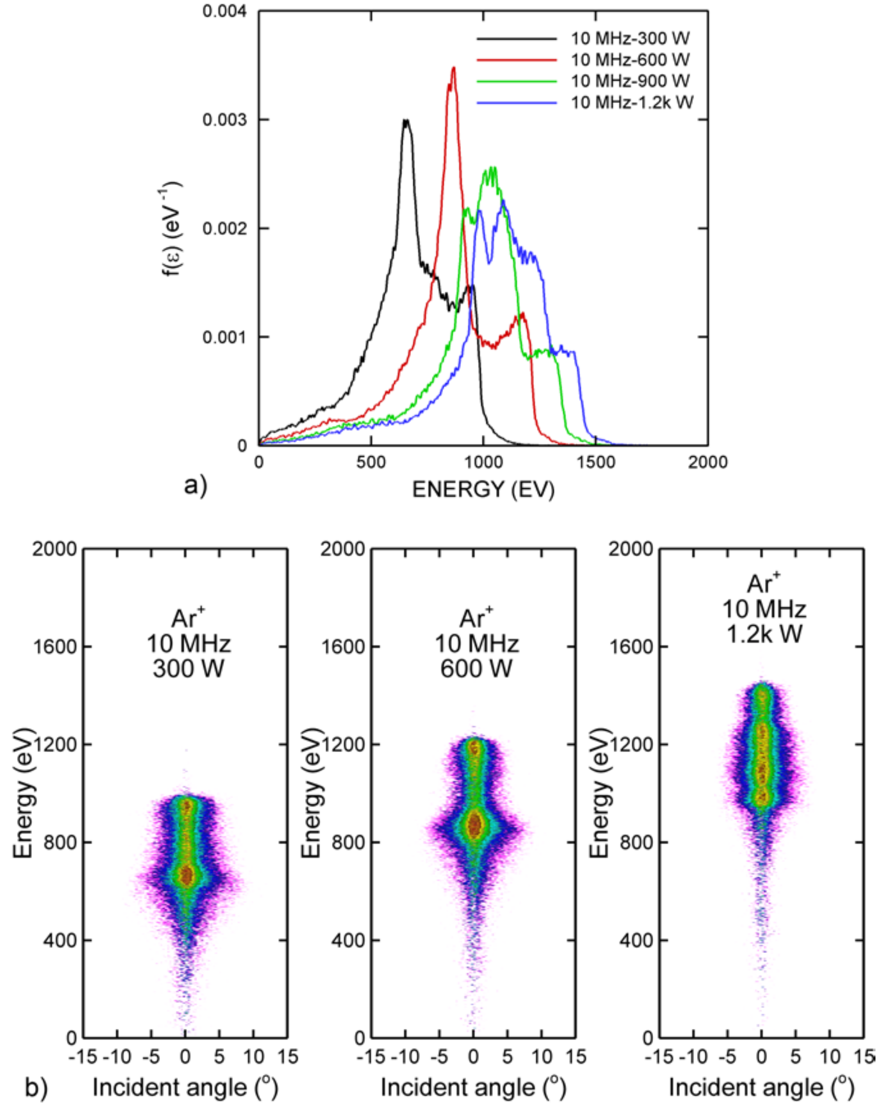

Fig. 6.11 Wafer averaged a) IED and b) IEADs for Ar^+ fluxes as a function of 10 MHz power variation.

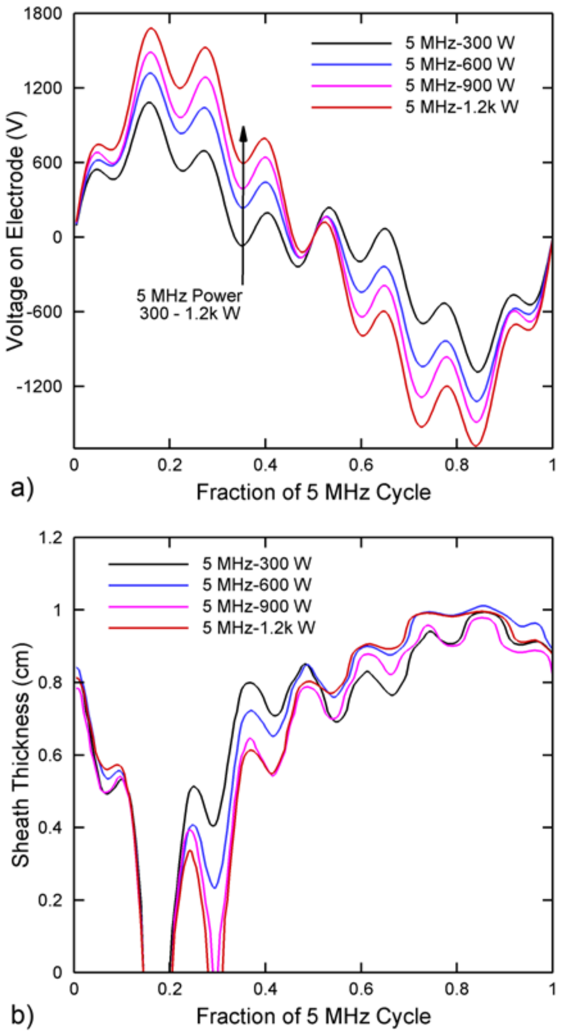

Fig. 6.12 a) Overall applied voltage and b) sheath thickness dynamics of TF-CCP within period of 5 MHz power, as a function of 5 MHz power.

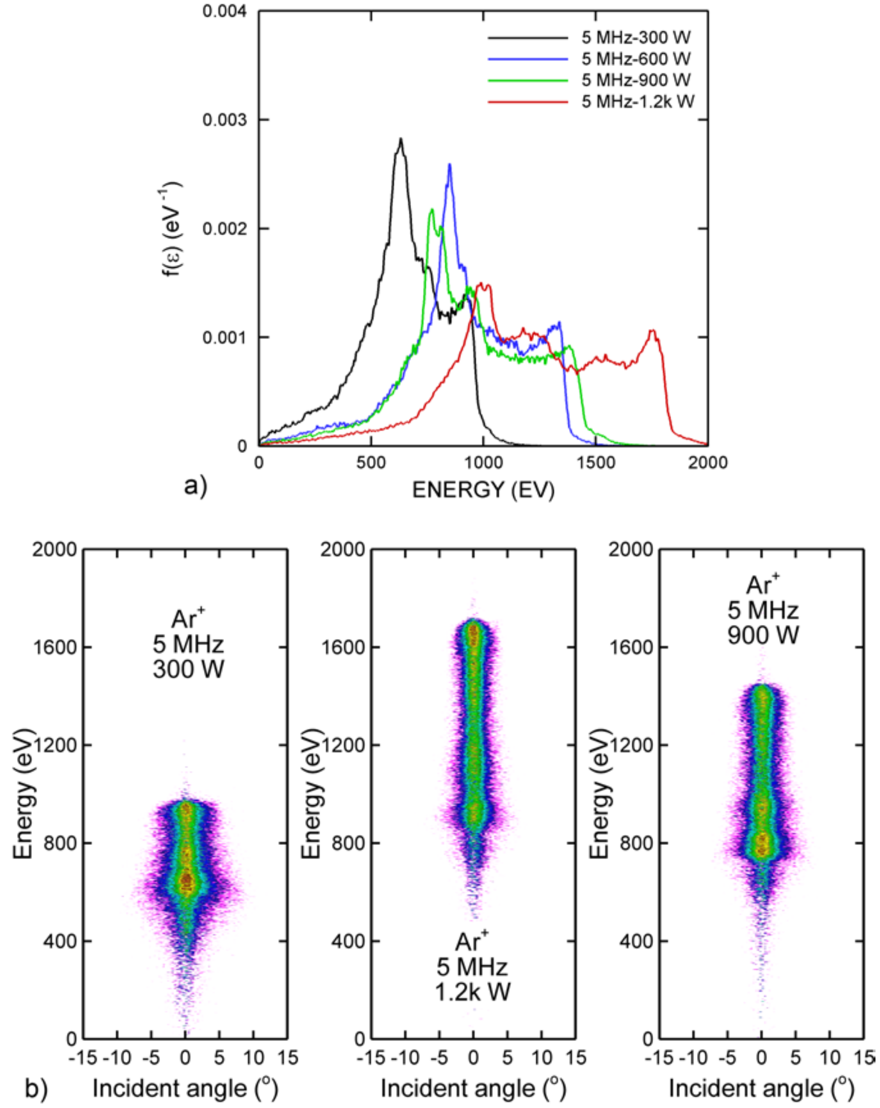

Fig. 6.13 wafer averaged a) IED and b) IEADs for Ar^+ fluxes as a function of 5 MHz power variation.

6.7 References

[1] J. K. Lee, O. V. Manuilenko, N. Y. Babaeva, H. C. Kim, and J. W. Shon, Plasma Sources Sci. Technol. **14**, 89 (2005)

[2] J. Liu, Y.-X. Liu, Z.-H. Bi, F. Gao, and Y.-N. Want, J. Appl. Phys. **115**, 013301 (2014)

[3] H. H. Goto, *et al.*, J. Vac. Sci. Technol. A **10** 3048 (1992)

[4] H. H. Goto, *et al.*, IEEE Trans. Semicond. Manuf. **6**, 58 (1993)

[5] W. Tsai*, et al.,* J. Vac. Sci. Technol. B, **14**, 3276 (1996)

[6] S. Wickramanayaka, *et al.*, Jpn. J. Appl. Phys. **37**, 6193 (1998)

[7] E. Semmler, P. Awakowicz, and A. Keudell, Plasma Sources Sci. Technol. **16**, 839 (2007)

[8] H. C. Kim, J. K. Lee, and J. W. Shon, Physics of Plasmas **10**, 4545 (2003)

[9] P. C. Boyle, A. R. Ellingboe and M. M. Turner, J. Phys. D: Appl. Phys. **37**, 697 (2004)

[10] Z.-H. Bi, Y.-X. Liu, W. Jiang, X. Xu and Y.-N. Wang, Current Applied Physics **11**, S2 (2011)

[11] U. Czarnetzki, B. G. Heil, J. Schulze, Z. Donkó, T. Mussenbrock, and R. P. Brinkmann, Journal of Physics: Conference Series **162**, 012010 (2009)

[12] J. Schulze, E. Schüngel and U. Czarnetzki, J. Phys. D: Appl. Phys. **42**, 092005 (2009)

[13] D. Ziegler, J. Trieschmann, T. Mussenbrock, R. P. Brinkmann, J. Schulze, U. Czarnetzki, E. Semmler, P. Aakowicz, D. O'Connell and T. Gans, Plasma Sources Sci. Technol. **19,** 045001 (2010)

[14] J. Schulze, E. Schüngel, Z. Donkó, and U. Czarnetzki, Plasma Sources Sci. Technol. **20**, 015017 (2011)

[15] J. Shulze, A. Derzsi and Z. Donkó, Plasma Sources Sci. Technol. **20**, 045008 (2011)

[16] I. Korolov, A. Derzsi, Z. Donkó, and J. Schulze, Appl. Phys. Lett. **103**, 064102 (2013)

[17] S. Bienholz, T. Styrnoll and P. Awakowicz, J. Phys. D: Appl. Phys. **47**, 065201 (2014)

[18] T. Lafleur and J. P. Booth, Appl. Phys. Lett. **102**, 154104 (2013)

[19] T. Lafleur, P. A. Delattre, E. V. Johnson and J. P. Booth, Appl. Phys. Lett. **101**, 124104 (2012)

[20] Q.-Z. Zhang, W. Jiang, L.-J. Hou, and Y.-N. Wang, J. Appl. Phys. **109**, 013308 (2011)

[21] B. Bruneau, T. Novikova, T. Lafleur, J. P. Booth and E. V. Johnson, Plasma Sources Sci. Technol. **23**, 065010 (2014)

[22] P.-A. Delattre, T. Lafleur, E. Johnson and J. P. Booth, J. Phys. D: Appl. Phys. **46**, 235201 (2013)

[23] Y. Zhang, A. Zafar, D. J. Coumou, S. C. Shannon and M. J. Kushner, J. Appl. Phys. **117**, 233302 (2015)

[24] A. V. Vasenkov, X. Li, G. S. Oehrlein and M. J. Kushner, J. Vac. Sci. Technol. A **22**, 511 (2004)

CHAPTER 7 PROPERTIES OF MICROPLASMAS EXCITED BY MICROWAVES FOR VUV PHOTON SOURCES

7.1 Introduction

Microplasma sources, plasmas having sizes of < 1 mm, typically leverage pd (pressure × dimension) scaling to achieve their small size.[1-4] By operating at higher pressures up to 1 atm, smaller dimensions are enabled. However, in many applications, microplasma-sized sources are required at lower pressures, a few Torr or less. Operating in this regime is problematic due to the high rate of diffusion loss which must then be balanced by a high specific power deposition. These plasma sources are also difficult to ignite and to sustain. An example of low pressure microplasmas is their use as an ionization source for chemical analysis. In this technology, the microplasma produces vacuum-ultraviolet (VUV) radiation which then selectively ionizes or dissociates the analyte at the entrance of a mass spectrometer or gas detector.[5] By using different gas mixtures (for example, different rare gases) in the microplasma discretely different VUV wavelengths can be produced. For example, a microplasma was used to produce VUV radiation as the fragmentation and ionization source for a high resolution time-of-flight mass spectrometer.[6]. The microplasma was separately operated in Ar, Kr and Xe, producing VUV photons having energies of 11.6/11.8 eV, 10.0/10.6 eV and 8.4/9.6 eV. With this tunability of the energy of the ionization and fragmentation source by the choice of source gas, different sensitivities were produced in detecting various aromatic molecules.

The small size of the low-pressure microplasma devices, typically a few hundred microns, motivates the use of high excitation frequencies to limit the rate of loss of electrons and ions by drift in the electric field. In one configuration, a split-ring resonator operated at 2.45 GHz is used to create a large voltage across an electrode gap of a few hundred microns. [7-9] The use of arrays of split ring resonators to produce high pressure (up to atmospheric) microplasmas has been demonstrated by Hopwood et al.[10,11]. The low pressure device operates in a cavity having typical dimensions of a few hundred microns to 1 mm wide with a length of up to 1 cm. Two parallel electrodes terminating the split ring are aligned with the long dimension of the microcavity. Flow rates of rare gases and rare gas mixtures of 1-10 sccm produce pressures of several Torr inside the cavity. A small hole produces a gas plume containing ions and metastable atoms, and is also the aperture for the VUV emission. With a power of 4 W in a few Torr of argon, metastable Ar($1s_5$) densities exceeding 10^{12} cm^{-3} were measured in the plume.[9] VUV photon fluxes in excess of 10^{14} cm^{-2}s^{-1} were also measured.

In this chapter, we report on results from a computational investigation of the plasma properties and VUV emission, and experimental measurements of excited state densities, in microwave excited microplasma devices sustained in argon and helium/argon mixtures. The configuration investigated is similar to that used for ionization sources for chemical analysis.[7-9] We found that the microplasma devices (MPDs) convert power deposited into the plasma into VUV emission with efficiencies of a few percent at low power deposition. In order to sustain the plasma at small values of pd, the excited state density must be large enough to take advantage of the efficiencies afforded by multi-step ionization. These conditions then lead to a near thermal equilibrium of the excited state densities with the electron temperature. The end result is a saturation in VUV emission with increasing power. The model and experimental techniques used in this investigation are discussed in Secs. II and III, followed by a discussion of plasma properties of the MPDs in Sec. IV. Our concluding remarks are in Sec. V.

7.2 Description of the Model

The model used in this investigation is the Hybrid Plasma Equipment Model (HPEM), which is described in detail in chapter 2. The HPEM is a modular simulator which captures different physical phenomena into modules and exchanges information between those modules. In this study, the modules of the HPEM utilized are the Electron Energy Transport Module (EETM), Fluid Kinetics-Poisson Module (FKPM), Radiation Transport Module (RTMCM) and the Plasma Chemistry Monte Carlo Module (PCMCM).

The densities of all charged and neutral species, and the electric potential, are obtained from the FKM. Continuity, momentum and energy equations are integrated in time for all heavy particles (ions and neutrals). The electron density is obtained from integrating a continuity equation with fluxes provided by the Sharffeter-Gummel formulation which analytically provides the appropriate upwind fluxes depending on the sign of the local velocity. In this technique, for positive velocities contributions to the local change in density are provided by fluxes from the left of the cell. For negative velocities, contributions to the local change in density are provided by fluxes from the right of the cell. The pressure inside the cavity, measured at the location of the pressure sensor in Fig. 1, is held constant by adjusting the gas flow speed. The electric potential is obtained by solution of Poisson's equation using a semi-implicit technique assuming all potentials are electrostatic. Charge densities on surfaces are computed as being due to the fluxes of electrons and ions from the bulk plasma, secondary electrons leaving the surface and secondary electrons from other locations collected by those surfaces. All spatial derivatives are couched in finite-volume form. Acceleration techniques are used to speed the convergence of the simulation. The electron Monte Carlo Simulation (eMCS) within the EETM is used to derive electron energy distributions (EEDs) for both bulk electrons and for the transport of sheath accelerated beam electrons. The eMCS is also used to compute separate electron impact source functions resulting from secondary electrons emitted from surfaces. The secondary electrons are produced by fluxes of ions, excited states and photons. The fluxes of ions and excited states are obtained from the FKPM. The fluxes of photons are obtained from the RTMCM. Secondary electrons that fall in energy below ≈4 eV are removed from the eMCS and are used as source functions in the bulk electron continuity equation. Secondary electrons that are collected on surfaces are included as sources of negative charge. Radiation transport is then addressed using RTMCM as described in chapter 2.

The simulation proceeds by integrating for 4 ns (or 10 microwave cycles) in the FKPM, followed by a call to the RTMCM and the EETM. Within the EETM, electron trajectories are followed for 10 ns (or 25 microwave cycles). Since in this case we desire a periodic steady state, it is not necessary for the integration time to be the same in the different modules. This exchange between modules is performed for 200 iterations with acceleration being performed twice per iteration for the first 100 iterations for ions and for the first 190 iterations for neutrals.

The model for Ar consists of 10 species in addition to electrons: Ar($3p^6$) (ground state argon, also referred to as simply Ar), Ar($1s_5$), Ar($1s_4$), Ar($1s_3$), Ar($1s_2$), Ar(4p), Ar(4d), Ar^+, Ar_2^*, Ar_2^+. (In Racah notation, the first 4 excited states are, in order, Ar($4s[3/2]_2$), Ar($4s[3/2]_1$), Ar($4s[1/2]_0$), Ar($4s[1/2]_1$).) The Ar(4p) state is an effective lumped state representing Ar(4p,3d,5s,5p). The Ar(4d) state is an effective lumped state representing Ar(4d,6s,Rydberg).[18] The reaction mechanism is listed in the Appendix A. The two resonance transitions Ar($1s_4$) → Ar($3p^6$) (106.7 nm) and Ar($1s_2$) → Ar($3p^6$) (104.8 nm), and the excimer radiation $Ar_2^* \rightarrow 2Ar$ (121 nm) are tracked in the RTM. The secondary electron emission coefficients from all surfaces are: 0.1 for ions, 0.03 for excited states and 0.01 for photons.

Mixtures of Ar/He were also investigated. The reaction mechanism for He/Ar mixtures has the following additional species: He, He(2^3S), He(2^1S), He(2^3P), He(2^1P), He(3s), He(3p) and He^+. He(3p) is a lumped state of all higher states. Emission from He(2^1P) → He (59.1 nm) is additionally considered in RTM. The reaction mechanism for He/Ar mixtures is also listed in the Appendix C.

7.3 Description of the Experiment

Laser diode absorption spectroscopy was used to measure the column densities of Ar($1s_3$). The experimental technique is described in Ref. [9]. A laser diode from Sacher Lasertechnik emitting at 794.8 nm is directed through the MPD cavity through two holes and directed perpendicular to the electrodes. The laser has roughly a 1 nm tuning range around its center wavelength. The laser being used is mounted on a commercial laser head (TEC-052) and is driven by a laser current and temperature controller (Pilot PC 0500). The laser, having a linewidth of 0.01 pm, is tuned to measure the absorption of the Ar($1s_3$) → Ar($2p_4$) transition. A beam splitter diverts half of the laser intensity into a Fabry-Perot interferometer (free spectral range of 1.5 GHz, finesse < 200, resolution < 7.5MHz), which is used to accurately calibrate the relative wavelength. The remainder of the beam is coupled to a single mode optical fiber. The output end of the fiber is mounted to a translation stage for alignment with the MPD. A lens, also mounted to the translation stage, focuses the beam to a 200 μm beam waist and this is the limit of the spatial resolution of this measurement.

Laser light was directed through holes in the MPD cavity made in the top roof and bottom substrate approximately at the mid-point along the axis. Measurements were made with the MPD mounted in a vacuum chamber. Laser light transmitted through the MPD cavity is detected with a Si photodetector. A neutral density filter is used to avoid pumping saturation effects. The signals of the interferometer and photo detector are acquired simultaneously and recorded by LabVIEW data acquisition software. More than 100 scans of each signal are accumulated and averaged to improve the signal to noise ratio. The absorption of the beam is measured and related to the absorption density by the Beer-Lampert law as described in Ref. [9]. The measurement provides a column density (atoms/cm^2) of the population difference between the Ar(1s$_3$) and Ar(2p$_4$) states. In interpreting the experimental data, we assumed that the density of the Ar(1s$_3$) is much greater than that of the Ar(2p$_4$).

7.4 Microplasma Characteristics

A schematic of the experimental device and the model geometry for the MPD are shown in Fig. 1. The microplasma cavity is made of alumina ($\varepsilon/\varepsilon_0 = 9$) having a wall thickness of 230 μm. The inside dimensions of the cavity are 1.5 mm wide × 0.75 mm tall × 6 mm deep. The model, being 2-dimensional, does not resolve the full complexity of the MPD device. In the experimental device, the gas enters in through a channel between the bottom of the substrate to the bottom of the MPD cavity in the front of the device. The gas exits through a hole in the back wall of the MPD cavity. The electrodes are parallel to the long dimension, on the bottom of the MPD device. The model resolves the plane perpendicular to the long axis of the MPD in Cartesian coordinates without any axes of symmetry. The gas inlet in the model is at the bottom with a width of 230 μm and gas is exhausted out a nozzle on the top having the same width. The top boundary of the computational domain is the pump port and the plane upon which photon fluxes are collected to characterize the VUV output of the MPD. This surface will be referred to as the *top collection surface* in the remainder of the chapter. The electrodes are 300 μm wide and are covered by quartz 30 μm thick. Since the actual thickness of the quartz is not resolved in the model, the dielectric constant of the overlying material is adjusted so that the capacitance of the dielectric covering the electrodes is the same as in the experiment. The outer boundary of the mesh is electrically grounded.

Since the inside surfaces of the microplasma cavity quickly charge and steady state conditions are being simulated, the proximity of the ground plane on the outside of the MPD does not affect the final plasma characteristics. This was verified by changing the capacitance (effective distance) between the microplasma cavity and the ground plane by changing the dielectric constant of the MPD walls. The depth of the MPD, 6 mm, only enters into the calculation in computing flow rates and power deposition where the total volume of the device is required, and in radiation transport where photons moving along the axis of the MPD striking the end walls are removed. An important distinction between the experimental MPD, as in Ref. [9], and the 2-d approximation here is the location of the gas inlet and nozzle. In the experimental MPD, the gas is injected through a hole in the bottom of the device. The hole for gas exit and VUV emission is in the end wall. In the model, the gas exits from the top along the entire axis of the MPD.

Voltage of equal amplitude is specified on the electrodes, 180 degrees out of phase. As such, the MPD appears to be a capacitive discharge in a push-pull configuration. The power deposition by each electrode is computed as a time average of the product of voltage and current, and the amplitude of the voltage is adjusted to deliver the desired power. These computations are done independently for each electrode assuming that half the power is deposited by each electrode. The base case operating conditions are a pressure of 4 Torr, power of 2 W and a nominal flow rate of 4 sccm. The flow rate is adjusted to provide the desired pressure as measured adjacent to the gas inlet port (as shown in Fig. 1.) For computational convenience, the applied voltages are at a frequency of 2.5 GHz though in the experiment the frequency is 2.45 GHz. The voltage amplitude on each electrode to deliver 2 W in this base case is 17.9 V.

7.4.1 Plasma Properties and Optical Emission in Ar Microplasmas

The cycle averaged electron and ion densities are shown in Fig. 2. The electron temperature (T_e), ionization sources from bulk electrons (S_e) and ionization sources from sheath accelerated secondary electrons from surfaces (S_{sec}) are shown in Fig. 3. The densities of the lowest metastable, Ar($1s_5$), lowest radiative state Ar($1s_4$) and highest excited state Ar(4d) are shown in Fig. 4. The peak electron density is 1×10^{14} cm^{-3} providing a peak partial ionization of about 0.2%. In spite of nonuniformities in the electron impact ionization source functions, the electrons have essentially a diffusion dominated profile inside the MPD cavity. The Ar_2^+ density constitutes 25% of the ion density in the center of the cavity. The dominant source of Ar_2^+ at this relatively low density is by associative charge Penning collisions of Ar(4d) with ground state Ar (maximum rate of 1.5×10^{20} cm^{-3}s^{-1}), which proceeds by virtue of the excitation energy of Ar(4d) being greater than the ionization potential of Ar_2^+.[19] Other sources of Ar_2^+ include associative Penning reactions between two excited states (5.6×10^{18} cm^{-3}s^{-1}) and 3-body associative charge exchange (1.2×10^{17} cm^{-3}s^{-1}), whose rates are small in comparison to the associative Penning reaction.

A plasma plume extends through the exit nozzle of the MPD cavity towards the observation plane, with ions being accelerated by the ambipolar electric fields produced by the peak plasma potential of 23 V in the center of the MPD. The axial electric field at the exit of the nozzle is 170 V/cm or an E/N (electric field/gas number density) of 210 Td (1 Td = 10^{-17} V-cm^2). During the transition of ions from the MPD cavity to the collection plane, the dominant ion transitions from Ar^+ to Ar_2^+ due in large part to associative charge exchange. The drift speed of Ar^+ through the nozzle and to the collection plane is 1-2 × 10^5 cm-s^{-1} over a distance of about 1 mm at a time when the electric field is significantly decreasing. A shallow double-layer-like structure develops in the exit of the nozzle.

The electron temperature, T_e, is fairly uniform with values of 2.1-2.2 eV in the MPD cavity with a heating rate dominated by stochastic heating in front of each electrode. This uniform distribution of T_e is a consequence of the high electron thermal conductivity afforded by electron-electron collisions resulting from the high fractional ionization. T_e, decreases to 1.5 eV in the plume extending out the MPD cavity as the electron density decreases and thermal conductivity decreases. Recall that T_e is the average energy across the EED and so is dominated by low energy electrons that are typically below the excitation thresholds, at least from the ground state.

The bulk electron impact ionization rate, S_e, has a large contribution from multi-step ionization. The profile of S_e mirrors that of the lowest metastable state that has the highest density, Ar($1s_5$), as long as the electron temperature is above about 2 eV. The majority of the remainder of the bulk ionization is directly from the ground state. The peak value of ionization by bulk electrons is 1.5×10^{20} cm^{-3} s^{-1}. Although T_e does not significantly change from the cavity to the plume, the tail of the EED does decay in the plume (which is poorly reflected in the value of T_e). The behavior of the EED will be discussed below. The decay of the tail of the EED is reflected in the abrupt cut-off of S_e in the exit nozzle while T_e does not appreciably change. The ionization source due to sheath accelerated secondary electrons, S_{sec}, is maximum in front of each electrode, with peak values of 8×10^{18} cm^{-3} s^{-1}, or about 0.1 that of the bulk electrons. The trajectories of the secondary electrons are generally in the axial direction although there is some pendular motion of the electrons in the MPD cavity. However, due to the push-pull configuration of the electrodes, those sheath accelerated electrons which do reflect from the top interior surface of the MPD cavity also have a high likelihood of being collected by the other electrode. Due to some curvature of the sheath at the corner of the dielectric covering the electrodes and scattering in the gas, a flux of sheath accelerated electrons penetrates through the nozzle, providing a weak ionization source outside the MPD which is shown by the inset to Fig. 3c.

The densities of Ar(1s$_5$), Ar(1s$_4$) and Ar(4d) are shown in Fig. 4. The peak density of Ar(1s$_5$) is 4×10^{13} cm^{-3} in front of the electrodes where excitation by sheath accelerated secondary electrons is maximum and there is some lifting of the tail of the electron energy distribution, $f(\varepsilon)$, of the bulk electrons. The peak density of Ar(1s$_4$) is 2×10^{13} cm^{-3}. The radiation trapping factor for Ar(1s$_4$) in the middle of the cavity is 295 providing an effective lifetime of 2.5 μs. (The trapping factor for Ar(1s$_2$) is 216, providing an effective lifetime of 0.42 μs.) Since the electron impact source functions for these states essentially mirrors that of the ionization, excitation largely occurs inside the MPD cavity. The short lifetime of the radiative state Ar(1s$_4$), even when trapped, restricts its density to be largely inside the cavity where the excitation occurs. This also the case of Ar(4d) which has a maximum density of 1×10^{12} cm^{-3}. The metastable state Ar(1s$_5$) extends as a plume outside the cavity, carried in the advective gas flow that has a speed of 6.5×10^{3} cm^{-}s^{-1} in the middle of the exit nozzle. Since Ar(1s$_5$) and Ar(1s$_4$) are rapidly collisionally mixed, a plume of Ar(1s$_4$) also extends outside the cavity, whereas Ar(4d), which is not rapidly collisionally mixed with Ar(1s$_5$), does not have a significant plume. There is some replenishment of the excited state manifold during the transit in the plume to the collection plane by dissociative recombination of Ar_2^+. This process accounts for about 50% of the excited state production at the top of the exit nozzle.

Infrared laser diode absorption measurements of Ar($1s_5$) densities in a similar MPD device were reported in Ref. [9]. The plume of the experimental MPD device emerges parallel and through the end wall at the end of the pair of electrodes. At the exit of the MPD, the Ar($1s_5$) and Ar($1s_3$) densities (metastable states) were measured as 1×10^{12} cm^{-3} and 3×10^{11} cm^{-3}.[9] The densities predicted by the model are 1.3×10^{12} cm^{-3} and 1.5×10^{11} cm^{-3}.

The average gas temperature in the center of the MPD is 550 K or about 225 K above ambient, and is 580 K adjacent to the electrodes. The majority of gas heating, 50-100 W-cm^{-3}, results from symmetric charge exchange in the presheath above the electrodes. The large surface-to-volume ratio of the MPD moderates the temperature rise through heat conduction to the walls even though there is a temperature-jump boundary condition due to slip.

Cycle averaged $f(\varepsilon)$ are shown along the vertical axis of the MPD and horizontally 100 μm above the electrodes in Fig 5. The $f(\varepsilon)$ as a function of height are 2-temperature distributions with the break-point being approximately at 12 eV, near the threshold energy of 11.6 eV for excitation of Ar($1s_5$). The high fractional ionization and the high rates of electron-electron collisions drives the $f(\varepsilon)$ towards a Maxwellian at lower energies and it is this part of $f(\varepsilon)$ that dominates the value of T_e. The electron density and thermal conductivity at the top of the nozzle and above the cavity are high enough to keep the bulk portion of the $f(\varepsilon)$ essentially Maxwellian. However, the rates of electron-electron collisions are insufficient to populate the tail of $f(\varepsilon)$. So at heights above the opening to the nozzle, the tail of the $f(\varepsilon)$ falls, which accounts for the rapid decrease in the electron impact ionization rate by bulk electrons. The $f(\varepsilon)$ as function of horizontal position above the electrodes are nearly indistinguishable in the bulk of the distribution, with the tail of $f(\varepsilon)$ moderately falling as the wall is approached.

The direction-averaged (or isotropic) VUV fluxes at 104.8 nm from Ar($1s_2$), 106.7 nm from Ar($1s_4$) and at 121 nm from Ar_2* are shown in Fig. 6. (The rays that appear in these figures result from statistically heavy photon pseudoparticles in the simulation. These pseudoparticles represent an unusually large number of photons. These statistically heavy particles result from the photon pseudoparticles being uniformly distributed across the lineshape function.[17]) The intra-cavity VUV flux at 104.8 nm is 3×10^{19} $cm^{-2}s^{-1}$ or an intensity of 56 W-cm^{-2}, which represents a considerable circulating optical intensity. At 106.7 nm, the flux is 1×10^{19} $cm^{-2}s^{-1}$ (or an intensity of 19 W-cm^{-2}). The mean free path at line center for reabsorption of the resonance radiation is about 0.1 μm which results in these lines being heavily trapped even for the small dimensions of the MPD cavity. The large circulating intensity within the cavity is dominantly radiation near line center which transports in a diffusional manner. That is, the quantum of energy represented by the photon is repeatedly emitted and reabsorbed with a mean-free-path about 1/1000 the size of the cavity. The radiation that strikes the wall or escapes through the top nozzle is composed of photons that are emitted in the wings of the lineshape where the mean free path is longer. Even these photons have some probability of reabsorption above the nozzle, which results in some diffusion-like transport. As a result, the resonant photon fluxes above the nozzle are not strictly line-of-sight out of the MPD cavity.

Although the VUV fluxes inside the MPD cavity are large, the photoionization cross sections from all excited states are not large, $\approx 10^{-19}$ cm^2.[20] This small cross section produces a rate of photoionization of 2-4 $\times$ 10^{14} $cm^{-3}s^{-1}$ in the center of the MPD cavity. As a result, the contribution of photoionization of excited states by VUV radiation to the total rate of ionization is small. At low power deposition, 0.5 W, photoionization contributes only 10^{-5} of the total ionization. This contribution drops to 10^{-6} for a power deposition of 5 W, a consequence of the decrease in trapping factor at the higher power. Although the contribution of photoionization is small inside the cavity compared to electron impact ionization, in the periphery of the plume the rate of electron impact ionization falls to small values due to the fall in the tail of $f(\varepsilon)$.while there is still photoionization of the long lived metastable states by the VUV flux emanating from the MPD cavity. Although the absolute magnitude of photoionization in the periphery of the plume is also small, 10^{8} - 10^{10} cm^{-3}s^{-1}, photoionization may be comparable to or exceeding ionization by electron impact in the plume.

The peak random photon flux at 121 nm from Ar_2* is considerably smaller than at the resonance lines, 8×10^{12} cm^{-2}s^{-1} or an intensity of 13 μW-cm^{-2}. This flux is small (despite the fact that the excimer radiation is not optically trapped) due to the much smaller peak density of Ar_2*, 5×10^{7} cm^{-3}, compared with the Ar(1s$_2$) and Ar(1s$_4$) radiative state densities. With the exception of a small amount of absorption from photoionization, the plasma is optically thin for the 121 nm radiation and so the transport of the excimer radiation is basically line-of-sight. There is no recirculation (or diffusional transport) of this radiation within the cavity and the radiation to the collection plane is line of sight from its radiating source.

The VUV intensity (sum of the 104.8 and 106.7 nm intensities) as a function of position on the top collection surface for different microwave powers, and optical line-shape functions for the 104.8 nm [Ar(1s$_2$) $\rightarrow$ Ar(3p^6)] transition are shown in Fig. 7. (The VUV flux is approximately 8×10^{14} cm^{-2}s^{-1} per mW/cm^2.) These data have been smoothed to lessen the statistical noise. The experimentally measured and predicted column densities of Ar(1s$_3$) are shown in Fig. 8. The column densities are the line integrated densities of excited states as measured by absorption spectroscopy. The peak optical powers (sum of the 104.8 and 106.7 nm fluxes) as a function of microwave power are also shown in Fig. 8. The peak VUV fluxes from the model onto the top collection surface in large part result from line of sight emission from the MPD cavity of photons in the wings of the lineshape function. (Line-of-sight from the center of the cavity corresponds to ±0.3 mm from the centerline.) Photons in the wings of the lineshape function have long mean free paths and so are optically thin. The fluxes that arrive at broader angles than line-of-sight from the interior of the MPD cavity result from absorption and re-emission of photons either in the nozzle or outside the cavity. The saturation of VUV emission with increasing power deposition can be severe and, in some cases, the VUV emission may decrease at higher power deposition. For example, relative values of experimentally measured VUV emission from Ar at 104.8 nm and 106.7 nm obtained with a photomultiplier tube are shown in Fig. 8c. The conditions and device for the experimental are similar to that described above – 2.8 Torr, 10 sccm.

The spectra, shown in Fig. 7b, are heavily self-absorbed, an indication of radiation trapping that aligns with the computed radiation trapping factors of 180-400. For a power deposition of 2 W, the gas temperature in the middle of the MPD is 550 K which produces a Doppler width of $\Delta\nu_D$=7.6 GHz, natural broadening of 80 MHz and pressure broadening of 8 MHz. The self-absorbed core of the lineshape function is well represented by the Doppler broadening. For a power deposition of 8 W, the trapping factors for the 106.7 nm [$Ar(1s_4) \rightarrow Ar(3p^6)$] transition having the longer natural lifetime, 8.4 ns, are about 150-160. The trapping factors for the 104.8 nm [$Ar(1s_2) \rightarrow Ar(3p^6)$] transition having the shorter natural lifetime, 2.0 ns, are 220-230. At a power deposition of 0.3 W, the trapping factors are 430-440 for the 106.7 nm transition and 200-210 for the 104.8 nm transition. The marked change in trapping factors is partly due to the change in gas temperature and ground state density. At 0.3 W, the mid-cavity gas temperature is 390 K and ground state absorber density is 9.6×10^{16} cm^{-3}, whereas at 8 W, the mid-cavity gas temperature is 890 K and ground state absorber density is 4.4×10^{16} cm^{-3}. The lower power deposition produces higher trapping factors due to there being a larger absorber density – the ground state. The higher temperature produces a wider Doppler width, $\Delta\nu_D$, that results in a broader self-absorbed core of the lineshape function and more VUV transmission in the wings of the lineshape relative to line center.

The spatially resolved VUV intensities (shown in Fig. 7) saturate with increasing power deposition above about 1 W. The maximum emitted VUV intensities and densities of Ar($1s_3$) as a function of MPD power deposition, shown in Fig. 8, also saturate with power deposition The experimentally measured column densities of Ar($1s_3$) have a small maximum at 1 W and saturate to 2×10^{11} cm^{-2} at higher powers. The predictions of the model show similar saturation with increasing power, with values about two times larger than in the experiment. Considering the 3-dimensional aspects of the experimental MPD that are not addressed in the model, the agreement is fairly good.

Over a range of power deposition of 0.15 to 8 W, the electron temperature is nearly constant – increasing from 1.9 eV at 0.15 W to 2.1 eV at 8 W. The peak electron density increases from 3×10^{13} cm^{-3} at 0.15 W to 2.1×10^{14} cm^{-3} at 8 W and the gas temperature increases from 370 K to nearly 900 K. The saturation in VUV output results, in part, from rarefaction of the gas. As the power increases and the gas temperature increases, the gas rarefies which reduces the density of the ground state and so decreases the maximum available density of radiators. The lower gas density also increases the rate of loss of charged particles by diffusion, which then reduces the rate of excitation of the resonant states by electron impact. However the dominant factor in the saturation of the VUV output is a close coupling of the radiative states Ar(1s$_2$) and Ar(1s$_4$) with the metastable states Ar(1s$_3$) and Ar(1s$_5$). With the high plasma density, even at low power deposition and moderate radiation trapping, Ar(1s$_5$) comes into near equilibrium with the ground state based on the electron temperature. The MPD cavity-averaged density of Ar(1s$_5$) saturates at about 3×10^{13} cm^{-3} at a power of 2 W. (The local thermodynamic equilibrium (LTE) value of the Ar(1s$_5$) density is about 1×10^{14} cm^{-3}.) With increasing power, and plasma density, superelastic and electron impact excitation collisions within the Ar(4s) manifold then drive Ar(1s$_3$) and Ar(1s$_4$) states into near equilibrium with Ar(1s$_5$) which has the largest density. Ar(1s$_3$) and Ar(1s$_4$) are also progressively depleted by multistep ionization.

The voltage amplitudes on the electrodes increase from 9 V at 0.5 W to 37 V at 8 W. These low voltages are enabled by the large densities of excited states that improve efficiency of ionization through multistep ionization. No specific blocking capacitor was included in the circuit model and so the capacitance of the MPD electrode structure and walls serve as the blocking capacitor. Since the electrode configuration is, in principle symmetric, one would not expect large dc biases to develop and nor there to be large currents at the harmonics. The dc bias is negligible and within the noise of the Monte Carlo method. At 2 W, the dominant current is at the 1st harmonic with 1-2% of the current at the 2nd and 3rd harmonics, and 0.5-1% at the 4th and 5th harmonic. The dielectrics on top of the electrodes do charge negatively by up to -24 V at 8 W with respect to the underlying electrodes. This charging is due, in part, to bulk electrons accelerated from the opposite electrode that are collected in the push-pull configuration.

The oscillation of the plasma potential, dynamics of charging and discharging the wall capacitances, and the capacitance of the dielectric layer covering the electrodes result in energetic ion bombardment of the inside surfaces of the MPD cavity. For example, the ion energy distributions for Ar^+ and Ar_2^+ striking the dielectrics on top of the electrodes and averaged over the inside surface of the MPD are shown in Fig. 9 for 1 W and 8 W. Since the excitation frequency is far above the ion response time, the IEDs have only the single peak corresponding to the average sheath potential. The energies of the peaks in the IED for Ar^+ ions striking the inside dielectric surfaces of the MPD cavity are 14-15 eV. These energies correspond to the time averaged floating potential, slightly higher for the 8 W case to reflect the modestly higher T_e at the higher power. The energies of the peak for Ar_2^+ are 16-17 eV. The lower energies for Ar^+ are due to this ion undergoing symmetric charge exchange reactions in the sheath, whereas Ar_2^+ can only undergo elastic collisions. The maximum energies of both ions are 30 eV at 1 W and 40 eV at 8 W. The RC charging time of the sidewalls is sufficiently small, in large part due to the high conductivity of the plasma, that changes in the dielectric constant of the walls has little effect on the plasma and IEDs. The plasma characteristics are nearly independent of the dielectric constant of the walls over a range of ε_r = 2-20.

There are larger disparities in the IEDs between the low and high power cases striking the dielectrics over the electrodes. At 1 W, the energies of the peaks in the IED are 21 and 23 eV for Ar^+ and Ar_2^+, with maximum energies of 50 eV for an amplitude of applied voltage of 13 V. At 8 W, the energies of the peaks in the IED are 43 and 46 eV for Ar^+ and Ar_2^+, with maximum energies of 75 eV, for an amplitude of applied voltage of 27 V. Recall that the density of Ar_2^+ is about 20% of the total ions and the Ar_2^+ flux is about 15% of the total. So in spite of the higher energies of Ar_2^+ ions, the majority of the power delivered to surfaces by ions is from Ar^+.

The agreement between the experiment and the model has some uncertainty due to the model being 2D and there being 3D effects in the experiments. There are also uncertainties in the model due to uncertainties in the rate coefficients in the reaction mechanism. Although an exhaustive sensitivity study was not performed, we did perform a sensitivity study on selected reactions which are known to be important or whose rates coefficients are known to be uncertain. The sensitivity was gauged by the density of Ar($1s_3$) at the center of the MPD cavity for 2 W power deposition. For example, when eliminating photoionization of all excited states, there was no significant change in the density of Ar($1s_3$) – less than 1%. A process that has significant effect on the ionization balance is associative ionization, Ar(4d) + Ar $\rightarrow$ Ar_2^+ + e, with rate coefficient 2.0×10^{-9} $(T_g/300)^{1/2}$ cm3-s^{-1} (T_g is the gas temperature in K).[21] When eliminating this reaction, the Ar($1s_3$) density increases by about 20%. This increase results from a reduction in the impedance of the plasma with the lower rate of ionization, which then requires a higher electron temperature to deliver the desired 2 W. The rate of formation of Ar($1s_3$) then increases with the increase in T_e. The rates of electron and heavy particle collisional mixing of the 4 levels in the Ar(4s) manifold are also somewhat uncertain. (See Ref. [17] for the sources of all such collision rates.) When increasing the heavy particle mixing rate coefficients by a factor of 2, the Ar($1s_3$) density does not significantly change. When increasing the electron impact cross sections for mixing by a factor of 2, the Ar($1s_3$) density increases by 15%. This increase comes at the expense of Ar($1s_5$) whose density decreases with more rapid redistribution of density throughout the Ar(4s).manifold.

7.4.2 He/Ar Gas Mixtures

It is a common practice in optimizing the performance of conventional lighting sources to use gas mixtures. For example, the common fluorescent lamp is typically an Ar/Hg mixture with the Ar fraction being 90-95%. The UV photons that excite the phosphor that produces the visible light are emitted by the Hg atoms. The purpose of the argon is to aid in the impedance matching to the power supply. The electron momentum collision frequency is dominated by the

Ar which has the larger mole fraction. Inelastic electron collisions and power deposition are dominated by the Hg due to the lower threshold energies of its excited states and ion. There is similar motivation to use gas mixtures in microwave excited MPDs since their placement is at the end of a transmission line. Poor impedance matching would result in unwanted reflections on the transmission line. With this motivation, He/Ar gas mixtures were investigated.

The first-order effect of changing gas mixture in the MPD device, here operating at 4 Torr and 2 W, is changing the electron energy distribution, $f(\varepsilon)$. For example, $f(\varepsilon)$ at the center of the MPD are shown in Fig. 10a for Ar/He mixtures with the fraction of Ar from 5% to 99%. The corresponding electron temperatures and densities, and the density of Ar($1s_2$) are in Fig. 10b. The spatial distributions of excited states and plasma density do not appreciably change when varying power with pure argon. These spatial distributions do change when changing mole fraction of Ar in He/Ar. The values shown in Fig. 10 are spatial averages inside the MPD cavity. With small fractions of Ar, the tail of $f(\varepsilon)$ is mildly cut-off at the inelastic threshold for excitation of He($^3S_1$) at 19.8 eV. As the mole fraction of Ar increases upwards from 5%, the energy of the cut-off switches to 11.6 eV, the inelastic threshold for excitation of Ar($1s_5$). This transition has largely occurred by a mole fraction of 30-50% argon. T_e decreases from 3.3 eV at an argon fraction of 5% to 2.2 eV at 50%. Higher mole fractions of Ar produce only a small decrease in T_e, to 2.0 eV at 99%. The average density of Ar($1s_2$) increases from 5×10^{12} cm^{-3} to 8.6×10^{12} cm^{-3} when increasing the Ar fraction from 5-50%, after which there is only a nominal increase. The electron density increases with increasing Ar fraction with less saturation than for the excited state densities.

These results suggest that in the He/Ar mixture, the majority of power deposition is dissipated in Ar by mole fractions of 35-40%. The saturation in the Ar($1s_2$) density and lack of change in *f(ε)* indicate that the losses by inelastic collisions with He are no longer important by this mole fraction. Any power dissipated in He by excitation or ionization is quickly transferred to Ar by Penning and charge exchange collisions. Experimental measurements of the column density of Ar($1s_3$) support this observation. In laser-diode-absorption experiments, the column density of Ar($1s_3$) increased in He/Ar mixtures by only 65% from an argon mole fraction of 10% to pure argon. The model predicts an increase of 40% over this range of mole fraction.

Changing the He/Ar gas mixture also affects radiation transport. For example, the spectra of the 104.8 nm emission from Ar and the 58.4 nm emission from He [He($^1P^0$) $\rightarrow$ He(^1S)], and their trapping factors predicted by the model are shown in Fig. 11. These lineshape functions are produced by the spectrally resolved photon pseudo-particles striking the top collection surface. Increasing the Ar mole fraction increases the optical depth for its resonant transition, thereby increasing the line center absorption which in turn increases trapping factors. This results in more observed emission coming from further in the wings of the lineshape function. The trend is the opposite for He as a decrease in its density reduces the self-absorption at line center and reduces its trapping factor. Some fraction of the reduction in trapping factor results from quenching of the He($^1P^0$) upper level of the 58.4 nm emission by collisions with Ar. The natural radiative lifetime of He($^1P^0$) is 0.56 ns. The rate coefficient for Penning ionization of Ar by He($^1P^0$) at operating temperatures is 10^{-9} cm^3/s.[22,23] For an Ar fraction of 30% at 4 Torr, the lifetime of He($^1P^0$) for Penning reactions is about 40 ns, which is nearly the same as the effective lifetime of the 58.4 nm transition with a trapping factor of 100. So quenching reactions compete with radiative relaxation.

A desirable feature of MPDs for VUV sources is spectral purity. That is, the VUV spectrum is dominated by a single VUV emission line or closely spaced emission lines, as in the case of Ar (104.8, 106.7 nm). The use of gas mixtures introduces the possibility that the VUV spectrum will have emission from both sources. In the case of He/Ar mixtures, the VUV emission has contributions from the 58.4 nm transition in He, and the 104.8 and 106.7 nm transitions in Ar. The VUV intensities from Ar (sum of 104.8 and 106.8 nm transitions) and He incident onto the top collection surface are shown Fig. 12a, and maximum values are shown in Fig. 12b as a function of Ar mole fraction in He/Ar mixtures. The intensities are shown in mW/cm^2. The VUV flux corresponding to 30 mW/cm^2 for emission from argon is 1.6×10^{16} cm^{-2}s^{-1}. The VUV flux for the same intensity of emission from He is 0.9×10^{16} cm^{-2}s^{-1}. For the He/Ar = 95/5 mixture, the VUV power flux from He is 25 mW/cm^2, about 80% that from Ar, 32 mW/cm^2. With increasing Ar mole fraction, the VUV emission from Ar increases to a maximum value of 55 mW/cm^2 for an Ar mole fraction of 20%. At this mole fraction, the He emission has decreased to 1 mW/cm^2. The small decrease in the VUV power from Ar with mole fractions greater than 50% results from the decrease in electron temperature and increase in electron density for these mole fractions. The decrease in T_e reduces the rate coefficient for excitation of the resonant states while the increase in n_e increases the rate of mixing and quenching of the radiating states.

Spectral purity – a spectrum dominated by VUV emission from Ar – is obtained with moderate Ar mole fractions (20-30%). The dramatic decrease in the VUV emission from He has at least two components. The first is the increasingly cut-off electron energy distribution, $f(\varepsilon)$, with increasing Ar mole fraction, as shown in Fig. 10a. From 5% to 30% Ar, the value of $f(\varepsilon)$ at 20 eV, the threshold for excitation of He, decreases by a factor of 100. Note that T_e decreases by only 0.7 eV over this range of Ar mole fraction due, in part, to the efficiency of electron-electron collisions at low energies which maintain a Maxwellian-like distribution. The second factor is the increasing rate of quenching of He excited states by the increasing Ar density which competes with radiative relaxation of the trapped resonance transition.

7.5 Concluding Remarks

Microplasmas sustained by microwave power in rare gases and rare gas mixtures are convenient sources of VUV radiation for use in chemical analysis (e.g., ionization sources for mass spectrometers). The use of microplasmas for these applications typically requires the devices to operate at low pressure, a few Torr. Since the internal dimensions of the devices of interest are hundreds of μm to 1 mm, diffusion losses are large ($pd < 0.1 – 0.2$ Torr-cm). Microwave excitation coupled with fully dielectric internal surfaces are able to sustain plasmas at few Torr with a few Watts of power deposition having plasma densities approaching 10^{14} cm^{-3} with electron temperatures of about 2 eV, values that are not particularly sensitive to power deposition. The resonant and metastable states of, for example, Ar come into a near equilibrium with the electron temperature, which results in the VUV emission saturating with power deposition above a few watts. The VUV fluxes are up to 40 mW/cm^2 a few mm from the aperture of the microplasma cavity. VUV radiation is heavily trapped, producing self-absorbed lineshape functions, which in turn contribute to the radiative states coming into equilibrium. In mixtures of He/Ar, VUV emission from Ar optimized at 15-20% mole fraction of Ar, at which point the majority of power deposition was channeled into the argon and the electron temperature was elevated above the pure Ar discharge. Spectral purity for VUV emission from Ar is greater than 99%.

7.6 Figures

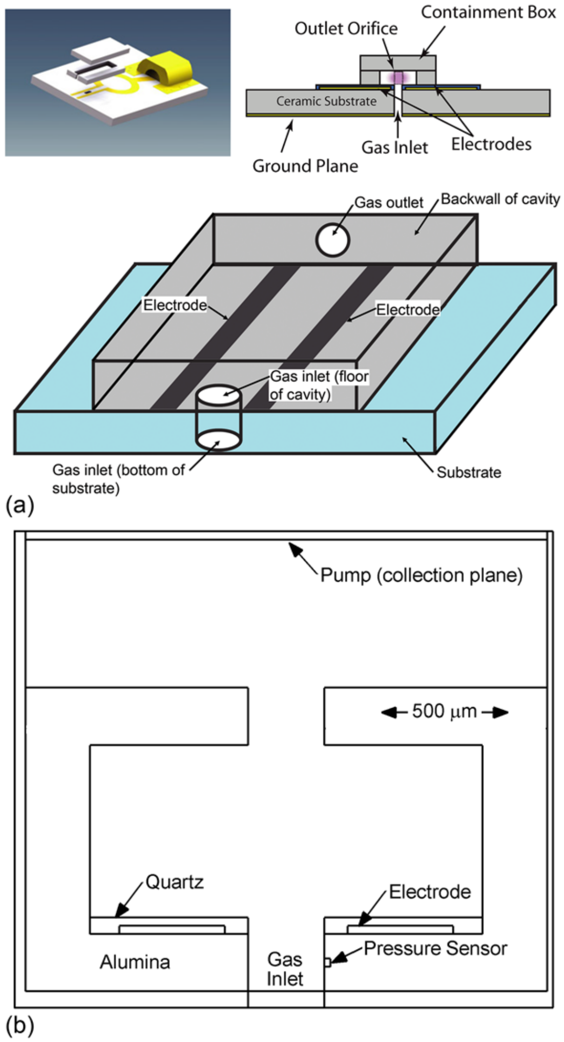

Fig. 7.1 Schematics of the microwave excited, microplasma device. a) Experimental configuration and b) geometry used in the model.

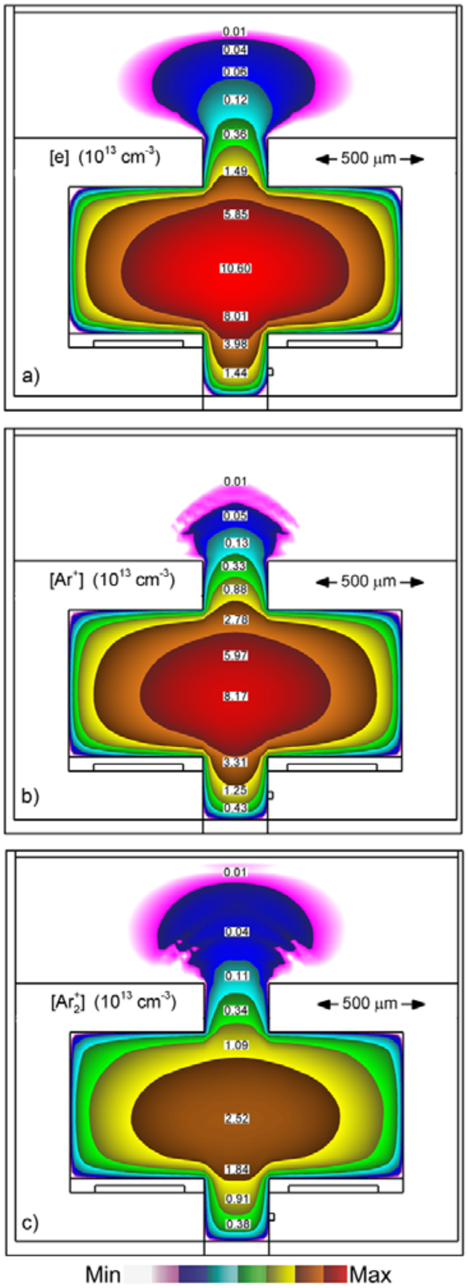

Fig. 7.2 Plasma properties for the base case conditions (Ar, 4 Torr, 2 W, 4 sccm). a) Electron density, b) Ar^+ density and c) Ar_2^+ density. The contour labels have the units indicated in each frame. A plume of plasma extends beyond the aperture.

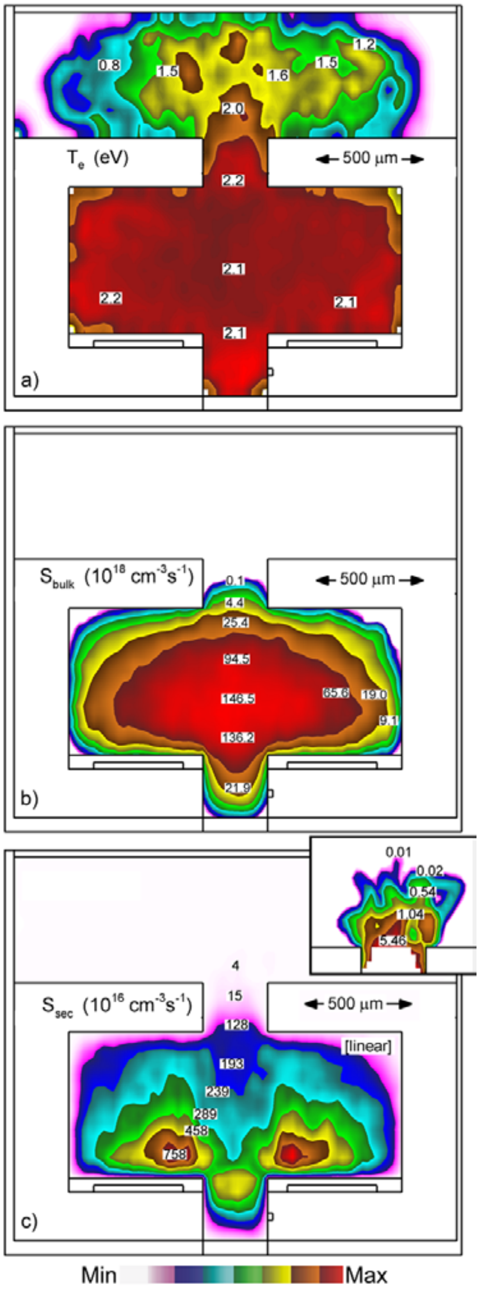

Fig. 7.3 Plasma properties for the base case conditions (Ar, 4 Torr, 2 W, 4 sccm). a) Electron temperature, b) electron impact ionization source by bulk electrons and c) electron impact ionization source by sheath-accelerated secondary electrons. The contour labels have the units indicated in each frame. The bulk ionization source terminates at the aperture due to the decay in the tail of the electron energy distribution. A few high energy secondary electrons scatter out of the aperture.

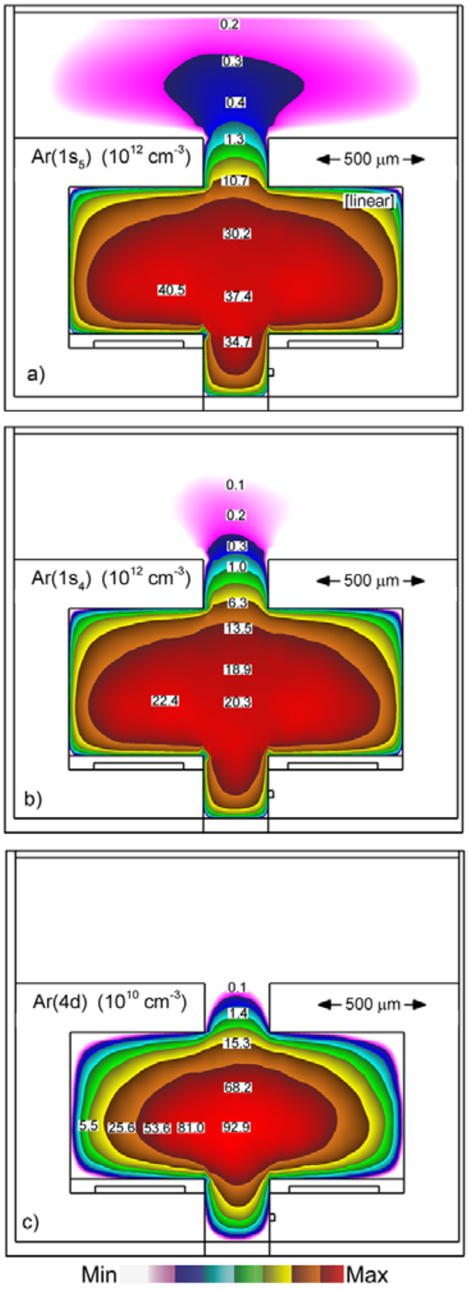

Fig. 7.4 Excited state densities for the base case conditions (Ar, 4 Torr, 2 W, 4 sccm). a) Ar(1s$_5$), b) Ar(1s$_4$) and c) Ar(4d), The contour labels have the units indicated in each frame. The metastable Ar(1s$_5$) produces a plume beyond the microplasma cavity.

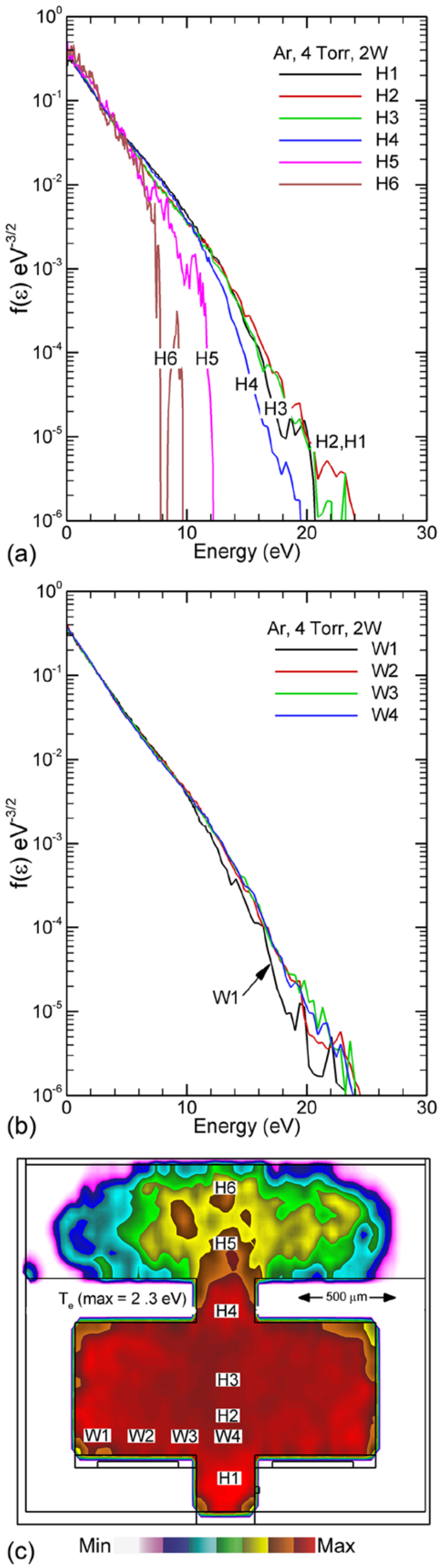

Fig. 7.5 Electron energy distributions for the base case conditions (Ar, 4 Torr, 2 W, 4 sccm) at different locations in the cavity. a) Along the vertical axis and b) horizontally above the electrode. c) The vertical locations where f(ε) are plotted are denoted by Hn and horizontal locations are denoted by Wn on a background of the electron temperature.

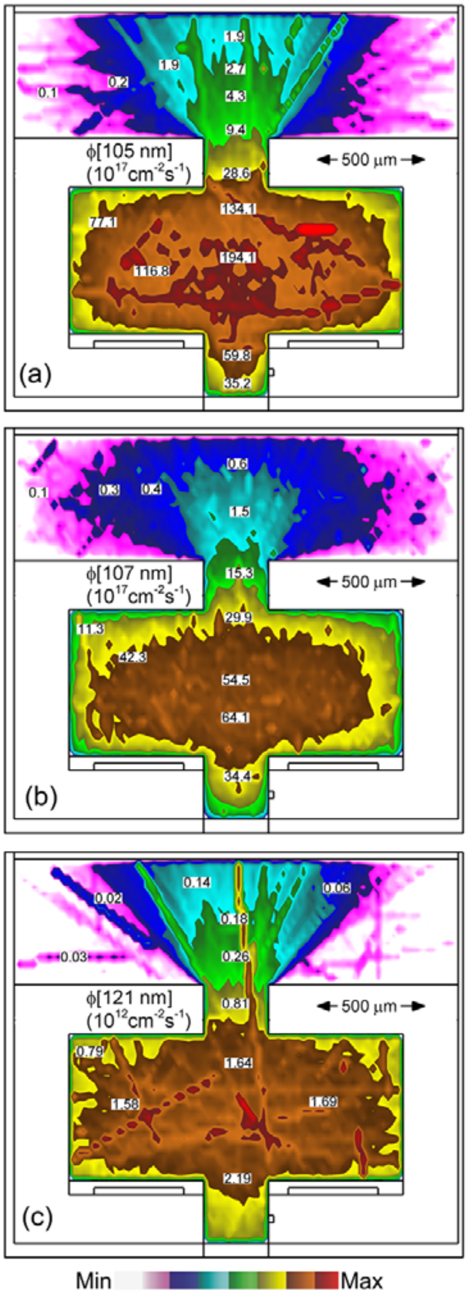

Fig. 7.6 Direction averaged intensity of VUV radiation at a) 104.8 nm, b) 106.7 nm and c) 121 nm.

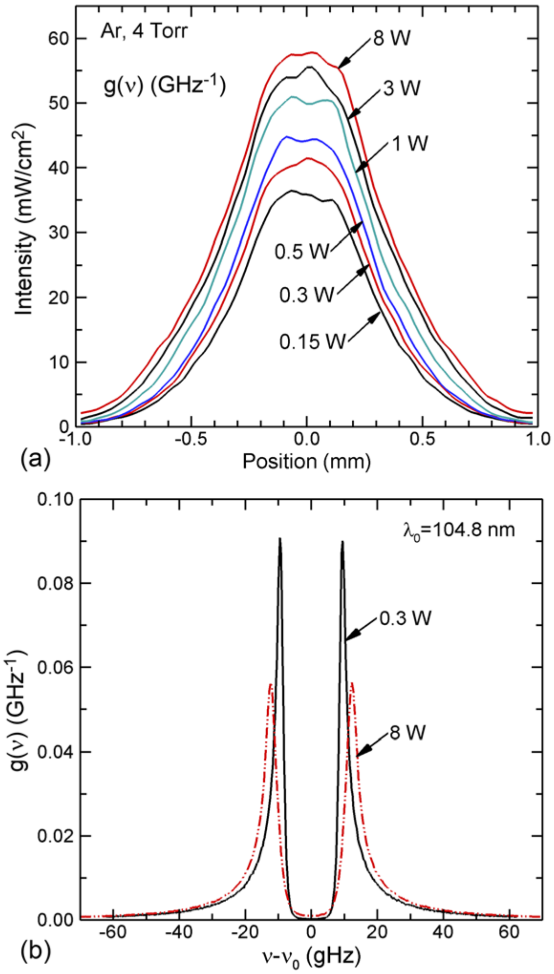

Fig. 7.7 Radiative properties as a function of power deposition for Ar at 4 Torr. a) Sum of the 104.8 nm and 106.7 nm VUV emission incident on the top collection surface. b) Lineshape function for 0.3 and 8 W for 104.8 nm for radiation escaping the plasma.

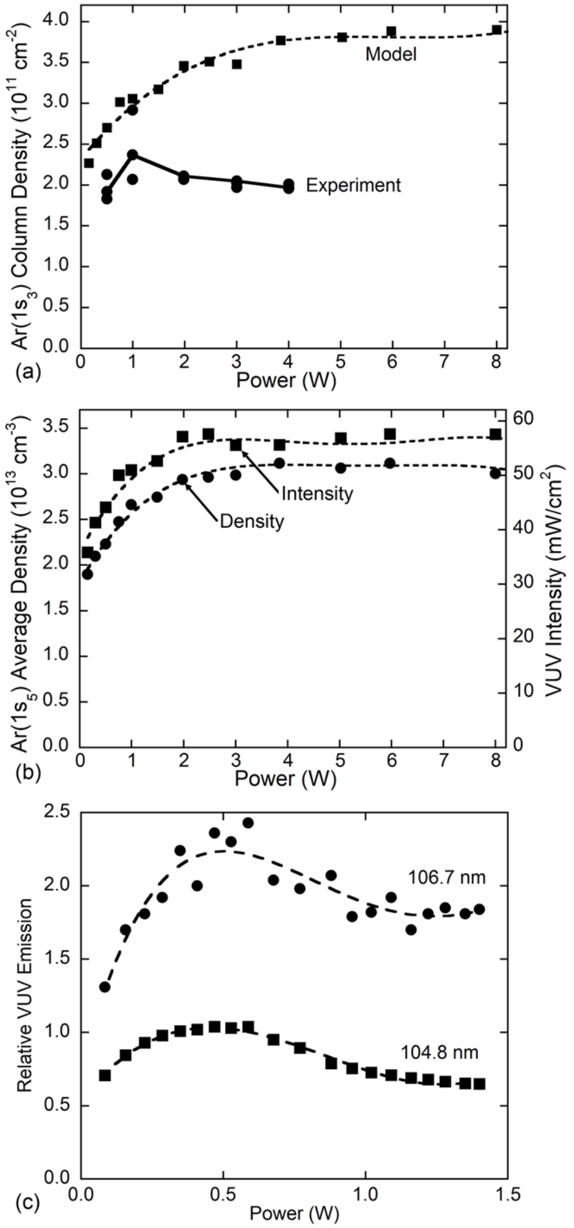

Fig. 7.8 Densities of excited states and VUV emission in the Ar microplasma. a) Column density for Ar(1s$_3$) as a function of power deposition measured by experiment and from the model. b) Model predictions of the Ar(1s$_5$) density and the VUV output intensity as a function of power, and c) experimental relative VUV emission at 104.8 nm and 106.7 nm for similar conditions.

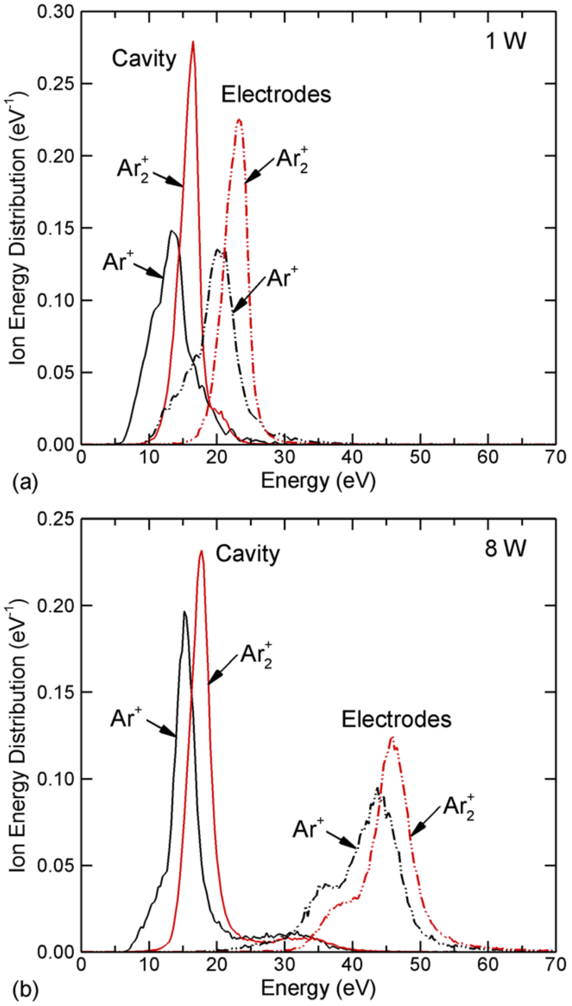

Fig. 7.9 Ion energy distributions incident onto the walls of the microplasma cavity and to the surfaces above the electrodes for Ar discharges. a) 1 W power deposition and b) 8 W.

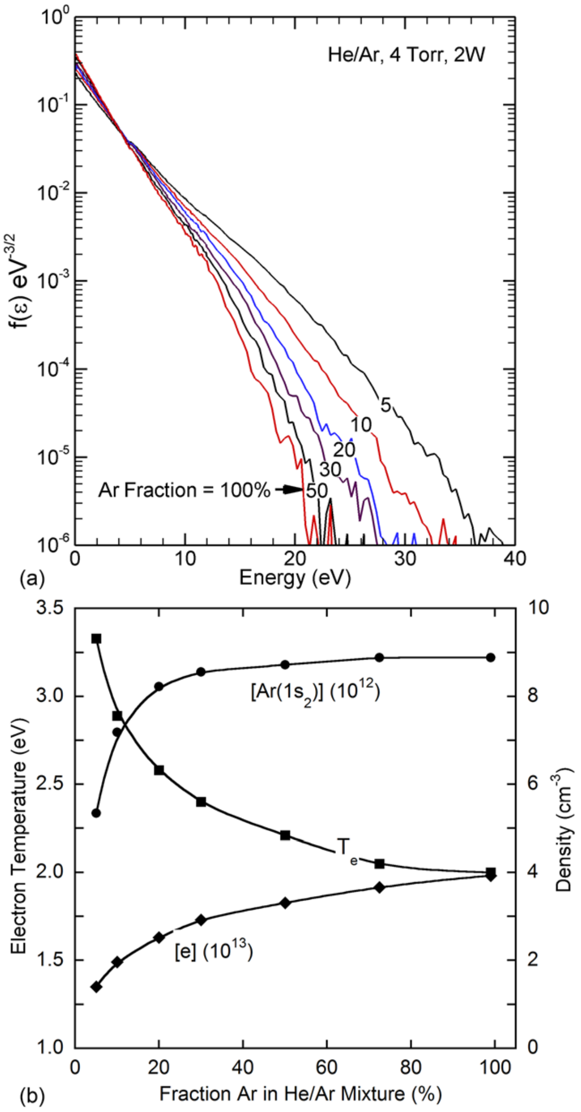

Fig. 7.10 Plasma properties for microplasmas sustained in He/Ar mixtures (4 Torr, 2 W). a) Electron energy distributions in the middle of the microplasma cavity for different Ar fractions. b) Electron temperature, electron density and density of Ar($1s_2$) as a function of Ar fraction.

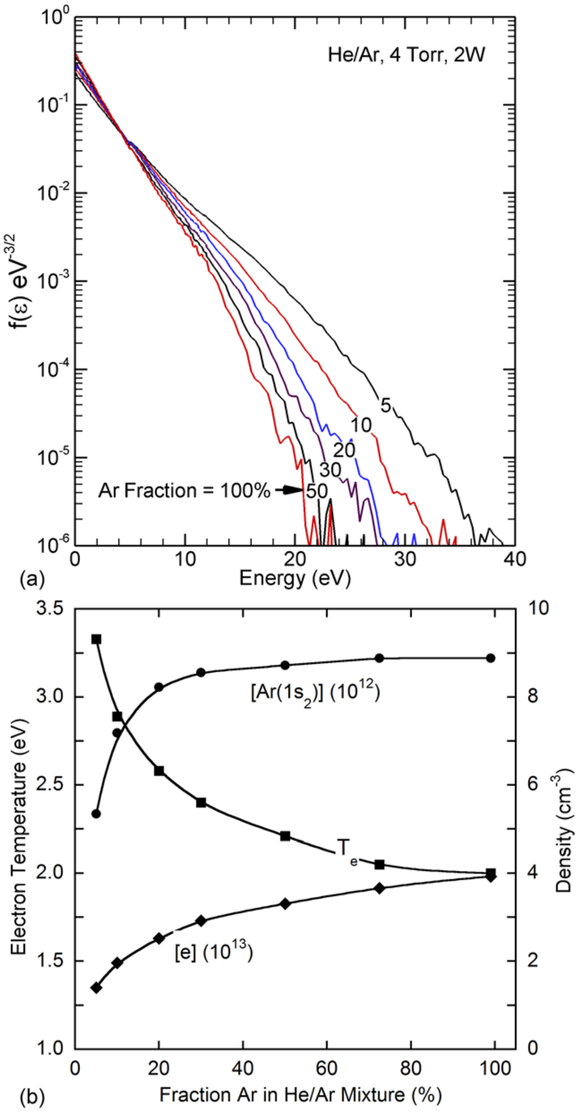

Fig. 7.11 Optical properties for microplasmas sustained in He/Ar mixtures: a) Lineshape functions for resonance radiation from Ar (104.8 nm) and He (58.4 nm) for different He/Ar mixtures. b) Optical trapping factors for Ar (104.8 nm, 106.7 nm) and He (58.4 nm) as a function of Ar fraction.

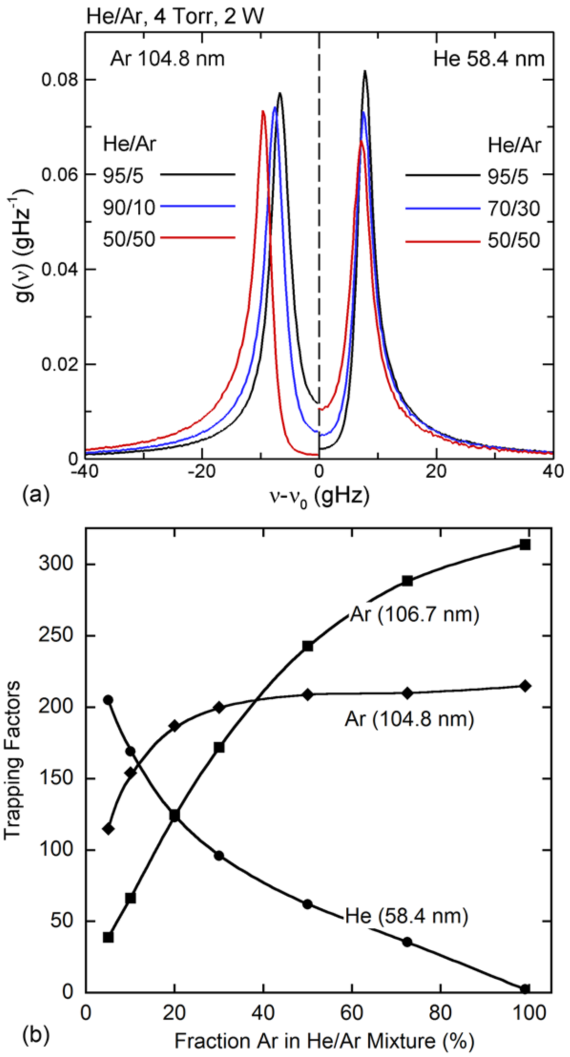

Fig. 7.12 VUV intensities for microplasmas sustained in He/Ar mixtures. a) Spatial profiles of VUV intensities incident on the top collection surface for different He/Ar mixtures, and b) peak VUV intensities striking the top surface as a function of Ar fraction in He/Ar mixtures.

7.7 References

[1] K. H. Becker, K. H. Schoenbach and J. G. Eden, “Microplasmas and Applications”, J. Phys. D: Applied Phys. **39**, R55 (2006).

[2] J. G. Eden and S-J. Park, “Microcavity and Microchannel Plasma: General Characteristics and Emerging Applications”, in M. Bonitz, J. Lopez, K. Becker and H. Thomsen, eds., *Complex Plasmas*, Springer Series on Atomic, Molecular, Optical and Plasma Physics **82**, 373 (2014).

[3] R. Hoskinson and J. Hopwood, “Spatially resolved spectroscopy and electrical characterization of microplasmas and switchable microplasma arrays”, Plasma Source Sci. Technol. **23**, 015024 (2014).

[4] K. H. Becker, H. Kersten, J. Hopwood and J. L. Lopez “Microplasmas: scientific challenges and technological opportunities”, *Eur. Phys. J.* D **60** 437 (2010).

[5] V. Lopez-Avila and M. Zoria, “Identification of methylhexaneamine by GC high-resolution TOFMS and soft ionization”, Forensic Sci. Intl**.** **231**, 113 (2013).

[6] V. Lopez-Avila, J. Cooley, R. Urdahl and M. Theviswill, “Determination of stimulants using gas chromatography/high-resolution time-of-flight mass spectrometry and a soft ionization source”, Rapid. Commun. Mass Spectrom **26**, 2714 (2012).

[7] R. Urdahl, J. E. Cooley, G. S. Lee, A. J. Hidalgo and M. L. Guth, US Patent 8,736,174.

[8] J. Xue, R. S. Urdahl and J. E. Cooley, “Plasma resonances in a microwave-driven microdischarge”, Appl. Phys. Lett. **100**, 064102 (2012).

[9] J. Xue, J. E. Cooley and R. S. Urdahl, “Density of metastable atoms in the plume of a low-pressure argon microplasma”, J. Phys. D **45**, 365201 (2012).

[10] R. Hoskinson and J. Hopwood, “Spatially resolved spectroscopy and electrical

characterization of microplasmas and switchable microplasma arrays”, Plasma Source Sci. Technol. **23**, 015024 (2014).

[11] Wu. A. R. Hoskinson and J. Hopwood, “Stable linear plasma arrays at atmospheric pressure”, Plasma Source Sci. Technol. **20**, 045022 (2011).

[12] M. J. Kushner, “Hybrid Modelling of Low Temperature Plasmas for Fundamental Investigations and Equipment Design", J. Phys. D **42**, 194013 (2009).

[13] S.-H. Song and M. J. Kushner, Plasma Source Sci. Technol. “Control of Electron Energy Distributions and Plasma Characteristics of Dual Frequency, Pulsed Capacitively Coupled Plasmas Sustained in Ar and Ar/CF_4/O_2", **21**, 055028 (2012).

[14] M. T. Herd, J. E. Lawler, and K. L. Menningen, “Radiation trapping of the Hg 254 nm resonance line”, J. Phys. D: Appl. Phys. **38**, 3304 (2005).

[15] J. E. Lawler, and M. G. Raizen, “Enhanced escape rate for Hg 254 nm resonance radiation in fluorescent lamps”, J. Phys. D: Appl. Phys. **46**, 415204 (2013).

[16] G. J. Parker, W. N. G. Hitchon, and J. E. Lawler, “Radiation trapping simulations using the propagator function method: complete and partial frequency redistribution”, J. Phys. B: At. Mol. Opt. Phys. **26**, 4643 (1993).

[17] P. Tian and M. J. Kushner, “Controlling VUV Photon Fluxes in Low Pressure Inductively Coupled Plasmas”, Plasma Source Sci. Technol. **24,** 035206 (2015).

[18] M. Petrov, J. L. Giuliani and A. Dasgupta, “Electron energy deposition in an electron-beam pumped KrF amplifier: Impact of beam power and energy”, J. Appl. Phys. **91**, 2662 (2002).

[19] P. M. Becker and F. W. Lampe, “Mass Spectroscopic Study of the Bimolecular Formation of the Diatomic Argon Ion”, J. Chem. Phys. 42, 3857 (1965).

[20] K. J. McCann, and M. R. Flannery, “Photoionization of metstable rate-gas atoms (He*, Ne*, Ar*, Kr*, Xe*)”, Appl. Phys. Lett. **31**, 599 (1977).

[21] P. M. Becker and F. W. Lampe, J. Chem. Phys. 42, 2857 (1965)

[22] W. Lindinger, A. L. Schmeltekopf, and F. C. Fehsenfeld, “Temperature dependence of de-excitation rate constants of He(2^3 *S*) by Ne, Ar, Xe, H_2, N_2, O_2, NH_3, and CO_2”, J. Chem. Phys. **61**, 2890 (1974).

[23] L. Schmeltekopf, and F. C. Fehsenfeld, “De-excitation Rate Constants for Helium Metastable Atoms with Several Atoms and Molecules”, J. Chem. Phys. **53**, 3173 (1970).

CHAPTER 8 CONCLUSION AND FUTURE WORK

8.1 Summary

Low pressure LTPs have been widely developed for industrial applications. This thesis focused on analyzing the dynamics and controlling fluxes of low pressure LTPs of interest, including ICP, CCP and microwave excited microplasmas. By using a 2-D hybrid hydrodynamic simulation platform, *HPEM*, fundamental understanding has been provided of scaling of those plasmas in the context of semiconductor fabrication and chemical analysis industries. These insights enable further optimization of LTP reactor design for those applications. In this chapter, brief summaries of each chapter are provided along with potential future works.

Chapter 3 discussed the dynamics of a pulsed low pressure ICP with a tunable circuit matching network. Plasma impedance is constantly changing at the beginning of pulse. Therefore a fixed matching network will always cause mismatch and power reflection in a pulsed ICP. However, by carefully choosing parameters of the matching network, matching can be achieved at a certain instantaneous time during the pulse at which point power reflection is minimized. The time of this match point can be controlled by tuning matching network configuration, which in turn affects the plasma properties during the pulse. When plasma is matched at an early time during the pulse, plasma density rises faster but settles at a lower steady state, a result of a larger mismatch as impedance of the plasma deviates further into the pulse. When matching network is fixed such that power reflection minimized at a later time, the steady state power delivery can be significantly larger while producing a higher-density plasma during the pulse-on period. This work is in collaboration with Prof. Steven Shannon's experiment group, while experimental observations has been successfully replicated in simulation and matched qualitatively. This work thus also serves as a validation of HPEM modeling platform for this thesis.

Chapter 4 investigated approaches of controlling VUV photon fluxes and VUV/ion flux ratio for low pressure ICPs sustained in rare gas mixtures. By addressing the radiation transport process using a Monte-Carlo technique, kinetics of VUV photon fluxes can be tracked using HPEM. It was discovered that the ratio of VUV photon to ion fluxes to surfaces β, generally increases with increasing pressure. When using pulsed plasmas, the instantaneous value of β can vary by a factor of 4 or more during the pulse cycle due to the VUV flux more closely following the pulsed power. The spectra of VUV photon fluxes can also be discretely tuned by adding Xe or Ne into the Ar plasma. Chapter 5 continues on this topic in ICPs sustained in real etching gas used in industry of Ar/Cl_2. The electronegative plasma caused by large density of Cl^- and Cl_2^- ions shows different scaling compared with pure rare gas. It was also discovered that while overall ratios of VUV photon flux to ion flux are controlled by pressure and pulse power, by varying the fraction of Cl_2 in the mixture, both the ratio of VUV to ion fluxes and the spectrum of VUV photons can be tuned. It was also found that the intensity of VUV emission from $Cl(3p^4 4s)$ can be independently tuned by controlling wall surface conditions. With this ability to control ratios of ion to photon fluxes, photon stimulated processes, as observed in halogen etching of Si, can be tuned to optimize the shape of the etched features.

Chapter 6 discusses the control of ion fluxes and ion energy distributions in a tri-frequency CCP operating in $Ar/CF_4/O_2$ gas mixtures at frequencies of 5 + 10 + 40 MHz applied to the same electrode. Unlike dual frequency capacitively coupled plasma with separate powered electrodes, the tri-frequency CCP shows a stronger power coupling between frequencies through the non-linear sheath interaction. Though ohmic heating scales with ω^2 of applied frequency, plasma density is still a strong function of lower frequency power caused by secondary electron ionization sources from the powered electrode. This result matches observation in DF-CCPs from the literature of similar electro-negative plasmas.[10] The ion fluxes scale more sensitively with lower frequency power, a result of higher voltage and a larger fraction of power delivered into ion acceleration at those low frequencies. In the configuration of this TF-CCP, ion transit time through sheath is comparable to the fundamental frequency period, in which scenario analytical solution of IED is difficult to solve. In this work, sheath thickness dynamics are used to explain and predict IEDs of the TF-CCP. With detailed analysis of the change of sheath thickness over the fundamental RF period at 5 MHz, and the combined waveform of the tri-frequency voltage, evolution of IEDs as a function of power deposition is well explained. Unconventional multi-peak IEDs are also successfully explained and predicted from this sheath analysis technique. This direct analysis of sheath thickness dynamics does not depend on the number or frequency of the applied power voltages, thus can be used in more general scenario with the information of applied voltage waveform and change of sheath thickness over time, to qualitatively predict the IEDs of a low pressure plasma source.

In Chapter 7, a microwave-excited microplasma is studied as a VUV photon source for a novel mass-spectrometer application. The high energy photon fluxes are intended to selectively ionize large sample molecules of a mass-spectrometer without diffraction of the sample through photon ionization processes. Operating at a few to 10 Torr in Ar and He/Ar mixtures, the microplasma reactor has a cavity of hundreds of microns to 1 mm. It is found that production of

VUV radiation from Ar microplasmas saturates as a function of power deposition due to a quasi-equilibrium that is established between the electron temperature, and the population of the Ar(4s) manifold.

8.2 Future works

This dissertation studied the dynamics of LTP using a computational platform. The following is a list of potential future works that could provide further benefits in two directions: LTP physics, and simulation technique.

1) E-H mode transition in pulsed ICP with tunable matching network

In Chapter 3, simulations performed for the ICP reactor assumes fully inductively coupled power deposition, which translates to a pure H-mode throughout the pulse. However, when power is low at the beginning of the pulse, plasma could first operate in E-mode before making the E-H transition further into the pulse. By adding capacitively coupled portion of the power to the power reflection model, we could potentially achieve an even better agreement between experiment and simulation results.

2) Parallelization of RTMCM in HPEM

As a Monte-Carlo model, a large number of pseudo-particles need to be launched for a good statistical result in RTMCM. It also takes one pseudo-particles considerable amount of integration time before getting quenched or escaping the plasma due to radiation trapping process, especially in an optically thick gas mixture. It is thus very computationally expensive to use RTMCM. With the scientific community moving towards highly parallelized computation scheme for heavy-load computation task,[1,2] it is reasonable to take advantage of parallel programming and increase the computational performance by scaling the simulation to multi-core systems. The parallelism can be performed either through a shared memory parallel application programming interface such as OPEN-MP[3] or a message passing interface (e.g. OPEN-MPI[4])

8.3 References

[1] G. Sgantchev, W. Dorland, and N. Gumerov, Journal of Parallel and Distributed Computing. **68**, 1339 (2008)

[2] A. Pukhov, Journal of Plasma Physics, **61**, 425 (1999)

[3] Open MP: Open Multi-Processing website. Online at: http://www.openmp.org

[4] Opem MPI: Open Source High Performance Computing Website. Online at: http://www.open-mpi.org/

APPENDIX A LIST OF REACTIONS OF AR

Species

Ar	$Ar(1s_5)$	$Ar(1s_4)$	$Ar(1s_3)$	$Ar(1s_2)$	
Ar(4p)	Ar(4d)	Ar^+	Ar_2*	Ar_2^+	e
$h\nu_{105nm}$	$h\nu_{107nm}$	$h\nu_{121nm}$			

Reactions

Process	Rate Coefficient$^{a)}$	Reference	$-\Delta H$ (eV)$^{a)}$
Photoionization			
$h\nu_{105nm} + Ar(1s_5) \rightarrow Ar^+ + e$	9.8×10^{-20} cm^2	[1], b)	
$h\nu_{105nm} + Ar(1s_4) \rightarrow Ar^+ + e$	9.8×10^{-20} cm^2	[1], b)	
$h\nu_{105nm} + Ar(1s_3) \rightarrow Ar^+ + e$	9.8×10^{-20} cm^2	[1], b)	
$h\nu_{105nm} + Ar(1s_2) \rightarrow Ar^+ + e$	9.8×10^{-20} cm^2	[1], b)	
$h\nu_{105nm} + Ar(4p) \rightarrow Ar^+ + e$	9.3×10^{-20} cm^2	[1], b)	
$h\nu_{105nm} + Ar(4d) \rightarrow Ar^+ + e$	9.0×10^{-20} cm^2	[1], b)	
$h\nu_{107nm} + Ar(1s_5) \rightarrow Ar^+ + e$	9.8×10^{-20} cm^2	[1], b)	
$h\nu_{107nm} + Ar(1s_4) \rightarrow Ar^+ + e$	9.8×10^{-20} cm^2	[1], b)	
$h\nu_{107nm} + Ar(1s_3) \rightarrow Ar^+ + e$	9.8×10^{-20} cm^2	[1], b)	
$h\nu_{107nm} + Ar(1s_2) \rightarrow Ar^+ + e$	9.8×10^{-20} cm^2	[1], b)	
$h\nu_{107nm} + Ar(4p) \rightarrow Ar^+ + e$	9.3×10^{-20} cm^2	[1], b)	
$h\nu_{107nm} + Ar(4d) \rightarrow Ar^+ + e$	9.0×10^{-20} cm^2	[1], b)	
$h\nu_{121nm} + Ar(1s_5) \rightarrow Ar^+ + e$	9.8×10^{-20} cm^2	[1], b)	
$h\nu_{121nm} + Ar(1s_4) \rightarrow Ar^+ + e$	9.8×10^{-20} cm^2	[1], b)	
$h\nu_{121nm} + Ar(1s_3) \rightarrow Ar^+ + e$	9.8×10^{-20} cm^2	[1], b)	
$h\nu_{121nm} + Ar(1s_2) \rightarrow Ar^+ + e$	9.8×10^{-20} cm^2	[1], b)	
$h\nu_{121nm} + Ar(4p) \rightarrow Ar^+ + e$	9.3×10^{-20} cm^2	[1], b)	
$h\nu_{121nm} + Ar(4d) \rightarrow Ar^+ + e$	9.0×10^{-20} cm^2	[1], b)	
Radiative Transitions			
$Ar(1s_4) \leftrightarrow Ar$	1.2×10^{8} s^{-1}	[2], c)	
$Ar(1s_2) \leftrightarrow Ar$	5.1×10^{8} s^{-1}	[2], c)	
$Ar(4p) \rightarrow Ar(1s_5)$	1.6×10^{7} s^{-1}	[3]	
$Ar(4p) \rightarrow Ar(1s_4)$	9.3×10^{7} s^{-1}	[3]	
$Ar(4p) \rightarrow Ar(1s_3)$	1.0×10^{7} s^{-1}	[3]	
$Ar(4p) \rightarrow Ar(1s_2)$	8.5×10^{7} s^{-1}	[3]	
$Ar(4d) \rightarrow Ar(1s_5)$	2.0×10^{5} s^{-1}	[3]	

Ar(4d) → Ar($1s_4$)	2.0×10^{5} s^{-1}	[3]	
Ar(4d) → Ar($1s_3$)	2.0×10^{5} s^{-1}	[3]	
Ar(4d) → Ar($1s_2$)	2.0×10^{5} s^{-1}	[3]	
Ar(4d) → Ar(4p)	1.0×10^{7} s^{-1}	[3]	
Ar_2* → Ar + Ar	6.0×10^{7} s^{-1}	[4]	1.08
Electron Impact Processes			
e + Ar → Ar + e	d)	[5]	j)
e + Ar ↔ Ar($1s_5$) + e	d)	[6], d)	
e + Ar ↔ Ar($1s_4$) + e	d)	[6], d)	
e + Ar ↔ Ar($1s_3$) + e	d)	[6], d)	
e + Ar ↔ Ar($1s_2$) + e	d)	[6], d)	
e + Ar ↔ Ar(4p) + e	d)	[6], d),e)	
e + Ar ↔ Ar(4d) + e	d)	[6], d),f)	
e + Ar → Ar^+ + e + e	d)	[7]	
e + Ar($1s_5$) ↔Ar($1s_4$) + e	d)	[8], d)	
e + Ar($1s_5$) ↔ Ar($1s_3$) + e	d)	[8], d)	
e + Ar($1s_5$) ↔Ar($1s_2$) + e	d)	[8], d)	
e + Ar($1s_5$) ↔ Ar(4p) + e	d)	[9], d),g)	
e + Ar($1s_5$) ↔ Ar(4d) + e	d)	[9], d),g)	
e + Ar($1s_5$) → Ar^+ + e + e	d)	[10]	
e + Ar($1s_4$) ↔ Ar($1s_3$) + e	d)	[8], d)	
e + Ar($1s_4$) ↔ Ar($1s_2$) + e	d)	[8], d)	
e + Ar($1s_4$) ↔ Ar(4p) + e	d)	[9], d),g)	
e + Ar($1s_4$) ↔ Ar(4d) + e	d)	[9], d),g)	
e + Ar($1s_4$) → Ar^+ + e + e	d)	[10]	
e + Ar($1s_3$) ↔ Ar($1s_2$) + e	d)	[8], d)	
e + Ar($1s_3$) ↔ Ar(4p) + e	d)	[9], d),g)	
e + Ar($1s_3$) ↔ Ar(4d) + e	d)	[9], d),g)	
e + Ar($1s_3$) → Ar^+ + e + e	d)	[10]	
e + Ar($1s_2$) ↔ Ar(4p) + e	d)	[9], d),g)	
e + Ar($1s_2$) ↔ Ar(4d) + e	d)	[9], d),g)	
e + Ar($1s_2$) → Ar^+ + e + e	d)	[10]	
e + Ar(4p) ↔ Ar(4d) + e	d)	[9], d),g)	
e + Ar(4p) → Ar^+ + e + e	d)	[10]	
e + Ar(4d) → Ar^+ + e + e	d)	[10]	
e + e + Ar^+ → Ar($1s_5$) + e	$5.0 \times 10^{-27} T_e^{-9/2} cm^6 s^{-1}$	[11]	
e + Ar^+ → Ar($1s_5$)	$4.0 \times 10^{-13} T_e^{-1/2}$	[11]	
Ar($1s_5$) + Ar → Ar($1s_4$) + Ar	$1.5 \times 10^{-15} T_n^{1/2} \exp(-881/T_g)$	[3]	-0.076
Ar($1s_4$) + Ar → Ar($1s_5$) + Ar	$2.5 \times 10^{-15} T_n^{1/2}$	[3]	0.076
Ar($1s_5$) + Ar → Ar($1s_3$) + Ar	$0.5 \times 10^{-15} T_n^{1/2} \exp(-2029/T_g)$	[3]	-0.175
Ar($1s_3$) + Ar → Ar($1s_5$) + Ar	$2.5 \times 10^{-15} T_n^{1/2}$	[3]	0.175
Ar($1s_5$) + Ar → Ar($1s_2$) + Ar	$1.5 \times 10^{-15} T_n^{1/2} \exp(-3246/T_g)$	[3]	-0.280

$Ar(1s_2) + Ar \rightarrow Ar(1s_5) + Ar$	$2.5 \times 10^{-15} T_n^{1/2}$	[3]	0.280
$Ar(1s_4) + Ar \rightarrow Ar(1s_3) + Ar$	$0.83 \times 10^{-15} T_n^{1/2} \exp(-1148/T_g)$	[3]	-0.099
$Ar(1s_3) + Ar \rightarrow Ar(1s_4) + Ar$	$2.5 \times 10^{-15} T_n^{1/2}$	[3]	0.099
$Ar(1s_4) + Ar \rightarrow Ar(1s_2) + Ar$	$2.5 \times 10^{-15} T_n^{1/2} \exp(-2365/T_g)$	[3]	-0.204
$Ar(1s_2) + Ar \rightarrow Ar(1s_4) + Ar$	$2.5 \times 10^{-15} T_n^{1/2}$	[3]	0.204
$Ar(1s_3) + Ar \rightarrow Ar(1s_2) + Ar$	$7.5 \times 10^{-15} T_n^{1/2} \exp(-1217/T_g)$	[3]	-0.105
$Ar(1s_2) + Ar \rightarrow Ar(1s_3) + Ar$	$2.5 \times 10^{-15} T_n^{1/2}$	[3]	0.105
$Ar^* + Ar^* \rightarrow Ar^+ + Ar + e$	$1.2 \times 10^{-9} T_n^{1/2}$	[3], h), i)	
$Ar^+ + Ar \rightarrow Ar^+ + Ar$	$5.66 \times 10^{-10} T_n^{1/2}$	[12]	k)
$Ar(1s_5) + Ar + Ar \rightarrow Ar_2^* + Ar$	$1.14 \times 10^{-32} T_n^{-1}$	[4]	0.72
$Ar(1s_4) + Ar + Ar \rightarrow Ar_2^* + Ar$	$1.14 \times 10^{-32} T_n^{-1}$	[4]	0.79
$Ar(1s_3) + Ar + Ar \rightarrow Ar_2^* + Ar$	$1.14 \times 10^{-32} T_n^{-1}$	[4]	0.89
$Ar(1s_2) + Ar + Ar \rightarrow Ar_2^* + Ar$	$1.14 \times 10^{-32} T_n^{-1}$	[4]	1.00
$Ar(4p) + Ar + Ar \rightarrow Ar_2^* + Ar$	$1.14 \times 10^{-32} T_n^{-1}$	[4]	2.08
$Ar(4d) + Ar + Ar \rightarrow Ar_2^* + Ar$	$1.14 \times 10^{-32} T_n^{-1}$	[4]	3.88
$Ar^* + Ar^* \rightarrow Ar_2^+ + e$	$5.7 \times 10^{-10} T_n^{1/2}$	[13], h), i)	
$Ar(4d) + Ar \rightarrow Ar_2^+ + e$	$2.0 \times 10^{-9} T_n^{1/2}$	[14]	0.33
$Ar^+ + Ar + Ar \rightarrow Ar_2^+ + Ar$	$2.5 \times 10^{-31} T_n^{-1}$	[15]	1.35
$Ar_2^* + Ar_2^* \rightarrow Ar_2^+ + Ar + Ar + e$	$5.0 \times 10^{-10} T_n^{1/2}$	[4]	
$e + Ar_2^+ \rightarrow Ar(1s_5) + Ar$	$2.69 \times 10^{-8}\ Te^{-0.67}$	[16], l)	2.89
$e + Ar_2^+ \rightarrow Ar + Ar$	$2.69 \times 10^{-8}\ Te^{-0.67}$	[16], l)	14.44
$e + Ar_2^* \rightarrow Ar_2^+ + e + e$	$9.0 \times 10^{-8} Te^{0.7} \exp(-3.66/T_e)$	[4]	
$e + Ar_2^* \rightarrow Ar + Ar + e$	1.0×10^{-7}	[4]	

a) Rate coefficients have units of $cm^3 s^{-1}$ unless noted. T_e is electron temperature (eV). T_g is gas temperature (K), T_n is normalized gas temperature (T_g/300 K). $-\Delta H$ is the contribution to gas heating (eV).

b) Photoionization cross sections for higher levels were scaled from that of the metastable state based on energy of the ejected electron.

c) Rate shown is for emission. Absorption is addressed using a radiation trapping factor. (See text.)

d) Cross section is for forward reaction. Reverse cross section obtained by detailed balance.

e) Lumped state has excitation cross sections to Ar(4p,3d,5s,5p)

f) Lumped state has excitation cross sections to Ar(4d,6s,Rydberg)

g) Sum of electron impact excitation to optically allowed and forbidden states comprising the lumped Ar(4p) or Ar(4d).

h) Ar* represents any excited atomic state of Ar.

i) The same Penning ionization rate coefficient was used for all pairings of excited states of Ar.

j) The rate of heating by elastic collisions is $k_m(3/2)k_B(2m_e/M)(T_e-T_g)$ eV-cm^3/s, for elastic rate coefficient k_m, electron mass m_e, neutral mass M and Boltzmann's constant k_B.

k) The rate of gas heating of the neutral by charge exchange is $k_{ce}(3/2)k_B(T_{ion}-T_g)$ eV-cm^3/s, for charge exchange rate coefficient k_{ce} and ion temperature T_{ion}.

l) Assumed equal branching.

APPENDIX B LIST OF REACTIONS OF AR/XE

Species

Ar $Ar(1s_5)$ $Ar(1s_4)$ $Ar(1s_3)$ $Ar(1s_2)$ $Ar(4p)$
$Ar(4d)$ Ar^+ Ar_2* Ar_2^+

Xe $Xe(1s_5)$ $Xe(1s_4)$ $Xe(1s_3)$ $Xe(1s_2)$ $Xe(6p)$
$Xe(5d)$ $Xe(7s)$ $Xe(3p)$ Xe_2^* Xe^+ Xe_2^+ e
$h\nu_{105nm}$ $h\nu_{107nm}$ $h\nu_{121nm}$ $h\nu_{130nm}$ $h\nu_{147nm}$ $h\nu_{172nm}$

Reactions   (Note: Reactions involving only Ar species are listed in Table I.)

Process	Rate Coefficient[a)]	Reference	-ΔH (eV) [a)]
Photoionization			
$h\nu_{130nm} + Xe(1s_5) \rightarrow Xe^+ + e$	$3.53 \times 10^{-20}\ cm^2$	[1], b)	
$h\nu_{130nm} + Xe(1s_4) \rightarrow Xe^+ + e$	$3.54 \times 10^{-20}\ cm^2$	[1], b)	
$h\nu_{130nm} + Xe(1s_3) \rightarrow Xe^+ + e$	$3.56 \times 10^{-20}\ cm^2$	[1], b)	
$h\nu_{130nm} + Xe(1s_2) \rightarrow Xe^+ + e$	$3.55 \times 10^{-20}\ cm^2$	[1], b)	
$h\nu_{130nm} + Xe(6p) \rightarrow Xe^+ + e$	$3.55 \times 10^{-20}\ cm^2$	[1], b)	
$h\nu_{130nm} + Xe(5d) \rightarrow Xe^+ + e$	$3.53 \times 10^{-20}\ cm^2$	[1], b)	
$h\nu_{130nm} + Xe(7s) \rightarrow Xe^+ + e$	$3.48 \times 10^{-20}\ cm^2$	[1], b)	
$h\nu_{130nm} + Xe(3p) \rightarrow Xe^+ + e$	$3.44 \times 10^{-20}\ cm^2$	[1], b)	
$h\nu_{147nm} + Xe(1s_5) \rightarrow Xe^+ + e$	$3.35 \times 10^{-20}\ cm^2$	[1], b)	
$h\nu_{147nm} + Xe(1s_4) \rightarrow Xe^+ + e$	$3.37 \times 10^{-20}\ cm^2$	[1], b)	
$h\nu_{147nm} + Xe(1s_3) \rightarrow Xe^+ + e$	$3.53 \times 10^{-20}\ cm^2$	[1], b)	
$h\nu_{147nm} + Xe(1s_2) \rightarrow Xe^+ + e$	$3.54 \times 10^{-20}\ cm^2$	[1], b)	
$h\nu_{147nm} + Xe(6p) \rightarrow Xe^+ + e$	$3.54 \times 10^{-20}\ cm^2$	[1], b)	
$h\nu_{147nm} + Xe(5d) \rightarrow Xe^+ + e$	$3.55 \times 10^{-20}\ cm^2$	[1], b)	
$h\nu_{147nm} + Xe(7s) \rightarrow Xe^+ + e$	$3.56 \times 10^{-20}\ cm^2$	[1], b)	
$h\nu_{147nm} + Xe(3p) \rightarrow Xe^+ + e$	$3.53 \times 10^{-20}\ cm^2$	[1], b)	
$h\nu_{172nm} + Xe(1s_5) \rightarrow Xe^+ + e$	$2.61 \times 10^{-20}\ cm^2$	[1], b)	
$h\nu_{172nm} + Xe(1s_4) \rightarrow Xe^+ + e$	$2.72 \times 10^{-20}\ cm^2$	[1], b)	
$h\nu_{172nm} + Xe(1s_3) \rightarrow Xe^+ + e$	$3.33 \times 10^{-20}\ cm^2$	[1], b)	
$h\nu_{172nm} + Xe(1s_2) \rightarrow Xe^+ + e$	$3.35 \times 10^{-20}\ cm^2$	[1], b)	
$h\nu_{172nm} + Xe(6p) \rightarrow Xe^+ + e$	$3.35 \times 10^{-20}\ cm^2$	[1], b)	
$h\nu_{172nm} + Xe(5d) \rightarrow Xe^+ + e$	$3.42 \times 10^{-20}\ cm^2$	[1], b)	
$h\nu_{172nm} + Xe(7s) \rightarrow Xe^+ + e$	$3.53 \times 10^{-20}\ cm^2$	[1], b)	

$h\nu_{172nm}$ + Xe(3p) → Xe^{+} + e	3.54×10^{-20} cm^{2}	[1], b)	
$h\nu_{107nm}$ + Xe(1s_5) → Xe^{+} + e	3.47×10^{-20} cm^{2}	[1], b)	
$h\nu_{107nm}$ + Xe(1s_4) → Xe^{+} + e	3.47×10^{-20} cm^{2}	[1], b)	
$h\nu_{107nm}$ + Xe(1s_3) → Xe^{+} + e	3.31×10^{-20} cm^{2}	[1], b)	
$h\nu_{107nm}$ + Xe(1s_2) → Xe^{+} + e	3.29×10^{-20} cm^{2}	[1], b)	
$h\nu_{107nm}$ + Xe(6p) → Xe^{+} + e	3.29×10^{-20} cm^{2}	[1], b)	
$h\nu_{107nm}$ + Xe(5d) → Xe^{+} + e	3.24×10^{-20} cm^{2}	[1], b)	
$h\nu_{107nm}$ + Xe(7s) → Xe^{+} + e	3.14×10^{-20} cm^{2}	[1], b)	
$h\nu_{107nm}$ + Xe(3p) → Xe^{+} + e	3.08×10^{-20} cm^{2}	[1], b)	
$h\nu_{105nm}$ + Xe(1s_5) → Xe^{+} + e	3.47×10^{-20} cm^{2}	[1], b)	
$h\nu_{105nm}$ + Xe(1s_4) → Xe^{+} + e	3.47×10^{-20} cm^{2}	[1], b)	
$h\nu_{105nm}$ + Xe(1s_3) → Xe^{+} + e	3.31×10^{-20} cm^{2}	[1], b)	
$h\nu_{105nm}$ + Xe(1s_2) → Xe^{+} + e	3.29×10^{-20} cm^{2}	[1], b)	
$h\nu_{105nm}$ + Xe6SP → Xe^{+} + e	3.29×10^{-20} cm^{2}	[1], b)	
$h\nu_{105nm}$ + Xe(5d) → Xe^{+} + e	3.24×10^{-20} cm^{2}	[1], b)	
$h\nu_{105nm}$ + Xe(7s) → Xe^{+} + e	3.14×10^{-20} cm^{2}	[1], b)	
$h\nu_{105nm}$ + Xe(3p) → Xe^{+} + e	3.08×10^{-20} cm^{2}	[1], b)	
$h\nu_{130nm}$ + Ar(1s_5) → Ar^{+} + e	1.01×10^{-19} cm^{2}	[1], b)	
$h\nu_{130nm}$ + Ar(1s_4) → Ar^{+} + e	1.01×10^{-19} cm^{2}	[1], b)	
$h\nu_{130nm}$ + Ar(1s_3) → Ar^{+} + e	1.01×10^{-19} cm^{2}	[1], b)	
$h\nu_{130nm}$ + Ar(1s_2) → Ar^{+} + e	1.01×10^{-19} cm^{2}	[1], b)	
$h\nu_{130nm}$ + Ar(4p) → Ar^{+} + e	9.92×10^{-20} cm^{2}	[1], b)	
$h\nu_{130nm}$ + Ar(4d) → Ar^{+} + e	9.61×10^{-20} cm^{2}	[1], b)	
$h\nu_{147nm}$ + Ar(1s_5) → Ar^{+} + e	9.61×10^{-20} cm^{2}	[1], b)	
$h\nu_{147nm}$ + Ar(1s_4) → Ar^{+} + e	9.72×10^{-20} cm^{2}	[1], b)	
$h\nu_{147nm}$ + Ar(1s_3) → Ar^{+} + e	9.78×10^{-20} cm^{2}	[1], b)	
$h\nu_{147nm}$ + Ar(1s_2) → Ar^{+} + e	9.82×10^{-20} cm^{2}	[1], b)	
$h\nu_{147nm}$ + Ar(4p) → Ar^{+} + e	1.01×10^{-19} cm^{2}	[1], b)	
$h\nu_{147nm}$ + Ar(4d) → Ar^{+} + e	9.97×10^{-20} cm^{2}	[1], b)	
$h\nu_{172nm}$ + Ar(1s_5) → Ar^{+} + e	7.81×10^{-20} cm^{2}	[1], b)	
$h\nu_{172nm}$ + Ar(1s_4) → Ar^{+} + e	7.91×10^{-20} cm^{2}	[1], b)	
$h\nu_{172nm}$ + Ar(1s_3) → Ar^{+} + e	8.06×10^{-20} cm^{2}	[1], b)	
$h\nu_{172nm}$ + Ar(1s_2) → Ar^{+} + e	8.22×10^{-20} cm^{2}	[1], b)	
$h\nu_{172nm}$ + Ar(4p) → Ar^{+} + e	9.78×10^{-20} cm^{2}	[1], b)	
$h\nu_{172nm}$ + Ar(4d) → Ar^{+} + e	1.01×10^{-19} cm^{2}	[1], b)	
Radiative Transitions			
Xe(1s_4) ↔ Xe	2.81×10^{8} s^{-1}	[17], c)	
Xe(1s_2) ↔ Xe	2.46×10^{8} s^{-1}	[17], c)	
Xe(3p) → Xe(7s)	1.0×10^{6} s^{-1}	[17],h)	
Xe(3p) → Xe(5d)	1.0×10^{6} s^{-1}	[17],h)	
Xe(3p) → Xe(1s_2)	2.9×10^{6} s^{-1}	[18]	
Xe(3p) → Xe(1s_3)	2.9×10^{6} s^{-1}	[18]	

$Xe(3p) \rightarrow Xe(1s_4)$	$4.64 \times 10^6\ s^{-1}$	[18]	
$Xe(3p) \rightarrow Xe(1s_5)$	$4.64 \times 10^6\ s^{-1}$	[18]	
$Xe(7s) \rightarrow Xe(6p)$	$2.0 \times 10^6\ s^{-1}$	h)	
$Xe(5d) \rightarrow Xe(6p)$	$2.0 \times 10^6\ s^{-1}$	[18]	
$Xe(5d) \rightarrow Xe(1s_4)$	$5.0 \times 10^5\ s^{-1}$	[18]	
$Xe(5d) \rightarrow Xe(1s_5)$	$5.0 \times 10^5\ s^{-1}$	[18]	
$Xe(6p) \rightarrow Xe(1s_4)$	$5.0 \times 10^5\ s^{-1}$	[18]	
$Xe(6p) \rightarrow Xe(1s_5)$	$5.0 \times 10^5\ s^{-1}$	[18]	
$Xe_2^* \rightarrow Xe + Xe$	$6.0 \times 10^7\ s^{-1}$	[19]	1.08
Electron Impact Processes			
$e + Xe \rightarrow Xe + e$		[5]	e)
$e + Xe \leftrightarrow Xe(1s_5) + e$	d)	[20]	
$e + Xe \leftrightarrow Xe(1s_4) + e$	d)	[20]	
$e + Xe \leftrightarrow Xe(1s_2) + e$	d)	[20]	
$e + Xe \leftrightarrow Xe(1s_3) + e$	d)	[20]	
$e + Xe \leftrightarrow Xe(6p) + e$	d)	[20]	
$e + Xe \leftrightarrow Xe(5d) + e$	d)	[20]	
$e + Xe \leftrightarrow Xe(7s) + e$	d)	[20]	
$e + Xe \leftrightarrow Xe(3p) + e$	d)	[20]	
$e + Xe \rightarrow Xe^+ + e + e$		[20]	
$e + Xe(1s_5) \leftrightarrow Xe(1s_4) + e$	d)	[7]	
$e + Xe(1s_5) \leftrightarrow Xe(1s_2) + e$	d)	[7]	
$e + Xe(1s_5) \leftrightarrow Xe(1s_3) + e$	d)	[7]	
$e + Xe(1s_5) \leftrightarrow Xe(6p) + e$	d)	[7]	
$e + Xe(1s_5) \leftrightarrow Xe(5d) + e$	d)	[7]	
$e + Xe(1s_5) \leftrightarrow Xe(7s) + e$	d)	[7]	
$e + Xe(1s_5) \leftrightarrow Xe(3p) + e$	d)	[7]	
$e + Xe(1s_5) \rightarrow Xe^+ + e + e$		[10]	
$e + Xe(1s_4) \leftrightarrow Xe(1s_2) + e$	d)	[7]	
$e + Xe(1s_4) \leftrightarrow Xe(1s_3) + e$	d)	[7]	
$e + Xe(1s_4) \leftrightarrow Xe(6p) + e$	d)	[7]	
$e + Xe(1s_4) \leftrightarrow Xe(5d) + e$	d)	[7]	
$e + Xe(1s_4) \leftrightarrow Xe(7s) + e$	d)	[7]	
$e + Xe(1s_4) \leftrightarrow Xe(3p) + e$	d)	[7]	
$e + Xe(1s_4) \rightarrow Xe^+ + e + e$		[10]	
$e + Xe(1s_3) \leftrightarrow Xe(1s_2) + e$	d)	[7]	
$e + Xe(1s_3) \leftrightarrow Xe(6p) + e$	d)	[7]	
$e + Xe(1s_3) \leftrightarrow Xe(5d) + e$	d)	[7]	
$e + Xe(1s_3) \leftrightarrow Xe(7s) + e$	d)	[7]	
$e + Xe(1s_3) \leftrightarrow Xe(3p) + e$	d)	[7]	
$e + Xe(1s_3) \rightarrow Xe^+ + e + e$		[10]	
$e + Xe(1s_2) \leftrightarrow Xe(6p) + e$	d)	[7]	

$e + Xe(1s_2) \leftrightarrow Xe(5d) + e$	d)	[7]	
$e + Xe(1s_2) \leftrightarrow Xe(7s) + e$	d)	[7]	
$e + Xe(1s_2) \leftrightarrow Xe(3p) + e$	d)	[7]	
$e + Xe(1s_2) \rightarrow Xe^+ + e + e$		[10]	
$e + Xe(6p) \leftrightarrow Xe(5d) + e$	d)	[7]	
$e + Xe(6p) \leftrightarrow Xe(7s) + e$	d)	[7]	
$e + Xe(6p) \leftrightarrow Xe(3p) + e$	d)	[7]	
$e + Xe(6p) \rightarrow Xe^+ + e + e$		[10]	
$e + Xe(5d) \leftrightarrow Xe(7s) + e$	d)	[7]	
$e + Xe(5d) \leftrightarrow Xe(3p) + e$	d)	[7]	
$e + Xe(5d) \rightarrow Xe^+ + e + e$		[10]	
$e + Xe(7s) \leftrightarrow Xe(3p) + e$	d)	[7]	
$e + Xe(7s) \rightarrow Xe^+ + e + e$		[10]	
$e + Xe(3p) \rightarrow Xe^+ + e + e$		[10]	
$e + e + Xe^+ \rightarrow Xe(1s_5) + e$	$5.0 \times 10^{-27} T_n^{-9/2}$	[11].	
$e + Xe^+ \rightarrow Xe$	$4.0 \times 10^{-13} T_n^{-1/2}$	[11]	
$e + Xe_2^+ \rightarrow Xe(1s_5) + Xe$	$2.2 \times 10^{-7} T_n^{-1/2}$	[19]	2.7
$e + Xe_2^* \rightarrow Xe + Xe + e$	1.0×10^{-9}	[31]	
Heavy Particles Processes			
$Xe^+ + Xe \rightarrow Xe^+ + Xe$	$3.78 \times 10^{-10} T_n^{-1/2}$	[28]	f)
$Xe^+ + Xe + Xe \rightarrow Xe_2^+ + Xe$	$3.6 \times 10^{-31} T_n^{-1/2}$ cm^{6}s^{-1}	[19]	
$Xe_2^* + Xe_2^* \rightarrow Xe_2^+ + Xe + Xe + e$	3.5×10^{-10}	[19]	
$Xe(1s_5) + Xe \rightarrow Xe(1s_4) + Xe$	$0.6 \times 10^{-13} T_n^{-1/2} \exp(-1405/T_g)$	[9]	-0.12
$Xe(1s_4) + Xe \rightarrow Xe(1s_5) + Xe$	$1 \times 10^{-13} T_n^{-1/2}$	[9]	0.12
$Xe(1s_5) + Xe \rightarrow Xe(1s_3) + Xe$	$0.9 \times 10^{-12} T_n^{-1/2} \exp(-13122/T_g)$	[9]	-1.13
$Xe(6p)M + Xe \rightarrow Xe(1s_5) + Xe$	$4.5 \times 10^{-12} T_n^{-1/2}$	[9]	1.13
$Xe(1s_5) + Xe \rightarrow Xe(1s_2) + Xe$	$2.7 \times 10^{-12} T_n^{-1/2} \exp(-14544/T_g)$	[9]	-1.25
$Xe(1s_2) + Xe \rightarrow Xe(1s_5) + Xe$	$4.5 \times 10^{-12} T_n^{-1/2}$	[9]	1.25
$Xe(1s_3) + Xe \rightarrow Xe(1s_2) + Xe$	$7.5 \times 10^{-11} T_n^{-1/2} \exp(-1421/T_g)$	[9]	-0.12
$Xe(1s_2) + Xe \rightarrow Xe(1s_3) + Xe$	$2.5 \times 10^{-11} T_n^{-1/2}$	[9]	0.12
$Xe(1s_2) + Xe \rightarrow Xe(6p) + Xe$	$1.67 \times 10^{-10} T_n^{-1/2} \exp(-120/T_g)$	[9]	-0.01
$Xe(6p) + Xe \rightarrow Xe(1s_2) + Xe$	$1.0 \times 10^{-10} T_n^{-1/2}$	[9]	0.01
$Xe(1s_3) + Xe \rightarrow Xe(6p) + Xe$	$1.85 \times 10^{-10} T_n^{-1/2} \exp(-1620/T_g)$	[9]	-0.13
$Xe(6p) + Xe \rightarrow Xe(1s_3) + Xe$	$3.7 \times 10^{-11} T_n^{-1/2}$	[9]	0.13
$Xe(6p) + Xe \rightarrow Xe(3p) + Xe$	$4.2 \times 10^{-10} T_n^{-1/2} \exp(-15300/T_g)$	[9]	-1.32
$Xe(3p) + Xe \rightarrow Xe(6p) + Xe$	$4.2 \times 10^{-10} T_n^{-1/2}$	[9]	1.32
$Xe(6p) + Xe \rightarrow Xe(5d) + Xe$	$9.5 \times 10^{-11} T_n^{-1/2} \exp(-3594/T_g)$	[18]	-0.31
$Xe(5d) + Xe \rightarrow Xe(6p) + Xe$	$9.5 \times 10^{-11} T_n^{-1/2}$	[18]	0.31
$Xe^* + Xe^* \rightarrow Xe^+ + Xe + e$	$1.9 \times 10^{-10} T_n^{-1/2}$	[9],g)	
$Xe^* + Xe + Xe \rightarrow Xe_2^* + Xe$	$8.0 \times 10^{-32} T_n^{-3/4}$ cm^{6}s^{-1}	[9], g)	
Ar and Xe Heavy Particles Processes			

Ar(1s$_5$) + Xe → Xe(3p) + Ar	$2.0 \times 10^{-10}\ T_n^{-1/2}$	est.	
Ar(1s$_4$) + Xe → Xe(3p) + Ar	$2.0 \times 10^{-10}\ T_n^{-1/2}$	est.	
Ar(1s$_3$) + Xe → Xe(3p) + Ar	$2.0 \times 10^{-10}\ T_n^{-1/2}$	est.	
Ar(1s$_2$) + Xe → Xe(3p) + Ar	$2.0 \times 10^{-10}\ T_n^{-1/2}$	est.	
Ar(4p) + Xe → Xe$^+$ + Ar + e	$2.0 \times 10^{-10}\ T_n^{-1/2}$	est.	
Ar(4p) + Xe* → Xe$^+$ + Ar + e	$2.0 \times 10^{-10}\ T_n^{-1/2}$	est., g)	
Ar(4d) + Xe → Xe$^+$ + Ar + e	$2.0 \times 10^{-10}\ T_n^{-1/2}$	est.	
Ar(4d) + Xe* → Xe$^+$ + Ar + e	$2.0 \times 10^{-10}\ T_n^{-1/2}$	est., g)	
Ar$^+$ + Xe → Xe$^+$ + Ar	$4.3 \times 10^{-13}\ T_n^{-1/2}$	est.	f)
Ar$^+$ + Xe* → Xe$^+$ + Ar	$4.3 \times 10^{-13}\ T_n^{-1/2}$	est. g)	
Xe(1s$_5$) + Ar → Xe(1s$_4$) + Ar	$0.6 \times 10^{-15}\ T_n^{-1/2} \exp(-1405/T_g)$	est.	-0.12
Xe(1s$_4$) + Ar → Xe(1s$_5$) + Ar	$1 \times 10^{-15}\ T_n^{-1/2}$	est.	0.12
Xe(1s$_5$) + Ar → Xe(1s$_3$) + Ar	$0.9 \times 10^{-14}\ T_n^{-1/2} \exp(-13122/T_g)$	est.	-1.13
Xe(6p)M + Ar → Xe(1s$_5$) + Ar	$4.5 \times 10^{-14}\ T_n^{-1/2}$	est.	1.13
Xe(1s$_5$) + Ar → Xe(1s$_2$) + Ar	$2.7 \times 10^{-14}\ T_n^{-1/2} \exp(-14544/T_g)$	est.	-1.25
Xe(1s$_2$) + Ar → Xe(1s$_5$) + Ar	$4.5 \times 10^{-14}\ T_n^{-1/2}$	est.	1.25
Xe(1s$_3$) + Ar → Xe(1s$_2$) + Ar	$7.5 \times 10^{-13}\ T_n^{-1/2} \exp(-1421/T_g)$	est.	-0.12
Xe(1s$_2$) + Ar → Xe(1s$_3$) + Ar	$2.5 \times 10^{-13}\ T_n^{-1/2}$	est.	0.12
Xe(1s$_2$) + Ar → Xe(6p) + Ar	$1.67 \times 10^{-11}\ T_n^{-1/2} \exp(-120/T_g)$	est.	-0.01
Xe(6p) + Ar → Xe(1s$_2$) + Ar	$1.0 \times 10^{-11}\ T_n^{-1/2}$	est.	0.01
Xe(1s$_3$) + Ar → Xe(6p) + Ar	$1.85 \times 10^{-11}\ T_n^{-1/2} \exp(-1620/T_g)$	est.	-0.13
Xe(6p) + Ar → Xe(1s$_3$) + Ar	$3.7 \times 10^{-12}\ T_n^{-1/2}$	est.	0.13
Xe(6p) + Ar → Xe(3p) + Ar	$4.2 \times 10^{-11}\ T_n^{-1/2} \exp(-15300/T_g)$	est.	-1.32
Xe(3p) + Ar → Xe(6p) + Ar	$4.2 \times 10^{-11}\ T_n^{-1/2}$	est.	1.32
Xe(6p) + Ar → Xe(5d) + Ar	$9.5 \times 10^{-12}\ T_n^{-1/2} \exp(-3594/T_g)$	est.	-0.31
Xe(5d) + Ar → Xe(6p) + Ar	$9.5 \times 10^{-11}\ T_n^{-1/2}$	est.	0.31
Ar(1s$_5$) + Xe → Ar(1s$_4$) + Xe	$1.5 \times 10^{-15}\ T_n^{1/2} \exp(-881/T_g)$	est.	-0.076
Ar(1s$_4$) + Xe → Ar(1s$_5$) + Xe	$2.5 \times 10^{-15}\ T_n^{1/2}$	est.	0.076
Ar(1s$_5$) + Xe → Ar(1s$_3$) + Xe	$0.5 \times 10^{-15}\ T_n^{1/2} \exp(-2029/T_g)$	est.	-0.175
Ar(1s$_3$) + Xe → Ar(1s$_5$) + Xe	$2.5 \times 10^{-15}\ T_n^{1/2}$	est.	0.175
Ar(1s$_5$) + Xe → Ar(1s$_2$) + Xe	$1.5 \times 10^{-15}\ T_n^{1/2} \exp(-3246/T_g)$	est.	-0.280
Ar(1s$_2$) + Xe → Ar(1s$_5$) + Xe	$2.5 \times 10^{-15}\ T_n^{1/2}$	est.	0.280
Ar(1s$_4$) + Xe → Ar(1s$_3$) + Xe	$0.83 \times 10^{-15}\ T_n^{1/2} \exp(-1148/T_g)$	est.	-0.099
Ar(1s$_3$) + Xe → Ar(1s$_4$) + Xe	$2.5 \times 10^{-15}\ T_n^{1/2}$	est.	0.099
Ar(1s$_4$) + Xe → Ar(1s$_2$) + Xe	$2.5 \times 10^{-15}\ T_n^{1/2} \exp(-2365/T_g)$	est.	-0.204
Ar(1s$_2$) + Xe → Ar(1s$_4$) + Xe	$2.5 \times 10^{-15}\ T_n^{1/2}$	est.	0.204
Ar(1s$_3$) + Xe → Ar(1s$_2$) + Xe	$7.5 \times 10^{-15}\ T_n^{1/2} \exp(-1217/T_g)$	est.	-0.105
Ar(1s$_2$) + Xe → Ar(1s$_3$) + Xe	$2.5 \times 10^{-15}\ T_n^{1/2}$	est.	0.105

[a)] Rate coefficients have units of cm^{3}s^{-1} unless noted. T_e is electron temperature (eV). T_g is gas temperature (K), T_n is normalized gas temperature (T_g/300 K). -ΔH is the contribution to gas heating (eV).

[b] Photoionization cross sections for higher levels were scaled from that of the metastable state based on energy of the ejected electron.

[c] Rate shown is for emission. Absorption is addressed using a radiation trapping factor. (See text.)

[d] Cross section is for forward reaction. Reverse cross section obtained by detailed balance.

[e] The rate of heating by elastic collisions is $k_m(3/2)k_B(2m_e/M)(T_e-T_g)$ eV-cm^3/s, for elastic rate coefficient k_m, electron mass m_e, neutral mass M and Boltzmann's constant k_B.

[f] The rate of gas heating of the neutral by charge exchange is $k_{ce}(3/2)k_B(T_{ion}-T_g)$ eV-cm^3/s, for charge exchange rate coefficient k_{ce} and ion temperature T_{ion}.

[g] Xe* represents any Xe excited state.

[h] Estimated based on an average radiative decay rate from the manifold of excited states.

APPENDIX C LIST OF REACTIONS OF HE/AR

Species

Ar $\quad$ $\text{Ar}(1s_5)$ $\quad$ $\text{Ar}(1s_4)$ $\quad$ $\text{Ar}(1s_3)$ $\quad$ $\text{Ar}(1s_2)$ $\quad$ Ar(4p)
Ar(4d) $\quad$ Ar^+ $\quad$ Ar_2^* $\quad$ Ar_2^+
He $\quad$ $\text{He}(2^3S)$ $\quad$ $\text{He}(2^1S)$ $\quad$ $\text{He}(2^3P)$ $\quad$ $\text{He}(2^1P)$ $\quad$ He(3s)
He(3p) $\quad$ He2* $\quad$ He^+ $\quad$ He_2^+ $\quad$ e
$h\nu_{105nm}$ $\quad$ $h\nu_{107nm}$ $\quad$ $h\nu_{121nm}$ $\quad$ $h\nu_{58nm}$

Reactions (Note: Reactions involving only Ar species are listed in Table I.)

Process	Rate Coefficient$^{a)}$	Reference	-ΔH (eV)$^{a)}$
Photoionization			
$h\nu_{58nm} + \text{Ar} \rightarrow \text{Ar}^+ + e$	3.5×10^{-17} cm^2	[1], b)	
$h\nu_{58nm} + \text{Ar}(1s_5) \rightarrow \text{Ar}^+ + e$	5.9×10^{-20} cm^2	[1], b)	
$h\nu_{58nm} + \text{Ar}(1s_4) \rightarrow \text{Ar}^+ + e$	5.9×10^{-20} cm^2	[1], b)	
$h\nu_{58nm} + \text{Ar}(1s_3) \rightarrow \text{Ar}^+ + e$	5.9×10^{-20} cm^2	[1], b)	
$h\nu_{58nm} + \text{Ar}(1s_2) \rightarrow \text{Ar}^+ + e$	5.9×10^{-20} cm^2	[1], b)	
$h\nu_{58nm} + \text{Ar}(4p) \rightarrow \text{Ar}^+ + e$	5.5×10^{-20} cm^2	[1], b)	
$h\nu_{58nm} + \text{Ar}(4d) \rightarrow \text{Ar}^+ + e$	5.0×10^{-20} cm^2	[1], b)	
$h\nu_{58nm} + \text{He}(2^3S) \rightarrow \text{He}^+ + e$	4.66×10^{-19} cm^2	[1], b)	
$h\nu_{58nm} + \text{He}(2^1S) \rightarrow \text{He}^+ + e$	4.34×10^{-19} cm^2	[1], b)	
$h\nu_{58nm} + \text{He}(2^3P) \rightarrow \text{He}^+ + e$	4.34×10^{-19} cm^2	[1], b)	
$h\nu_{58nm} + \text{He}(2^1P) \rightarrow \text{He}^+ + e$	4.34×10^{-19} cm^2	[1], b)	
$h\nu_{58nm} + \text{He}(3s) \rightarrow \text{He}^+ + e$	4.34×10^{-19} cm^2	[1], b)	
$h\nu_{58nm} + \text{He}(3p) \rightarrow \text{He}^+ + e$	4.34×10^{-19} cm^2	[1], b)	
$h\nu_{105nm} + \text{He}(2^3S) \rightarrow \text{He}^+ + e$	1.51×10^{-18} cm^2	[1], b)	
$h\nu_{105nm} + \text{He}(2^1S) \rightarrow \text{He}^+ + e$	1.35×10^{-18} cm^2	[1], b)	
$h\nu_{105nm} + \text{He}(2^3P) \rightarrow \text{He}^+ + e$	1.28×10^{-18} cm^2	[1], b)	
$h\nu_{105nm} + \text{He}(2^1P) \rightarrow \text{He}^+ + e$	1.23×10^{-18} cm^2	[1], b)	
$h\nu_{105nm} + \text{He}(3s) \rightarrow \text{He}^+ + e$	1.02×10^{-18} cm^2	[1], b)	
$h\nu_{105nm} + \text{He}(3p) \rightarrow \text{He}^+ + e$	0.98×10^{-18} cm^2	[1], b)	
$h\nu_{107nm} + \text{He}(2^3S) \rightarrow \text{He}^+ + e$	1.53×10^{-18} cm^2	[1], b)	
$h\nu_{107nm} + \text{He}(2^1S) \rightarrow \text{He}^+ + e$	1.36×10^{-18} cm^2	[1], b)	
$h\nu_{107nm} + \text{He}(2^3P) \rightarrow \text{He}^+ + e$	1.29×10^{-18} cm^2	[1], b)	
$h\nu_{107nm} + \text{He}(2^1P) \rightarrow \text{He}^+ + e$	1.24×10^{-18} cm^2	[1], b)	
$h\nu_{107nm} + \text{He}(3s) \rightarrow \text{He}^+ + e$	1.03×10^{-18} cm^2	[1], b)	

$h\nu_{107nm}$ + He(3p) → He^{+} + e	0.99×10^{-18} cm^{2}	[1], b)	
$h\nu_{121nm}$ + He(2^{3}S) → He^{+} + e	1.95×10^{-18} cm^{2}	[1], b)	
$h\nu_{121nm}$ + He(2^{1}S) → He^{+} + e	1.72×10^{-18} cm^{2}	[1], b)	
$h\nu_{121nm}$ + He(2^{3}P) → He^{+} + e	1.63×10^{-18} cm^{2}	[1], b)	
$h\nu_{121nm}$ + He(2^{1}P) → He^{+} + e	1.56×10^{-18} cm^{2}	[1], b)	
$h\nu_{121nm}$ + He(3s) → He^{+} + e	1.24×10^{-18} cm^{2}	[1], b)	
$h\nu_{121nm}$ + He(3p) → He^{+} + e	1.20×10^{-18} cm^{2}	[1], b)	
<u>Radiative Transitions</u>			
He(2^{1}P) ↔ He	1.8×10^{9} s^{-1}	[17], c)	
He(2^{3}P) → He(2^{3}S)	1.02×10^{7} s^{-1}	[17]	
He(3p) → He(2^{3}S)	9.47×10^{6} s^{-1}	[17]	
He(3p) → He(2^{1}S)	1.34×10^{7} s^{-1}	[18]	
He(3s) → He(2^{3}P)	1.55×10^{7} s^{-1}	[18]	
He(3s) → He(2^{1}P)	1.83×10^{7} s^{-1}	[18]	
<u>Electron Impact Processes</u>			
e + He → He + e		[20]	e)
e + He ↔ He(2^{3}S) + e	d)	[20]	
e + He ↔ He(2^{1}S) + e	d)	[20]	
e + He ↔ He(2^{3}P) + e	d)	[20]	
e + He ↔ He(2^{1}P) + e	d)	[20]	
e + He ↔ He(3s) + e	d)	[20]	
e + He ↔ He(3p) + e	d)	[20]	
e + He → He^{+} + e + e		[20]	
e + He(2^{3}S) ↔ He(2^{1}S) + e	d)	[20]	
e + He(2^{3}S) ↔ He(2^{3}P) + e	d)	[20]	
e + He(2^{3}S) ↔ He(2^{1}P) + e	d)	[20]	
e + He(2^{3}S) ↔ He(3s) + e	d)	[20]	
e + He(2^{3}S) ↔ He(3p) + e	d)	[20]	
e + He(2^{3}S) → He^{+} + e + e	d)	[10]	
e + He(2^{1}S) ↔ He(2^{3}P) + e	d)	[20]	
e + He(2^{1}S) ↔ He(2^{1}P) + e	d)	[20]	
e + He(2^{1}S) ↔ He(3s) + e	d)	[20]	
e + He(2^{1}S) ↔ He(3p) + e	d)	[20]	
e + He(2^{1}S) → He^{+} + e + e	d)	[10]	
e + He(2^{3}P) ↔ He(2^{1}P) + e	d)	[20]	
e + He(2^{3}P) ↔ He(3s) + e	d)	[20]	
e + He(2^{3}P) ↔ He(3p) + e	d)	[20]	
e + He(2^{3}P) → He^{+} + e + e	d)	[10]	
e + He(2^{1}P) ↔ He(3s) + e	d)	[20]	
e + He(2^{1}P) ↔ He(3p) + e	d)	[20]	
e + He(2^{1}P) → He^{+} + e + e	d)	[10]	
e + He(3s) ↔ He(3p) + e	d)	[20]	

$e + He(3s) \rightarrow He^+ + e + e$	d)	[10]	
$e + He(3p) \rightarrow He^+ + e + e$	d)	[10]	
$e + e + He^+ \rightarrow He(2^3S) + e$	$2.69 \times 10^{-26} T_n^{-4}$	[21],[22]	
$e + He^+ \rightarrow He(2^3S)$	$6.76 \times 10^{-13} T_n^{-1/2}$	[11]	
$e + He^+ + He \rightarrow He(2^3S) + He$	$1.20 \times 10^{-33} T_n^{-4}$	[11]	
$e + He_2^+ \rightarrow He(2^3S) + He$	$1.6 \times 10^{-9} T_n^{-1/2}$	[23]	
$e + e + He_2^+ \rightarrow He(2^3S) + He + e$	$4.5 \times 10^{-25} T_n^{-1/2}$	[21],[22]	
$e + e + He_2^+ \rightarrow He_2^* + e$	$1.35 \times 10^{-26} T_n^{-4}$	[21],[22]	
$e + He_2^+ + He \rightarrow He(2^3S) + He + He$	$1.29 \times 10^{-28} T_n^{-1}$	[21],[22]	
$e + He_2^* \rightarrow He + He + e$	3.8×10^{-9}	[21]	
<u>Heavy Particle Processes</u>			
$He^+ + He \rightarrow He^+ + He$	6.08×10^{-10}	[12]	f)
$He^* + He^* \rightarrow He^+ + He + e$	$4.5 \times 10^{-10} T_n^{1/2}$	[21],[22], g)	
$He^* + He^* \rightarrow He_2^+ + e$	$1.05 \times 10^{-9} T_n^{1/2}$	[21],[22], g)	
$He^* + He_2^* \rightarrow He^+ + He + He + e$	$2.25 \times 10^{-11} T_n^{1/2}$	[21],[22], g)	
$He^* + He_2^* \rightarrow He_2^+ + He + e$	$1.28 \times 10^{-10} T_n^{1/2}$	[21],[22], g)	
$He_2^* + He_2^* \rightarrow He^+ + 3He + e$	$2.25 \times 10^{-11} T_n^{1/2}$	[21],[22]	
$He_2^* + He_2^* \rightarrow He_2^+ + 2He + e$	$1.28 \times 10^{-10} T_n^{1/2}$	[21],[22]	
$He^+ + He + He \rightarrow He_2^+ + He$	$1.10 \times 10^{-31} T_n^{-0.38}$ cm^6s^{-1}	[15]	
$He + He_2^* \rightarrow He + He + He$	1.5×10^{-15}	[24]	
$He^* + He + He \rightarrow He_2^* + He$	2×10^{-34} cm^6s^{-1}	[22],[25], g)	
<u>Ar and He Heavy Particle Processes</u>			
$He^+ + He + Ar \rightarrow He_2^+ + Ar$	$1.10 \times 10^{-31} T_n^{-0.38}$ cm^6s^{-1}	[15]	
$He^* + He + Ar \rightarrow He_2^* + Ar$	2.0×10^{-34} cm^6s^{-1}	[22],[25], g)	
$He(2^3S) + Ar^0* \rightarrow Ar^+ + He + e$	$6.75 \times 10^{-10} \exp(-684/T_g)$	[26], g)	
$He(2^1S) + Ar^0* \rightarrow Ar^+ + He + e$	$2.07 \times 10^{-9} \exp(-684/T_g)$	[26],[27], g)	
$He(2^3P) + Ar^0* \rightarrow Ar^+ + He + e$	$2.07 \times 10^{-9} \exp(-684/T_g)$	[26],[27], g)	
$He(2^1P) + Ar^0* \rightarrow Ar^+ + He + e$	$2.07 \times 10^{-9} \exp(-684/T_g)$	[26],[27], g)	
$He(3s) + Ar^0* \rightarrow Ar^+ + He + e$	$2.07 \times 10^{-9} \exp(-684/T_g)$	[26],[27], g)	
$He(3p) + Ar^0* \rightarrow Ar^+ + He + e$	$2.07 \times 10^{-9} \exp(-684/T_g)$	[26],[27], g)	
$He_2^* + Ar^0* \rightarrow Ar^+ + He + He + e$	1×10^{-10}	est., g)	
$He^+ + Ar^0* \rightarrow Ar^+ + He$	$5 \times 10^{-14} T_n^{1/2}$	[28],[29], g)	f)
$He_2^+ + Ar^0* \rightarrow Ar^+ + He + He$	$2 \times 10^{-10} T_n^{1/2}$	[30], g)	
$He + Ar(1s_5) \rightarrow Ar(1s_4) + He$	$1.5 \times 10^{-15} T_n^{1/2}\exp(-881.2/T_g)$	est.	
$He + Ar(1s_4) \rightarrow Ar(1s_5) + He$	$2.5 \times 10^{-15} T_n^{1/2}$	est.	0.07
$He + Ar(1s_5) \rightarrow Ar(1s_3) + He$	$0.5 \times 10^{-15} T_n^{1/2}\exp(-2029/T_g)$	est.	
$He + Ar(1s_3) \rightarrow Ar(1s_5) + He$	$2.5 \times 10^{-15} T_n^{1/2}$	est.	0.17
$He + Ar(1s_5) \rightarrow Ar(1s_2) + He$	$1.5 \times 10^{-15} T_n^{1/2}\exp(-3246/T_g)$	est.	
$He + Ar(1s_2) \rightarrow Ar(1s_5) + He$	$2.5 \times 10^{-15} T_n^{1/2}$	est.	0.28

He + Ar($1s_4$) → Ar($1s_3$) + He	$0.83 \times 10^{-15} T_n^{1/2}\exp(-1148/T_g)$	est.	
He + Ar($1s_3$) → Ar($1s_4$) + He	$2.5 \times 10^{-15} T_n^{1/2}$	est.	0.10
He + Ar($1s_4$) → Ar($1s_2$) + He	$2.5 \times 10^{-15} T_n^{1/2}\exp(-2365/T_g)$	est.	
He + Ar($1s_2$) → Ar($1s_4$) + He	$2.5 \times 10^{-15} T_n^{1/2}$	est.	0.21
He + Ar($1s_3$) → Ar($1s_2$) + He	$7.5 \times 10^{-15} T_n^{1/2}\exp(-1217/T_g)$	est.	
He + Ar($1s_2$) → Ar($1s_3$) + He	$2.5 \times 10^{-15} T_n^{1/2}$	est.	0.11

[a] Rate coefficients have units of cm^3s^{-1} unless noted. T_e is electron temperature (eV). T_g is gas temperature (K), T_n is normalized gas temperature (T_g/300 K). $-\Delta H$ is the contribution to gas heating (eV).

[b] Photoionization cross sections for higher levels were scaled from that of the metastable state based on energy of the ejected electron.

[c] Rate shown is for emission. Absorption is addressed using a radiation trapping factor. (See text.)

[d] Cross section is for forward reaction. Reverse cross section obtained by detailed balance.

[e] The rate of heating by elastic collisions is $k_m(3/2)k_B(2m_e/M)(T_e-T_g)$ eV-cm^3/s, for elastic rate coefficient k_m, electron mass m_e, neutral mass M and Boltzmann's constant k_B.

[f] The rate of gas heating of the neutral by charge exchange is $k_{ce}(3/2)k_B(T_{ion}-T_g)$ eV-cm^3/s, for charge exchange rate coefficient k_{ce} and ion temperature T_{ion}.

[g] He* represents any He excited state. Ar^0* represents any Ar state (including ground state).

APPENDIX D LIST OF REACTIONS OF AR/CL$_2$

Species

Ar Ar(1s$_5$) Ar(1s$_4$) Ar(1s$_3$) Ar(1s$_2$)
Ar(4p)$^{a)}$ Ar(4d)$^{b)}$ Ar$^+$ Ar$_2$* Ar$_2^+$
Cl$_2$ Cl$_2$(v) Cl Cl(3p^{4}4s) Cl(3p^{4}4p) Cl(3p^{4}3d)
Cl$_2^+$ Cl$^+$ Cl$^-$ e
$h\nu_{105nm}$ $h\nu_{107nm}$ $h\nu_{121nm}$ $h\nu_{139nm}$

(Reactions involving only Ar species are the same as in Ref. [24])

Process	Rate Coefficient$^{c)}$	Reference	-ΔH (eV)$^{d)}$
Photoionization			
$h\nu_{139nm}$ + Ar(1s$_5$) → Ar$^+$ + e	9.97×10^{-20} cm^2	est. [1], e)	
$h\nu_{139nm}$ + Ar(1s$_4$) → Ar$^+$ + e	9.97×10^{-20} cm^2	est. [1], e)	
$h\nu_{139nm}$ + Ar(1s$_3$) → Ar$^+$ + e	9.97×10^{-20} cm^2	est. [1], e)	
$h\nu_{139nm}$ + Ar(1s$_2$) → Ar$^+$ + e	9.97×10^{-20} cm^2	est. [1], e)	
$h\nu_{139nm}$ + Ar(4p) → Ar$^+$ + e	1.0×10^{-19} cm^2	est. [1], e)	
$h\nu_{139nm}$ + Ar(4d) → Ar$^+$ + e	1.0×10^{-19} cm^2	est. [1], e)	
$h\nu_{105nm}$ + Cl(3p^{4}4s) → Cl$^+$ + e	9.6×10^{-20} cm^2	est. [1], e)	
$h\nu_{105nm}$ + Cl(3p^{4}4p) → Cl$^+$ + e	8.4×10^{-20} cm^2	est. [1], e)	
$h\nu_{105nm}$ + Cl(3p^{4}3d) → Cl$^+$ + e	8.7×10^{-20} cm^2	est. [1], e)	
$h\nu_{107nm}$ + Cl(3p^{4}4s) → Cl$^+$ + e	9.6×10^{-20} cm^2	est. [1], e)	
$h\nu_{107nm}$ + Cl(3p^{4}4p) → Cl$^+$ + e	8.4×10^{-20} cm^2	est. [1], e)	
$h\nu_{107nm}$ + Cl(3p^{4}3d) → Cl$^+$ + e	8.7×10^{-20} cm^2	est. [1], e)	
$h\nu_{121nm}$ + Cl(3p^{4}4s) → Cl$^+$ + e	9.0×10^{-20} cm^2	est. [1], e)	
$h\nu_{121nm}$ + Cl(3p^{4}4p) → Cl$^+$ + e	9.0×10^{-20} cm^2	est. [1], e)	
$h\nu_{121nm}$ + Cl(3p^{4}3d) → Cl$^+$ + e	9.0×10^{-20} cm^2	est. [1], e)	
$h\nu_{139nm}$ + Cl(3p^{4}4s) → Cl$^+$ + e	9.9×10^{-20} cm^2	est. [1], e)	
$h\nu_{139nm}$ + Cl(3p^{4}4p) → Cl$^+$ + e	9.9×10^{-20} cm^2	est. [1], e)	
$h\nu_{139nm}$ + Cl(3p^{4}3d) → Cl$^+$ + e	9.9×10^{-20} cm^2	est. [1], e)	
$h\nu_{105nm}$ + Cl$_2$ → Cl$_2^+$ + e	1.0×10^{-19} cm^2	est.	
$h\nu_{105nm}$ + Cl$_2$(v) → Cl$_2^+$ + e	1.0×10^{-19} cm^2	est.	
$h\nu_{105nm}$ + Cl → Cl$^+$ + e	1.0×10^{-19} cm^2	est.	
$h\nu_{107nm}$ + Cl$_2$ → Cl$^+$ + e	1.0×10^{-19} cm^2	est.	
$h\nu_{107nm}$ + Cl$_2$(v) → Cl$_2^+$ + e	1.0×10^{-19} cm^2	est.	
$h\nu_{107nm}$ + Cl → Cl$^+$ + e	1.0×10^{-19} cm^2	est.	
Radiative Transitions			
Cl(3p^{4}4s)↔ Cl	3.7×10^{5} s^{-1}	[17], f)	

Electron Impact Processes			
$e + Cl_2 \rightarrow Cl_2 + e$	g)	[32]	h)
$e + Cl_2 \rightarrow Cl + Cl^-$	g)	[32]	1.2
$e + Cl_2 \rightarrow Cl_2(v) + e$	g)	[32]	
$e + Cl_2 \rightarrow Cl + Cl + e$	g)	[32]	0.8
$e + Cl_2 \rightarrow Cl + Cl + e$	g)	[32]	5.8
$e + Cl_2 \rightarrow Cl_2^+ + e + e$	g)	[32]	
$e + Cl_2(v) \rightarrow Cl_2(v) + e$	g)	[32] i)	h)
$e + Cl_2(v) \rightarrow Cl + Cl^-$	g)	[32] i)	1.2
$e + Cl_2(v) \rightarrow Cl_2 + e$	g)	[32] j)	
$e + Cl_2(v) \rightarrow Cl + Cl + e$	g)	[32] i)	0.8
$e + Cl_2(v) \rightarrow Cl + Cl + e$	g)	[32] i)	5.7
$e + Cl_2(v) \rightarrow Cl_2^+ + e + e$	g)	[32] i)	
$e + Cl_2^+ \rightarrow Cl_2^+ + e$	g)	[33]	h)
$e + Cl \rightarrow Cl + e$	g)	[34]	h)
$e + Cl \leftrightarrow Cl(3p^44s)^+ e$	g), j)	[34]	
$e + Cl \leftrightarrow Cl(3p^44p)^+ e$	g),j)	[34]	
$e + Cl \leftrightarrow Cl(3p^43d)^+ e$	g),j)	[34]	
$e + Cl \rightarrow Cl^+ + e + e$	g)	[35]	
$e + Cl^+ \rightarrow Cl^+ + e$	g)	[33]	h)
$e + Cl(3p^44s) \rightarrow Cl(3p^44s) + e$	g)	[34]	h)
$e + Cl(3p^44s) \leftrightarrow Cl(3p^44p) + e$	g),e)	[9],j)	
$e + Cl(3p^44s) \leftrightarrow Cl(3p^43d) + e$	g),e)	[9],j)	
$e + Cl(3p^44s) \rightarrow Cl^+ + e + e$	g)	[10]	
$e + Cl(3p^44p) \rightarrow Cl(3p^44p) + e$	g)	[34]	h)
$e + Cl(3p^44p) \leftrightarrow Cl(3p^43d)^+ e$	g),e)	[9],j)	i)
$e + Cl(3p^44p) \rightarrow Cl^+ + e + e$	g)	[10]	
$e + Cl(3p^43d) \rightarrow Cl(3p^43d) + e$	g)	[34]	h)
$e + Cl(3p^43d) \rightarrow Cl^+ + e + e$	g)	[10]	
$e + Cl^- \rightarrow Cl + e + e$	g)	est.	
$e + Cl_2^+ \rightarrow Cl + Cl$	$1.0 \times 10^{-7} T_e^{-1/2}$	est. [36][37]	9.0
Heavy Particles Processes			
$Cl^- + Cl^+ \rightarrow Cl + Cl$	$1.0 \times 10^{-7} T_n^{1/2}$	est. [38]	
$Cl^- + Cl_2^+ \rightarrow Cl + Cl + Cl$	$1.0 \times 10^{-7} T_n^{1/2}$	est. [38]	7.9
$Cl + Cl_2(v) \leftrightarrow Cl + Cl_2$	$1.0 \times 10^{-10} T_n^{1/2}$	est., j)	0.07
$Cl_2 + Cl_2(v) \leftrightarrow Cl_2 + Cl_2$	$1.0 \times 10^{-10} T_n^{1/2}$	est, j.	0.07
$Cl^+ + Cl_2 \rightarrow Cl + Cl_2^+$	$5.4 \times 10^{-10} T_n^{1/2}$	est. [39]	k)
$Cl^+ + Cl_2(v) \rightarrow Cl + Cl_2^+$	$5.4 \times 10^{-10} T_n^{1/2}$	est. [39]	k)
$Cl^+ + Cl \rightarrow Cl + Cl^+$	$1.0 \times 10^{-9} T_n^{1/2}$	est.	k)
$Cl_2^+ + Cl_2 \rightarrow Cl_2 + Cl_2^+$	$0.8 \times 10^{-9} T_n^{1/2}$	est.	k)
$Cl_2^+ + Cl_2(v) \rightarrow Cl_2 + Cl_2^+$	$0.8 \times 10^{-9} T_n^{1/2}$	est.	j)
$Cl^- + Ar^+ \rightarrow Cl + Ar$	$1.0 \times 10^{-7} T_n^{1/2}$	est.	12.4

$Ar^* + Cl_2 \rightarrow Cl_2^+ + Ar + e$	$2.2 \times 10^{-10}\ T_n^{1/2}$	[40]	
$Ar^* + Cl_2(v) \rightarrow Cl_2^+ + Ar + e$	$2.2 \times 10^{-10}\ T_n^{1/2}$	[40]	
$Ar^* + Cl_2(v) \rightarrow Cl + Cl(3p^4 4s) + Ar$	$1.1 \times 10^{-10}\ T_n^{1/2}$	[40]	-0.5~2.7
$Ar^* + Cl \rightarrow Cl(3p^4 4s) + Ar$	$0.7 \times 10^{-11}\ T_n^{1/2}$	est.	2.7~5.8
$Ar^+ + Cl_2 \rightarrow Cl_2^+ + Ar$	$0.84 \times 10^{-10}\ T_n^{1/2}$	[39]	4.5
$Ar^+ + Cl_2 \rightarrow Cl^+ + Cl + Ar$	$0.64 \times 10^{-10}\ T_n^{1/2}$	[39]	-0.2
$Ar^+ + Cl_2(v) \rightarrow Cl_2^+ + Ar$	$0.84 \times 10^{-10}\ T_n^{1/2}$	[39]	4.6
$Ar^+ + Cl_2(v) \rightarrow Cl^+ + Cl + Ar$	$0.64 \times 10^{-10}\ T_n^{1/2}$	[39]	-0.1
$Ar^+ + Cl \rightarrow Cl^+ + Ar$	$2.0 \times 10^{-10}\ T_n^{1/2}$	[39]	3.0
$Cl + Cl + Ar \rightarrow Cl_2 + Ar$	$1.28 \times 10^{-32}\ cm^6s^{-1}$	est. [41],[42]	-3.2
$Cl + Cl + Cl \rightarrow Cl_2 + Cl$	$3.84 \times 10^{-32}\ cm^6s^{-1}$	est. [41],[42]	-3.2
$Cl + Cl + Cl_2 \rightarrow Cl_2 + Cl_2$	$2.00 \times 10^{-32}\ cm^6s^{-1}$	est. [41],[42]	-3.2
$Cl + Cl + Cl_2(v) \rightarrow Cl_2 + Cl_2$	$2.00 \times 10^{-32}\ cm^6s^{-1}$	est. [41],[42]	-3.1
$Cl(3p^4 4s) + Cl(3p^4 4s) \rightarrow Cl^+ + Cl + e$	$1.0 \times 10^{-9}\ T_n^{1/2}$	est.	
$Cl(3p^4 4s) + Cl(3p^4 4p) \rightarrow Cl^+ + Cl + e$	$1.0 \times 10^{-9}\ T_n^{1/2}$	est.	
$Cl(3p^4 4s) + Cl(3p^4 3d) \rightarrow Cl^+ + Cl + e$	$1.0 \times 10^{-9}\ T_n^{1/2}$	est.	
$Cl(3p^4 4p) + Cl(3p^4 4p) \rightarrow Cl^+ + Cl + e$	$1.0 \times 10^{-9}\ T_n^{1/2}$	est.	
$Cl(3p^4 4p) + Cl(3p^4 3d) \rightarrow Cl^+ + Cl + e$	$1.0 \times 10^{-9}\ T_n^{1/2}$	est.	
$Cl(3p^4 3d) + Cl(3p^4 3d) \rightarrow Cl^+ + Cl + e$	$1.0 \times 10^{-9}\ T_n^{1/2}$	est.	
$Cl(3p^4 4s) + Cl(3p^4 4s) \rightarrow Cl_2^+ + e$	$1.0 \times 10^{-10}\ T_n^{1/2}$	est.	
$Cl(3p^4 4s) + Cl(3p^4 4p) \rightarrow Cl_2^+ + e$	$1.0 \times 10^{-10}\ T_n^{1/2}$	est.	
$Cl(3p^4 4s) + Cl(3p^4 3d) \rightarrow Cl_2^+ + e$	$1.0 \times 10^{-10}\ T_n^{1/2}$	est.	
$Cl(3p^4 4p) + Cl(3p^4 4p) \rightarrow Cl_2^+ + e$	$1.0 \times 10^{-10}\ T_n^{1/2}$	est.	
$Cl(3p^4 4p) + Cl(3p^4 3d) \rightarrow Cl_2^+ + e$	$1.0 \times 10^{-10}\ T_n^{1/2}$	est.	
$Cl(3p^4 3d) + Cl(3p^4 3d) \rightarrow Cl_2^+ + e$	$1.0 \times 10^{-10}\ T_n^{1/2}$	est.	

m) Ar(4p) is a lumped state having excitation cross sections to Ar(4p,3d,5s,5p)

n) Ar(4d) is a lumped state has excitation cross sections to Ar(4d,6s,Rydberg)

o) Rate coefficients have units of cm^3s^{-1} unless noted. T_e is electron temperature (eV). T_g is gas temperature (K), T_n is normalized gas temperature (T_g/300 K).

p) -ΔH is the contribution to gas heating (eV).

q) Estimated from corresponding Ar photoionization reactions. Cross sections for higher levels were scaled based on energy of the ejected electron

r) Rate shown is for emission. Absorption is addressed using a radiation trapping factor. (See text.)

s) Rate coefficient obtained from electron energy distribution and cross section from the indicated reference.

t) The rate of heating by elastic collisions is $k_m(3/2)k_B(2m_e/M)(T_e-T_g)$ eV-cm^3/s, for elastic rate coefficient k_m, electron mass m_e, neutral mass M and Boltzmann's constant k_B.

u) Same cross section as as for Cl_2 while shifting threshold energy by 0.0689 eV for inelastic processes.

v) Cross section or rate is for forward reaction. Reverse cross section or rate obtained by detailed balance

w) The rate of heating exchange of energy between the neutral and ionized reaction partners..

APPENDIX E LIST OF REACTIONS OF SI ETCHING

M(s) surface site
M gas phase species
M$^+$ ion
M# hot neutral from neutralized ion
ϕ photon species]

Reactions$^{a)-c)}$	Probability : P_0	Threshold Energy (eV)	Ref., Footnote
$M^+ + M(s) \rightarrow M^\# + M(s)$	c)		d)
$M^\# + M(s) \rightarrow M^\# + M(s)$	c)		d)
$M(s) + Si \rightarrow M(s) + Si(s)$	c)		d)
$M(s) + \phi \rightarrow M(s)$	c)		d)
Chlorination Reactions			
$Si(s) + Cl \rightarrow SiCl(s)$	0.99		
$SiCl(s) + Cl \rightarrow SiCl_2(s)$	0.4		
$SiCl_2(s) + Cl \rightarrow SiCl_3(s)$	0.3		
$SiO_2(s) + Cl \rightarrow SiO_2Cl(s)$	0.1		
$SiO_2Cl(s) + Cl \rightarrow SiO_2Cl_2(s)$	0.1		
$Si(s) + SiCl \rightarrow Si(s) + SiCl(s)$	0.15		
$SiCl(s) + SiCl \rightarrow SiCl(s) + SiCl(s)$	0.15		
$SiCl_2(s) + SiCl \rightarrow SiCl_2(s) + SiCl(s)$	0.15		
$SiCl_3(s) + SiCl \rightarrow SiCl_3(s) + SiCl(s)$	0.15		
$SiO_2(s) + SiCl \rightarrow SiO_2(s) + SiCl(s)$	0.1		
$SiO_2Cl(s) + SiCl \rightarrow SiO_2Cl(s) + SiCl(s)$	0.1		
$SiO_2Cl_2(s) + SiCl \rightarrow SiO_2Cl_2(s) + SiCl(s)$	0.1		
$Si(s) + SiCl_2 \rightarrow Si_2Cl_2(s)$	0.9		
$SiCl(s) + SiCl_2 \rightarrow Si_2Cl_3(s)$	0.9		
$SiCl_2(s) + SiCl_2 \rightarrow Si_2Cl_4(s)$	0.9		
$SiCl_3(s) + SiCl_2 \rightarrow SiCl_3(s) + SiCl_2(s)$	0.15		
$SiO_2(s) + SiCl_2 \rightarrow SiO_2(s) + SiCl_2(s)$	0.05		
$SiO_2Cl(s) + SiCl_2 \rightarrow SiO_2Cl(s) + SiCl_2(s)$	0.05		
$SiO_2Cl_2(s) + SiCl_2 \rightarrow SiO_2Cl_2(s) + SiCl_2(s)$	0.05		
$Si(s) + SiCl_3 \rightarrow Si(s) + SiCl_3(s)$	0.15		
$SiCl(s) + SiCl_3 \rightarrow SiCl(s) + SiCl_3(s)$	0.15		
$SiCl_2(s) + SiCl_3 \rightarrow SiCl_2(s) + SiCl_3(s)$	0.15		

$SiCl_3(s) + SiCl_3 \rightarrow SiCl_3(s) + SiCl_3(s)$	0.15		
$SiO_2(s) + SiCl_3 \rightarrow SiO_2(s) + SiCl_3(s)$	0.1		
$SiO_2Cl(s) + SiCl_3 \rightarrow SiO_2Cl(s) + SiCl_3(s)$	0.1		
$SiO_2Cl_2(s) + SiCl_3 \rightarrow SiO_2Cl_2(s) + SiCl_3(s)$	0.1		
$Si\text{-}O(s) + Cl \rightarrow Si\text{-}OCl(s)$	0.3		
$Si\text{-}O(s) + SiCl \rightarrow Si\text{-}O(s) + SiCl(s)$	0.25		
$Si\text{-}O(s) + SiCl_2 \rightarrow Si\text{-}O(s) + SiCl_2(s)$	0.15		
$Si\text{-}O(s) + SiCl_3 \rightarrow Si\text{-}O(s) + SiCl_3(s)$	0.05		
$Si\text{-}OCl(s) + SiCl \rightarrow Si\text{-}OCl(s) + SiCl(s)$	0.25		
$Si\text{-}OCl(s) + SiCl_2 \rightarrow Si\text{-}OCl(s) + SiCl_2(s)$	0.15		
$Si\text{-}OCl(s) + SiCl_3 \rightarrow Si\text{-}OCl(s) + SiCl_3(s)$	0.05		
$Si_2Cl_2(s) + SiCl \rightarrow Si_2Cl_2(s) + SiCl(s)$	0.15		
$Si_2Cl_3(s) + SiCl \rightarrow Si_2Cl_3(s) + SiCl(s)$	0.15		
$Si_2Cl_4(s) + SiCl \rightarrow Si_2Cl_4(s) + SiCl(s)$	0.15		
$Si_2Cl_2(s) + SiCl_2 \rightarrow Si_2Cl_2(s) + SiCl_2(s)$	0.15		
$Si_2Cl_3(s) + SiCl_2 \rightarrow Si_2Cl_3(s) + SiCl_2(s)$	0.15		
$Si_2Cl_4(s) + SiCl_2 \rightarrow Si_2Cl_4(s) + SiCl_2(s)$	0.15		
$Si_2Cl_2(s) + SiCl_3 \rightarrow Si_2Cl_2(s) + SiCl_2(s)$	0.15		
$Si_2Cl_3(s) + SiCl_3 \rightarrow Si_2Cl_3(s) + SiCl_2(s)$	0.15		
$Si_2Cl_4(s) + SiCl_3 \rightarrow Si_2Cl_4(s) + SiCl_2(s)$	0.15		
$Si(s) + SiCl_2^+ \rightarrow Si_2Cl_2(s)$	0.5		e)
$SiCl(s) + SiCl_2^+ \rightarrow Si_2Cl_3(s)$	0.5		e)
$SiCl_2(s) + SiCl_2^+ \rightarrow Si_2Cl_4(s)$	0.5		e)
$SiO_2(s) + SiCl_2^+ \rightarrow SiO_2(s) + SiCl_2(s)$	0.01		e)
$SiO_2Cl(s) + SiCl_2^+ \rightarrow SiO_2Cl(s) + SiCl_2(s)$	0.01		e)
$SiO_2Cl_2(s) + SiCl_2^+ \rightarrow SiO_2Cl_2(s)+ SiCl_2(s)$	0.01		e)
$Si\text{-}O(s) + SiCl_2^+ \rightarrow Si\text{-}O(s) + SiCl_2(s)$	0.03		e)
$Si\text{-}OCl(s) + SiCl_2^+ \rightarrow Si\text{-}OCl(s) + SiCl_2(s)$	0.03		e)
$Si_2Cl_2(s) + SiCl_2^+ \rightarrow Si_2Cl_2(s) + SiCl_2(s)$	0.15		e)
$Si_2Cl_3(s) + SiCl_2^+ \rightarrow Si_2Cl_3(s) + SiCl_2(s)$	0.15		e)
$Si_2Cl_4(s) + SiCl_2^+ \rightarrow Si_2Cl_4(s) + SiCl_2(s)$	0.15		e)
Etching Reactions			
$SiCl_2(s) + Cl \rightarrow SiCl(s) + Cl_2$	0.02		
$SiCl_3(s) + Cl \rightarrow SiCl_4$	0.0001		[43]
$SiCl_3(s) + Cl \rightarrow SiCl_2(s) + Cl_2$	0.08		
$Si(s) + Cl^+ \rightarrow SiCl$	0.001	16	[44],e)
$Si(s) + Cl_2^+ \rightarrow SiCl_2$	0.001	16	[44],e)
$SiCl(s) + Cl^+ \rightarrow SiCl_2$	0.2	16	[44],e)
$SiCl_2(s) + Cl^+ \rightarrow SiCl_2 + Cl\#$	0.5	16	[44], e,f)
$SiCl_3(s) + Cl^+ \rightarrow SiCl_3 + Cl\#$	0.5	16	[44], e,f)

$SiCl(s) + Cl_2^+ \rightarrow SiCl_2 + Cl\#$	0.2	16	[44], e,f)
$SiCl_2(s) + Cl_2^+ \rightarrow SiCl_3 + Cl\#$	0.25	16	[44], e,f)
$SiCl_3(s) + Cl_2^+ \rightarrow SiCl_3 + Cl_2\#$	0.25	16	[44], e,f)
$SiCl_3(s) + Cl_2^+ \rightarrow SiCl_4 + Cl\#$	0.25	16	[44], e,f)
$SiCl(s) + Ar^+ \rightarrow SiCl + Ar\#$	0.2	16	[44], e,f)
$SiCl_2(s) + Ar^+ \rightarrow SiCl_2 + Ar\#$	0.5	16	[44], e,f)
$SiCl_3(s) + Ar^+ \rightarrow SiCl_3 + Ar\#$	0.5	16	[44], e,f)
$SiO_2Cl_2(s) + Ar^+ \rightarrow Si\text{-}O(s) + SiCl_2 + Ar$	0.025	20	e,f)
$SiO_2Cl_2(s) + Cl^+ \rightarrow Si\text{-}O(s) + SiCl_2 + Cl$	0.025	20	e,f)
$SiO_2Cl_2(s) + Cl_2^+ \rightarrow Si\text{-}O(s) + SiCl_2 + Cl_2$	0.025	20	e,f)
$Si\text{-}OCl(s) + Ar^+ \rightarrow Si(s) + ClO + Ar$	0.025	20	e,f)
$Si\text{-}OCl(s) + Cl^+ \rightarrow Si(s) + ClO + Cl$	0.025	20	e,f)
$Si\text{-}OCl(s) + Cl_2^+ \rightarrow Si(s) + ClO + Cl_2$	0.025	20	e,f)
$Si_2Cl_2(s) + Cl \rightarrow SiCl(s) + SiCl_2$	0.008		
$Si_2Cl_3(s) + Cl \rightarrow SiCl(s) + SiCl_2 + Cl$	0.008		
$Si_2Cl_4(s) + Cl \rightarrow SiCl_2(s) + SiCl_2 + Cl$	0.008		
$Si_2Cl_2(s) + Cl^+ \rightarrow SiCl(s) + SiCl_2$	0.9		e)
$Si_2Cl_3(s) + Cl^+ \rightarrow SiCl(s) + SiCl_2 + Cl$	0.99		e)
$Si_2Cl_4(s) + Cl^+ \rightarrow SiCl_2(s) + SiCl_2 + Cl$	0.99		e)
$Si_2Cl_2(s) + Ar^+ \rightarrow Si(s) + SiCl_2 + Ar$	0.9		e)
$Si_2Cl_3(s) + Ar^+ \rightarrow SiCl(s) + SiCl_2 + Ar$	0.99		e)
$Si_2Cl_4(s) + Ar^+ \rightarrow SiCl_2(s) + SiCl_2 + Ar$	0.99		e)
$Si_2Cl_2(s) + Cl_2^+ \rightarrow Si(s) + SiCl_2 + Cl_2\#$	0.6		e)
$Si_2Cl_3(s) + Cl_2^+ \rightarrow SiCl(s) + SiCl_2 + Cl_2\#$	0.6		e)
$Si_2Cl_4(s) + Cl_2^+ \rightarrow SiCl_2(s) + SiCl_2 + Cl_2\#$	0.6		e)
Photon-Assisted Etching Reactions			
$SiCl(s) + \phi(105\ nm) \rightarrow SiCl$	0.1		g)
$SiCl(s) + \phi(106\ nm) \rightarrow SiCl$	0.1		g)
$SiCl(s) + \phi(139\ nm) \rightarrow SiCl$	0.1		g)
$SiCl_2(s) + \phi(105\ nm) \rightarrow SiCl_2$	0.2		g)
$SiCl_2(s) + \phi(106\ nm) \rightarrow SiCl_2$	0.2		g)
$SiCl_2(s) + \phi(139\ nm) \rightarrow SiCl_2$	0.2		g)
$SiCl_3(s) + \phi(105\ nm) \rightarrow SiCl_3$	0.2		g)
$SiCl_3(s) + \phi(106\ nm) \rightarrow SiCl_3$	0.2		g)
$SiCl_3(s) + \phi(139\ nm) \rightarrow SiCl_3$	0.2		g)

[a] Unless specified, all ions neutralize on surfaces, returning as their neutral counterparts

[b] Gas phase species have units of flux (cm-2s-1). Surface species have units of fractional coverage.

[c] This is the default reaction of other material altering reactions do not occur.

[d] Reactions are applicable to all surfaces unless otherwise noted.

[e] All reactions of ions are applicable to corresponding hot neutrals.

f) When threshold energy (E_{th}) is not zero, reaction probability (P_e) is a function of ion incident energy (E_{in}) with a reference energy (E_{ref}) of 100 eV:

$P_e = P_0 \times (E_{in} - E_{th})^{0.5}/(E_{ref} - E_{th})^{0.5} \times$ Angular yield

g) See text.

APPENDIX REFERENCES

[1] K.J. McCann, and M.R. Flannery, Appl. Phys. Lett. **31**, 599 (1977).

[2] G. M. Lawrence, Phys. Rev. **175**, 40 (1968).

[3] N. A. Dyatko, Y. Z. Ionikh, I. V. Kochetov, D. L. Marinov, A. V. Meshchanov, A. P. Napartovich, F. B. Petrov, and S. A. Starostin, J. Phys. D. **41**, 055204 (2008).

[4] F. Kannari, M. Obara, and T. Fujioka, J. Appl. Phys. **57**, 4309 (1985).

[5] M. Hayashi, Nagoya Institute of Technology Report, No.IPPJ-AM-19, 1991.

[6] G. M. Petrov, J. L. Giuliani, and A. Dasgupta, J. Appl. Phys. **91**, 2662 (2002).

[7] D. Rapp, and P. Englander-Golden, J. Chem. Phys. **43**, 1464 (1965).

[8] A. Bogaerts, R. Gijbels, and J. Vlcek, J. Appl. Phys. **84**, 121, (1988).

[9] J. Vlcek, J. Phys. D **22**, 623 (1989).

[10] L. Vriens, Phys. Lett. **8**, 260 (1964).

[11] M. A. Biondi in “Principles of Laser Plasmas” ed. G. Bekefi (Wiley, New York, 1976), Ch. 4.

[12] W. W. Ellis, R. Y. Pai, E. W. McDaniel, E. A. Mason, and L. A. Viehland, At. Data Nucl. Data Tables **17**, 177 (1976).

[13] A. Bogaerts, and R. Gijbels, J. Appl. Phys. **86**, 4124 (1999).

[14] P. M. Becker, and F. W. Lampe, J. Chem. Phys. **42**, 2857 (1965).

[15] R. Johnsen, A. Chen, and M. A. Biondi, J. Chem. Phys. **73**, 1717 (1980).

[16] P. Lukac, O. Mikus, I. Morva, Z. Zabudla, J. Trnovec, and M. Morvova, Plasma Source Sci. Technol. **20**, 055012 (2011).

[17] http://www.nist.gov/pml/data/asd.cfm.

[18] M. Ohwa, T. J. Moratz and M. J. Kushner, J. Appl. Phys, **66**, 5131 (1989).

[19] H. Hokazono, K. Midorikawa, M. Obara, and T. Fujioka J. Appl. Phys. **56**, 680 (1984).

[20] Biagi-v8.9 Database, www.lxcat.net, retrieved on July 2, 2012.

[21] R. Deloche, P. Monchicourt, M. Cheret, and F. Lambert, Phys. Rev. A **13**, 1140 (1976).

[22] K. Niemi, J. Waskoenig, N. Sadeghi, T. Gans, and D O'Connell, Plasma Sources Sci. Technol. **20**, 055005 (2011).

[23] A. W. Johnson, and J. B. Gerardo, Phys. Rev. A **5**, 1410 (1972).

[24] T. J. Miller, P. R. A. Farquhar, and K. Willacy, Astron. Astrophys. Suppl. Ser. **121**, 139 (1997).

[25] F. Emmert, H. H. Angermann, R. Dux, and H. Langhoff, J. Phys. D **21**, 667 (1988).

[26] W. Lindinger, A. L. Schmeltekopf, and F. C. Fehsenfeld, J. Chem. Phys. **61**, 2890 (1974).

[27] A. L. Schmeltekopf, and F. C. Fehsenfeld, J. Chem. Phys. **53**, 3173 (1970).

[28] J. D. C. Jones, D. G. Lister, and N. D. Twiddy, J. Plas. Phys. **12**, 2723 (1979).

[29] F. C. Fehsenfeld, A. L. Schmeltekopf, P. D. Goldan, H. I. Schiff, and E. E. Ferguson, J. Chem. Phys. **44**, 4087 (1966).

[30] D. K. Bohme, N. G. Adams, M. Mosesman, D. B. Dunkin, and E. E. Ferguson, J. Chem. Phys. **52**, 5094 (1970).

[31] D. C. Lorents, D. J. Eckstrom and D. Huestis, "Excimer and Decay Processes in Rare Gases" Stanford Research Institute, Report No. N00014-72-C-0457, Sept. 1973.

[32] G. L. Rogoff, J. M. Kramer and R. B. Piejak, Trans. Plasma Sci. **14**, 103 (1986)

[33] M. Mitchner and C. H. Kruger, Partially Ionized Gases (Wiley, New York, 1973), p. 255.

[34] P. S. Ganas, J. Appl. Phys. **63**, 277 (1988).

[35] E. S. Aydil and D. J. Economou, J. Electrochem. Soc. **139**, 1396 (1992).

[36] J. B. A. Mitchell, Phys. Rep. **186**, 215 (1990).

[37] A. I. Florescu-Mitchell and J. B. A. Mitchell, Phys. Rep. (2006).

[38] M. J. Church and D. Smith , J. Chem Phys. **98** 8660 (1993)

[39] Y. Ikezoe, S. Matsuoka, M. Takabe, and A. Viggiano, Gas Phase IonMolecule Reaction Rate Constants Through 1986 (Mass Spectroscopy Society of Japan, Tokyo, 1987).

[40] L. A. Gundel, D. W. Setser, M. A. A. Clyne, J. A. Coxon and W. Nip, J. Chem. Phys. **64**, 4390 (1976).

[41] A. C. Lloyd, Int. J. Chem. Kinet. **3**, 39 (1971).

[42] N. L. Bassett and Demetre J. Economou, J. Appl. Phys. **75**, 1931 (1994).

[43] J. P. Chang, J. C. Arnold, G. C. H. Zau, H-S. Shin, and H. H. Sawin, J. Vac. Sci. Technol. A **15**, 1853 (1997)

[44] H. Shin, W. Zhu, V. M. Donnelly, and D. J. Economou, J. Vac. Sci. Technol. A **30**, 021306 (2012).